From grains to planetesimals

the microphysics of dust coagulation

ISBN: 978-94-6259-630-6
Printed by Ipskamp Drukkers

Cover: Dust aggregates growing above Prague. Background image credit: ALMA (ESO/NAOJ/NRAO)/M. Kornmesser (ESO)

From grains to planetesimals

the microphysics of dust coagulation

Proefschrift

ter verkrijging van
de graad van Doctor aan de Universiteit Leiden,
op gezag van de Rector Magnificus prof. mr. C. J. J. M. Stolker,
volgens besluit van het College voor Promoties
te verdedigen op woensdag 29 april 2015
klokke 13.45 uur

door

Sebastiaan Krijt

geboren te Leidschendam, Nederland
in 1987

Promotiecommissie

Promotores:	Prof. dr. A. G. G. M. Tielens
	Prof. dr. C. Dominik
Overige leden:	Prof. dr. H. J. A. Röttgering
	Prof. dr. T. Henning
	Prof. dr. C. P. Dullemond
	Prof. dr. H. Tanaka
	Dr. M. R. Hogerheijde

"I believe that we do not know anything for certain, but everything probably."
– Christiaan Huygens

Contents

1

Introduction

We live in an exciting time. The discovery of an enormous number of exoplanets (planets that revolve around stars other than the Sun) marks one of the most important scientific findings of this age. Since the detection of the first exoplanet around a main-sequence star approximately 20 years ago (Mayor & Queloz 1995), over 1800 have now been detected, and it is becoming clear that the universe is teeming with planets. On average, every star has a planetary system, and every 5^{th} Sun-like star is orbited by an Earth-like planet.

Already in 1695, Dutch astronomer Christiaan Huygens reached a similar conclusion, though not supported by observations. In his *Cosmotheoros*, he wrote:

> "What a wonderful and amazing Scheme have we here of the magnificent Vastness of the Universe! So many Suns, so many Earths, and every one of them stock'd with so many Herbs, Trees and Animals, and adorn'd with so many Seas and Mountains! And how must our wonder and admiration be encreased when we consider the prodigious distance and multitude of the Stars?"

Huygens' vision was spot on. Little over three centuries later, we have indeed discovered many Suns and many Earths. On planets we could study up close, we have discovered Seas (though none of them made of liquid water) and Mountains.

But we have discovered more than just Earths; we have discovered a very diverse population of exoplanets. Fig. 1.1 shows the masses and semi-major axes of all known exoplanets as of January 13, 2015. The Earth ($\oplus$) and the Jovian planets (Jupiter, Saturn, Uranus, and Neptune) are shown for comparison. Planets appear to come in a lot of varieties; some very massive and on very wide orbits, others much smaller and on orbits with periods of only several days. Of particular interest are planets that are located in the *habitable zone*, i.e., at a distance from their star where the temperature is such that

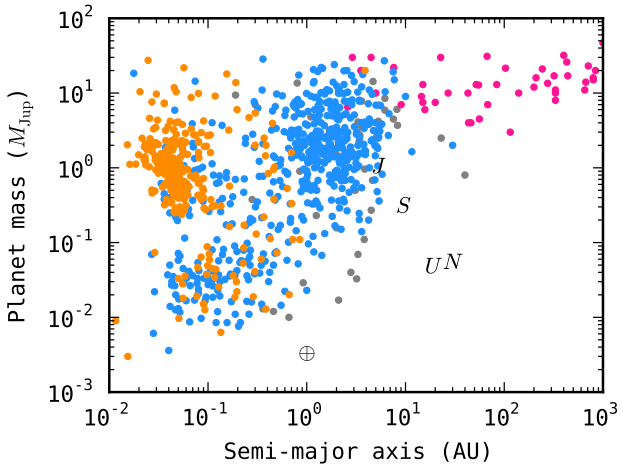

Figure 1.1: Mass and separation of all 1876 exoplanets known as of January 13, 2015. Color-coding indicates detection method: transit (●); radial velocity (●); direct imaging (●); and other methods (●). The Earth and Jovian planets are indicated as well. Data from `http://exoplanet.eu/`.

it allows the presence of liquid water. As of January 2015, 8 small rocky exoplanets have been discovered that lie in the habitable zone of their parent star, and it is estimated that 22% of Sun-like stars have a Earth-sized planet orbiting within their habitable zone (Petigura et al. 2013). If life elsewhere resembles life as we know it, these worlds should be good places to look for Huygens' Herbs, Trees, and Animals.

With the realization that planetary systems are common and planets in the habitable zone are widespread, come questions about their formation. How are planets made? What determines their characteristics? Today, astronomers have a coarse picture of how planets are created, though many details prove elusive. The general paradigm dictates that planet formation takes place inside protoplanetary disks, the left-overs of the star formation process. These disks, with sizes up to several 100 AU, consist of mostly hydrogen gas, and live for several million years. In the disk, the wide variety of gas densities, temperatures, and intensities of stellar radiation, give rise to complex chemistry, and the presence of many different molecules, including water, has been confirmed observationally in disks around young stars. A small fraction of the disk's mass (∼1%) is accounted for by microscopic dust particles. Suspended in the gaseous nebula, these dust particles collide and coalesce, growing into aggregates, then boulders, planetesimals, and eventually planetary embryos. The embryos have sufficient gravity to capture gas from the nebula, and start to form primitive atmospheres. Eventually, the embryos merge to form fully-grown planets. The full journey from dust grain to planet constitutes an increase in mass of over 36 orders of magnitude, and takes place over millions of years.

The key unanswered questions in planet formation are then: what are the key processes that make this growth possible, and how do they depend on environment? What is the inventory of planets, and in particular, of planets in the habitable zone? Focussing

on the planet's atmosphere and potential to harbor life: what are the principle sources of organics and volatiles, and what are the processes that played a role in their delivery?

In this thesis, we focus on the first - and least understood - step in the planet-formation process: the coagulation, through successive sticking collisions, of microscopic dust particles into planetary building blocks several kilometers across (planetesimals). The structure of the protoplanetary disk, as well as the composition, size, and shape of the dust particles determine the efficiency of this growth process. In particular, the dust grain *porosity* (a measure for the internal density) plays an central role. For compact particles, current theories predict several growth barriers, making it very difficult for them to gain mass and grow larger than a meter in size. In fact, were it not for the observed ubiquity of exoplanets, one might be tempted to conclude that planetesimal formation is a hopeless endeavor. However, recent studies suggest dust grains might not be compact at all, but rather form very open, porous structures. These porous aggregates behave very differently from compact ones - both aerodynamically and mechanically. As a result, some of the growth barriers that limit the growth of compact particles might not apply to highly porous ones.

The principle objective of this thesis is to understand how the microphysics of initially tiny dust grains influence their potential to coagulate into macroscopic planetesimals. In other words, how does a grain's (collisional) history determine its porosity, and how does that porosity influence the grain's future? To answer these questions, we start at the smallest scales, and slowly work our way up. Chapters 2 and 3 deal with the adhesive contact between micrometer-size spheres, and describe the forces and energies needed to break and re-arrange single adhesive bonds. In Chapter 4, porous dust coagulation is modeled in detail in a localized part of the protoplanetary nebula. Then, in Chapter 5, we address the global dust evolution in a full protoplanetary disk, directly connecting the microphysics of the growing aggregates to the eventual formation of a population of planetesimals. Chapter 6 focusses on small dust grains in evolved debris disks: the relics of planet-forming disks.

In the remainder of the introduction, the general concepts of star- and planet formation (Sect. 1.1) and the perilous journey from dust grain to planetesimal (Sect. 1.2) are described. Dust microphysics, and its importance to the early stages of planet formation, is described in Sect. 1.3, and an outline of this thesis is presented in Sect. 1.4.

1.1 Overview of the planet formation process

The standard theory of planet formation is that planets form out of a thin disk of gas and dust that surrounds young stars (Safronov 1972; Goldreich & Ward 1973). These protoplanetary disks, or accretion disks, are the natural by-products of star formation, and their structure was first described by Shakura & Sunyaev (1973) and Lynden-Bell & Pringle (1974). The main stages of star- and planet-formation, as they are believed to occur in isolated and low-mass systems, are depicted in Fig. 1.2.

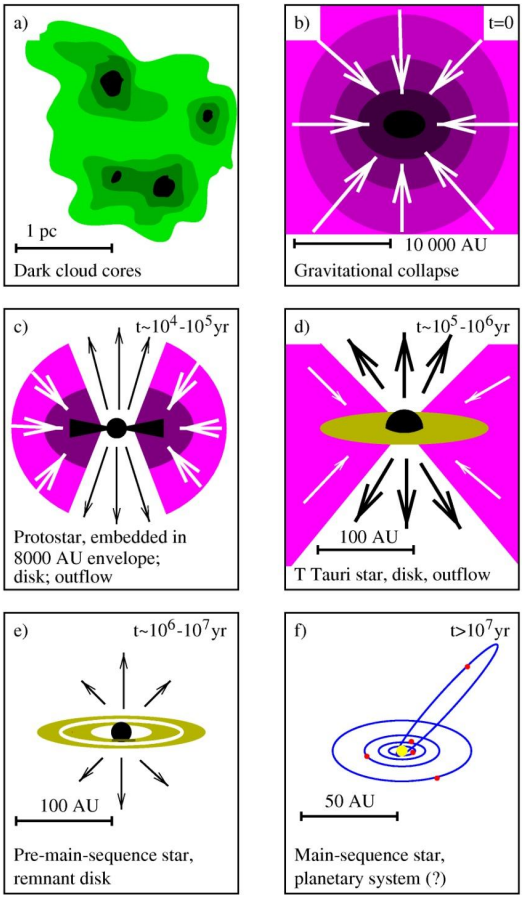

Figure 1.2: Schematic of the star- and planet formation process for low-mass stars. (a) Molecular clouds, composed of mostly hydrogen gas, form dark and cold cores. (b) When cores become massive enough, they collapse under their own gravity. (c) The cloud's non-zero angular momentum prevents the material from accreting onto the core, forming an accretion disk. The accretion rate is very high and angular momentum is removed by a (radial) outflow. (d) Accretion is slowing down, and the protoplanetary disk, with a typical size of ~100 AU is clearly visible. (e) The gas in the protoplanetary disk is slowly dissipated. At the same time, dust particles are colliding, coagulating into larger grains, and potentially forming planetary building blocks. (f) A planetary system has formed. Figure from Hogerheijde (1998), after Shu et al. (1987).

1.1.1 Protoplanetary disk formation and structure

Low-mass stars form out of the gravitational collapse of the cold, dense cores of molecular clouds (Fig. 1.2a). These cores, with sizes $\lesssim$0.1 pc, consist mainly of H_2 gas, with about 1% of their mass present in the form of dust. The temperatures are around $T \sim 10-20$ K,

and gas number densities are of the order of $n \sim 10^4 - 10^5$ cm^{-3}. When such a core becomes massive enough, the gas pressure can no longer support its self-gravity, and the core will start to collapse. The critical mass above which clouds become unstable is called the Jeans mass

$$M_{\rm J} \simeq 2.9\ M_\odot \left(\frac{T}{10\ {\rm K}}\right)^{3/2} \left(\frac{n}{10^4\ {\rm cm}^{-3}}\right)^{-1/2}. \tag{1.1}$$

Thus, the typical mass of an unstable core is close to the mass of our Sun. When a core exceeds the Jeans mass, it will start to collapse on a timescale comparable to the free-fall timescale

$$t_{\rm ff} \sim (G\rho)^{-1/2} \sim 10^5\ {\rm yr} \left(\frac{n}{10^4\ {\rm cm}^{-3}}\right)^{-1/2}, \tag{1.2}$$

with G the gravitational constant and $\rho = n\mu m_{\rm H}$ the gas density, written in terms of the mean molecular mass $\mu \simeq 2.34$ and the hydrogen mass $m_{\rm H}$. The collapse of a protostellar core is depicted in Fig. 1.2b. Describing the collapsing core as a sphere of uniform density in solid body rotation, and assuming typical ratio of rotational to gravitational energy of $\beta = 0.02$, we obtain a total angular momentum of $J_{\rm core} \sim 10^{54}$ g cm^2 s^{-1}, and a specific angular momentum of $l_{\rm core} \sim J_{\rm core}/M_\odot \sim 10^{20}$ cm^2 s^{-1}. Because of conversation of angular momentum, the infalling material will create a rotationally supported disk (Fig. 1.2c), the size of which can be estimated by looking at the specific angular momentum in a Keplerian disk

$$R_{\rm disk} = \frac{l_{\rm core}^2}{GM_\odot} \sim 100\ {\rm AU}. \tag{1.3}$$

These disks, dubbed circumstellar disks, protoplanetary disks, or protoplanetary nebula, are believed to be the sites of planet formation. The protoplanetary disk is clearly visible during phases d) and e) of Fig. 1.2, but might already be present in the earlier phases (e.g., Tobin et al. 2012; Murillo et al. 2013).

Assuming the disk is more or less axisymmetric, the general structure is described by a temperature $T(R, z)$ and density $\rho_{\rm g}(R, z)$, both functions of the radial distance to the star R, and the height above the midplane z. We focus first on the vertical structure. The gas is orbiting perpendicular to z, so there is no angular momentum keeping the gas from falling to the midplane as a result of the vertical component of the central star's gravity. Thus, for the disk to be supported vertically, a pressure gradient has to balance the gravitational force

$$c_s^2 \frac{{\rm d}\rho_{\rm g}}{{\rm d}z} = -\frac{GM_\star z}{(R^2 + z^2)^{3/2}} \rho_{\rm g}, \tag{1.4}$$

with c_s the sound-speed, and $M_\star$ the mass of the central star. Assuming that the disk is vertically isothermal, i.e., $T(R, z) = T(R)$, and relatively flat, $z \ll R$, the solution can be obtained as

$$\rho(z) = \rho_{\rm g,0} \exp\left(-z^2/2h_{\rm g}^2\right), \tag{1.5}$$

with $\rho_{\rm g,0}$ the density in the midplane, $h_{\rm g} \equiv c_s/\Omega$ the vertical disk scale height, and $\Omega = (GM_\star/R^3)^{1/2}$ the Kepler frequency. The temperature structure can be approximated by a simple power law

$$T(R) = T_0 \left(\frac{R}{R_c}\right)^{-q}\ {\rm K}. \tag{1.6}$$

For optically thin disks, the radiation flux directly received by a part of the disk scales as $\mathcal{F} \propto 1/R^2$. Since $\mathcal{F} \propto T^4$, this results in an exponent $q = 1/2$ for the temperature power law. Similar values have been found observationally (e.g., Andrews & Williams 2005). Then, since $h_\mathrm{g} = c_s/\Omega$ and $c_s = (k_\mathrm{B}T/\mu m_\mathrm{H})^{1/2}$, we obtain $h_\mathrm{g}/R \propto R^{1/4}$, i.e., the 'opening angle' of the disk increases with radius; such disks are dubbed flaring disks. More complex models for the disk temperature can be constructed by taking into account radiative transfer, accretion, and dust opacities. Such models typically find that the midplane is considerably colder than the surface layer of the disk, as stellar photons with short wavelengths cannot penetrate this deep (e.g., Dullemond et al. 2007). The wide range of densities, temperatures, and UV-intensities leads to a wide range of complex chemistry, and variation in the gas-ice balance of volatiles (e.g., Dutrey et al. 2014; Pontoppidan et al. 2014). Of special importance for the dust evolution is the *snowline*, the location in the protoplanetary disk behind which volatiles freeze out onto solid dust grains. The resulting icy grains have very different sticking properties from bare silicate grains, which greatly influences their collisional evolution (Sect. 1.2). The location of the snow line depends on the stellar parameters and structure of the disk and the dust within it, but typically $R_\mathrm{snow} \sim 3$ AU (Min et al. 2011).

By integrating over the vertical direction, we obtain the gas surface density

$$\Sigma_\mathrm{g}(R) = \int_\infty^\infty \rho_\mathrm{g}(R,z)\,\mathrm{d}z = \sqrt{2\pi}\rho_{\mathrm{g},0}h_\mathrm{g}. \tag{1.7}$$

It is customary to describe the gas surface density with a truncated powerlaw (Lynden-Bell & Pringle 1974; Hartmann et al. 1998a)

$$\Sigma_\mathrm{g}(R) = \Sigma_0\left(\frac{R}{R_c}\right)^{-\gamma}\exp\left[-\left(\frac{R}{R_c}\right)^{2-\gamma}\right], \tag{1.8}$$

although observational constraints on the form of $\Sigma_\mathrm{g}(R)$ are poor, especially in the outer regions of the disk. The total disk mass equals

$$M_\mathrm{D} = 2\pi\int_0^\infty R\Sigma_\mathrm{g}\,\mathrm{d}R = \frac{2\pi}{(2-\gamma)}\Sigma_0 R_c^2 \tag{1.9}$$

provided $\gamma \neq 2$. The critical radius R_c is of the order of R_disk (Eq. 1.3), and there are several ways of constraining γ and/or M_D. One is to look at how the solids are distributed in our own Solar System. By looking at the radial distribution of solids (mostly rocky planets and the cores of gas giants), and assuming a dust-to-gas ratio of 10^{-2}, one finds that $\Sigma(R) = R^{-3/2}$ is fairly accurate within 30 AU (the location of Neptune), with $\Sigma_\mathrm{g}(1\ \mathrm{AU}) = 1.7\times10^3\ \mathrm{g\ cm^{-3}}$ (Weidenschilling 1977b; Hayashi 1981). This model is called the Minimum Mass Solar Nebula (MMSN), and yields a total disk mass of $\sim10^{-2}M_\odot$. However, the MMSN model assumes a number of things that are not necessarily true; for example, it assumes the majority of solids originally present in the disk ended up in planets, and that these planets did not move (migrate) significantly after their formation. From observations, one finds $M_\mathrm{D}/M_\odot \simeq 10^{-3} - 0.2$ and $\gamma \simeq 0.9$ around Sun-like stars (Andrews et al. 2009).

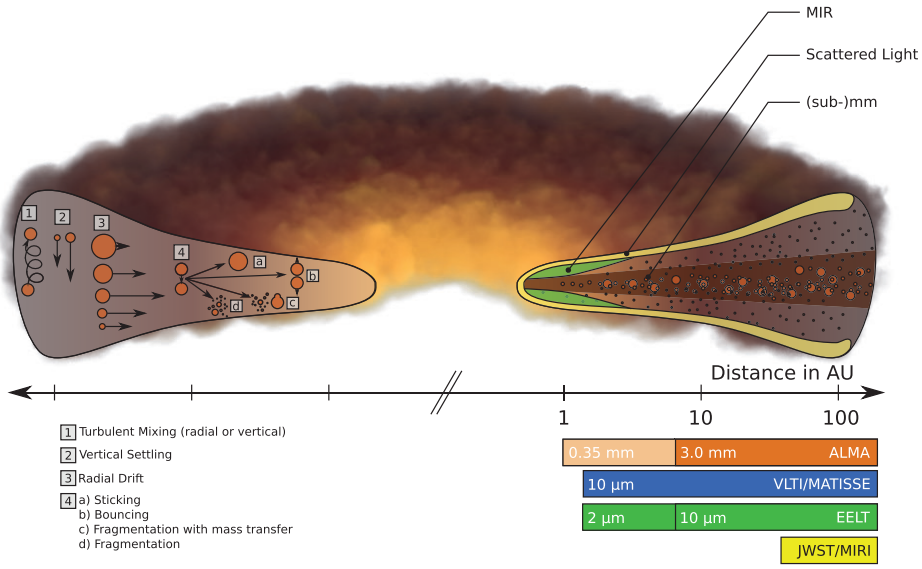

Figure 1.3: Schematic of a turbulent protoplanetary disk. On the left, various grain processes are illustrated: turbulent diffusion (1); settling (2); radial drift (3); and grain-grain collisions with different outcomes (4). On the right, the colored areas indicate which regions of the disk can be probed by which instrument/telescope. Figure from Testi et al. (2014).

If the gas disk itself is very massive, it can become gravitationally unstable, and collapse or fragment. The strength of the disk's self-gravity is described by the Toomre parameter

$$Q_{\rm T} \equiv \frac{c_s \Omega}{\pi G \Sigma}, \tag{1.10}$$

and disks with $Q_{\rm T} \geq 1$ are unstable. This condition can be rewritten as $M_{\rm D}/M_\star \gtrsim h_{\rm g}/R$. Typically $h_{\rm g}/R = 0.05 - 0.1$, and gravitational instability will only occur for the most massive disks.

1.1.2 Gas and dust evolution

The picture sketched in the previous paragraph might suggest the protoplanetary disk is a static, quiet environment. It is, however, anything but. The majority of protoplanetary disks are accreting matter onto the central star, with typical accretion rates anywhere between $\dot{M} \sim 10^{-10} - 10^{-7}\ M_\odot\ {\rm yr}^{-1}$ (e.g., Muzerolle et al. 2000). The accretion rate, and the timescale on which disks evolve in general, are related to the disk viscosity.

One source of viscosity are collisions between molecules; the resulting molecular viscosity equals $\nu_{\rm mol} \sim c_s \lambda_{\rm mfp}$, with $\lambda_{\rm mfp} \sim \mu m_{\rm H}/\rho_{\rm g}\sigma_{\rm mol}$ the gas molecule mean free path, and $\sigma_{\rm mol} \simeq 2 \times 10^{-15}\ {\rm cm}^2$ the molecular cross section. Plugging in the numbers for an MMSN disk, we obtain $\nu_{\rm mol} \sim 10^5\ {\rm cm}^2\ {\rm s}^{-1}$. This results in a viscous timescale

of $t_{\rm vis} \sim R^2/\nu_{\rm mol} \sim 10^{13}$ yr, much longer than the timescales on which gas disks evolve (Sect. 1.1.4). Clearly, other sources of viscosity must be present. Without, for now, specifying the source, it is instructive to assume an effective, turbulent viscosity, which can be parametrized as (Shakura & Sunyaev 1973)

$$\nu_{\rm T} = \alpha c_s^2/\Omega, \tag{1.11}$$

with α a dimensionless parameter governing the strength of the turbulence. In this description, energy is put in at the largest scales (fluctuations with a size L, that evolve on timescales t_L), and trickles down to smaller scales. It makes sense to assume the turn-over time of the largest eddies is set by the orbital period, i.e., $t_L \sim \Omega^{-1}$. These largest eddies have velocities of $v_L = L/t_L$, and because $Lv_L \sim \nu_{\rm T}$, this leads to $v_L \simeq \alpha^{1/2} c_s$. At the bottom of the Kolmogorov cascade, the smallest eddies have a characteristic timescale $t_\eta = {\rm Re}^{-1/2} t_L$, where ${\rm Re} = \nu_{\rm T}/\nu_{\rm mol} \gg 1$ is the turbulence Reynolds number. For a steady-state accretion disk, one can show that $\dot{M} = 3\pi\Sigma_{\rm g}\nu_{\rm T}$. Thus, if α does not vary with radius, we find $\gamma = 1$ for the exponent of the surface density. Inserting numbers appropriate for an MMSN-like disk at 30 AU, one finds $\alpha \simeq 10^{-2}$ corresponds to an accretion rate of $10^{-7}\ M_\odot\ {\rm yr}^{-1}$, and a viscous timescale of about a million years.

The parametrization of Eq. 1.11 is very idealized and might not be accurate depending on the mechanism driving the turbulence. Furthermore, even if the turbulence can be parametrized locally, the strength of the turbulence (i.e., α) need not be constant in the radial and vertical direction. Various candidates have been proposed as sources for the turbulent viscosity, including self-gravity (Gammie 2001), magneto rotational instability (MRI) (Balbus & Hawley 1991), and baroclinic vortices (Klahr & Bodenheimer 2003; Klahr 2004). The current understanding of turbulence in relation to accretion in protoplanetary disks is reviewed in Turner et al. (2014).

Apart from accreting onto the central star, several other disk dispersal mechanisms are at work, including disk photo-evaporation and disk winds. A recent review on disk dispersal mechanisms is given by Alexander et al. (2014). Observations indicate a disk lifetime of ∼3 Myr (Sect. 1.1.4), and put constraint on the efficiency of the disk removal mechanisms, but also on the timescales of giant planet formation, which must take place *before* the gas is dissipated (Pollack et al. 1996). Crudely, planet formation can be split into two stages: the formation of planetesimals out of microscopic dust grains (e.g., Testi et al. 2014; Johansen et al. 2014); and the subsequent formation of planets out of said planetesimals (e.g., Raymond et al. 2014). The word planetesimal usually refers to solid bodies with sizes of $\gtrsim$km, approximately the size above which self-gravity starts to play a role for their further evolution. Sect. 1.2 expands upon the journey from dust grain to planetesimal.

1.1.3 Evolved systems

After the disk gas has been removed, hopefully, a 'naked' planetary system remains (Fig. 1.2f). This phase lasts for the remainder of the lifetime of the central star, around ∼10 Gyr for Sun-like stars.

Planetary systems

A large number of exoplanets has now been discovered and characterized with a variety of observational techniques (Fig. 1.1), and it is held that the average star in our galaxy is orbited by several planets (Lissauer et al. 2011). These findings challenge, and put to the test current models of planet formation, which have to explain the high occurrence rate and diversity of observed (exo)planets.

One example is the discovery of so-called *hot Jupiters*: planets with a mass comparable to Jupiter's on tight compact orbits, with orbital periods that can be as short as several days (the planets in the upper left part of Fig. 1.1). In an MMSN-like disk, these inner regions of a protoplanetary disk do not hold enough mass to form Jupiter-size planets. The existence of these hot Jupiters led to the realization that planets may migrate through a disk, or be scattered later.

Indeed, the current distribution of planets does not necessarily reflect their formation history exactly. First, newly-formed planets will interact with the disk, exchanging angular momentum. These interactions can cause the planets to move radially through the disk, crossing considerable distances. This *migration* can happen in both directions and at different rates, depending on the disk structure and mode of migration (Baruteau et al. 2014). Second, even after the gas has dissipated, the young planetary system might not be dynamically stable, and gravitational interactions between the planets (or even fly-by's of other stars) can result in dynamical instabilities, and major make-overs for the system's structure (e.g., Davies et al. 2014).

Debris disks

The final stage of planet formation is not necessarily efficient in all disks, or in all regions within a disk. In the Solar System for example, the asteroid belt, located between Mars and Jupiter, can be thought of as the remains of an unsuccessful attempt. It is believed that in this particular case, the many mean motion resonances with Jupiter prevented bodies from conglomerating further; but planet formation could be unsuccessful for many reasons, not all of them related to nearby planets. For example, the original protoplanetary disks might not have contained enough solids in the first place, or, the turbulence and temperature structure of the disk might have made it a hostile environment for the growing aggregates.

Many old systems have now been discovered that have so-called *debris disks*, rings of debris similar to our asteroid belt, but often more massive and at larger separations (see Matthews et al. 2014, for a complete review). In debris disks, the mass is usually dominated by large, (super)km-size bodies, invisible to our telescopes. In the absence of gas, these bodies suffer violent collisions resulting in a collisional cascade. At the bottom of this cascade, dust particles with sizes of $\sim\mu$m are created, which can be observed. In some of these systems, planets have been reported as well (Kalas et al. 2005, 2008; Marois et al. 2008; Lagrange et al. 2010).

1.1.4 Observational contraints

The star- and planet formation paradigm, as summarized by Fig. 1.2, can be tested directly by studying the solids in the Solar System, and indirectly by observing radiation from other systems.

Disk observations

Observations of young stellar objects provide valuable information about the properties of protoplanetary disks. Here, we only skim the surface of the field of disk observations, and refer the reader to Williams & Cieza (2011) and Testi et al. (2014) for extensive reviews.

Initially, because of their small angular size, protoplanetary disks could not be resolved, and their existence was inferred by studying the stellar spectral energy distribution (SED) (Beckwith et al. 1990). The spectrum of a Sun-like star peaks in the UV and the optical. When a disk surrounds the star however, significant flux is observed at longer wavelengths, ranging from the mid-IR, to mm-wavelenghts; the result of both reprocessing of stellar radiation, and of thermal emission of dust grains. The right-hand side of Fig. 1.3 shows approximately which regions of the disk emit mid-IR and mm emission. By looking at the fraction of stars in star clusters that show such excess radiation, a typical disk lifetime of ~3 Myr can be inferred (e.g., Haisch et al. 2001), though some studies suggest lifetimes beyond 10 Myr (Pfalzner et al. 2014).

Continuum observations at (sub)mm wavelengths probe the interior of the protoplanetary disk, where most of the dust mass is located. The flux at these wavelengths is dominated by thermal emission of the dust grains, and can be approximated as

$$\nu F_\nu \approx \nu \kappa_\nu B_\nu(T) \frac{M_\mathrm{d}}{R^2}, \tag{1.12}$$

with $B_\nu(T)$ the temperature-dependent Planck function, ν the frequency, κ_ν the dust opacity (per unit mass), and M_d the total dust mass. By measuring the flux at multiple wavelengths, it is possible to constrain the slope of the opacity function $\kappa_\nu \propto \nu^\beta$, where β is called the spectral index. At (sub)mm wavelengths, the spectral index β depends on the dust properties and its size-distribution, and can be used to constrain grain growth (Natta & Testi 2004; Natta et al. 2007; Wilner et al. 2005; Ricci et al. 2010). Furthermore, when the disk can be resolved angularly, observed variations in β can provide clues about how grain growth varies with location in the disk (e.g., Pérez et al. 2012). However, interpretation of mm-observations is a precarious business, as the spectral index varies greatly with not just particle size and distribution, but also grain chemical composition and porosity (Cuzzi et al. 2014; Kataoka et al. 2014), and grain temperature (Demyk et al. 2012).

Now, facilities such as the Atacama Large Millimeter Array (ALMA), the Very Large Telescope Interferometer (VLTI), and soon the James Webb Space Telescope (JWST), are able to resolve protoplanetary disks down to scales approaching a few AU at micrometer-millimeter wavelengts (see also Fig. 1.3). Such high-resolution observations reveal the distribution of matter in disks, and variations in the disk's structure at smaller and smaller scales. So far, these observations have revealed coherent spatial structures such as gaps,

spiral arms, and azimuthal asymmetries in the disk and dust structure (e.g., van der Marel et al. 2013; Casassus et al. 2013; Pérez et al. 2014), possibly signs of planet formation in action. Furthermore, tentative direct observations of young (forming) planets inside protoplanetary disks confirm these disks are the principle sites of planet formation (Kraus & Ireland 2012; Quanz et al. 2013).

Solar System

As an evolved system, our own Solar System holds clues to its formation history. Some obvious, some less so. First, there are the planets; we already saw how the distribution of planets led to the concept of the Minimum Mass Solar Nebula. Focussing on the properties of the planets, we notice a dichotomy: small rocky planets in the inner Solar System, and massive gas giants in the outer parts. The division occurs somewhere between Mars and Jupiter, and it is tempting to attribute this devision to the location of the snow line.

Moving to much smaller objects, a tremendous amount of information can be obtained from studying meteorites (e.g., Russell et al. 2006; Connelly et al. 2012), small chunks of asteroids that fall onto Earth. The largest class of meteorites are the chondritic meteorites, which constitute the oldest known undifferentiated bodies in the Solar System. These chondrites consist of three components: chondrules, calcium-aluminum-rich inclusions (CAIs), and matrix material. Chondrules are spherical silicate crystals with sizes between $\sim$50 μm and several mm, and are the dominant component in meteorites. CAIs are slightly larger, with sizes $\lesssim$cm, but less common. The matrix material is composed of (sub)micron-size silicate grains, and fills the spaces between the chondrules (and CAIs). Of these components, the CAIs are the oldest, and are believed to be the first condensates in the Solar System. Radioactive dating places the formation of the CAIs at 4.567 Gyr ago, while differences between CAIs indicate they formed during an interval of $\sim$0.25 Myr. Dating indicates chondrules formed over a period of $\sim$2 Myr, starting $1-2$ Myr after the formation of the CAIs. It is now held that chondrules also formed earlier, perhaps together with CAIs, but that these early chondrules were incorporated into parent bodies that underwent differentiation (the magmatic iron meteorites). The spread in formation ages between CAIs and chondrules suggest coagulation and planetesimal formation occurred over several Myrs, a timespan comparable to the typical age of a protoplanetary disk. Another interesting finding is that while chondrule sizes vary between meteorites, their size distribution within a single parent body is relatively narrow. This seems to indicate that a size-sorting mechanism was acting in the early protoplanetary disk; and that the parent bodies formed only after some sorting was done. Much more can be learned from the primitive materials in our Solar System, and the interested reader is referred to the recent review of Gail et al. (2014).

1.2 From dust to planetesimal

For the formation of planets, the accumulation of solids is key. The molecular clouds of the previous section form out of the tenuous interstellar medium (ISM). Thus, like

the ISM, about 1% of their mass is in solid dust particles; typically particles with sizes $\lesssim$0.3 μm (Mathis et al. 1977). Because of the high densities in the disk midplane, these grains can collide and grow to larger sizes. Here, we discuss the main processes that govern the growth of these particles towards, eventually, planetesimal sizes.

1.2.1 Dynamics of dust grains

The dynamics of small dust particles, suspended in a young protoplanetary disk, are governed mainly by their interaction with the turbulent gas. An important concept is the particle stopping time t_s, which describes how much time is needed for a dust particle to loose its momentum due to friction with the surrounding gas. The stopping time is often multiplied by the orbital frequency to form the *Stokes number*, Ωt_s, a dimensionless quantity.

Imagine a dust particle with a size a, and mass m. Depending on the size of the particle with respect to the gas mean free path, the stopping time is set either by Epstein or Stokes drag

$$t_s = \begin{cases} t_s^{(\mathrm{Ep})} = \dfrac{3m}{4\rho_\mathrm{g} v_\mathrm{th} A} & \text{for } a < \dfrac{9}{4}\lambda_\mathrm{mfp}, \\ t_s^{(\mathrm{St})} = \dfrac{4a}{9\lambda_\mathrm{mfp}} t_s^{(\mathrm{Ep})} & \text{for } a > \dfrac{9}{4}\lambda_\mathrm{mfp}, \end{cases} \tag{1.13}$$

where $v_\mathrm{th} = \sqrt{8/\pi} c_s$ is the mean thermal velocity of the gas molecules, and $A \simeq \pi a^2$ is the particle's cross section. In the midplane at 5 AU, $\lambda_\mathrm{mfp} \sim 1$ m, and small dust grains are always in the Epstein regime.

While the gas is supported by a vertical pressure gradient, there is nothing stopping the dust grains from settling to the midplane of the protoplanetary disk. By comparing the vertical component of the stellar gravity to the gas drag experienced by a particle, one obtains the terminal settling velocity $v_z = \Omega^2 z t_s$ with z the height above (or below) the midplane. The timescale for settling then equals $t_\mathrm{sett} = (\Omega^2 t_s)^{-1}$. At 1 AU, a millimeter-size dust particle has $t_\mathrm{sett} \sim 10^2$ yr, very short compared to the disk lifetime. However, the presence of turbulence will lead to particles diffusing (back) to the upper layers of the disk. For relatively well-coupled particles, the diffusion timescale equals $t_\mathrm{diff} \sim (\alpha\Omega)^{-1}$. Particles for which the diffusion timescale is shorter/comparable to the settling timescale, i.e., with $t_s \leq \alpha/\Omega$, will not settle efficiently, and inhabit the same volume as the gas. Particles that are more decoupled will settle into a disk with a scale height (Youdin & Lithwick 2007)

$$\frac{h_\mathrm{d}}{h_\mathrm{g}} = \left(1 + \frac{\Omega t_s}{\alpha}\frac{1 + 2\Omega t_s}{1 + \Omega t_s}\right)^{-1/2}, \tag{1.14}$$

where $h_\mathrm{d}/h_\mathrm{g} \leq 1$.

Apart from settling to the midplane, largish grains will also drift radially towards the central star. The reason for this is that large grains, orbiting on Keplerian orbits, loose angular momentum to the gas, which is orbiting at a slightly sub-Keplerian velocity

because of the radial pressure gradient. As a result, grains drift inward with a velocity (Weidenschilling 1977a)

$$v_{\rm drift} = -\frac{2\Omega t_s}{1+(\Omega t_s)^2}\eta v_{\rm K}, \tag{1.15}$$

where an important quantity is the dimensionless pressure gradient η, defined as (Nakagawa et al. 1986)

$$\eta \equiv -\frac{1}{2}\left(\frac{c_s}{v_{\rm K}}\right)^2 \frac{\partial \ln(\rho_{\rm g} c_s^2)}{\partial \ln R}. \tag{1.16}$$

with $v_{\rm K} = R\Omega$ the Keplerian orbital velocity. The timescales on which decoupled particles drift in can be quite short, and radial drift poses a serious problem for further growth (Sect. 1.2.3).

Finally, an important concept for coagulation is the dust particle relative velocity, i.e., the velocity at which two grains with masses m_1 and m_2 collide. For (sub)micrometer grains, the relative velocity is dominated by Brownian motion, and given by

$$\Delta v_{\rm BM} = \sqrt{\frac{8k_{\rm B}T(m_1+m_2)}{\pi m_1 m_2}}, \tag{1.17}$$

with $k_{\rm B}$ the Boltzmann constant. For these small grains, the relative velocity $\Delta v_{\rm BM} \sim$ mm s^{-1}, but quickly decreases with increasing mass. For larger grains, an important source for relative velocities is the turbulence. Relative velocities resulting from interaction with the turbulent eddies are challenging to calculate. Based on the work of Voelk et al. (1980), closed-form expression were derived by Ormel & Cuzzi (2007), as a function of the stopping times of both particles. An important notion is that the largest turbulent-induced relative velocities are achieved when $\Omega t_s \sim 1$, in which case $\Delta v_{\rm turb} \sim \alpha^{1/2} c_s$. In addition, when two aggregates have very dissimilar stopping times, their different drift and settling rates can be an important source of relative velocities. Differential drift velocities also peak at a Stokes number of unity, at $\Delta v_{\rm drift} \sim \eta v_{\rm K}$.

1.2.2 Coagulation

Assuming all dust particles have similar properties (i.e., mass, size, stopping time), and stick together upon colliding, the growth timescale is given by

$$t_{\rm grow} \sim \frac{1}{n_{\rm d}\sigma_{\rm coll}\Delta v}, \tag{1.18}$$

with $n_{\rm d}$ the dust particle number density, Δv the relative velocity between the dust particles, and $\sigma_{\rm coll}$ the collisional cross section. Thus, simply speaking, growth is fastest when densities are high, collisional cross sections are large, and relative velocities are high.

1.2.3 Growth barriers

There are several obstacles (or barriers) that have to be overcome by growing dust grains in order to become planetesimals. In general, there are two distinct types of growth bar-

riers: one pertaining to the collisional outcomes; the other involving rapid removal of the dust particles from the disk.

Collisional barriers

When particles collide at high velocities, sticking will not be the most likely outcome, and particles are more likely to bounce of each other, or even destroy and fragment. Over the last two decades, a wealth of collision experiments has been collected in order to identify exactly at which velocities growth is possible (see Blum & Wurm 2008, for an in-depth review). For silicates, Güttler et al. (2010) have combined this 'zoo' of experiments into the so-called *Braunschweig collision model*. In this model, colliding grains are divided into 'porous' and 'compact' grains, and collisions are either between 'similar-size' or 'different-size' particles; resulting in 8 possible collision types. Based on the large collection of experiments, Güttler et al. (2010) then provided maps for each collision type, showing, as a function of particle mass and velocity, where sticking, bouncing, and fragmentation are expected to occur. For ices, experimental studies become increasingly challenging, mainly because of the low temperatures that have to be maintained during the preparation and execution of the collision experiments. Nonetheless, experimental results are becoming available (Gundlach et al. 2011; Aumatell & Wurm 2014), indicating microscopic icy particles can achieve sticking at very high velocities (Gundlach & Blum 2015).

The velocity above which sticking is unlikely depends on many factors, some of which will be discussed in more detail in Sect. 1.3; but as a rough estimate, compact mm-size aggregates of refractory particles tend to bounce at velocities $\gtrsim$1 cm s^{-1}, and fragment above $v_{\rm frag} \sim 1$ m s^{-1}. In the inner regions of protoplanetary disks typical collision velocities are well above the fragmentation velocity for silicate particles. In general, full models of dust coagulation find that, when dust grains are assumed to be compact at all times, the bouncing and fragmentation prevent dust particles from growing much larger than ~cm (e.g., Brauer et al. 2008a; Birnstiel et al. 2010; Testi et al. 2014). However, experiments suggest that grains might still gain mass in destructive collisions with smaller particles (Wurm et al. 2005; Kothe et al. 2010). Such mass-transfer might then allow these larger bodies to grow further (Windmark et al. 2012a).

In the cold outer regions, where sticky ices are present, the relative velocities are lower (the turbulent velocity $\Delta v_{\rm turb} \propto c_s^{1/2}$ decreases with disk radius). In addition, porous icy aggregates are stickier, and can dissipate collisional energy more easily. A bouncing regime is then not expected for these aggregates, and the transition between sticking and fragmentation occurs at several tens of m s^{-1}. These icy aggregates are expected to survive collisions with similar-size particles, offering a pathway for further growth (Okuzumi et al. 2012).

The drift barrier

In the previous section it was shown that marginally decoupled grains will drift inward with a velocity $v_{\rm drift}$ (Eq. 1.15). The drift timescale $t_{\rm drift} = R/v_{\rm drift}$ is shortest for grains

with $\Omega t_s = 1$, for which $t_{\rm drift} \sim (\eta\Omega)^{-1}$. Typically $\eta \sim 10^{-2}$, which means the drift timescale can be very short indeed, ∼100 orbital periods. In other words, grains with $\Omega t_s \sim 1$, situated around 1 AU from a Sun-like star, will drift inward on a 100 yr timescale (Weidenschilling 1977a). This rapid removal of grains is often referred to as the radial drift barrier.

Several ways have been suggested to circumvent the drift barrier. First, the existence of pressure bumps in the gas disk can locally decrease (or even invert) the pressure gradient, trapping particles in the pressure maxima (e.g., Kretke & Lin 2007; Pinilla et al. 2012a,b) (see also Sect. 1.2.4). Second, if the growth timescale is (much) shorter than the timescale for drift, i.e., $t_{\rm grow} < t_{\rm drift}$, particles can outgrow the radial drift problem (Okuzumi et al. 2012). For this to work, aggregates with $\Omega t_s \sim 1$ must be able to grow through collisions, despite the the fact that relative velocities peak at these Stokes numbers.

1.2.4 Particle concentration mechanisms

The growth timescale of Eq. 1.18 depends on the dust particle number density. If the dust and gas are well-mixed, the mass density of dust particles is roughly $\rho_{\rm d} \sim \Sigma_{\rm d}/h_{\rm d}$, and increases when grains settle to the midplane. There exist however several particle concentration mechanisms that can locally and/or temporarily increase $n_{\rm d}$ much further, potentially leading to rapid growth. First, tightly-coupled particles ($t_s \sim t_\eta$) can accumulate in the high-pressure regions between the smallest turbulent eddies (Cuzzi et al. 2001, 2008), though the total mass present in these particle concentrations might be small (Pan et al. 2011). Second, pressure bumps or vortices, giving rise to variations of the order $h_{\rm g}$, can effectively concentrate particles with $0.1 < \Omega t_s < 10$ (e.g., Kretke & Lin 2007), though it is not clear how common such bumps and/or vortices are. Finally, populations of bodies with $10^{-2} < \Omega t_s < 1$ can result in streaming instability, and collapse to form planetesimals in a timescale compared to the orbital period (Youdin & Goodman 2005; Johansen et al. 2007; Bai & Stone 2010a,b). For this to be possible, a dense midplane layer of solids is required, where the dust-to-gas ratio is approximately unity. These concentration mechanisms are described in more detail in Johansen et al. (2014).

In summary, the turbulent gas disk is a complex environment, and the interplay between dust and gas can give rise not only to growth barriers, but also to particle concentration mechanisms that are beneficial for growth. The efficiency of these mechanisms however, depends sensitively on the aerodynamical properties of the present dust grains.

1.3 Dust microphysics

The microphysical structure of dust aggregates plays a major role in their (collisional) evolution. First, the microstructure profoundly influences the aggregate's mechanical properties, and therefor the collisional outcomes. For example, highly porous aggregates can dissipate collision energy more easily, and are less likely to bounce. Second, the shape and size of an aggregate influence its coupling to the gas, changing the particle's stop-

ping time, thus influencing the settling/drift behavior, collision velocities, and efficiency of particle concentration mechanisms. Finally, porosity influences grain opacities (i.e., κ_ν in Eq. 1.12), changing the appearance of dust in disks. It is clear then that an intimate understanding of the porosity evolution of dust aggregates is needed to understand the details of dust coagulation (the first stages of planetesimal formation), and to accurately interpret observations of dust in protoplanetary disks.

Two quantities are often used to describe the structure of porous aggregates; the first is the filling factor ϕ, which represents the fraction of the aggregate's volume that is taken up by solids. A solid sphere has $\phi = 1$, and the maximum filling factor of an aggregate made up of mono disperse spheres is $\phi \simeq 0.74$. Depending on the specifics of the growth process, the filling factor of aggregates in astrophysical environments may be $\ll 1$. The second parameter is the fractal dimension δ_f, which relates the mass and the size of the aggregate through

$$m = k_f \left(\frac{a}{r}\right)^{\delta_f}, \tag{1.19}$$

with r the monomer radius. The fractal dimension can range from anywhere between 1 (for linear chains) to 3 (for homogeneous particles). It should be noted that $\delta_f \simeq 3$ does not necessarily imply a compact aggregate, since k_f can still be very small.

1.3.1 Early growth

Initially, the microscopic grains present in the protoplanetary disk collide very gently, at velocities set by Brownian motion. When small grains meet at these velocities, they readily stick together as the result of attractive surface forces. In this low-velocity hit-and-stick regime, two modes of growth can be identified: one where aggregates grow by colliding with same-size partners (CCA for cluster-cluster aggregation); and one where aggregates grow by sweeping up small grains (PCA for particle-cluster aggregation). During CCA growth, very open, porous aggregates are formed, that evolve with $\delta_f \approx 2$, as found by experimental studies (Blum et al. 2000; Krause & Blum 2004) and theoretical work (Ossenkopf 1993; Kempf et al. 1999). This fractal growth is generally held to be an accurate description of the start of the coagulation process in protoplanetary disks.

As the fluffy aggregates gain mass, the turbulence and differential settling begin to dominate their collision velocities, which tend to increase. Then, as grains collide with more momentum, collisions will be energetic enough to start to restructure the aggregates, possibly compacting them. A schematic of hit-and-stick growth and compaction is shown in Fig. 1.4. As illustrated in panel (b), hit-and-stick growth leads to the addition of voids to the aggregate's structure, leading to a decrease in ϕ, while the fractal dimension stays constant at $\delta_f \approx 2$. In the case of aggregate compaction (Fig. 1.4c), the changes in the internal structure are more complex, and the most popular methods to study this process have been so-called molecular dynamics simulations.

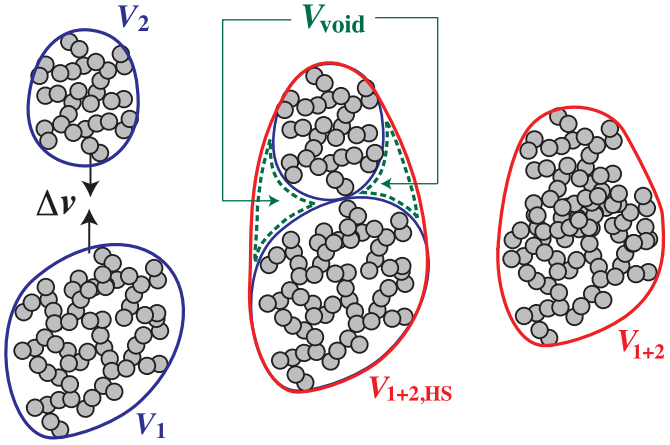

Figure 1.4: Sticking of porous aggregates. (a) Two aggregates, with volumes V_1 and V_2, collide at a velocity Δv. (b) At low velocities, the collision results in sticking without restructuring. Voids are added, and the total volume of the resulting aggregate is $V_{1+2,\rm HS} > V_1 + V_2$. (c) At higher collision velocities, significant restructuring takes place, and $V_{1+2} < V_{1+2,\rm HS}$. Figure from Okuzumi et al. (2012).

1.3.2 Molecular dynamics simulations

One way to study the effects of restructuring, is to perform dynamic simulations that resolve the (internal) forces between the aggregate's constituents during a collision. Dominik & Tielens (1997) were the first to tackle coagulation using such an approach. In their seminal paper, Dominik & Tielens simulated collisions between aggregates composed of $\lesssim$100 micron-size monomers at a range of velocities, and defined various collision regimes, based on the characteristic energies of the monomer-monomer contact. The various regimes are shown in Table 1.1. The two characteristic energies $E_{\rm break}$ and $E_{\rm roll}$ correspond, respectively, to the breaking of a single adhesive bond, and to the rolling of one monomer over another monomer by 90°. The value of these critical energies depends on monomer size and material, and will be discussed further in Sect. 1.3.3. Blum & Wurm (2000) found their experimental results on sticking, restructuring, and fragmentation of silicate aggregates to be in qualitative agreement with the picture drawn in Table 1.1, adding that theory and experiments were in agreement when the critical energies were adjusted by some factors of 10.

The work of Dominik & Tielens sparked many follow-up studies, involving an ever-increasing number of monomers N. Studies have been performed looking at the mechanical properties of aggregates (e.g., Paszun & Dominik 2008; Seizinger et al. 2012; Kataoka et al. 2013b); specifically looking at collisions between rotating partners (Paszun & Dominik 2006); investigating the bouncing behavior of aggregates (Wada et al. 2011;

Collision energy	Outcome of collision
$E_{\rm K} < 5E_{\rm roll}$	Sticking without restructuring
$E_{\rm K} > 5E_{\rm roll}$	Onset of compaction
$E_{\rm K} \sim n_c E_{\rm roll}$	Maximum compression
$E_{\rm K} > n_c E_{\rm break}$	Loss of some monomers
$E_{\rm K} > 10 n_c E_{\rm break}$	Catastrophic disruption

Table 1.1: Collision outcomes for roughy equal-size aggregates in terms of the characteristic energies $E_{\rm break}$ and $E_{\rm roll}$, and the total number of contacts n_c. Based on Dominik & Tielens (1997, Table 3).

Seizinger & Kley 2013); focussing on the porosity evolution of aggregates in head-on collisions (Wada et al. 2007, 2009; Suyama et al. 2008, 2012) and offset collisions (Paszun & Dominik 2009); and examining the transition from growth to mass-loss with increasing collision velocity (Wada et al. 2013). Fig. 1.5 shows how numerical aggregates have evolved from 2D structures[1] with $N \sim 10^2$, to 3D aggregates with $N \sim 10^6$ (e.g., Wada et al. 2013). With monomer radii typically between $0.1 - 1\ \mu$m, the largest of these aggregates have sizes $\lesssim 100\ \mu$m. Even though larger aggregates are challenging to simulate, universal scaling laws can be obtained from the large collections of simulations. Recently, Okuzumi et al. (2012) and Suyama et al. (2012) developed expressions for the total volume of a newly-formed porous aggregate, based on the collision velocity, and the properties of the colliders. They found that aggregates that grow through subsequent compressive collisions with ~same-size partners can maintain a highly porous structure, with a nearly constant porosity that can be as low as $\phi \sim 10^{-5}$ for aggregates consisting of submicron icy monomers. Another interesting outcome of these simulations has been that bouncing is only possible for aggregates whose coordination number (the average number of contacts per monomer) is higher than ~6. In terms of porosity, this corresponds to $\phi \gtrsim 0.3$ (Wada et al. 2011; Seizinger & Kley 2013).

Full coagulation models that include particle porosity as a second property (in addition to particle mass) confirm that porosity matters a lot (Ormel et al. 2007; Okuzumi et al. 2009; Zsom et al. 2011). If particles can keep on growing highly-porously, which ice aggregates might, rapid growth through the drift barrier could even be possible (Okuzumi et al. 2012).

1.3.3 Radial and lateral forces

The main physical ingredient of the simulations of the previous section are the laws that describe the various inter-monomer forces. Long-range forces such as gravity or electrostatic forces are usually not included, and monomers can only exchange forces when they are touching. When two grains are in contact (i.e., touching), 4 principle modes of

[1] It should be noted that, despite the subsequent addition of a third spatial dimension and the enormous increase in the simulated number of monomers, the aggregates of Dominik & Tielens (1997) remain the only ones in which the monomers had a distribution of radii, rather than being mono disperse.

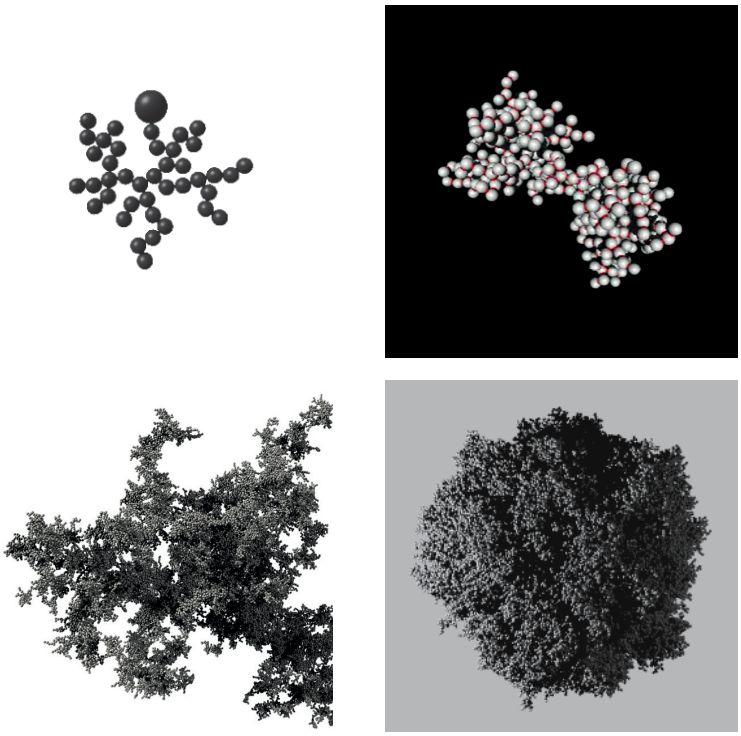

Figure 1.5: Improvements in numerical modeling of dust aggregates. *Top left:* Two-diminsional aggregate consisting of 40 monomers (Dominik & Tielens 1997). *Top right:* Aggregate consisting of 200 monomers (Paszun & Dominik 2009). *Bottom left:* Fractal aggregate consisting of 6×10^4 monomers (Seizinger et al. 2013). *Bottom right:* Relatively compact aggregate consisting of 1.28×10^5 monomers (Wada et al. 2013). Images not to scale.

motion can occur: radial motion, rolling motion, sliding motion, and twisting (Fig. 1.6). Prescriptions for the individual forces were obtained by Chokshi et al. (1993); Dominik & Tielens (1995, 1996), and summarized in Dominik & Tielens (1997). These descriptions were based on the Johnson-Kendall-Roberts (JKR) model of an adhesive and perfectly elastic contact (Johnson et al. 1971; Johnson 1987).

The JKR contact model is an extension of the non-adhesive theory of Hertz (1882). Hertz imagined two perfectly elastic spheres of radii r_1 and r_2. When the two spheres are pressed together, a circular contact area with a radius a is created, and the spheres are compressed slightly, so that their centers of mass ($\vec{x}_1$ and $\vec{x}_2$) are separated by less then $r_1 + r_2$. Then, the mutual approach can be defined as $\delta = r_1 + r_2 - |\vec{x}_1 - \vec{x}_2| > 0$. By looking at the elastic energy stored in such a configuration, Hertz derived the repulsive

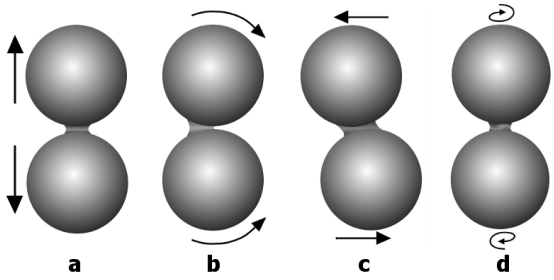

Figure 1.6: Main modes of motion in an adhesive contact between (sub)micrometer-size adhesive monomers: (a) radial (i.e., normal) motion, (b) rolling, (c) sliding, and (d) twisting. Figure from Seizinger et al. (2013), after Dominik & Tielens (1997).

radial force between two spheres to equal

$$F_{\rm H} = \frac{4E^* a^3}{3r}, \tag{1.20}$$

while the size of the contact being related to the approach through $a^2 = r\delta$, and typically $\delta \ll a \ll r$. Here, the elastic properties of the spheres are described in a single combined elastic modulus E^*, and $r^{-1} = r_1^{-1} + r_2^{-1}$ is the reduced radius. For a finite contact radius, $F_{\rm H} > 0$, and thus, the spheres will move apart in the absence of additional forces.

For microscopic bodies however, attractive surface forces can play an important role. By realizing that the presence of a mutual contact area results in a reduction of the total surface energy $\Delta U_S = \pi a^2 \gamma$, with γ the mutual surface energy, Johnson et al. (1971) obtained

$$\delta = \frac{a^2}{r} - \sqrt{2\pi\gamma a/E^*}, \tag{1.21}$$

and

$$F_{\rm JKR} = \frac{4E^* a^3}{3r} - \sqrt{8\pi\gamma E^* a^3}. \tag{1.22}$$

These relations are qualitatively different from the ones obtained by Hertz. First, the force can change signs, i.e., become attractive, for certain combinations of δ and a. As a result, there now exists an equilibrium solution where $F_{\rm JKR} = 0$ but the contact area is finite, given by

$$a_{\rm JKR} = \left(\frac{9\pi\gamma r^2}{2E^*}\right)^{1/3}. \tag{1.23}$$

Second, contact can persist at negative values of δ. Physically, this means that when spheres are pulled apart, a 'neck' of material will be formed that keeps the spheres in contact even for $\vec{x}_1 - \vec{x}_2 > r_1 + r_2$. When this neck becomes too long, the situation becomes unstable, contact is lost, and the spheres return to their spherical shape. The force needed to achieve pull-off equals $F_c = (3/2)\pi\gamma r$, independent of elastic properties.

These two effects have the consequence that a finite amount of energy has to be provided to break an existing bond. This energy is roughly

$$E_{\rm break} \sim \left(\frac{\gamma^5 r^4}{E^{*3}}\right)^{1/3}. \tag{1.24}$$

Thus, contacts between sticky (high γ), soft (low E^*) materials cost more energy to break. When two monomers collide head-on, they will stick and remain together if the initial kinetic energy $E_{\rm K} \leq E_{\rm break}$. Equating these two energies results in a sticking velocity $v_{\rm stick} \propto r^{-5/6}$; in other words, smaller spheres stick at higher velocities. Comparing ices and silicates, these considerations predict particles made of ice stick at velocities $\sim$10 times higher than silicate particles of a similar size.

When a lateral force is applied to center of mass of the sphere, a torque about the contact area is created. Starting from the JKR adhesive contact, Dominik & Tielens (1995) derived the critical rolling energy

$$E_{\rm roll} = 6\pi\gamma r\xi, \tag{1.25}$$

as the energy needed to roll two spheres over each other over 90°. Here, ξ is the *rolling displacement*, related to the asymmetry of the contact area during the rolling motion. Dominik & Tielens connected the displacement to the intermolecular length scale, i.e., $\xi \sim 0.1$ nm.

Recent developments in molecular dynamics simulations have focussed on the ability to include an increasing number of monomers, and the contact description has not evolved much since its introduction in Dominik & Tielens (1997), despite a number of discrepancies with experimental results. First, the sticking velocity of individual monomers has been measured by Poppe et al. (2000) to be around $v_{\rm stick} \simeq 1$ m s^{-1} for micron-size silicate grains, while the sticking velocity estimated from JKR theory is roughly 10 times lower. Second, the experimentally obtained rolling forces of Heim et al. (1999) indicate a value of $\xi \gg 0.1$ nm. Several reasons have been suggested for these discrepancies, including elastic waves, surface roughness, and deviations from elasticity, with many of the subsequent molecular dynamics simulations employing additional numerical factors to remove the disagreement with theoretical predictions.

1.4 This thesis

In this introduction we started from scales of $\sim$100 AU, corresponding to the typical size of a protoplanetary disk, and slowly worked our way down to through planets, planetesimals, dust grains, and eventually monomers, to eventually argue that the physical properties of the adhesive contact (corresponding to a scale $\lesssim\mu$m) are important for the early phases of planet formation. In the remainder of this thesis, we will walk the opposite route; starting from studying a single monomer-monomer contact (Chapters 2 and 3), we simulate dust coagulation in a local part of a nebula (Chapter 4), and finally study the

global evolution of dust in a full protoplanetary disk (Chapter 5), before making a short excursion into the much older debris disk systems (Chapter 6).

The JKR model of an adhesive contact assumes the spheres are perfectly elastic, and that the contact area is in equilibrium. The size of the contact area is then found by minimizing the total surface- and elastic energy. Collisions however, are very dynamic processes, with typical durations of the order of 10^{-8} s for μm-size spheres. Furthermore, deviations from perfect elasticity are expected for realistic materials. In Chapter 2, we set out to extend the contact model to include dissipation of energy in the bulk of the colliding materials, and at the periphery of the adhesive contact. The new viscoelastic contact model is tested by comparing the predicted sticking velocity, and coefficients of restitution to a large set of published experiments on head-on collisions of small spheres.

In Chapter 3, we build on the viscoelastic model, and use it to re-evaluate the rolling force between adhesive monomers (i.e., Fig. 1.6b). The main goal is to achieve a better understanding of the rolling displacement parameter ξ (Eq. 1.25).

After these excursions into the world of contact mechanics, Chapter 4 constitutes the return to astronomy. In this chapter, the collisional evolution of a population of dust particles (initially all submicron grains) in a single column outside the snow line of a protoplanetary disk is studied. Coagulation is simulated using a special Monte Carlo technique (based on Ormel & Spaans 2008) that allows us to resolve the entire mass distribution, even parts that hardly contribute to the total dust mass budget. As the aggregates grow through collisions, the evolution of their filling factor is calculated self-consistently, as it is influenced by collisions, and non-collisional forces such as gas-drag or self-gravity. The main goal of this chapter is to determine whether erosion, caused by high-velocity impacts of small grains, can halt the rapid growth of porous aggregates through the radial drift barrier. In addition to the full Monte Carlo simulations, a semi-analytical model is introduced that is capable of capturing the evolution of the mass-dominating particles.

In Chapter 5, this semi-analytical model is developed further, and a new method is introduced to simulate the evolution of the dust surface density on a global scale, as it is changed by the combination of (porous) coagulation and radial drift. The method is used to study the formation of the first generation of planetesimals, the generation that is capable of forming out of a smooth gaseous nebula. Focussing on Sun-like stars, we study where in the disk porous coagulation can result in the formation of planetesimals, either through direct coagulation, or through streaming instability (Sect. 1.2.4) following coagulation/erosion equilibrium.

Chapter 6 takes a different perspective on the particles in debris disks, and addresses the lower end of the particle size distribution in these evolved systems. In debris disks (Sect. 1.1.3), the mass is typically dominated by km-size objects while the surface area of the solids resides in small dust particles, the results of a collisional cascade. In this chapter, we investigate which processes determine the observed cut-off of the particle size distribution around a few micrometer.

Finally, in Chapter 7, the main results of this thesis are summarized and promising avenues for future work are discussed.

2

Energy dissipation in head-on collisions of spheres

S. Krijt, C. Güttler, D. Heißelmann, C. Dominik, and A. G. G. M. Tielens
Journal of Physics D: Applied Physics, Volume 46, Issue 43 (2013)

Abstract

Collisions between spheres are a common ingredient in a variety of scientific problems, and the coefficient of restitution is a key parameter to describe the outcome of those. We present a new collision model that treats adhesion and viscoelasticity self-consistently, while energy losses arising from plastic deformation are assumed additive. Results show that viscoelasticity can significantly increase the energy that is dissipated in a collision, enhancing the sticking velocity. Furthermore, collisions well above the sticking velocity remain dissipative. We systemically compare the model to a large and unbiased set of published laboratory experiments to show its general applicability. The model is well capable of reproducing the important relation between impact velocity and coefficient of restitution as measured in the experiments, covering a wide range of materials, particle sizes, and collision velocities. Furthermore, the fitting parameters from those curves provide physical parameters like the surface energy, yield strength, and characteristic viscous relaxation time. Our results show that all three aspects – adhesion, viscoelastic dissipation and plastic deformation – are required for a proper description of the kinetic energy losses in sphere collisions.

2.1 Introduction

The study of the normal impact of a sphere and a second sphere or a substrate is a fundamental one, with applications in many different fields and scientific problems. The outcome of a collision is typically described by the coefficient of restitution, the ratio of the relative post- and pre-collision velocities, a measure of the amount of kinetic energy that is lost during the collision. Its value determines the energy balance in collisional systems such as granular gasses (Brilliantov et al. 1996; Pöschel et al. 2003), which find applications in a wide range of physical environments. The question whether or not a collision results in sticking is of importance for many practical problems, such as the transportation of powders or granular materials, as well as for the study of the evolution of agglomerates, for instance in astrophysical environments such as dense molecular clouds (Ossenkopf 1993), protoplanetary disks (Dominik & Tielens 1997; Paszun & Dominik 2008; Wada et al. 2009), and planetary rings (Salo 1995; Salo et al. 2001). Conversely, a proper description of these systems requires good understanding of the physical processes involved and the material parameters describing them.

During a collision, various physical mechanisms can work together to dissipate kinetic energy. The magnitude of the energy associated with these mechanisms will in general depend on the target and projectile materials, their sizes, and the collision velocity. At low collision velocities, the surface energy of the materials associated with the mutual contact area is comparable to the kinetic energy, and will influence the collisional outcome, often resulting in sticking. In more energetic collisions, adhesion becomes less important, and sticking cannot be achieved through surface forces alone. Energy-loss mechanisms that are dominant in this regime can include the excitation of elastic waves (Rayleigh 1906; Reed 1985) and viscoelasticity (Brilliantov et al. 1996; Kuwabara & Kono 1987). During high impact velocities, the stresses in and around the contact area may become so large that the material stops to behave elastically. Kinetic energy will then go into plastic deformation, and this becomes the most important energy sink (Johnson 1987).

Despite extensive theoretical work studying these underlying physical processes, and experimental studies with measurements of the coefficient of restitution for certain velocities (e.g., Dahneke 1975; Wall et al. 1990; Dunn et al. 1995; Li et al. 1999; Kim & Dunn 2007a; Sorace et al. 2009), few attempts have been made to combine different experiments and systematically compare the observed coefficient of restitution to theoretical predictions. In general, the experimental results show three different features (Güttler et al. 2012): (1) A rapidly increasing coefficient of restitution for low velocities, possibly preceded by sticking collisions. (2) A region where the coefficient of restitution does not vary with collision velocity, and has a value that is significantly smaller than unity. (3) At high velocities, the coefficient of restitution is seen to fall of with velocity. A complete model for the collisional outcome has to be able to reproduces all three of these characteristics.

In this work, we set out to create collision model for viscoelastic adhesive spheres, which will be tested against published experimental results. While theoretical studies including either viscoelasticity (Brilliantov et al. 1996; Kuwabara & Kono 1987), or ad-

hesion (Johnson 1987; Chokshi et al. 1993) have been around for some time, combining these two effects has proven notoriously difficult. In Sect. 2.2, we propose a dynamic contact model for adhesive viscoelastic spheres. The main advancement of our model is that the two variables that describe the contact – the contact radius and the distance between the sphere's centers – are treated as mutually independent, where most theories assume an equilibrium relation between these quantities. The contact description is used in Sect. 2.3 to describe head-on collisions between spheres, after which it is expanded to include plastic deformation at high velocities. Next, the collision model is compared to a large and unbiased set of collision experiments (Güttler et al. 2012). Fitting the model to the various experimental results will reveal how well it is able to reproduce the collisional outcomes, and allows to get a handle on the material properties governing the adhesive, viscous, and plastic behavior in question (Sect. 2.4). The results are discussed in Sect. 2.5, after which the main conclusions are presented in Sect. 2.6.

2.2 Contact model

In the section we briefly revisit elastic contact theory (with and without adhesion), before deriving the equations describing a viscoelastic contact.

2.2.1 Static contact

When two smooth elastic spheres of radii R_1 and R_2 are pressed together, they will deform locally and share a circular contact area with radius a (Fig. 2.1). Assuming the contact is small compared to the reduced radius R, and there are no forces acting outside the contact area, we can write the pressure distribution in the contact area as a function of $0 \leq r \leq a$ (Muller et al. 1980)

$$p(r) = \frac{E^*}{\pi R} \frac{a^2 - 2r^2 + R\delta}{\sqrt{a^2 - r^2}}, \tag{2.1}$$

where $R^{-1} \equiv R_1^{-1} + R_2^{-1}$, and $E^{*-1} \equiv (1 - \nu_1^2)/E_1 + (1 - \nu_2^2)/E_2$ is the combined elastic modulus, combining the Young's Moduli E_i and Poisson Ratios ν_i of the spheres. The mutual approach is defined as $\delta \equiv R_1 + R_2 - |\vec{r_1} - \vec{r_2}|$, where $\vec{r_i}$ is the position of a sphere's center of mass. The pressure at a radius r is then completely defined by a and δ, and can be both positive (compressive) and negative (tensile). The largest compressive stress is found at $r = 0$, and for now we will assume this stress does not reach the material yield strength, and thus plastic deformation does not occur.

While there is a singularity at the edge of the contact, the integral over the entire area is convergent and yields the (elastic) inter-particle force

$$F_{\mathrm{E}} = \int_0^a 2\pi r p(r)\,\mathrm{d}r = \frac{2E^*}{3R}\left(3a\delta R - a^3\right). \tag{2.2}$$

The elastic strain energy stored in the contact equals (Muller et al. 1980)

$$U_{\mathrm{E}} = \frac{E^* a^3}{3R}\left[\delta\left(\frac{3\delta R}{a^2} - 1\right) - \frac{a^2}{5R}\left(\frac{5\delta R}{a^2} - 3\right)\right]. \tag{2.3}$$

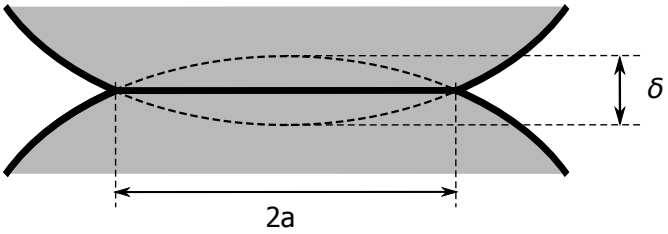

Figure 2.1: Schematic of the contact between two elastic spheres, showing the contact radius a and mutual approach δ.

So far we have deliberately not assumed any relation between a and δ. In some cases however, such relations do exist, and we will discuss two of these here, as we will compare them to the viscoelastic model later.

Hertz theory

In the non-adhesive case, as described by Hertz (1882), only repulsive forces are considered. For a given δ, the corresponding equilibrium contact size can be found by minimizing U_{E}, resulting in

$$a^2 = R\delta, \tag{2.4}$$

which, together with Eq. 2.2 returns the famous Hertzian force

$$F_{\mathrm{H}} = \frac{4E^* a^3}{3R}. \tag{2.5}$$

From these two equations we see that in the non-adhesive case the force and contact size go to zero for $\delta = 0$, and no solution exists for $\delta < 0$. Additionally, the force is always positive, so no stable configuration of touching spheres is possible in the absence of external forces.

Johnson Kendall Roberts theory

To describe the adhesive case, Johnson et al. (1971) added a surface energy term

$$U_{\mathrm{S}} = -\pi a^2 \gamma, \tag{2.6}$$

where γ is the surface energy. Thus, when the circular contact area shrinks or expands, the surface energy changes. For a certain value of δ, the contact area will adjust itself so that

$$\frac{\partial}{\partial a}\left(U_{\mathrm{E}} + U_{\mathrm{S}}\right) = 0, \tag{2.7}$$

which can be solved to give

$$\delta = \frac{a^2}{R} - \sqrt{2\pi\gamma a / E^*}, \tag{2.8}$$

and consequently

$$F_{\mathrm{JKR}} = \frac{4E^* a^3}{3R} - \sqrt{8\pi\gamma E^* a^3}. \tag{2.9}$$

These final two relations describe Johnson Kendall Roberts theory (hereafter JKR theory), and show that contact between adhesive particles can be maintained even for negative approaches and negative forces. An important point is that an equilibrium exists at

$$a_{\mathrm{eq}} = \left(\frac{9\pi\gamma R^2}{2E^*}\right)^{1/3}, \tag{2.10}$$

where the inter particle force equals zero, assuming no external forces are acting. Indeed, a pull-off force of $F_c = -(3/2)\pi\gamma R$, independent of elastic properties, has to be overcome in order to separate two spheres.

Several alternative adhesive theories exist. JKR theory is the result of assuming that no forces act outside of the contact area. Also in the seventies, Derjaguin et al. (1975) took the opposite approach, by assuming the contact size is Hertzian, and adhesive forces to act in a ring around it. It was shown by Tabor (1977) that both theories are in fact limiting cases, whose validity depends on the value of the Tabor parameter, defined as

$$\mu \equiv \left(\frac{R\gamma^2}{E^{*2} z_0^3}\right)^{1/3}, \tag{2.11}$$

with $z_0 = 0.2 \sim 0.4\,\mathrm{nm}$ the spacing between atoms. For $\mu > 5$, i.e., large compliant spheres, JKR theory is valid, while for $\mu < 0.1$ Derjaguin Muller Toporov (DMT) theory is preferred. In the transition regime the Maugis-Dugdale solution can be used (Dugdale 1960; Maugis 1992; Johnson & Greenwood 1997).

2.2.2 Dynamic contact

Here we ask ourselves what happens when the material making up the spheres is not perfectly elastic. More specifically, the material will be assumed to be linearly viscoelastic, with a single relaxation time T_{vis}. We focus first on what this means for the contact edge, after which we turn our attention to the bulk of the material.

Viscoelastic crack theory

The growing or receding contact area can be described as a Mode I crack of length $2\pi a$ that is either closing or opening. For an infinite linear elastic material the crack is adequately described by Griffith theory (Griffith 1921), returning Eq. 2.6. For viscoelastic materials however, this approach breaks down as it predicts infinite strain rates for any non-zero crack velocity[1]. The basis for a more advanced theory comes from Barenblatt (1962),

[1] This problem was circumvented by Brilliantov et al. (2007), who integrated over the elastic stresses *before* taking the time-derivative (their Eq. 30). While the integral over the elastic stress is finite, and indeed equal to the elastic force, the integral over the time-derivative of the elastic stress does not converge. More specific,

who provided a solution for the infinite stresses. Based on this concept numerous theories for propagating viscoelastic cracks have been developed (Schapery 1975a,b; Greenwood & Johnson 1981; Schapery 1989; Hui et al. 1998; Baney & Hui 1999). The main result of these studies is that energy is dissipated at the crack tip, creating an asymmetry between opening and closing cracks, which causes Eq. 2.7 to break down. However, providing

$$\frac{\partial U_{\mathrm{S}}^*}{\partial a} = -2\pi a G_{\mathrm{eff}}(\dot{a}), \tag{2.12}$$

is the energy released/absorbed when the crack is closed/opened, and includes any viscoelastic losses at the crack tip, we may write

$$\frac{\partial}{\partial a}\left(U_{\mathrm{E}} + U_{\mathrm{S}}^*\right) = 0. \tag{2.13}$$

In Eq. 2.12, the effective surface energy G_{eff} is a function of crack velocity $\dot{a}$. For sufficiently slow cracks, $G_{\mathrm{eff}} = \gamma$, and Eq. 2.13 reduces to Eq. 2.7 as expected. In Appendix 2.A we show for which crack opening velocity this occurs. For larger crack speeds however, $G_{\mathrm{eff}} > \gamma$ for opening cracks, and $G_{\mathrm{eff}} < \gamma$ for healing ones. This causes so-called adhesion hysteresis at the contact edge, and has been experimentally verified (Maugis & Barquins 1978). Combining Eqs. 2.12 and 2.13 yields

$$G_{\mathrm{eff}}(\dot{a}) = \frac{E^*}{2\pi a R^2}(a^2 - \delta R)^2. \tag{2.14}$$

For a certain combination of a and δ, the above relation can be used to find the current effective surface energy, and thus $\dot{a}$. The exact shape of $G_{\mathrm{eff}}(\dot{a})$ is quite complex. Here, we will use results of Greenwood (2004), who combined the work of Barenblatt and Schapery with a Maugis-Dugdale potential around the crack tip. The material is described as a three-element solid, with a relaxation timescale T_{vis} and a ratio of relaxed to instantaneous elastic modulus k. The effective surface energy is then written as

$$G_{\mathrm{eff}}(\dot{a}) \equiv \beta(\dot{a})\gamma, \tag{2.15}$$

which can be inserted into Eq. 2.12. Analytical functions are provided relating $\dot{a}$ to β. For the majority of crack speeds, and almost independent of k, we can use (Greenwood 2004)

$$\frac{\sigma_0^2 T_{\mathrm{vis}}}{E^*\gamma}\dot{a} = \begin{cases} 0.15\left[\beta \log\left(\dfrac{1-k}{1-\beta}\right)\right]^{-1} & \text{for } \dot{a} > 0, \\ -0.24\beta\left[\log\left(\dfrac{1-k}{1-1/\beta}\right)\right]^{-1} & \text{for } \dot{a} < 0, \end{cases} \tag{2.16}$$

swapping the integral and derivative using Leibniz's rule results in a boundary term proportional to $\dot{a}p(a)$, which is infinite in JKR-theory. A more detailed theory of what happens close to the contact edge is needed, and has become available in the form of viscoelastic crack theory described here.

where $\sigma_0 \simeq \gamma/z_0$ is the size of the attractive force acting in the region described by the Maugis-Dugdale model. For low speeds, Eq. 2.16 looses accuracy, and Greenwood (2004) provides, specifically for $k = 0.02$,

$$\frac{\sigma_0^2 T_{\text{vis}}}{E^* \gamma}\dot{a} = \begin{cases} (0.1035x + 0.3421)\, x^{1.116} & \text{for } 0.29 < \beta < 1, \\ \quad \text{where } x = (1/\beta - 1) & \\ & \\ -(0.2112x + 0.3939)\, x^{1.1403} & \text{for } 1 < \beta < 3.7, \\ \quad \text{where } x = (\beta - 1). & \end{cases} \tag{2.17}$$

These relations have successfully been used to explain adhesion hysteresis in oscillatory normal loading (Wahl et al. 2006), and in the rolling contact of polymers (Greenwood et al. 2009). More recently, Barthel & Frétigny (2009) studied viscoelastic cracks for the same three-element material model, but replaced the Maugis-Dugdale potential with a more realistic one, finding results similar to Eqs. 2.16 and 2.17.

The above form of adhesion hysteresis is often called mechanical hysteresis (Chen et al. 1991), and disappears when the contact loading/unloading cycle is performed at infinitely low velocities. A different kind is 'chemical hysteresis', where material close to the surface is left in a physically different state after the loading/unloading cycle (Chen et al. 1991; Chaudhury & Whitesides 1991; Chaudhury & Owen 1993). In this work, we assume mechanical hysteresis to be the dominant process.

Bulk dissipative force

When two viscoelastic spheres are pressed together at a finite velocity, a significant amount of energy might also be dissipated in the bulk of the material. When dissipation and strain rates are small everywhere, the total stress tensor can be written as a linear combination of the elastic and a dissipative stress tensor (Landau & Lifshitz 1965). We follow this approach, and write the dissipative stress as being proportional to the time-derivative of the elastic one (Brilliantov et al. 1996; Kuwabara & Kono 1987). Realizing we are interested only in the normal component of the dissipative stress within the contact area, we can write

$$\sigma_{\text{dis}}(r) = A\frac{\mathrm{d}}{\mathrm{d}t}p(r) = A\left[\frac{\partial p(r)}{\partial \delta}\dot{\delta} + \frac{\partial p(r)}{\partial a}\dot{a}\right], \tag{2.18}$$

where $p(r)$ is the elastic pressure distribution given by Eq. 2.1, and the proportionality constant A is a combination of viscous and elastic constants with units of time, which we approximate as $A \sim T_{\text{vis}}/v^2$ (Brilliantov et al. 1996, 2007).

Similar to Eq. 2.2, the dissipative stresses can be integrated to yield the bulk dissipative force. The integration should be over all the dissipative stresses, except for those arising from the crack propagation, which are accounted for by the viscoelastic crack theory described in Sect. 2.2.2. More specifically, we will separate the influence of the bulk deformation from the crack-induced stresses by only taking into account the $\dot{\delta}$-term in Eq.

2.18. This allows us to write

$$F_{\mathrm{D}} = A \int_0^a 2\pi r \dot{\delta} \frac{\partial p(r)}{\partial \delta} \,\mathrm{d}r = 2AE^* a\dot{\delta}. \tag{2.19}$$

The dissipative force thus depends on both a and $\dot{\delta}$, becomes negligible when the contact size goes to zero, and always has the same sign as $\dot{\delta}$, ensuring it will act like a true drag term and always oppose motion.

2.3 Head-on collisions

The contact model put forward in Sect. 2.2 can be used to calculate the evolution of the contact between two spheres that collide head-on. In this section, we limit ourselves to equal-sized spheres of the same material, but the theory described here can be applied to sphere-wall collisions by adjusting the effective mass and radius accordingly. The material properties are chosen to resemble water-ice microspheres (table 2.2). This combination of material properties has a Tabor parameter of $\mu \simeq 14$, which would put this in the JKR limit when viscoelasticity was not present. The value of T_{vis} is regarded as unknown, and will be varied later on to probe the effect the viscoelastic nature has on the evolution of the collision.

In Sect. 2.2.2 we obtained the elastic and dissipative force between two spheres as a function of the contact size, their mutual approach, and the time-derivatives of these variables. These are all the tools we need to numerically integrate a collision at a certain velocity, realizing that the evolution of the mutual approach is given by

$$\ddot{\delta} = -\frac{1}{m^*} \left(F_{\mathrm{E}} + F_{\mathrm{D}}\right), \tag{2.20}$$

where the forces are given by Eqs. 2.2 and 2.19. The reduced mass $m^{*-1} = m_1^{-1} + m_2^{-1}$ can be written in terms of density and radius. Meanwhile, the evolution of the contact size is governed by Eqs. 2.14 – 2.17. The moment of first contact is taken as $t = 0$, and as we do not allow for long-range forces the initial conditions for the mutual approach are

$$\begin{cases} \delta(0) = 0, \\ \\ \dot{\delta}(0) = v_{\mathrm{in}}. \end{cases} \tag{2.21}$$

As Eq. 2.14 does not allow $a = 0$, we have to make an analytical approximation for the initial growth of the contact area, see Appendix 2.B. Using these initial conditions, Eqs. 2.14, 2.16, 2.17 and 2.20 have to be solved simultaneously to obtain the evolution of δ and a in time.

2.3.1 Bouncing collision

Figure 2.2 shows the evolution of the contact size and elastic force as a function of mutual approach, for a head-on collision at 8 m s^{-1}, and $T_{\mathrm{vis}} = 10^{-11}$ s. The relations from Hertz

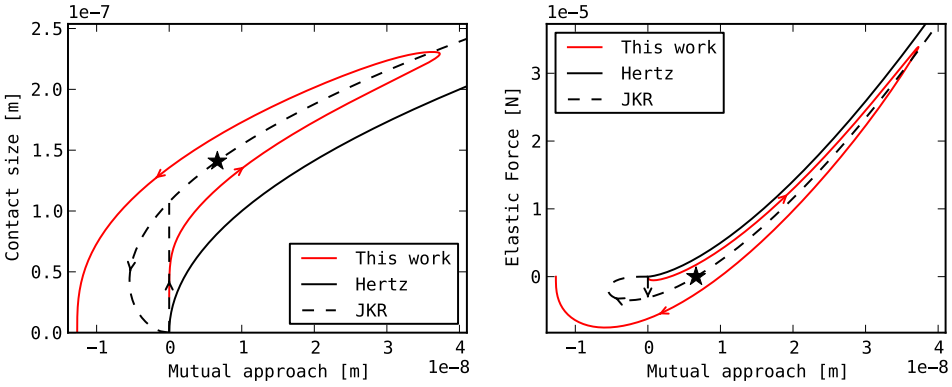

Figure 2.2: Evolution of the contact size (left) and elastic force (right) versus mutual approach, for an 8 m s^{-1} bouncing collision with the properties of ice (table 2.2) and a viscous relaxation time of $T_{\rm vis} = 10^{-11}$ s. Predictions of Hertz (Eqs. 2.4 and 2.5) and JKR theory (Eqs. 2.8 and 2.9) are also plotted, and the star marks the equilibrium point in JKR theory. The vertical dashed lines show the snap-on in JKR theory, where the contact radius and force jump to a finite value when the spheres first touch at $\delta = 0$.

theory and JKR theory are also shown, and the star marks the equilibrium point in JKR theory ($F_{\rm JKR} = 0$). At the start of the collision, $\delta = 0$, and it is clearly visible in the left panel of Fig. 2.2 that the contact area initially grows very fast, as its radius increases to $\sim$0.1 μm with δ hardly changing. This 'snapping on' is a consequence of the adhesive forces, and results in the contact being larger then predicted by Hertz theory. As a direct consequence, the force is negative early on, and the spheres are accelerated towards each other. However, the effective surface energy is smaller than the static value, so both the contact radius and the force do not reach the JKR-value. As the spheres compress, kinetic and surface energy are converted into elastic energy[2], and the spheres are brought to a halt at some maximum δ. Here, the motion is reversed, and the spheres start to move apart. During unloading (rebound), the contact area is shrinking, and the effective surface energy is larger than the static one, causing the contact area to be larger than expected from JKR, and the force to be smaller. During the rebound, the spheres will cross the point $\delta = 0$, but maintain contact as a result of the attractive surface forces. Because of the large effective surface energy, the maximum tensile force can be seen to be a factor 2 or so larger than the classic pull-off force from JKR theory, and contact can be maintained for even longer. Since both a and δ are followed individually, the collision can be integrated as a goes to zero. The total collision time, $\sim 1.7 \times 10^{-8}$ s, can be compared to the one expected from Hertz theory, which can be estimated as (Rayleigh 1906; Johnson 1987)

$$t_{\rm H} = 2.87 \left(\frac{m^{*2}}{R E^{*2} v_{\rm in}} \right)^{1/5}, \tag{2.22}$$

[2]In Appendix 2.C the energy budget during the collision is described in more detail.

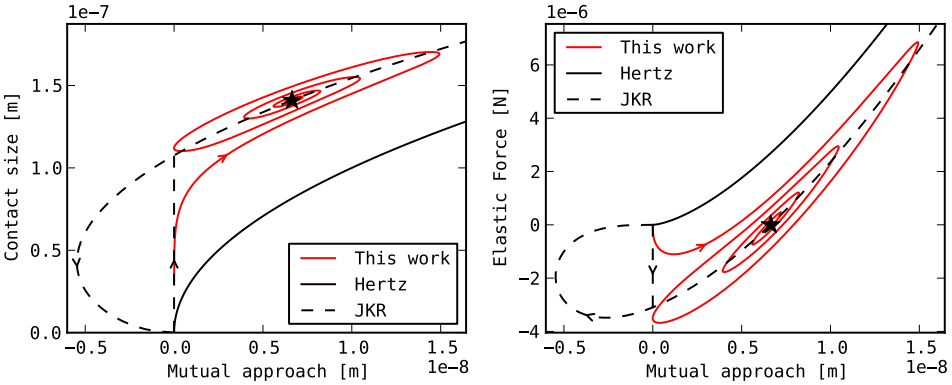

Figure 2.3: Evolution of the contact size (left) and elastic force (right) versus mutual approach, for a 2 m s^{-1} sticking collision with the properties of ice (table 2.2) and a viscous relaxation time of $T_{\text{vis}} = 10^{-11}$ s. Predictions of Hertz (Eqs. 2.4 and 2.5) and JKR theory (Eqs. 2.8 and 2.9) are also plotted, and the star marks the equilibrium point in JKR theory. The vertical dashed lines show the snap-on in JKR theory, where the contact radius and force jump to a finite value when the spheres first touch at $\delta = 0$.

and equals, for this particular set-up, 1.4×10^{-8} s. Thus, the combined effects of viscoelasticity and adhesion have lengthened the collision by about one fifth.

2.3.2 Sticking collision

At lower velocities, the pre-collision kinetic energy becomes comparable to the dissipated energy, and sticking can be achieved. Figure 2.3 shows the evolution of the contact for a collision similar to the one from Fig. 2.2, but at a velocity of $v_{\text{in}} = 2\,\text{m s}^{-1}$. Initially, the collision resembles the faster one, but as there is less kinetic energy available, the maximum contact size and mutual approach reached are somewhat smaller. During rebound, the spheres are not able to separate, and instead oscillate back and forth, spiraling towards the JKR equilibrium point as a result of the dissipative effects. In a purely elastic scenario, the oscillation would not be dampened. The kinetic energy is dissipated within a couple of oscillations, on a timescale of a few times 10^{-8} s (see Appendix 2.C). The energy absorbed as a result of the dissipative properties will be converted into heat. At this stage, we do not take into account any effects an increased temperature might have on the material properties, and simply view this energy as lost.

2.3.3 Coefficient of restitution

To capture the outcome of a collision in a single quantity, we calculate the coefficient of restitution e_{A}. There are several definitions for this coefficient in terms of velocity or energy (Stronge 1990), but for the normal collisions described in this work the two are

identical, and we can write the coefficient of restitution as

$$e_{\rm A} = -\frac{\dot{\delta}(t_c)}{\dot{\delta}(0)}, \tag{2.23}$$

where t_c is the collision time. The resulting value can be compared to two cases in which analytical estimates are possible. In the elastic JKR limit the coefficient of restitution equals (Johnson 1987; Thornton & Ning 1998)

$$e_{\rm JKR} = \sqrt{1 - \left(\frac{v_c}{v_{\rm in}}\right)^2}, \tag{2.24}$$

where

$$v_c = \left(\frac{14.18}{m^*}\right)^{1/2} \left(\frac{\gamma^5 R^4}{E^{*2}}\right)^{1/6}, \tag{2.25}$$

is the sticking velocity, below which all collisions will result in sticking. Alternatively, we may look at the non-adhesive viscoelastic case. In the limit where dissipation is small, the coefficient of restitution can be estimated as (Brilliantov et al. 1996; Schwager & Pöschel 1998)

$$e_{\rm D} \simeq 1 - 1.92\left(\frac{A}{t_{\rm H}}\right). \tag{2.26}$$

If one were to assume adhesion and viscoelastic dissipation do not influence each other, these two energy losses can be added to yield

$$e_{\rm I} = \sqrt{e_{\rm JKR}^2 + e_{\rm D}^2 - 1}. \tag{2.27}$$

However, adhesion and viscoelasticity cannot be treated independently as substantially more energy is dissipated. For example; the collision described in Fig. 2.2 has $e_{\rm I} = 0.92$, while the numerical viscoelastic model employed here results in $e_{\rm A} = 0.66$.

Figure 2.4 shows the variation of the coefficient of restitution with velocity, and compares it to the above estimates. Focussing first on the lowest velocities, we see that the sticking velocity is increased substantially. Towards the higher velocities, the results appear to approach the limit described by Eq. 2.26. Comparison with Eq. 2.27 shows that treating adhesion and viscoelasticity separately will significantly underestimate not only the sticking velocity, but the amount of energy dissipation over the entire velocity range. The effect of varying the reduced radius is shown in Fig. 2.5, where collisional outcomes at a fixed velocity are shown. Again, the difference between the theory developed here and Eq. 2.27 is substantial, although it vanishes for larger spheres, where the kinetic energy is much larger than the dissipated energy, and collisions are almost completely elastic.

An important parameter for many studies is the sticking threshold velocity v_s; the maximum velocity at which colliding particles will stick. Figure 2.5 shows the sticking velocity as a function of reduced radius and viscous relaxation time for water-ice particles. The sticking velocity in the non-viscous case (Eq. 2.25) is plotted for comparison. For very small values of $T_{\rm vis}$ the material effectively behaves elastically and Eq. 2.25 is retrieved. For larger values of the relaxation time, the sticking velocity can be increased significantly, especially for small particle sizes.

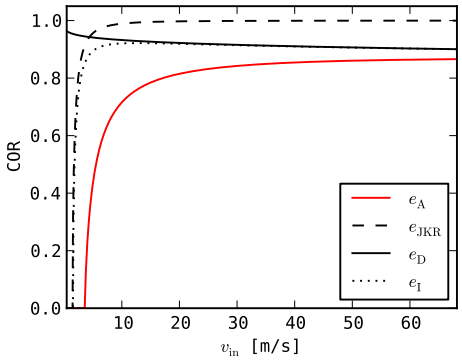

Figure 2.4: Coefficient of restitution (COR) for head-on collisions as a function of impact velocity (solid red). Properties of ice and a viscous relaxation time of $T_{\mathrm{vis}} = 10^{-11}$ s are used.

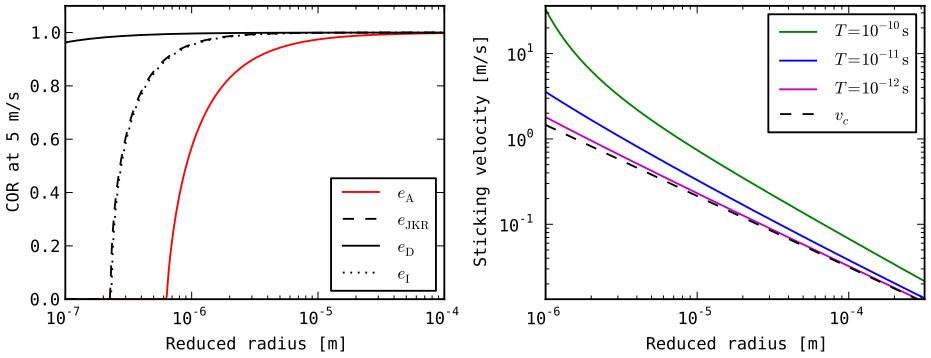

Figure 2.5: *Left:* Coefficient of restitution for head-on collisions as a function of reduced radius. The material properties of ice and a viscous relaxation time of $T_{\mathrm{vis}} = 10^{-11}$ s have been assumed. *Right:* Sticking velocity as a function of reduced radius for the material properties of ice. The non-viscous sticking velocity of Eq. 2.25 is plotted for comparison.

2.3.4 Plastic deformation

During a collision, the stress in the material can become so large that it starts to yield plastically. In a contact between spheres, ignoring adhesion and viscosity, the maximum shear stress is attained right beneath the contact area and on the axis of symmetry. Using either the Tresca or von Mises criterion, it can be shown that plastic deformation in the region below the contact will start when the pressure in the center of the contact area p_0 exceeds 1.6 times the yield strength Y of the material in simple tension (Johnson 1987). We can write a condition for the impact velocity for which yield is just initiated.

$$v_{\mathrm{y}}^2 = 10.2 \frac{R^3 p_{\mathrm{y}}^5}{m^* E^{*4}}, \tag{2.28}$$

where $p_y = 1.6Y$ denotes the pressure at the center of the contact area at the onset of plastic deformation (Johnson 1987). Note that since v_y scales with R^3/m^*, the yield velocity does not depend on size, assuming Y is independent of size. When the impact velocity is larger than v_y, a plastic region will be created underneath the contact area, and the pressure distribution will flatten off (Hardy et al. 1971). For even faster collisions the maximum pressure grows from $1.6Y$ to about $3Y$, at which point the plastic region reaches the sphere's free surface, plastic flow is no longer contained and the situation becomes more complicated (Johnson 1987).

An analytical model for the coefficient of restitution is provided by Thornton & Ning (1998), where the pressure distribution is cut off above a critical p_y. It is shown that this cutoff results in a force which depends linearly on the approach δ. In addition, Thornton and Ning assumed that during the rebound phase the forces are Hertzian, but the radius of curvature is altered because of the plastic yield during loading. The resulting coefficient of restitution equals

$$e_P = \begin{cases} 1 & \text{for } \hat{v} > 1, \\ \left(6\sqrt{3}/5\right)^{1/2}\left(1-\frac{1}{6}\hat{v}^2\right)^{1/2} & \\ \quad \times\left[\hat{v}/\left(\hat{v}+2\sqrt{\frac{6}{5}-\frac{1}{5}\hat{v}^2}\right)\right]^{1/4} & \text{for } \hat{v} \le 1, \end{cases} \tag{2.29}$$

where $\hat{v} = (v_y/v_{in})$. If no plastic deformation occurs, the collision is perfectly elastic and $e_P = 1$. If the impact velocity exceeds v_y, the coefficient of restitution will drop off. At velocities well above the yield velocity $e_P \propto (v_y/v_{in})^{1/4}$. More advanced models exist, that treat the variation of the central pressure and the unloading phase more carefully (Wu et al. 2003; Wu et al. 2005) or include adhesion (Mesarovic & Fleck 2000). However, for the purpose of this work, we choose the model of Thornton & Ning to describe the plastic behavior. For the constant cutoff pressure we use $p_y = 1.6Y$.

For typical material parameters the yield velocity lies well above the sticking velocity (Thornton & Ning 1998), and it seems reasonable to assume the effects of adhesion and plastic deformation can be treated separately. Assuming the energy losses resulting from adhesion/viscosity and plastic deformation are being additive, we can write the total coefficient of restitution as

$$e = \sqrt{e_A^2 + e_P^2 - 1}, \tag{2.30}$$

where e_A is obtained by numerically integrating $\dot{\delta}$ in Eq. 2.23.

2.4 Comparison to experiments

The model presented in Sect. 2.3 can be compared to experiments performed on colliding spheres where adhesion is of some importance, i.e., small spheres and/or low velocities. Experiments with colliding microspheres have been performed for some decades now, with results often in the form of a series of coefficients of restitution as a function of velocity. In general, most experimental results look similar to Fig. 2.4, and also show some

Experiments with micrometer particles				
Projectile material	target material	diameter (μm)	velocity (m s^{-1})	Ref.
polystyrene latex	quartz	1.27	2 - 15	Dahneke (1975)
polyvynil-toluene	quartz	2.02	5 - 35	Dahneke (1975)
ammonium fluorescein	mica	4.9	5 - 120	Wall et al. (1990)
ammonium fluorescein	silicon	4.9	5 - 110	Wall et al. (1990)
ammonium fluorescein	tedlar	4.9	3 - 16	Wall et al. (1990)
ammonium fluorescein	molubdenum	4.9	5 - 60	Wall et al. (1990)
Ag-coated glass	aluminium	8.6	2 - 20	Dunn et al. (1995)
Ag-coated glass	copper	8.6	2 - 20	Dunn et al. (1995)
Ag-coated glass	coated steel	8.6	2 - 20	Dunn et al. (1995)
Ag-coated glass	steel	8.6	2 - 20	Dunn et al. (1995)
Ag-coated glass	tedlar	8.6	2 - 20	Dunn et al. (1995)
steel	silicon	55	0.4 - 2	Li et al. (1999)
steel	silicon	90	0.4 - 2	Li et al. (1999)
Ag-coated glass	silicate	40	0.04 - 0.44	Kim & Dunn (2007a)
Experiments with millimeter particles				
Projectile material	target material	diameter (mm)	velocity (m s^{-1})	Ref.
acrylic	acrylic	3.96	0.1 - 1	Sorace et al. (2009)
steel	steel	3	0.05 - 0.5	Sorace et al. (2009)
ceramics	ceramics	03	0.05 - 0.5	Sorace et al. (2009)

Table 2.1: Summary of experiments used in this work. For a more detailed review of these experiments the reader is referred to Güttler et al. (2012).

dissipation towards higher velocities. In addition, fitting a purely elastic adhesive model has on some occasions yielded unrealistically high values for the surface energy (Sorace et al. 2009). In this section we set out to fit the model to a large set of published experimental results, with the aims of testing its applicability, and deriving the key parameters that govern the adhesive, viscoelastic, and plastic behavior.

2.4.1 Method

Available collision experiments reporting coefficients of restitution have been collected and reviewed by Güttler et al. (2012). Here, we select those experiments from the dataset that resemble head-on and non-rotating collisions, and where the effects of surface roughness are believed to be small. Moreover, we are interested only in the data where a drop in the coefficient of restitution towards lower velocities is visible. With this, we hope to choose an unbiased sample, which is also as complete as possible to the best of our knowledge. The selected experiments are summarized in table 2.1, where the materials, particle sizes, and examined velocities are shown. The micrometer experiments are all sphere-wall collisions, while the millimeter particles were collided sphere on sphere. Table 2.2 lists the various materials, together with their properties.

To fit the experimental results, we use the elastic material properties from table 2.2, and treat γ, T_{vis} and Y as fitting parameters. While the surface energy might be considered as known, the values listed in table 2.2 under γ_{L} correspond to clean surfaces in perfect contact. These conditions are not necessarily met during an experiment, and the value of the surface energy might differ accordingly. Therefore, we allow γ to vary and will compare the result to the literature value in Sect. 2.4.2. For a particular experiment, the best fit is obtained by minimizing

$$\chi^2 = \frac{1}{N}\sum_{n=1}^{N}\left[e_{\mathrm{exp}}(v_n) - e(v_n)\right]^2, \tag{2.31}$$

where N is the total number of data points, and the theoretical $e(v_n)$ is given by Eq. 2.30. The value of χ^2 is calculated for a grid of values for γ, T_{vis} and Y, after which the uncertainty in each individual parameter is taken as the range in which this parameter can vary without χ^2 growing by more than a factor of 2. For experiments where the error on the coefficient of restitution was provided, this method yielded uncertainties comparable to the size of the 1σ confidence limit.

2.4.2 Results

We recognize three global characteristics in the experiments: (1) At low velocities, the outcome is dominated by adhesive and viscous forces, sometimes resulting in sticking. Just above the sticking velocity the COR rises steeply but does not reach unity. (2) Towards slightly higher velocities, the kinetic energy increases and the effects of adhesive forces decrease. However, as a result of the bulk dissipative force collisions are still dissipative, and regions where the COR is nearly constant and well below unity are observed

Material	E (GPa)	ν	ρ (g cm^{-3})	c_s (m s^{-1})	γ_L (J m^{-2})
METALS/MINERALS					
aluminium alloy	70	0.345	2.7	5092	0.59
(stainless) steel	190	0.28	7.92	4898	1.62
molubdenum	320	0.33	10.28	5579	2.81
polished quartz	54	0.17	2.6	4557	0.025
silicon	180	0.33	2.33	8789	1.42
mica	90	0.33	3.	5477	0.77
copper	130	0.34	8.94	3813	1.11
Ag-coated glass	72	0.21	2.6	5261	0.61
POLYMERS					
PSL	3.4	0.33	1.026	1820	0.025
tedlar	2	0.33	1.46	1170	0.018
acrylic	3	0.35	1.22	1568	0.02
lucite	2.6	0.3	1.18	1484	0.02
PVT	3	0.33	1.2	1581	0.02
AF	1.17	0.33	1.35	931	0.01
OTHERS					
ceramics	370	0.26	3.86	9790	0.04-5
water ice	7	0.25	1.00	2645	0.37

Table 2.2: Different materials with their elastic properties and densities. The soundspeed has been calculated as $c_s = (E/\rho)^{1/2}$. Surface energy values come from Chokshi et al. (1993); Gilman (1960); Mark (1999); Siegel et al. (2003); Król & Król (2006); Kim & Dunn (2007b), and references therein.

for almost every experiment. These regions, covering up to factors of 3–4 in velocity, cannot be adequately explained by purely elastic adhesive theory, as the COR is expected to rise to 1 rapidly above the sticking velocity. (3) Some experiments show a drop in the COR towards high velocities. This drop is explained by plastic deformation. In the majority of the experiments however, the high velocities needed to observe this part are not reached.

Figure 2.6 shows two examples of the produced fits. All other fits, as well as a table giving the fitting parameters and uncertainties for each individual experiment, are presented in Appendix 2.D. Perusal of the fits reveals good agreement between model and experiments. The three global characteristics outlined above are in a natural way contained with this theory in terms of the adhesion and the viscous dissipation at the contact edge, the bulk viscous dissipation, and plastic deformation. For comparison, we plot in Fig. 2.6 curves neglecting viscoelasticity (dashed lines). It is clear that a model including only adhesive forces and plastic deformation is unable to describe the experimental results at intermediate velocities.

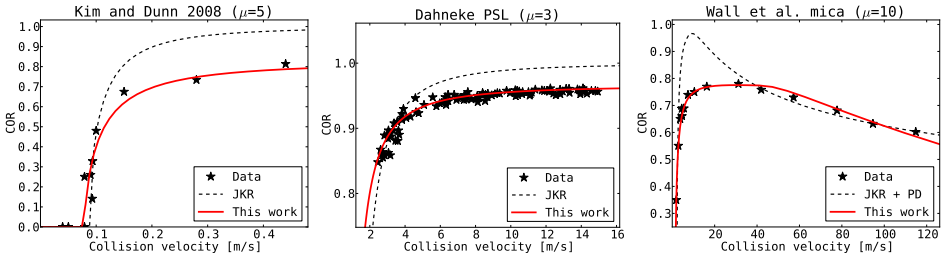

Figure 2.6: Three typical examples of the fits produced in Sect. 2.4. Of these, only the rightmost experiment covers the plastic deformation regime. The dashed curves show JKR theory (Eq. 2.24), where the surface energy has been chosen such that the low velocity part of the data is described well. For the rightmost curve, plastic deformation (Eq. 2.29) was added when creating the dashed curve.

Surface energy

Figure 2.7(a) shows the surface energy values for the best fitting models. The values have been normalized to the literature value, obtained by combining[3] the corresponding surface energies from table 2.2. The solid gray line indicates $\gamma = \gamma_{\mathrm{L}}$. The majority of the derived surface energies lie very close to the literature value.

A handful of experiments show a large uncertainty in the determination of γ, and we briefly discuss why. For Dahneke's PVT experiment, the reason is that the drop in the COR towards low velocities is not very distinct. For the mm-sized experiments the large uncertainty is a result of the scatter in the data, and the fact that the majority of the data points lie close to unity. As a result, model curves that combine a negligibly small value for T_{vis} with a large surface energy, cannot be rejected on the basis of the method outlined above. However, non-zero values for the viscous relaxation time do describe the data more accurately, and the surface energies for these fits lies significantly closer to γ_{L}, alleviating the issue of the high apparent surface energies as put forward by Sorace et al. (2009). Moreover, measurements by Sorace et al. of the COR at high speeds[4] range between 0.90 and 0.95, supporting the hypothesis that the energy loss observed is caused by more than just adhesive forces.

Yield strength

The obtained yield strengths are shown in Fig. 2.7(b), normalized to the Young's modulus of the softer material. The gray arrows correspond to experiments where plastic deformation does not occur at the velocities studied, and therefore give lower limits on the

[3] For like materials, γ equals twice the surface free energy, and for different materials the surface energies can be combined as $\gamma \simeq 2\sqrt{\gamma_1\gamma_2}$.

[4] These results are not included in the fitting procedure as it is unclear at which velocity they were obtained.

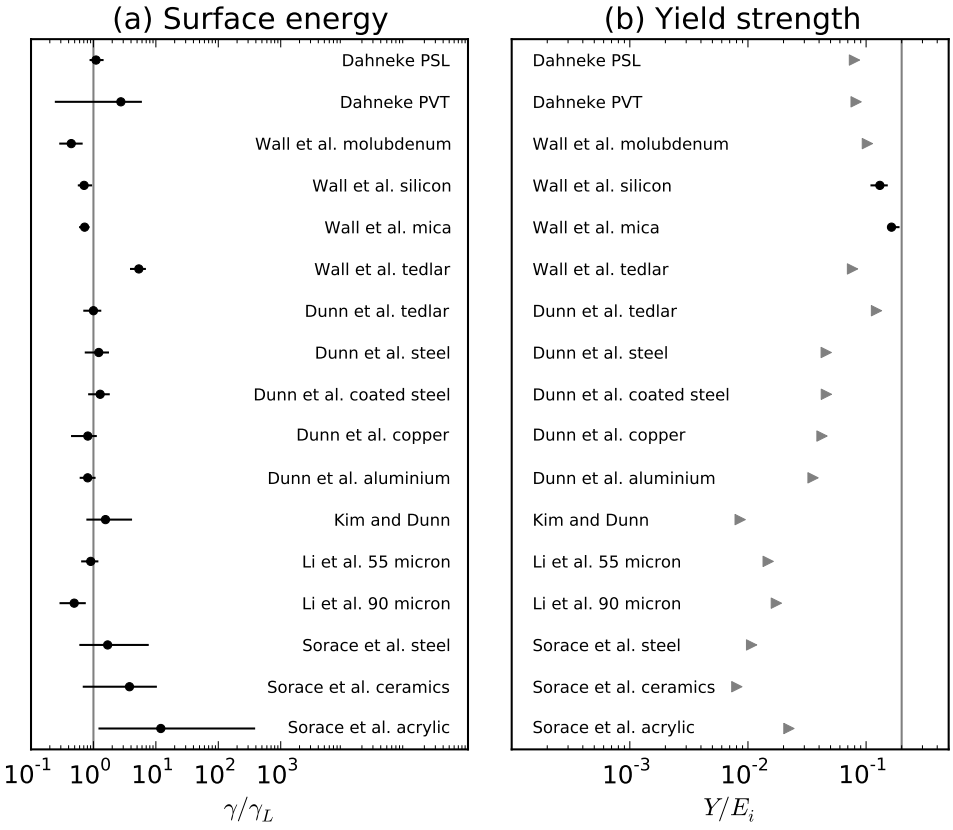

Figure 2.7: Best fit values for the surface energy and yield strength. The surface energy has been normalized to the literature value obtained from table 2.2, and the yield strength is normalized to the Young's Modulus of the softer particle. The estimated error is indicated by the solid lines, and gray arrows indicate lower limits. Experiments are ordered from smallest (top) to largest (bottom) reduced radius.

material strength[5].

In macroscopic metal bodies plastic flow is the result of the motion of a dislocation through the crystalline lattice structure, and the yield strength is typically orders of magnitude smaller than the Young's modulus. The typical density of such dislocations that intersect a unit plane equals $10^{12} - 10^{13}$ m^{-2}, or between 1 and 10 per square micrometer (Kraft et al. 2010). On sub-micrometer scales, very few dislocations are available and the yield strength is expected to approach the theoretical strength of $0.2\,E_i$, largely independent of material (Petch 1968). To describe the size dependence of the yield strength, an

[5]For the PVT (Dahneke 1975) and tedlar and molubdenum experiments (Wall et al. 1990), the best fitting models did include plastic deformation towards high velocities, but models without could not be rejected.

empirical power law of the form

$$Y = Y_0 + kl^{-n}, \tag{2.32}$$

is often used, with Y_0 the macroscopic yield strength, l the characteristic length scale, k a constant, and $n = 0.5$ the classical Hall-Petch value (Petch 1953). Experimentally derived values range between $0.5 > n > 1$ for metals (Brenner 1956, 1957; Volkert & Lilleodden 2006; Zhu et al. 2012), suggesting there are multiple deformation mechanisms acting, that cannot be captured in a single power law (Kraft et al. 2010). For polymers a theoretical strength of $0.2\,E_i$ has been predicted by Frenkel (1926), while experimental values of the yield strength in bulk glassy polymers (Brown 1971; Kozey & Kumar 1994) and metallic glasses (Johnson & Samwer 2005) are about an order of magnitude smaller, and appear to be correlated with temperature as well as elastic modulus.

We estimate the length scale l on which the plastic deformation occurs in the collision experiments, as being equal to the maximum Hertzian contact radius

$$l = \left(\frac{15 m^* v_{\mathrm{in}}^2 R^2}{16 E^*} \right)^{1/5}. \tag{2.33}$$

To obtain a single value for l for every experiment in table 2.1, we use a representative velocity equal to half the maximum velocity used in that particular set up. The obtained normalized yield strengths are plotted in Fig. 2.8(a) as a function of l. For comparison, we plot the result of Lifshitz & Kolsky (1964), who found a yield velocity of $0.3\,\mathrm{m\,s^{-1}}$ for steel spheres with a 3.18 mm radius. The observed material strengths vary by about a factor of 20, and appear to approach the theoretical strength for the smallest length-scales. These results confirm that the drop in coefficient towards high velocities is indeed caused by plastic yield.

Relaxation timescale

Of the fitted parameters, the viscous relaxation time is considered the most uncertain. Figure 2.8(b) shows the best fit values plotted against the reduced radius. For the theory of Sect. 2.2 to be valid, the relaxation time needs to be small compared to the collision time t_c. As a lower limit for the collision time we can use the Hertzian approximation (Eq. 2.22), realizing that any adhesive and/or viscous effects will act to increase the collision time. The Hertzian collision time is plotted as a gray solid line in Fig. 2.8(b) for typical properties ($E^* = 10\,\mathrm{GPa}$, $\rho = 2\,\mathrm{g\,cm^{-3}}$ and $v_{\mathrm{in}} = 10\,\mathrm{m\,s^{-1}}$). The gray dashed line corresponds to $t_{\mathrm{H}} \times 10^{-3}$. The fitted values for the relaxation time lie well below the collision time, validating the use of our model. While the mm-sized experiments technically yield upper limits, we prefer to think viscoelastic behavior is important also at these sizes, as negligibly small values for T_{vis} result in very large surface energies, and fail to explain the high-velocity points presented by Sorace et al. (2009). The apparent relation between the relaxation time and reduced radius is curious, and will be further discussed in Sect. 2.5.

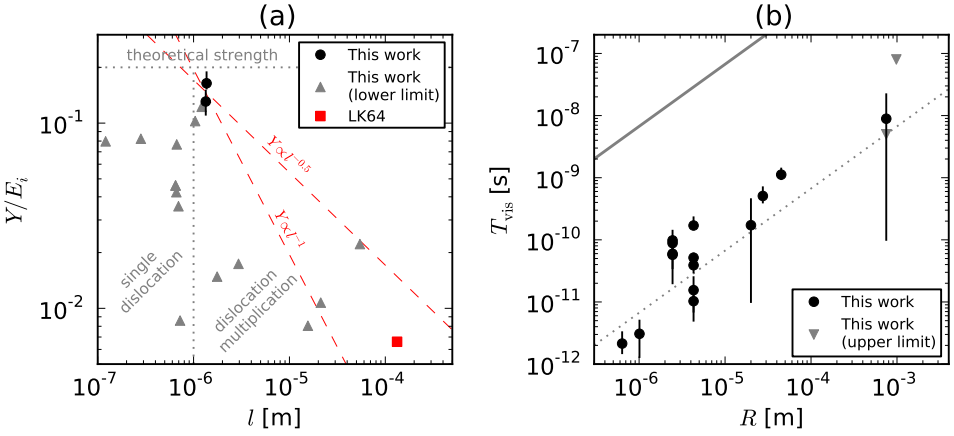

Figure 2.8: (a) Variation of normalized yield strength with particle radius. Gray triangles represent lower limits, and the horizontal dotted line shows the theoretical strength of $Y/E_i = 0.2$. For $l > 10^{-6}$ m many dislocations will be available, while they are scarce for smaller sizes (see text). The red square corresponds to data from Lifshitz & Kolsky (1964). The red dashed lines show $Y \propto l^{-0.5}$ and $Y \propto l^{-1}$ (Kraft et al. 2010). (b) Relaxation times as a function of reduced radius. The solid and dashed gray lines indicate typical values for $t_{\rm H}$ and $t_{\rm H} \times 10^{-3}$ respectively.

2.5 Discussion

A collision between spherical particles results in some kinetic energy being lost. As a result, the rebound velocity is smaller than the incoming velocity. In this work we put forward a collision model that treats adhesion and viscoelasticity in a self-consistent way, and assume the energy losses arising from plastic deformation to be additive.

Incorporating dissipative viscoelastic stresses into a static contact description such as JKR theory is not straightforward. The problem is the existence of a theoretically infinite tensile stress at the contact edge, which causes infinite stress rates when the contact area grows or shrinks at a finite rate. Integration of the dissipative stresses will then inevitably result in an infinitely large dissipative force. A solution to this problem comes from viscoelastic crack theory (Greenwood 2004), and is included in the contact description by allowing for an effective surface energy, which varies as a function of the rate with which the contact advances/recedes. To be able to describe the contact hysteresis that ensues, we follow the evolution in time of both the contact radius and the mutual approach. Some distance from the contact edge, the stress rates are dominated by the changes in the mutual approach, rather than the crack opening or closing. The dissipative stresses arising here can be integrated to yield a dissipative stress. With analytic expressions for the total normal force between two non-rotating particles, a head-on collision at a certain velocity can be solved numerically, yielding the total energy loss and coefficient of restitution.

Regarding the particle size and elastic modulus as known, the model is fitted to experimental results and yields values for the surface energy, the viscous relaxation timescale,

and the yield strength. While the obtained values for the surface energy and yield strength compare well to expected values, it is difficult to judge whether the inferred material relaxation time is realistic, partly because of the viscoelastic model that is used, in which the material relaxes linearly on a single timescale. This is a very simplistic view, as more realistic materials contain numerous characteristic time- and length scales corresponding to (parts of) molecules, chains of molecules, or lattice structures. The experiments clearly reveal the effect of viscous dissipation for all particle sizes and therefore, by necessity, at all collision timescales. This immediately implies that the relevant viscous dissipation timescale is longer for collisions between larger grains (Fig. 2.8(b)). We interpret this along the lines outlined above: when larger volumes are involved in the collision process, larger structures can be activated in the dissipation process, and these larger structures by necessity require longer timescales to act.

The collision model used throughout this work does not take into account energy lost in the excitation of elastic waves, or the presence of surface asperities. We shall discuss these assumptions briefly. During a collision of two bodies, elastic waves will be excited that travel back and forth and carry a part of the initial kinetic energy. In the non-adhesive case this energy is expected to be negligible if the collision velocity is well below the material soundspeed (Rayleigh 1906), which is the case for the experiments encountered in this work (see table 2.2). However, the presence of adhesion might enhance the elastic wave energy around the lower velocities, increasing the sticking velocity slightly (Chokshi et al. 1993).

The presence of surface asperities can influence the collisional outcome profoundly. Irregularities that are large compared to the contact size will alter the local reduced radius, while smaller asperities can be crushed to dissipate energy (Tsai et al. 1990) or survive and act to reduce the effective surface area and therefore the effect of adhesive forces (Tabor 1977). Several authors provided information on the particle roughness. For the fluorescein particles, Wall et al. (1990) provided an upper limit on the roughness of 3 nm. The steel particles were stated to be smooth to within the resolution of the scanning electron microscope (SEM), while the surface of the target showed a height standard deviation of $\sim$ 1 nm (Li et al. 1999). An SEM was also used by Dunn et al. (1995) to study their surfaces, who found the steel to be virtually flawless within the resolution of 4 nm. The softer targets showed some irregularities on the micron scale. Unfortunately, Dahneke (1975) and Sorace et al. (2009) provided no information on the roughness of the particles they used. For more details on the surface conditions in the various experiments the reader is referred to Güttler et al. (2012) or the original experimental works. The typical diameter of the contact area ranges between about 100 nm and 20 μm for the smallest and largest spheres described here, while the mutual approach is a factor (a/R) smaller. Thus, contact will be made over many small asperities simultaneously, and their presence is not expected to significantly alter the collisional outcome. The obtained surface energies, as plotted in Fig. 2.7, show no systematic deviation from literature values. Therefore, we believe that in general the effects of both elastic wave excitation and surface asperities are small. The collision model also assumes a Tabor parameter $\mu > 5$ (Tabor 1977; Johnson & Greenwood 1997). The values of the Tabor parameter (calculated using γ_{L}) are given in Fig. 2.6 and in the supplementary material. While two experiments are perhaps limit-

ing cases, the majority of the experiments have $\mu \gg 5$, justifying the use of the collision model.

2.6 Conclusions

In this work we have studied the collision between adhesive, viscoelastic spheres in a self-consistent way, by following the evolution of both the contact size, and the mutual approach of the sphere's centers of mass independently. The contact edge is described using viscoelastic crack theory, whereas deformations in the bulk of the material give rise to a dissipative force. The main results are:

1. The combined effects of viscoelasticity in the bulk and at the contact edge can cause significant deviations from static adhesive contact theory. As a result, there is no unique relation between the contact size and the mutual approach.

2. Because energy is dissipated through viscoelastic effects both in the bulk and at the contact edge, the sticking velocity can be significantly increased from the value predicted based on elastic adhesive theory. Well above the sticking velocity the viscoelastic effects still cause significant energy loss, and a coefficient of restitution of less then unity.

3. Assuming viscoelasticity and adhesion can be treated separately results in a significant underestimation of the energy lost during a collision.

The model is extended to include plastic deformation at high velocities, and compared to a large set of experimental results resulting in the determination of the surface energy, material yield strength, and viscous relaxation time. The main findings can be summarized as follows:

4. The collision model is remarkably successful in describing a large number of experiments, varying in experimental set-up, particle materials, particle size, and collision velocity. Removing any one of the three energy-loss mechanisms results in a dramatic decrease in the quality of the fit.

5. The surface energy values obtained from the experiments are in good agreement with literature values. The majority of the derived surface energies lies within a factor of two of the expected values. The remaining small differences are expected and can easily be attributed to elastic waves and surface roughness.

6. Through fitting the yield velocity, a value for the material yield strength can be obtained. For the majority of experiments plastic yield is not observed, resulting in a lower limit for this parameter. The resulting values for the yield strength lie within the expected range, and approach the theoretical strength of about 0.2×Young's modulus for the smallest sizes.

7. When viscous dissipation is important, the relaxation timescale has to be well below the collision timescale. We observe a correlation between the relaxation timescale and the reduced radius of the sphere(s). We suggest that this relationship reflects the activation of relaxation in larger and larger structures as the collision size scale increases.

Acknowledgements

Dust studies at Leiden Observatory are supported through the Spinoza Premie of the Dutch science agency, NWO. C.G. is grateful for the support of the Japan Society for the Promotion of Science (JSPS). D.H. acknowledges funding from the German Research Council (DFG) under grant B1298/11-1. The authors would like to thank J. Blum for encouraging discussions.

2.A Quasi-static limit

Here we estimate the timescales below which the effects of viscosity are small, and the elastic limit is retrieved. Turning our attention first to the bulk dissipation, the effect of $T_{\rm vis}$ becomes negligible when

$$\frac{F_{\rm D}}{F_{\rm E}} < 10^{-2}. \tag{2.34}$$

Plugging in Eqs. 2.2 and 2.19, and assuming the Hertzian relation Eq. 2.4 reduces the above equation to

$$T_{\rm vis} < 10^{-2}\, \nu^2 t_c, \tag{2.35}$$

where we have used $(\delta/\dot{\delta}) \sim t_c$. Thus, bulk dissipation will have little effect on the energy balance if the relaxation timescale is much smaller than the collision timescale. A similar result can be obtained directly from Eq. 2.26.

The magnitude of the adhesion hysteresis depends on the crack velocity. We assume the quasi-static limit to be retrieved when the difference between effective and static surface energy is of order 10^{-2}. Making use of Eq. 2.17, appropriate for low crack velocities, we find this holds when

$$\left(\frac{\sigma_0^2 T_{\rm vis}}{E^* \gamma}\right) |\dot{a}| < 10^{-3}. \tag{2.36}$$

In a collision, $\dot{a}$ will vary significantly, but we may obtain a typical value from Hertzian theory, where $\dot{a} = \dot{\delta}(R/2a)$, allowing us to rewrite the above limit as

$$T_{\rm vis} < 10^{-3} \frac{z_0}{a} \left(\frac{2E^* z_0}{\gamma}\right) t_c. \tag{2.37}$$

Relaxation timescales longer than this will result in adhesion hysteresis, and affect the collisional outcome if the energy that is dissipated in this way is comparable to the kinetic energy. The fraction $E^* z_0/\gamma$ is relatively small for materials like ice or polymers, but can

be substantially larger for metals or minerals like quartz (see table 2.2). As a result, the relative importance of crack and and bulk dissipation will vary per material.

For the ice particles considered in Sect. 2.3, the term in brackets is of order unity, while $(z_0/a) \sim 10^{-3}$. Comparison of Eqs. 2.35 and 2.37 reveals energy dissipation at the contact edge can take place for shorter timescales, and when the bulk of the material behaves elastically. For a $4\,\mathrm{m\,s^{-1}}$ collision between the ice spheres of table 2.2, Eqs. 2.35 and 2.37 both hold for $T_{\mathrm{vis}} = 10^{-14}\,\mathrm{s}$. For this value of the relaxation time, numerical integration of the equations of motion yields $e = 0.93$, which is in excellent agreement with the quasi-static result: $e_{\mathrm{JKR}} = 0.93$.

2.B Intial condition for contact area

At the point of first contact, $a = \delta = 0$, causing G_{eff}, as defined by Eq. 2.14, to be indefinite. To account for this, we take an approach very similar to Sect. 4.1 of Greenwood & Johnson (2006), the main difference being that our approximation is focussed on $\delta = 0$, whereas the former uses $F_{\mathrm{E}} = 0$.

Setting the mutual approach to zero in Eq. 2.14 returns

$$a = \left(\frac{2\pi R^2 G_{\mathrm{eff}}}{E^*}\right)^{1/3}. \tag{2.38}$$

As $\dot{a}$ is practically infinite, we can assume G_{eff} should have the minimum value of $k\gamma$. In this case ($\beta = k$), Eq. 2.16 cannot be used, and an analytical approximation is required. Following a similar approach as Greenwood & Johnson (2006), we can approximate the time since contact formation, for a given β, as

$$\begin{aligned} 1.198\, T_{\mathrm{vis}}\sigma_0^2\left(\frac{R}{E^{*2}\gamma}\right)^{2/3} t \simeq \quad & (s^4-1)\log\left(\frac{1-k}{1-s^4}\right) - 1.5\log(1+s+s^2) \\ & - \sqrt{3}\arctan\left(\frac{2s+1}{\sqrt{3}}\right) + 3s(1+s^3/4), \end{aligned} \tag{2.39}$$

where $s \equiv \beta^{1/3}$. Now, a value of β arbitrarily close to k can be chosen, and the above two equations will return the corresponding contact size, and time difference, providing a starting point for $\dot{a}$. The assumption that $\delta = 0$ is justified as the contact initially grows so rapidly, the mutual approach hardly changes. For our numerical integrations, we have used the starting value of $G_{\mathrm{eff}} = 1.01k\beta$.

2.C Energy budget during collision

It proves useful to examine the various energies in the system during the collision. First, the kinetic energy is taken to equal

$$U_{\mathrm{K}} = \frac{1}{2}m^*\dot{\delta}^2. \tag{2.40}$$

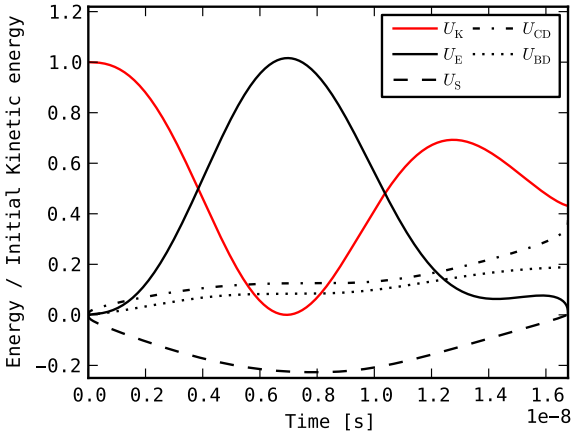

Figure 2.9: Evolution of the kinetic energy (U_K), elastic energy (U_E), surface energy (U_S), and energy dissipated at the crack (U_{CD}) and in the bulk (U_{BD}), for a 8 m s^{-1} bouncing collision with the ice properties of table 2.2 and a viscous relaxation time of $T_{vis} = 10^{-11}$ s. The energies are normalized to the initial kinetic energy of the collision.

We already have an expression for the elastic energy in Eq. 2.3, and the surface energy is given by Eq. 2.6. The total amount of energy that has been dissipated at the crack tip at a time t' can be written as

$$U_{CD} = \int_0^{t'} 2\pi a(1-\beta)\gamma\dot{a}\,\mathrm{d}t. \tag{2.41}$$

This quantity is always positive, as $\dot{a}$ has the same sign as $(1-\beta)$. Lastly, the energy that has been dissipated in the bulk by F_D at some time t' is obtained through

$$U_{BD} = \int_0^{t'} F_D\dot{\delta}\,\mathrm{d}t. \tag{2.42}$$

Figure 2.9 shows these energies, normalized to the kinetic energy at $t = 0$, for the same collision as described in Fig. 2.1. The brief acceleration phase the spheres go through immediately after $t = 0$ can be seen to have a negligible effect on the kinetic energy in this particular case. During the loading phase, the growth of the contact area results in energy being added to the system, and the surface energy grows increasingly negative. Energy is steadily dissipated in the bulk and at the crack tip. As the motion is reversed, the elastic energy starts to decrease while the surface energy grows, as new surface is being created. At the end of the collision, 37% and 19% of the initial kinetic energy has been dissipated at the crack tip and in de bulk of the material respectively, indicating that the adhesion hysteresis has a large influence on the energy balance in the system. Furthermore, the collision is clearly asymmetric, as the rebounding phase, which starts after U_K reaches zero, is significantly longer than the loading phase. Figure 2.10 shows the various energies for the sticking collision of Fig. 2.4. Most of the initial kinetic

energy and the released surface energy are dissipated (mainly at the crack tip), while a fraction remains stored in elastic energy.

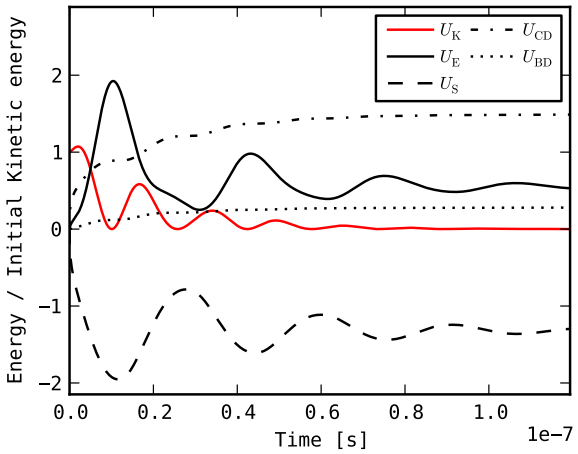

Figure 2.10: Evolution of kinetic energy (U_K), elastic energy (U_E), surface energy (U_S), and energy dissipated at the crack (U_{CD}) and in the bulk (U_{BD}), for a 2 m s^{-1} sticking collision with the ice properties of table 2.2 and a viscous relaxation time of $T_{vis} = 10^{-11}$ s.

2.D Fits

Experiment	γ (J m^{-2})	Y (MPa)	T_{vis} (s)
Sorace et al. acrylic	$0.48^{+14.52}_{-0.43}$	> 67	$< 8 \times 10^{-8}$
Sorace et al. ceramics	$37.8^{+62.2}_{-30.8}$	> 2980	$< 5 \times 10^{-9}$
Sorace et al. steel	$5.47^{+18.53}_{-3.47}$	> 2040	$8.90^{+13.10}_{-8.80} \times 10^{-9}$
Li et al. 90 micron	$1.49^{+0.71}_{-0.59}$	> 3130	$1.12^{+0.28}_{-0.17} \times 10^{-9}$
Li et al. 55 micron	$2.74^{+0.76}_{-0.74}$	> 2670	$5.08^{+1.92}_{-1.08} \times 10^{-10}$
Kim and Dunn	$0.39^{+0.61}_{-0.19}$	> 464	$1.72^{+2.78}_{-1.62} \times 10^{-10}$
Dunn et al. aluminium	$0.97^{+0.28}_{-0.22}$	> 2490	$5.16^{+0.84}_{-0.66} \times 10^{-11}$
Dunn et al. copper	$1.34^{+0.46}_{-0.59}$	> 3050	$3.90^{+1.10}_{-0.90} \times 10^{-11}$
Dunn et al. coated steel	$2.55^{+0.95}_{-0.85}$	> 3320	$1.03^{+0.67}_{-0.53} \times 10^{-11}$
Dunn et al. steel	$2.42^{+0.98}_{-0.92}$	> 3310	$1.55^{+0.95}_{-0.85} \times 10^{-11}$
Dunn et al. tedlar	$0.21^{+0.06}_{-0.06}$	> 245	$1.70^{+0.60}_{-0.20} \times 10^{-10}$
Wall et al. tedlar	$0.16^{+0.04}_{-0.04}$	> 90	$8.85^{+5.15}_{-2.85} \times 10^{-11}$
Wall et al. mica	$0.13^{+0.02}_{-0.02}$	192^{+28}_{-12}	$9.79^{+1.21}_{-1.79} \times 10^{-11}$
Wall et al. silicon	$0.17^{+0.05}_{-0.03}$	153^{+22}_{-23}	$5.97^{+2.03}_{-2.47} \times 10^{-11}$
Wall et al. molubdenum	$0.15^{+0.07}_{-0.05}$	> 120	$5.74^{+3.26}_{-3.74} \times 10^{-11}$
Dahneke PVT	$0.11^{+0.12}_{-0.10}$	> 280	$3.07^{+1.93}_{-1.77} \times 10^{-12}$
Dahneke PSL	$0.11^{+0.03}_{-0.02}$	> 271	$2.14^{+1.11}_{-0.64} \times 10^{-12}$

Table 2.3: Fit parameters obtained in Sect. 2.4. The experiments are ordered from largest (top) to smallest reduced radius.

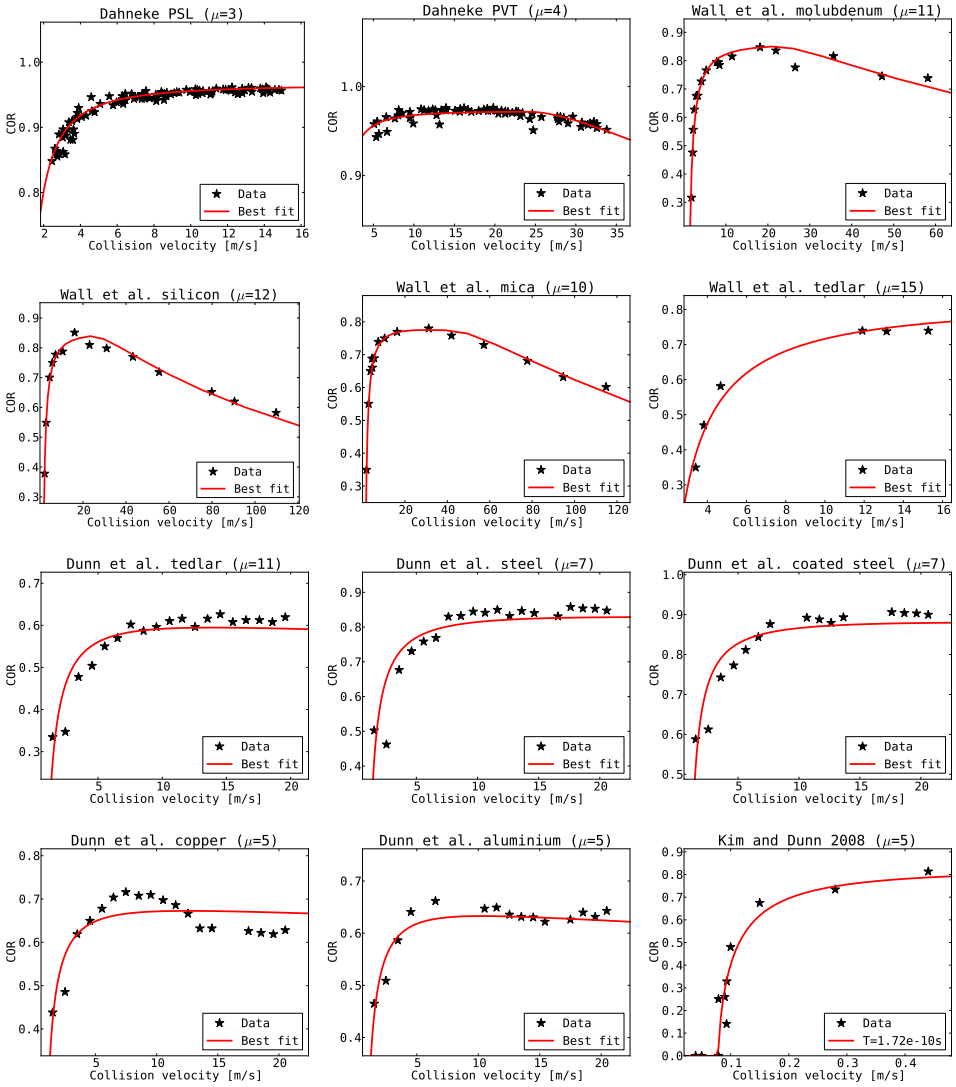

Figure 2.11: Best fitting models for the complete set of experiments. Note that the scale on the vertical axis varies. The value of the Tabor parameter μ (Sect. 2.5) is shown above each plot.

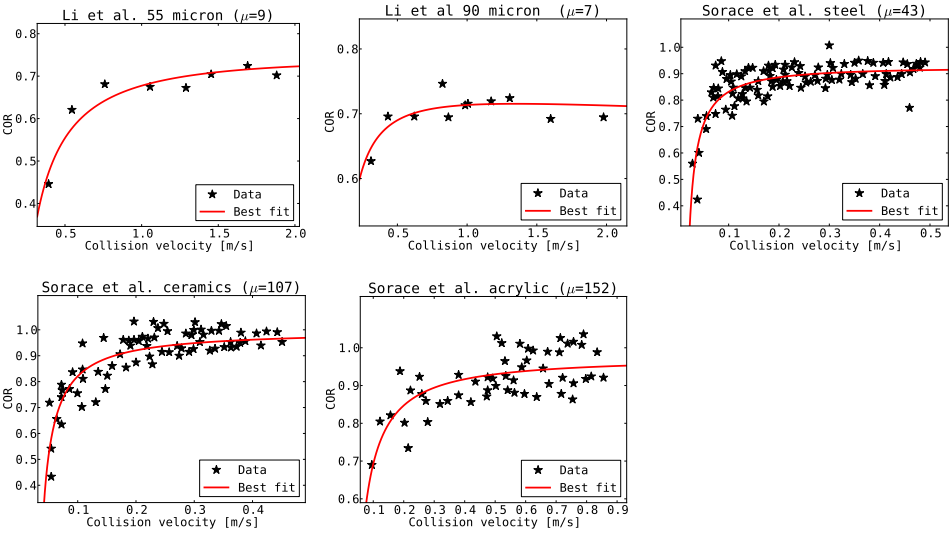

Figure 2.11: (continued) Best fitting models for the complete set of experiments. Note that the scale on the vertical axis varies. The value of the Tabor parameter μ (Sect. 2.5) is shown above each plot.

3

Rolling friction of adhesive microspheres

S. Krijt, C. Dominik, and A. G. G. M. Tielens
Journal of Physics D: Applied Physics, Volume 47, Issue 17 (2014)

Abstract

The rolling friction of adhesive microspheres is an important quantity as it determines the strength and stability of larger aggregates. Current models predict rolling forces that are 1 to 2 orders of magnitude smaller than observed experimentally. Starting from the well-known Johnson-Kendall-Roberts (JKR) contact description, we derive an analytical theory for the rolling friction based on the concept of adhesion hysteresis, e.g., a difference in apparent surface energies for opening/closing cracks. We show how adhesion hysteresis causes the pressure distribution within the contact to become asymmetrical, leading to an opposing torque. Analytical expressions are derived relating the size of the hysteresis, the rolling torque, and the rolling displacement, ξ. We confirm the existence of a critical rolling displacement for the onset of rolling, the size of which is set by the amount of adhesion hysteresis and the size of the contact area. We demonstrate how the developed theory is able to explain the large rolling forces and particle-size dependence observed experimentally. Good agreement with experimental results is achieved for adhesion hysteresis values of $(\Delta\gamma/\gamma) \simeq 3$ for polystyrene, and $(\Delta\gamma/\gamma) \simeq 0.5$ for silicates, at crack propagation rates of $0.1\,\mu\mathrm{m\,s^{-1}}$ and $1-10\,\mu\mathrm{m\,s^{-1}}$ respectively.

3.1 Introduction

The forces between contacting micrometer-sized particles are an important ingredient in scientific studies in many different fields. Some applications include industrial issues as the transportation of powders and sands, the coagulation of aerosols in the Earth's atmosphere, and the initial steps of planet formation in proto-planetary disks around newly-born stars.

As a result of the small surface-to-mass ratio of micrometer-sized bodies, attractive Van der Waals forces have an important effect on the inter particle forces (Johnson et al. 1971; Derjaguin et al. 1975). For the normal (i.e., radial) motion, the surface forces can cause the particles to adhere together and coagulate, the details of which have been studied extensively both theoretically (Dominik & Tielens 1997; Kempf et al. 1999) and experimentally (Blum & Wurm 2000). Lateral forces experienced during rolling or sliding have received somewhat less attention, but are equally crucial when studying the structure and strength of larger aggregates (Dominik & Tielens 1997). Except for very compact aggregates, the restructuring of aggregates will occur by bending arms or chains of microspheres, and individual sphere-sphere contacts act as hinge points. If little friction is associated with the rolling or sliding motion, aggregates will be weak against restructuring. More specifically, Kataoka et al. (2013b) have shown the compressive strength of a porous macroscopic aggregate depends directly on the rolling friction between its constituent particles.

Experimentally measuring the torque between adhesive micro particles is challenging. Still, numerous authors have succeeded using very different techniques, including manipulating single (Ding et al. 2007; Sümer & Sitti 2008) or chains of microspheres (Heim et al. 1999) with an atomic force microscope (AFM), resolving restructuring events in time (Blum & Wurm 2000; Gundlach et al. 2011), and non-contact techniques (Peri & Cetinkaya 2005; Peri & Cetinkaya 2005a,b).

From the theoretical side, the rolling force between adhesive microspheres has been studied by Dominik & Tielens (1995), who showed an asymmetry in the mutual contact area will give rise to an opposing torque. The size of this asymmetry was assumed to equal the interatomic distance. The theory is still widely used in N-body simulations studying the behaviour of large ensembles of micrometer-sized particles (Okuzumi et al. 2012; Kataoka et al. 2013b; Seizinger et al. 2013), despite the fact that the parameter governing the asymmetry has to be increased by one to two orders of magnitude to match the experimental results.

In this work we set out to expand the model of Dominik & Tielens (1995) to allow for adhesion hysteresis and viscoelastic losses in the contact area, in an attempt to explain the large rolling forces observed experimentally. In Sect. 3.2, we investigate how viscoelasticity affects the contact region, and we derive analytical expressions relating the rolling torque, the level of asymmetry of the contact, and relevant material properties. The developed theory is compared to experimental results on rolling spheres in Sect. 3.3. Results are discussed in Sect. 3.4 before the main conclusions are summarized in Sect. 3.5.

3.2 Theory of rolling friction

3.2.1 Equilibrium adhesive contact

To determine the rolling friction of an adhesive microsphere, a detailed knowledge is required of the contact area, and how it changes in time. Here, we briefly revisit elastic contact theory in the absence of external torques. When discussing normal forces between spheres of radii R_1 and R_2, two parameters suffice to describe the mutual contact. These are the contact radius a and the distance of mutual approach δ. Combining equations 5 and 11 of Muller et al. (1980), the pressure distribution within the contact area is given as a function of $0 \leq r \leq a$

$$p(r) = \frac{E^*}{\pi R} \frac{a^2 - 2r^2 + R\delta}{\sqrt{a^2 - r^2}}, \tag{3.1}$$

where $R^{-1} \equiv R_1^{-1} + R_2^{-1}$ equals the effective radius, and $E^{*-1} \equiv (1-\nu_1^2)/E_1 + (1-\nu_2^2)/E_2$ is the combined elastic modulus, with E_i the Young's Moduli and ν_i the Poisson Ratios of the spheres – see also Johnson (1987). We deliberately write the pressure distribution in terms of both a and δ, because the presence of adhesion hysteresis will lead to non-equilibrium configurations (Krijt et al. 2013). The elastic normal force between the spheres is found by integrating the pressure distribution

$$F_{\mathrm{E}} = \int_0^a 2\pi r p(r)\,\mathrm{d}r = \frac{2E^*}{3R}\left(3a\delta R - a^3\right), \tag{3.2}$$

To describe the contact between a sphere and a flat surface, $R_2 \to \infty$ and $R = R_1$ equals the sphere radius.

In the non-adhesive and perfectly elastic case, a unique relation between these two parameters exist, as described by Hertz (1882). In this limit, the elastic force is always repulsive. Almost a century later, Johnson et al. (1971) expanded the work of Hertz to include adhesion. Their theory (hereafter JKR theory) shows that when the material's surface energy is taken into account, the contact area is enlarged compared to the Hertzian case, and contact can be maintained for negative values of δ by the formation of an adhesive neck. In addition, a stable point exists where particles stay in contact when no external force is present. At this equilibrium point, $F_{\mathrm{E}} = 0$ and the contact radius is given by

$$a_{\mathrm{eq}} = \left(\frac{9\pi\gamma R^2}{2E^*}\right)^{1/3}, \tag{3.3}$$

with γ the combined surface energy. In JKR theory, a unique relation between a and δ exists,

$$\delta = \frac{a^2}{R} - \sqrt{2\pi\gamma a/E^*}, \tag{3.4}$$

and in principle a single parameter suffices to describe the contact region and the inter particle force.

It should be noted that JKR theory is valid only for large values of the Tabor parameter (Tabor 1977):

$$\mu \equiv \left(\frac{R\gamma^2}{E^{*2} z_0^3} \right)^{1/3}, \tag{3.5}$$

with $z_0 \sim 0.2 - 0.4\,\mathrm{nm}$ the spacing between atoms. For $\mu > 5$, JKR theory can be used, while for $\mu < 0.1$ Derjaguin-Muller-Toporov theory is accurate (Derjaguin et al. 1975).

In the JKR contact description, the stresses at the contact's periphery are singular. Treating the contact edge as a circular Mode I crack of length $2\pi a$, we can define a stress intensity factor as

$$N = \lim_{r \to a} p(r) \sqrt{a - r}. \tag{3.6}$$

The energy release associated with the creation of new surface, the 'strain energy release rate', then equals

$$G = \pi \frac{N^2}{E^*} = \frac{E^*}{2\pi} \frac{\left(a^2 - R\delta\right)^2}{aR^2}, \tag{3.7}$$

similar to the case of rolling cylinders (Greenwood et al. 2009). In the perfectly elastic case, we may identify this as the surface energy, and set $G \equiv \gamma$. When adhesion hysteresis is present however, the value of G needed for crack propagation depends on whether the crack is opening ($G_{\mathrm{op}} > \gamma$) or closing ($G_{\mathrm{cl}} < \gamma$), and is often written as a function of opening/closing rate, i.e., the crack velocity (Maugis & Barquins 1978; Greenwood 2004; Greenwood & Johnson 2006; Barthel & Frétigny 2009). The difference between the opening/closing effective surface energies $\Delta\gamma \equiv (G_{\mathrm{op}} - G_{\mathrm{cl}})$, is called adhesion hysteresis, and can be caused in a number of ways. For viscoelastic materials, the high strain rates close to the crack tip give rise to viscoelastic hysteresis, where $(\Delta\gamma/\gamma)$ can vary between effectively zero to several orders of magnitude, depending on the rate with which the surfaces are brought together or separated (Schapery 1975a,b; Maugis & Barquins 1978; Greenwood & Johnson 1981; Schapery 1989; Hui et al. 1998; Baney & Hui 1999). Alternatively, so-called interdigitation[1] of molecular groups across the interface can give rise to substantial adhesion hysteresis, $(\Delta\gamma/\gamma)$ up to about unity, depending on the dynamics of the surface molecules involved (Chen et al. 1991; Chaudhury & Whitesides 1991; Yoshizawa et al. 1993; Chaudhury & Owen 1993). For silicates, Vigil et al. (1994) have shown adhesion hysteresis can occur as a result of slow structural and chemical changes at the surface. Depending on the amount of water in the gas surrounding the silicates, the hysteresis varied significantly from 0 to $10\,\mathrm{mJ\,m^{-2}}$ (see Fig. 12 of Vigil et al. 1994).

3.2.2 Asymmetric contact description

When the sphere is subjected to an external torque, the sphere's centre of mass will move, and this will have an effect on the contact area itself. In the perfectly elastic case, the applied torque will cause the sphere to roll virtually without any resistance. In reality,

[1] Following Yoshizawa et al. (1993), the term interdigitation is used to describe any thermally activated processes involving molecular reorientation across an interface, including interdiffusion, interpenetration, entanglement, and any other molecular reorientation process occurring across an interface.

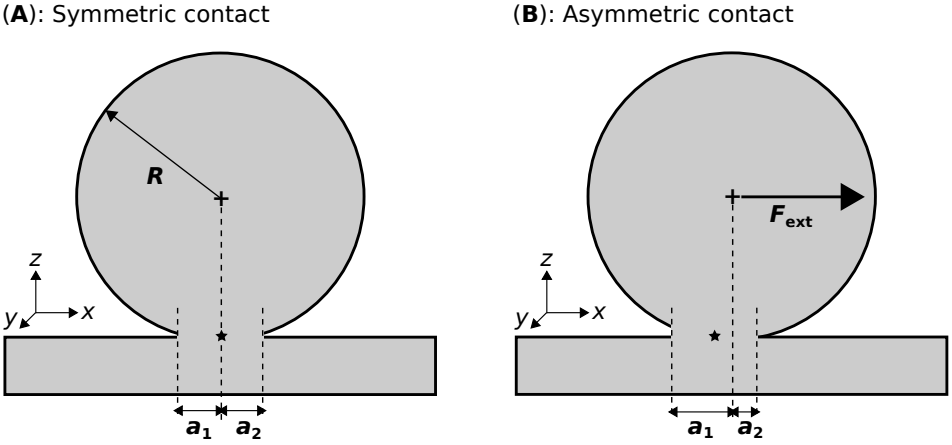

Figure 3.1: Side view of an adhesive sphere on a flat substrate. (A) shows the symmetric case, when there are no torques acting and $a_1 = a_2 = a_{eq}$. (B) Asymmetric situation during rolling under the influence of an external force in the x-direction. Here, $a_1 > a_{eq} > a_2$. The centre of mass of the sphere (+), and the centre of the contact (★) are also shown.

materials are not perfectly elastic, and energy will be dissipated in the bulk of the material, and at the edges of the adhesive contact; in the remainder of the text these regions are referred to as the 'bulk' and 'crack' regions. The dissipation in both of these regions will give rise to torques opposing the rolling motion. In the remainder of this section, we focus on the torque arising from the crack region, and develop a more detailed theory of what happens to the contact during rolling. In Sect. 3.4, we give estimates for the bulk dissipation.

In rolling, the contact is asymmetric, where one side is an opening crack and the other a closing crack. Hence, it follows from Eq. 3.7 that the contact radius will vary for different parts of the contact region, causing it to no longer be spherical. For the contact between a cylinder and a flat, the contact region is rectangular and an analytical solution is possible (Greenwood et al. 2009). In the case of a sphere, we expect G to vary continuously along the periphery of the contact, as the angle between the opening/closing crack and the direction of motion changes. However, in the interest of obtaining an analytical solution, we follow Dominik & Tielens (1995) in approximating the contact as being comprised of two semi-circles with radii a_1 and a_2. The pressure distribution then becomes

$$p(r,\phi) = \begin{cases} p(r)_{a=a_1} & \text{for } r\cos\phi > 0, \\ \\ p(r)_{a=a_2} & \text{for } r\cos\phi < 0, \end{cases} \tag{3.8}$$

where δ is the same for both halves, and the pressure in each half is given by Eq. 3.1. Note that while both halves share the same δ, the radii of the two semi-circles differ, as a result of the different values of G at the leading and trailing edges. It is for this reason

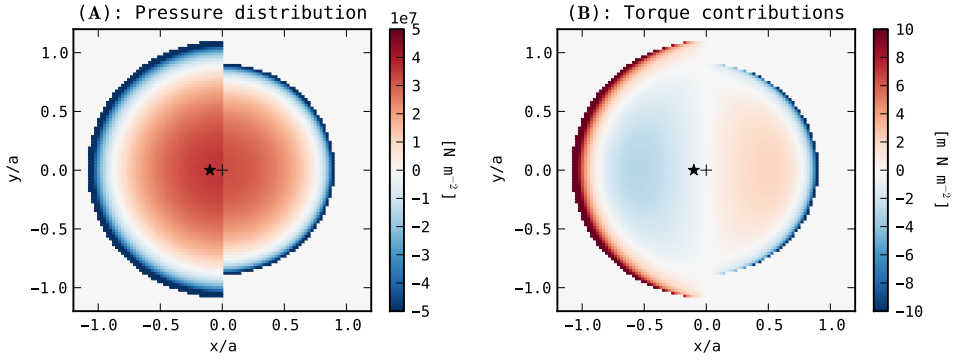

Figure 3.2: (A) The asymmetric pressure distribution for $\xi/a = 0.1$ viewed from the top, for a sphere rolling in the x-direction. (B) shows the torque contributions for the same contact. The centre of mass of the sphere (+), and the centre of the contact (★) are offset. These particular numbers correspond to the contact between a PSL microsphere with radius 5 μm and a PSL table.

that we avoided using an equilibrium relation between a and δ in Eq. 3.1. There is a finite displacement between the centre of mass of the sphere (projected onto the contact surface, $x = 0$) and the centre of the contact, given by

$$\xi = \frac{1}{2}(a_2 - a_1). \tag{3.9}$$

Writing $a = (a_1 + a_2)/2$, the contact can now be fully described by the three parameters ξ, a and δ. Figure 3.2A shows the pressure distribution of Eq. 3.8 for $\xi/a = 0.1$, while a and δ correspond to JKR equilibrium.

The contributions to the torque about the y-axis have been plotted in Fig. 3.2B. From the figure it is clear that the largest torques originate close to the crack at locations furthest from the y-axis. The region close to $x = 0$, where the assumption that the cracks are in Mode I is expected to loose accuracy, has a negligible contribution. To find the (total) opposing torque that results from such a pressure distribution we have to integrate over all torque contributions in the contact area

$$\begin{aligned} M &= \int\int_{\text{contact}} x p(x,y)\,\mathrm{d}x\,\mathrm{d}y \\ &= \frac{E^*}{4R}\left[(a_1^2 - \delta R)^2 - (a_2^2 - \delta R)^2\right]. \end{aligned} \tag{3.10}$$

With the aid of Eq. 3.7, the torque can be written as

$$M = \frac{R}{2}\left(\pi a_1 G_1 - \pi a_2 G_2\right). \tag{3.11}$$

where G_1 and G_2 are the strain energy release rates at the trailing and leading edges of the contact. From conservation of energy, one might expect to find $M = 2R(a_1 G_1 - a_2 G_2)$,

slightly different from Eq. 3.11. We attribute the different prefactor to the geometry of the contact area, and the fact that different parts of the crack region contribute to the torque with different lever arms (see Fig. 3.2B).

Realizing that, in the asymmetric case, the total elastic force equals

$$F_{\mathrm{E}} = \frac{2E^*a}{3R}\left(3\delta R - a^2 - 3\xi^2\right), \tag{3.12}$$

the torque of Eq. 3.10 can be rewritten as

$$\begin{aligned} M &= (a_1 + a_2)(a_1 - a_2)\frac{E^*(a_1^2 + a_2^2 - 2\delta R)}{4R} \\ &= \xi\left[-F_{\mathrm{E}} + \frac{4E^*a^3}{3R}\right]. \end{aligned} \tag{3.13}$$

In the case of zero load ($F_{\mathrm{E}} = 0$) and small asymmetry, the contact size is approximately given by the Eq. 3.3, and we obtain

$$M = 6\pi\gamma R\xi, \tag{3.14}$$

in agreement with Dominik & Tielens (1995). Lastly, it is useful to obtain a relation between the rolling displacement and the strain energy release rates. For small asymmetries, $a_1 \simeq a_2 \simeq a_{\mathrm{eq}}$ and we can compare Eqs. 3.11 and 3.14 to find

$$\xi = \frac{a_{\mathrm{eq}}}{12}\frac{(G_1 - G_2)}{\gamma}. \tag{3.15}$$

With this mathematical framework in place, we can now discuss what happens when an external torque is exerted on a stationary sphere.

3.2.3 The onset of rolling

The general picture is then the following. Imagine, as in Fig. 3.1A, a sphere on a substrate in JKR equilibrium, so that $a_1 = a_2 = a_{\mathrm{eq}}$ and $G_1 = G_2 = \gamma$. When the sphere is subjected to an external torque, the displacement between the centre of mass and the centre of the contact will grow, as illustrated in Fig. 3.1B. As a direct consequence, a_1 and a_2 will change (we will take subscript 1 to refer to the trailing half, in accordance with Fig. 3.1B). As a result of a_1 and a_2 changing, the strain energy release rates will start to differ from γ as dictated by Eq. 3.7. Initially however, $\gamma < G_1 < G_{\mathrm{op}}$, and the crack is unable to open at the trailing edge, effectively pinning the contact. Only when G_1 reaches G_{op}, crack propagation will start at the trailing edge. Setting $(G_1 - G_2) = (G_{\mathrm{op}} - G_{\mathrm{cl}}) \equiv \Delta\gamma$, we can identify a critical displacement for the onset of true rolling motion

$$\xi_{\mathrm{crit}} = \frac{a_{\mathrm{eq}}}{12}\frac{\Delta\gamma}{\gamma}. \tag{3.16}$$

This relation is an important result. It reveals that the critical rolling displacement ξ_{crit} is set by the size of the contact radius and the difference between the opening and closing apparent surface energy[2]. This picture is different from the approach of Dominik & Tielens (1995), where the critical displacement was assumed to equal the inter-atomic distance, about 0.3 nm, independent of the particle's radius and elastic properties. If $(\Delta\gamma/\gamma)$ is constant, the critical displacement represents a fixed fraction of the contact radius, and is expected to scale with $R^{2/3}$. When $(\Delta\gamma/\gamma)$ varies, deviations from this slope are to be expected.

3.2.4 Steady-state rolling

When a sphere has started rolling, the opposing torque is given by Eq. 3.11, with the strain energy release rates now equal to G_{op} and G_{cl}. Viscoelastic materials often show G_{op} and G_{cl} to depend on the crack velocity. This behaviour slightly complicates the picture described above, and it might prove necessary to solve the evolution of the sphere and the cracks in time. This method has been used by Greenwood et al. (2009) for the adhesive contact of a rolling cylinder. However, in the case of a constant externally-applied torque, a steady state will be realised where the contact shape is preserved and $\dot{a}_1 = \dot{a}_2 = 0$. The external torque is then balanced by the opposing torque arising from the contact area, and the crack opening/closing velocity is equal to the velocity of the sphere's centre of mass. In this case, we can still make use of Eq. 3.11 developed here, realizing $\Delta\gamma$ corresponds to the adhesion hysteresis at that particular crack velocity.

It should be noted that most viscoelastic theories predict adhesion hysteresis to disappear as the crack opening or closing rate approaches zero (Greenwood 2004; Barthel & Frétigny 2009). In the absence of other sources of hysteresis, this assumption leads to frictionless rolling at infinitely low rolling velocities, and would imply structures built from adhesive spheres are unstable under external forces (e.g., gravity) on very long timescales. We are not aware of such behaviour having been observed experimentally.

3.2.5 Rocking motion

Interesting behaviour is observed when the external force is removed before ξ_{crit} is reached. Suppose a sphere in equilibrium receives a velocity kick in the horizontal direction at a time $t = 0$. Provided the angle over which the sphere rocks is small, it can be written as $\theta = \xi/R$. The evolution of ξ in time is then given by

$$I\ddot{\xi}(t) = RM \tag{3.17}$$

with M the torque arising from the contact area, and $I = (2/5)mR^2$ the moment of inertia of the sphere. Of course, the size of the torque depends on the asymmetry of the contact.

[2]This approach was originally proposed by professor K. L. Johnson in a private letter to the authors of Dominik & Tielens (1995) in 2005.

Quantity	Silicate	PSL
E (GPa)	54	3.4
ν (-)	0.17	0.33
ρ (g cm^{-3})	2.6	1.026
γ (J m^{-2})	0.025	0.025

Table 3.1: Material properties for silicate and polystyrene (PSL) as used in this work. Note that for like materials, the total surface energy is twice the value listed here, which corresponds to an individual surface.

For $\xi < \xi_{\text{crit}}$, the contact is pinned and we can write

$$\begin{aligned} a_1(t) &= a_{\text{eq}} - \xi(t) \\ a_2(t) &= a_{\text{eq}} + \xi(t). \end{aligned} \tag{3.18}$$

Making use of Eq. 3.14, the equation of motion becomes

$$\ddot{\xi}(t) = \frac{6\pi\gamma R^2}{I}\xi(t), \tag{3.19}$$

which is readily identified as a harmonic oscillator with frequency

$$f_0 = \frac{1}{2\pi}\left(\frac{6\pi\gamma R^2}{I}\right)^{1/2} = \frac{3}{4\pi}\left(\frac{5\gamma}{\rho R^3}\right)^{1/2}. \tag{3.20}$$

For microspheres, this frequency is typically of the order of 100 kHz, and has been observed experimentally (Peri & Cetinkaya 2005; Peri & Cetinkaya 2005a,b). We will discuss these experiments in Sect. 3.3.1.

3.3 Comparison to experiments

Now that we have a theory of rolling friction, we can compare the predictions to a number of published experiments measuring either the rolling torque or the rolling displacement. For this purpose, we will focus on two materials: polystyrene (PSL) and silicates (SiO_2), see table 3.1. In this section, we will discuss various experimental results within the framework of the theory developed in Sect. 3.2.

3.3.1 Polystyrene microspheres

Constant-velocity rolling

For PSL, Sümer & Sitti (2008) have measured the rolling force using an atomic force microscope (AFM) for 5, 10, and 15 μm. The spheres were pushed over a glass substrate at a constant velocity of 0.1 μm/s. As care was taken to apply the pushing force a height

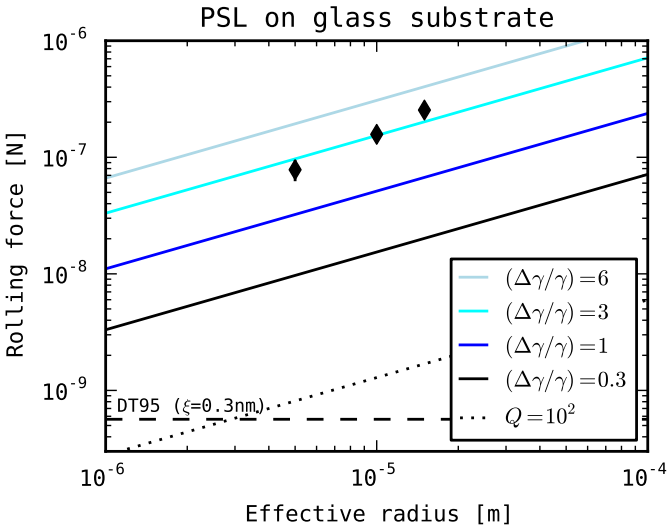

Figure 3.3: Experimental results of Sümer & Sitti (2008) (♦) for the rolling force of a PSL microspheres on a glass substrate. Solid lines correspond to Eq. 3.11 assuming different values for $(\Delta\gamma/\gamma)$ and $a_1 = a_2 = a_{\rm eq}$, in which case the rolling force scales with $R^{2/3}$. The black dashed line corresponds to Eq. 3.14, assuming $\xi = 0.3$ nm, and the dotted line shows the expected bulk torque for $Q = 10^2$ (see Sect. 3.4).

R from the substrate, we can relate this force to a rolling torque via $F_{\rm ext} = M_{\rm ext}/R$. Figure 3.3 shows the results of (Sümer & Sitti 2008) in comparison to Eq. 3.11, for various values of $(\Delta\gamma/\gamma)$. The theory of Dominik & Tielens (1995), i.e., Eq. 3.14 with $\xi = 0.3$ nm, is shown for comparison.

Figure 3.3 shows how the theory of Sect. 3.2 explains two key features of the experimental results: the rolling force is substantially larger than expected from $\xi = 0.3$ nm, and the rolling force increases with increasing radius. Indeed, a hysteresis characterized by $(\Delta\gamma/\gamma) \simeq 3$ reproduces the experimentally observed rolling force well for all three microsphere radii. For these particular particles, this corresponds to a rolling displacement of several tens of nanometers, approximately two orders of magnitude larger than z_0.

Critical displacement

In a somewhat similar study, Ding et al. (2007) moved PSL microspheres across a flat silicon substrate, by pushing the spheres with an AFM cantilever. The diameters of the spheres used varied between 22.5 and 26.8 μm. After each push, a scanning electron microscope (SEM) image was obtained to find the new position of the microsphere, while the pushing force could be calculated from the cantilever's deflection. As a result of this experimental setup, the motion of the spheres is discontinues, and difficult to simulate in detail. An interesting result of Ding et al. (2007) however is that a change in rolling

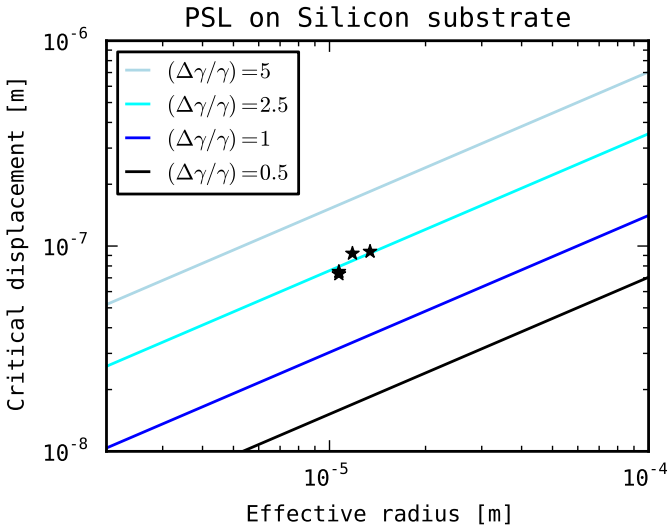

Figure 3.4: Experimental results of Ding et al. (2007) (★) for the critical rolling displacement of a PSL microspheres on a silicon substrate. Solid lines refer to Eq. 3.15, for different values of $(\Delta\gamma/\gamma)$.

stiffness was observed for most particles, after a total displacement between 73 and 94 nm. Ding et al. attributed this change in rolling stiffness to the transition from pre-rolling (no contact readjustment) to true rolling motion.

Figure 3.4 shows the observed critical rolling displacements, and compares them to predictions of Eq. 3.16. While the rolling displacements are orders of magnitudes larger than the atomic spacing, the results can be understood in terms of adhesion hysteresis. The inferred value of $(\Delta\gamma/\gamma) \simeq 2.5$. Unfortunately, the variation in particle radius[3] is too small to test the correlation between ξ_{crit} and R predicted by Eq. 3.16.

Rocking microsphere

Another interesting opportunity to study the critical displacement comes in the form of the experiments conducted by Peri & Cetinkaya (2005); Peri & Cetinkaya (2005a,b), where rocking motions are excited in the adhesive contact of a PSL microsphere (21.4 μm in diameter) on various substrates. From the fact the microsphere oscillates in the lateral direction, it was inferred that the contact edges are effectively pinned (see Sect. 3.2.5). Moreover, the motion is damped within a dozen oscillations, something that might well be explained by the bulk dissipative torque. The experimental results can be understood within the framework of the theory of Sect. 3.2.5.

We choose to focus on the aluminium substrate, as the experimental results appear to be the cleanest (see Figs. 10 and 14 of Peri & Cetinkaya 2005), and use the elastic

[3] In fact, the size of the particle corresponding to the left-most point in Fig. 3.4 was not determined individually, and assumed equal to the nominal sphere diameter of 21.4 μm (see table 1 of Ding et al. 2007)

properties of table 1 of Peri & Cetinkaya (2005) and a surface energy of 0.1 J m^{-2}. For this particular setup, $a_{eq} \simeq 380$ nm. When the sphere is excited and the contact pinned, the centre of mass will oscillate with frequency f_0 set by Eq. 3.20. This frequency, 150 kHz for this particular PSL-aluminium system, was found by Peri & Cetinkaya (2005); Peri & Cetinkaya (2005a,b) to compare very well with the experimental observations.

The maximum observed rocking angle in the experiments[4] was 0.16°, corresponding to $\xi = 30$ nm (two orders of magnitude larger than z_0), and a maximum torque of roughly $M = 6 \times 10^{-13}$ Nm. Comparing this offset to the contact radius we find $\xi = 0.08 a_{eq}$. Since this maximum $\xi < \xi_{crit}$, we can use Eq. 3.16 to find a lower limit of $(\Delta\gamma/\gamma) > 0.95$.

3.3.2 Silicate microspheres

Silicates (SiO_2) are thought to play an important role in the formation of Earth-like planets, and because of this many experiments involving silicates have been performed over the last decade or two (see Blum & Wurm 2008; Güttler et al. 2010 for excellent reviews). Heim et al. (1999) measured a rolling force of $(8.5 \pm 0.3 \pm 1.3) \times 10^{-10}$ N for 1.9 μm-diameter silicate particles, by taking a chain of microspheres and bending it in a periodic manner. The frequency of the bending motion varied between 0.1 and 1 Hz. Blum & Wurm (2000) examined several restructuring events in microsphere structures and obtained a rolling force of $(5.0 \pm 2.5) \times 10^{10}$ N, for coated SiO_2 particles of 1.9 μm in diameter. Lastly, using a similar approach Gundlach et al. (2011) measured a rolling force of $(12.1 \pm 3.6) \times 10^{-10}$ N for 1.5 μm-diameter SiO_2.

The experimental results are compared to the adhesion hysteresis model in Fig. 3.5. At first sight, it appears the rolling force drops with particle radius. However, we attribute the scatter in rolling force values to differences in experimental procedures, and believe that the current data with its uncertainties is not enough to test the radius-dependence of the rolling force. Nonetheless, the results can be understood in terms of $(\Delta\gamma/\gamma) \sim 0.5$. This suggests the size of the adhesion hysteresis is smaller than for the polystyrene of Figs. 3.3 and 3.4. The absolute size of the rolling displacement is significantly smaller than the one found for PSL particles in the previous section. The reason is twofold. For one, the smaller value of $(\Delta\gamma/\gamma)$ causes ξ to be a smaller fraction of the contact radius. Second, the contact radius itself is much smaller for the silicate particles considered here, as they are smaller and harder.

We must address that the contact model presented here is a continuum one, and is expected to break down when the sizes of individual atoms start to play a role. In Fig. 3.5 for example, we see that for some radii, the predicted torque lies below the curve corresponding to Dominik & Tielens (1995). When that occurs, the rolling displacement ξ is smaller than the size of an atom, and one might question whether it is physically meaningful to have a difference between a_1 and a_2 that is arbitrarily small. The question whether continuum descriptions can still be used in this regime is beyond the scope of this

[4]This maximum angle was quoted for the PSL-silicon combinations, but as the values of the vertical displacement is very similar for the PSL-aluminum system (compare Figs. 8 and 10 Peri & Cetinkaya 2005) we expect it applies here as well.

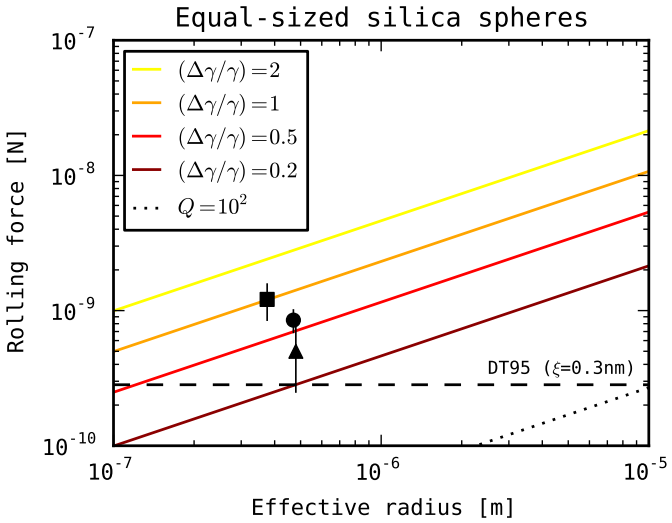

Figure 3.5: Rolling force versus effective radius for equal-sized silica microspheres. Symbols refer to experimental results of Heim et al. (1999) (●), Blum & Wurm (2000) (▲), and Gundlach et al. (2011) (■). Solid lines correspond to Eq. 3.11 assuming $a_1 = a_2 = a_{\rm eq}$ and different values for $(\Delta\gamma/\gamma)$. The black dashed line corresponds to Eq. 3.14, assuming $\xi = 0.3\,$nm, and the dotted line corresponds to the bulk rolling force for $Q = 10^2$ (see Sect. 3.4).

work, and has to be addressed with the use of molecular dynamics simulations (Tanaka et al. 2012).

3.4 Discussion

In this work we propose a model for the rolling friction of microspheres based on the concept of adhesion hysteresis. In the case of rolling of a spherical contact area, the geometry does not allow for an analytical solution. However, by assuming that the contact consists of two semi-circles with different radii, an approximate analytical solution can be achieved. When the contact is close to JKR equilibrium, and the asymmetry is small compared to the contact radius itself, simple expressions relating the torque, contact asymmetry, and adhesion hysteresis exist, and are given by Eqs. 3.14 and 3.15. In the presence of external loads, the more general result Eq. 3.13 can be used, while the effect of the external load on the size of the contact radius and the approach should be taken into account.

Comparison of the theory to experiments of rolling microspheres reveals that the new model is capable of explaining two key results; the variation of the rolling force with particle radius, and the observation that the rolling displacement can be much larger than the inter-atomic distance. Good agreement between theory and experiments is achieved for adhesion hysteresis values of $(\Delta\gamma/\gamma) \simeq 3$ for PSL, and $(\Delta\gamma/\gamma) \simeq 0.5$ for silicates.

When the asymmetry in the contact is small, the strain energy release rate at the contact edge is not large enough to cause the crack to move, effectively pinning the contact area. If no external forces are acting, this will cause the sphere to oscillate back and forth. An example of such behaviour is observed in the experiments of Peri & Cetinkaya (2005). From the maximum rocking angle reached in the experiments, we infer $(\Delta\gamma/\gamma) > 0.95$.

Two main origins of adhesion hysteresis are mechanical, i.e., arising from viscoelastic losses near the crack tip, or chemical hysteresis, connected to the state and dynamics of surface groups and molecule chains (see Sect. 3.2.1). The latter can give rise to $(\Delta\gamma/\gamma) \sim 1$, similar to the values observed in Sect. 3.3. However, further comparison would require a detailed knowledge of the molecular dynamics at the surfaces involved, and is beyond the scope of this work. For viscoelastic materials, a theoretical prediction for the apparent surface energy has been obtained by Greenwood (2004); Greenwood & Johnson (2006). For a three-element solid, characterized by a single viscoelastic relaxation time, T, they show that the departure of G from γ is set by the non-dimensional crack velocity $v^* \equiv \dot{a}\gamma T/(z_0^2 E^*)$, with $\dot{a}$ the crack opening/closing velocity. A difference in apparent surface energy of 3 and 0.5 then corresponds to a v^* of 2 and 0.1 respectively (through Fig. 6 of Greenwood 2004). For the experiments of Sümer & Sitti (2008), the crack velocity equals the rolling velocity of 10^{-7} m s^{-1}. For the experiments plotted in Fig. 3.5, the rolling velocities are estimated[5] to lie between $10^{-6} - 10^{-5}$ m s^{-1}. Plugging in the material properties and correct $\dot{a}$ returns $T = 7 \times 10^{-2}$ s for the PSL particles of Fig. 3.3, and $T = 5 \times 10^{-4}$ s for the silicates of Fig. 3.5. For polystyrene at room temperature, the obtained T^{-1} does not coincide with either α or β relaxation peaks, which occur at much lower frequencies (Fig. 8.20 of Sperling 2007), but might correspond to one of several other relaxation peaks (Yano & Wada 1971). Alternatively, much shorter relaxation timescales were obtained by Krijt et al. (2013) by fitting rebound experiments of micrometer-sized spheres, indicating that a viscoelastic model with a single characteristic relaxation time might not accurately describe the material response over a large range of strain frequencies. However, as there is virtually no variation in rolling velocity in the experiments used in Sect. 3.3, connecting the observed adhesion hysteresis to a viscous relaxation time remains speculative.

Thus, measurements of the rolling friction of adhesive spheres provide a powerful window into adhesion hysteresis of the materials involved, as the observed torque can be directly related to the difference in apparent surface energies on both sides of the contact. So-called JKR experiments (e.g., Chaudhury & Owen 1993; Lorenz et al. 2013) are also powerful, but require knowledge of the contact size throughout the loading-unloading experiment, which is challenging for the relatively small contacts between microspheres. Additional experiments, that measure the rolling force of microspheres in a controlled manner, will provide valuable insight in the behaviour at the crack tip. Specifically, experiments probing a broad range of rolling velocities will allow a more thorough comparison to viscoelastic crack theory.

So far, we have neglected the effects of bulk energy dissipation on the rolling torques.

[5]These numbers are obtained by estimating the rolling angle and timescales from Figs. 3 of Blum & Wurm (2000) and 7 of Gundlach et al. (2011).

The elastic energy stored in a spherically symmetric contact equals (Muller et al. 1980; Brilliantov et al. 2007)

$$U_{\rm E} = \frac{E^* a^3}{3R}\left[\delta\left(\frac{3\delta R}{a^2} - 1\right) - \frac{a^2}{5R}\left(\frac{5\delta R}{a^2} - 3\right)\right], \tag{3.21}$$

where again we have deliberately omitted making use of an equilibrium relation between a and δ. Assume now the sphere rolls over a distance $2a$. In that case, a surface element that passed through the contact area has undergone a complete stress cycle. Assuming the bulk dissipation is small, the total energy loss associated with the elastic strain energy can then be estimated as $U_{\rm B} \sim (\pi/Q)U_{\rm E}$, with Q the 'quality factor'[6]. The reciprocal of the quality factor is associated with the ratio of energy dissipated to the energy stored in dynamic loading, and can be viewed as a fundamental measure of mechanical dissipation (Lakes 2009). In the case of rolling friction, the reciprocal of the quality factor is identical to Tabor's hysteresis loss factor (Tabor 1955), apart from a numerical factor of order unity (Johnson 1987).Typical values for the quality factor in solids are $10 - 10^2$ for polymers, 10^3 for glass and soft metals, but may vary with frequency. As the sphere rolled over $2a$, the torque associated with this bulk energy loss can be written as[7]

$$M_{\rm B} = \frac{U_{\rm B} R}{2a} \sim \frac{\pi U_{\rm E}}{Q}\frac{R}{2a}. \tag{3.22}$$

Earlier we obtained the torque arising from the region close to the crack. Making use of Eq. 3.11 while plugging in $a_1 \sim a_2 \sim a_{\rm eq}$ and the surface energy $U_{\rm S} = -\pi a_{\rm eq}^2 \gamma$, we can compare the sizes of the two torques to find

$$\frac{M_{\rm B}}{M_{\rm C}} \sim \left(\frac{U_{\rm E}}{U_{\rm S}}\right)\left(\frac{\pi}{Q}\right)\left(\frac{\gamma}{\Delta\gamma}\right). \tag{3.23}$$

While approximate, the above expression is very instructive; and we will briefly discuss the three terms on the right-hand side of Eq. 3.23. Firstly, in a JKR equilibrium contact, the total energy is always negative, as the particles are bound. This immediately tells us the surface energy dominated the elastic energy. If external forces are present, the elastic energy can be increased significantly, potentially changing the value of $(U_{\rm E}/U_{\rm S})$. In the specific case of a sphere resting on a flat surface, the gravitational force on the sphere is such an external force. For a silicate sphere, gravity will cause significant deviation from the JKR equilibrium only for sphere radii larger than a millimeter. Alternatively, the potential presence of dust or asperities can decrease the effective contact area, and reduce the overall importance of the surface energy and adhesion (Tabor 1977). Secondly, the

[6] In treatises of viscoelastic materials, the loss tangent $\tan\delta$ is often used. To avoid confusion with the mutual approach, we will use the quality factor instead. These are related through $Q^{-1} \simeq \tan\delta$.

[7] In the Hertzian case, Eq. 3.22 is in agreement with the results of Brilliantov & Pöschel (1998, 1999), who obtained an expression for the rolling torque for non-adhesive elastic spheres by integrating small dissipative stresses in the contact area, provided their viscoelastic constant, A, is related to the quality factor through $Q \sim (2a/v_{\rm roll})/A$. This relation is expected since A has units of time, and $(2a/v_{\rm roll})$ is the typical stress timescale probed by the moving contact.

ratio (π/Q) is very small for solids. At different frequencies, different mechanisms will be responsible for demoing, and the behaviour of Q as a function of frequency will differ per material. A wide range of experimental techniques are used across the frequency spectrum to measure Q (Lakes 2009, Fig. 6.25), but typical values at Hz to kHz frequencies and at room temperatures are $10 - 10^2$ for polymers, 10^3 for glass and soft metals, and orders of magnitude larger for structural metals and quartz (Lakes 2009, p.208). In a typical crystalline solid, the quality factor is relatively constant as a function of frequency, while the Q-spectrum of a typical amorphous polymer shows more pronounced peaks, corresponding to various molecular motions (Lakes 2009, Figs. 8.1 and 8.2). Thus, we expect $(M_B/M_C) \ll 1$ for small and smooth adhesive spheres in a JKR equilibrium contact, justifying the approach of Sect. 3.2. This finding is supported by experiments on adhesive cylinders (Maugis 1985; She et al. 1998; Greenwood et al. 2009), where the observed rolling torque was attributed solely to adhesion hysteresis. Alternatively, the presence of asperities, additional external loads, very low quality factors, or negligible adhesion hysteresis, will act to increase the relative importance of the bulk dissipation.

From the damped oscillation in the experiment of Peri & Cetinkaya (see Sect. 3.3.1), we can derive an order-of-magnitude number for the quality factor. First, we modify the expression for the total elastic energy to include the contact asymmetry

$$U_E(a_1, a_2, \delta) = \frac{1}{2}\left[U_E(a_1, \delta) + U_E(a_2, \delta)\right], \tag{3.24}$$

where $U_E(a_i, \delta)$ is given by Eq. 3.21. Using this relation, we see that for an asymmetry of $\xi/a = 0.08$, the elastic energy is increased by about $\Delta U_E = 0.1 U_E$ compared to the symmetric case. During the oscillation, this energy is converted into rocking motion and vice versa, and in a single oscillation to a maximum ξ and back, a fraction π/Q of ΔU_E is dissipated. Now, we can write down a condition for the timescale on which this excess energy is dissipated, and the oscillation is stopped. It is instructive to express this timescale in a number of periods:

$$f_0 \frac{\Delta U_E}{(\mathrm{d}/\mathrm{d}t)\Delta U_E} \sim \frac{Q}{\pi}. \tag{3.25}$$

From the observation that the oscillations is damped in roughly 10 periods, we obtain $Q \sim 30$, in agreement with typical quality factors of polymeric materials at kHz frequencies (Lakes 2009), strengthening our assumption that the damping originates from energy dissipation in the bulk of the material.

3.5 Conclusions

Our main findings can be summarized as follows:

1. For microspheres in JKR equilibrium, rolling friction will be dominated by dissipation associated with the opening and closing of the cracks on both sides of the contact region (e.g., adhesion hysteresis).

2. For a fixed adhesion hysteresis ($\Delta\gamma/\gamma$), the critical rolling displacement equals a constant fraction of the contact radius, and therefore scales with $R^{2/3}$.

3. The theory is capable of reproducing a variety of experimental results, explaining in a natural way the large observed values of the rolling force and rolling displacement during pushing experiments (Figs. 3.3, 3.4 and 3.5); the rocking motion of microspheres for small rolling angles, and the observed radius-dependence of the rolling force (Fig. 3.3).

4. Applying the theory to experimental results indicates adhesion hysteresis for polystyrene roughly equals ($\Delta\gamma/\gamma$) $\simeq 3$, and ($\Delta\gamma/\gamma$) $\simeq 0.5$ for silicate particles.

Owing to their simple forms, Eqs. 3.14 and 3.15 can be directly integrated in simulations of systems of adhesive spheres, while future experiments measuring the rolling forces for different velocities and particle sizes can be used to test and discriminate between different models of adhesion hysteresis.

Acknowledgements

Dust studies at Leiden Observatory are supported through the Spinoza Premie of the Dutch science agency, NWO. The authors would like to thank professor K. L. Johnson for pointing out the relation between rolling friction and adhesion hysteresis in an adhesive contact. The authors want to thank the anonymous referees, whose comments have helped to improve the manuscript.

4

Erosion and the limits to planetesimal growth

S. Krijt, C. W. Ormel, C. Dominik, and A. G. G. M. Tielens
Astronomy & Astrophysics, Volume 574, A83 (2015)

Abstract

The coagulation of microscopic dust into planetesimals is the first step towards the formation of planets. The composition, size, and shape of the growing aggregates determine the efficiency of this early growth. In particular, it has been proposed that fluffy ice aggregates can grow very efficiently in protoplanetary disks, suffering less from the bouncing and radial drift barriers. While the collision velocity between icy aggregates of similar size is thought to stay below the fragmentation threshold, they may nonetheless lose mass from collisions with much smaller projectiles. As a result, erosive collisions have the potential to terminate the growth of pre-planetesimal bodies. We investigate the effect of these erosive collisions on the ability of porous ice aggregates to cross the radial drift barrier. We develop a Monte Carlo code that calculates the evolution of the masses and porosities of growing aggregates, while resolving the entire mass distribution at all times. The aggregate's porosity is treated independently of its mass, and is determined by collisional compaction, gas compaction, and eventually self-gravity compaction. We include erosive collisions and study the effect of the erosion threshold velocity on aggregate growth. For erosion threshold velocities of 20 – 40 m s^{-1}, high-velocity collisions with small projectiles prevent the largest aggregates from growing when they start to drift. In these cases, our local simulations result in a steady-state distribution, with most of the dust mass in particles with Stokes numbers close to unity. Only for the highest erosion threshold considered (60 m s^{-1}) do porous aggregates manage to cross the radial drift barrier in the inner 10 AU of MMSN-like disks. Erosive collisions are more effective in limiting the growth than

fragmentary collisions between similar-size particles. Conceivably, erosion limits the growth before the radial drift barrier, although the robustness of this statement depends on uncertain material properties of icy aggregates. If erosion inhibits planetesimal formation through direct sticking, the sea of $\sim 10^9$ g, highly porous particles appears suitable for triggering streaming instability.

4.1 Introduction

Despite the apparent ease with which nature is forming planets, current models of planet and even planetesimal formation have problems growing large bodies within the typical gas disk lifetime of $\sim 10^6$ years (Haisch et al. 2001). The process of planetesimal formation is a complex one, with many different processes acting on a variety of lengths and timescales (see Testi et al. 2014 and Johansen et al. 2014 for recent reviews).

The first step towards planetesimal formation is the coagulation of small dust aggregates that stick together through surface forces. As aggregates collide and stick to form larger aggregates, these aggregates have to overcome several hurdles on their way to becoming planetesimals. One important obstacle faced by a growing dust aggregate is the radial drift barrier (Whipple 1972; Weidenschilling 1977a). When aggregates grow to a certain size (about a meter at 1 AU and a millimeter at 100 AU, assuming compact particles) they will decouple from the pressure-supported gas disk, and start to lose angular momentum to the gas around them. As a result, said particles will drift inward.

Even before radial drift becomes problematic, the coagulation of aggregates can be frustrated by catastrophic fragmentation or bouncing (Blum & Wurm 2008; Güttler et al. 2010; Zsom et al. 2010), which prevents colliding aggregates from gaining mass. These problems are alleviated somewhat by including velocity distributions between pairs of particles (Windmark et al. 2012b; Garaud et al. 2013) in combination with mass transfer in high-velocity collisions (Wurm et al. 2005; Kothe et al. 2010), though these solutions require the presence of relatively compact targets.

Recently, it has been proposed that icy aggregates, if they can manage to stay very porous, suffer less from these barriers, and might be able to form planetesimals locally and on relatively short timescales (Okuzumi et al. 2012; Kataoka et al. 2013a). Very porous, or fluffy, aggregates are less likely to bounce (Wada et al. 2011; Seizinger & Kley 2013), and icy particles have much higher fragmentation threshold velocities than refractory ones (Dominik & Tielens 1997; Wada et al. 2013), but perhaps most surprising was the finding that porous aggregates can outgrow the radial drift barrier, by growing very rapidly as a result of their enhanced collisional cross section (Okuzumi et al. 2012). However, Okuzumi et al. (2012) assumed perfect sticking between colliding aggregates, neglecting possible mass-loss in aggregate-aggregate collisions.

We study the effects of the existence of an erosive regime for icy aggregates, where collisions at low mass ratios will produce erosive fragments at velocities below a critical erosion threshold velocity (Schräpler & Blum 2011; Seizinger et al. 2013; Gundlach & Blum 2015). Our goal is to quantify how erosion influences the direct formation of planetesimals through coagulation. To this end, we develop a local Monte Carlo coagulation code, capable of simulating the vertically-integrated dust population, tracing both

the evolution of the mass and the porosity of the entire mass distribution self-consistently. Sect. 4.2 describes the models we use for the protoplanetary disk and the dust aggregates. In Sect. 4.3, we present the numerical method, which is based on the work of Ormel & Spaans (2008). Then, we test our model against the results of Okuzumi et al. (2012) (Sect. 4.4.1), after which we expand the model to include compaction from gas pressure and self-gravity according to Kataoka et al. (2013a) (Sect. 4.4.1), and erosive collisions (Sect. 4.4.2). In Sect. 4.5, we compare the results to a simple semi-analytical model, and describe which processes can limit coagulation in different parts of protoplanetary disks. Discussion of the results and implications takes place in Sect. 4.6, and conclusions are presented in Sect. 4.7.

4.2 Disk and dust models

The disk model and collisional compaction prescription are based on Okuzumi et al. (2012), to which we add non-collisional compaction processes (Sect. 4.2.4) and a model for erosive collisions (Sects. 4.2.3 and 4.2.3).

4.2.1 Disk structure

The disk model used in this work is based on the minimum-mass solar nebula (MMSN) of Hayashi (1981). The evolution of the gas surface density and temperature as a function of radial distance R from the Sun-like central star are given as

$$\Sigma_g = 152\left(\frac{R}{5\ \mathrm{AU}}\right)^{-3/2}\ \mathrm{g\ cm^{-2}}, \tag{4.1}$$

$$T = 125\left(\frac{R}{5\ \mathrm{AU}}\right)^{-1/2}\ \mathrm{K}. \tag{4.2}$$

The gas sound speed is given by

$$c_s = \sqrt{k_\mathrm{B}T/m_g} = 6.7\times10^2\left(\frac{R}{5\ \mathrm{AU}}\right)^{-1/4}\ \mathrm{m\ s^{-1}}, \tag{4.3}$$

with k_B the Boltzmann constant and $m_g = 3.9\times10^{-24}$ g the mean molecular weight. The Kepler frequency equals

$$\Omega = \sqrt{GM_\odot/R^3} = 1.8\times10^{-8}\left(\frac{R}{5\ \mathrm{AU}}\right)^{-3/2}\ \mathrm{s^{-1}}. \tag{4.4}$$

Assuming an isothermal column, the gas density drops with increasing distance from the mid plane z according to

$$\rho_g = \frac{\Sigma_g}{\sqrt{2\pi}h_g}\exp\left(\frac{-z^2}{2h_g^2}\right), \tag{4.5}$$

with the relative vertical scale height of the gas $h_g/R = 0.05(R/5\ \mathrm{AU})^{1/4}$. The turbulent viscosity is parametrized as $\nu_\mathrm{turb} = \alpha c_s^2/\Omega$ following Shakura & Sunyaev (1973), and α is

assumed to be constant in both the radial and the vertical direction. The eddie turn-over time of the largest eddies equals $t_L = \Omega^{-1}$.

In our local model, the surface density of the dust is related to the gas surface density through $\Sigma_d/\Sigma_g = 10^{-2}$, but the vertical distribution of dust depends on its aerodynamic properties. The dust is described by a Gaussian, with the dust scale height h_d set by the stopping time t_s of the dust particle through (Youdin & Lithwick 2007)

$$\frac{h_d}{h_g} = \left(1 + \frac{\Omega t_s}{\alpha}\frac{1 + 2\Omega t_s}{1 + \Omega t_s}\right)^{-1/2}. \tag{4.6}$$

Thus, settling becomes important when a dust particle reaches $\Omega t_s \sim \alpha$.

4.2.2 Dust properties

Initially, all dust particles are assumed to be spherical (sub)micron-size monomers. In time, these monomers coagulate through collisions, and aggregates of considerable mass can be formed. Any aggregate is described by two parameters: the mass m, and the filling factor ϕ. Since aggregates are made up of monomers the mass can be written as $m = Nm_0$, with N the number of monomers and m_0 the monomer mass. Following Okuzumi et al. (2012), we define the internal density of an aggregate as $\rho_{\rm int} = m/V$, with $V = (4/3)\pi a^3$ the volume of the aggregate, and a its radius. An aggregate's radius is defined as $a = [5/(3N)\sum_{k=1}^{N}(\vec{r}_k - \vec{r}_{\rm CM})^2]^{1/2}$, with $\vec{r}_k$ the position of monomer k and $\vec{r}_{\rm CM}$ the position of the aggregate's center of mass (Mukai et al. 1992; Suyama et al. 2008; Okuzumi et al. 2009). By definition, monomers have an internal density of $\rho_{\rm int} = m_0/V_0 = \rho_0$, while aggregates can have $\rho_{\rm int} \ll \rho_0$. Since we are interested in region beyond the snow-line, we focus here on monomers composed of mostly ice, and use a density of $\rho_0 = 1.4$ g cm^{-3}. For the monomer radius we use $a_0 = 0.1$ μm. We define the filling factor as

$$\phi \equiv \frac{\rho_{\rm int}}{\rho_0}, \tag{4.7}$$

as a measure for the internal density.

In the rest of this section, we describe the main ingredients for the simulations presented in Sect. 4.3. These are: the relative velocities between aggregates, the equations governing the evolution of $\rho_{\rm int}$ through mutual collisions as well as gas ram pressure and self-gravity, and models for the destructive processes of erosion and fragmentation.

Relative velocities

We take into account relative velocities arising from Brownian motion, turbulence, settling, radial drift and azimuthal drift (see Sect. 2.3.2 of Okuzumi et al. 2012). The relative contribution of the velocity components depends strongly on the size and aerodynamic properties of the dust grains in question. More specifically, the relative velocity is a function of the stopping times of the particles. Depending on the size of the particle, the

stopping time is set either by Epstein or Stokes drag

$$t_s = \begin{cases} t_s^{(\mathrm{Ep})} = \dfrac{3m}{4\rho_g v_{\mathrm{th}} A} & \text{for } a < \dfrac{9}{4}\lambda_{\mathrm{mfp}}, \\ t_s^{(\mathrm{St})} = \dfrac{4a}{9\lambda_{\mathrm{mfp}}} t_s^{(\mathrm{Ep})} & \text{for } a > \dfrac{9}{4}\lambda_{\mathrm{mfp}}, \end{cases} \tag{4.8}$$

where $v_{\mathrm{th}} = \sqrt{8/\pi} c_s$ is the mean thermal velocity of the gas molecules, and $\lambda_{\mathrm{mfp}} = m_g/(\sigma_{\mathrm{mol}}\rho_g)$ is the gas molecule mean free path. Taking $\sigma_{\mathrm{mol}} = 2 \times 10^{-15}$ cm^2, we obtain $\lambda_{\mathrm{mfp}} = 120(R/5\ \mathrm{AU})^{11/4}$ cm at the disk mid plane. In Eq. 4.8, $a = a_0(V/V_0)^{1/3}$ refers to the dust particle radius, while A is the projected cross section of the particle averaged over all orientations, which can be obtained using the formulation of Okuzumi et al. (2009).

Equation 4.8 is accurate when the particle Reynolds number $\mathrm{Re_p} = 4av_{\mathrm{dg}}/(v_{\mathrm{th}}\lambda_{\mathrm{mfp}}) < 1$, with v_{dg} the relative velocity between the gas and the dust particle. The Reynolds number can become large when aggregates grow very big or their velocity relative to the gas is very large. In general, the stopping time can be written as

$$t_s = \frac{2m}{C_D \rho_g v_{\mathrm{dg}} A}. \tag{4.9}$$

In the Stokes regime the drag coefficient equals $C_D = 24/\mathrm{Re_p}$, and the stopping time becomes independent of v_{dg}. However, for larger Reynolds number the stopping time becomes a function of the velocity relative to the gas. This regime is called the Newton drag regime. Since the relative velocity depends in turn on the stopping time, we have to iterate to find the corresponding stopping time. Following Weidenschilling (1977a), we use

$$C_D = \begin{cases} 24(\mathrm{Re_p})^{-1} & \text{for } \mathrm{Re_p} < 1, \\ 24(\mathrm{Re_p})^{-3/5} & \text{for } 1 < \mathrm{Re_p} < 800, \\ 0.44 & \text{for } 800 < \mathrm{Re_p}. \end{cases} \tag{4.10}$$

Figure 4.1 shows Stokes numbers (Ωt_s) for different particles in the mid plane of a MMSN disk at 5 AU. Different lines show compact particles (red), porous aggregates with constant $\phi = 10^4$ (yellow), and aggregates with a constant fractal dimension of 2.5 (green). For the solid lines, all drag regimes (Epstein, Stokes and Newton) have been taken into account, while the dashed lines indicate the results using only Epstein and Stokes drag, i.e., assuming that $\mathrm{Re_p} < 1$. Focussing on the $D_f = 2.5$ aggregates, we can clearly distinguish the different drag regimes. The smallest particles are in the Epstein regime, and switch to the Stokes regime around $\Omega t_s = 10^{-3}$. Then, at a mass of $m/m_0 \sim 10^{21}$, the Reynolds number exceeds unity and we enter the second regime of Eq. 4.10. We note that this transition occurs before $\Omega t_s = 1$. The most massive particles, $m/m_0 > 10^{26}$ are in the regime where $C_D = 0.44$. Compact particles on the other hand, reach $\Omega t_s = 1$ while still in the Epstein drag regime.

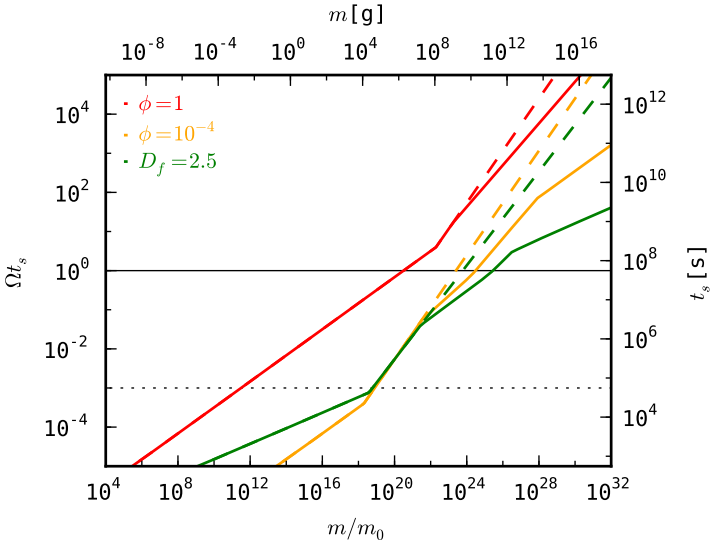

Figure 4.1: Particle Stokes numbers as a function of mass, in the mid plane of an MMSN disk at 5 AU. Different lines show compact particles (red), porous aggregates with constant $\phi = 10^4$ (yellow), and aggregates with a constant fractal dimension of 2.5 (green). For the solid lines, all drag regimes (Epstein, Stokes and Newton) have been taken into account, while the dashed lines indicate the results using only Epstein and Stokes drag. Horizontal lines indicate $\Omega t_s = 1$ (where drift is fastest) and $\Omega t_s = \alpha = 10^{-3}$ (where particles start to settle to the mid plane).

The turbulence-induced relative velocity between two particles with stopping times $t_{s,1}$ and $t_{s,2} \leq t_{s,1}$ has three regimes (Ormel & Cuzzi 2007)

$$v_{\rm turb} \simeq \delta v_g \times \begin{cases} {\rm Re_t}^{1/4}\, \Omega(t_{s,1} - t_{s,2}) & \text{for } t_{s,1} \ll t_\eta, \\ 1.4 \ldots 1.7\, (\Omega t_{s,1})^{1/2} & \text{for } t_\eta \ll t_{s,1} \ll \Omega^{-1}, \\ \left(\dfrac{1}{1+\Omega t_{s,1}} + \dfrac{1}{1+\Omega t_{s,2}} \right)^{1/2} & \text{for } t_{s,1} \gg \Omega^{-1}, \end{cases} \tag{4.11}$$

where $\delta v_g = \alpha^{1/2} c_s$ is the mean random velocity of the largest turbulent eddies, and $t_\eta = {\rm Re_t}^{1/2} t_L$ is the turn-over time of the smallest eddies. The turbulence Reynolds number is given by ${\rm Re_t} = \alpha c_s^2/(\Omega \nu_{\rm mol})$, with the molecular viscosity $\nu_{\rm mol} = v_{\rm th} \lambda_{\rm mfp}/2$. We will refer to the first two cases of Eq. 4.11 as the first and second turbulence regimes. Relative velocities between similar particles (similar in the sense that they have comparable stopping times) are very small[1] in the first turbulence regime because of the $(t_{s,1} - t_{s,2})$ term, but considerably larger in the second regime.

[1] According to Eq. 4.11, $v_{\rm turb} = 0$ for aggregates with identical stopping times in the first turbulence regime. In reality, the dispersion in the aggregate's mass-to-area ratio will give rise to a small relative velocity. We treat this dispersion in the same way as Okuzumi et al. (2012), by taking into account the standard deviation in the

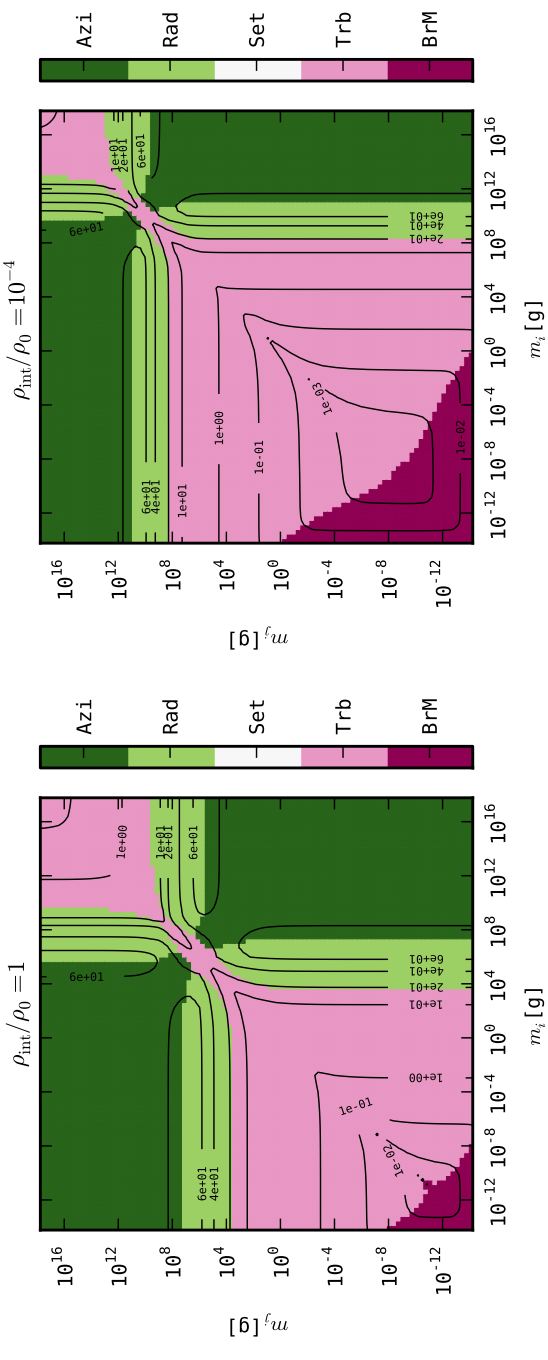

Figure 4.2: Relative velocities between compact (left) or very porous (right) particles with masses m_i and m_j at the mid plane of an MMSN-disk at 5 AU with $\alpha = 10^{-3}$. The masses range from single monomers to aggregates containing 10^{32} monomers. The contours give relative velocities in m s^{-1}, and the colors indicate the dominating source for the relative velocity: Brownian motion (BrM), turbulence (Trb), settling (Set), radial drift (Rad), or azimuthal drift (Azi). Epstein, Stokes, and Newton drag regimes have been taken into account.

Figure 4.2 shows the mid plane relative velocity in m s^{-1} (contours), and its dominant source (color), for a range of combinations of masses m_i and m_j. The velocities have been calculated for the disk properties of Sect. 4.2.1, at 5 AU, and assuming a turbulence $\alpha = 10^{-3}$. The left plot corresponds to two compact particles ($\rho_{\rm int} = \rho_0$), and the right plot to two very porous ones ($\rho_{\rm int} = 10^{-4}\rho_0$). The general picture is the same for all porosities: Brownian motion dominates the relative velocity at the smallest sizes, followed by turbulence for larger particles, and systematic drift for bodies that have $\Omega t_s \sim 1$. However, the masses at which various transitions occur can vary by several orders of magnitude depending on the particle porosity. For this particular location and turbulence strength, there is no combination of particle masses whose relative velocity is dominated by differential settling.

4.2.3 Collisional outcomes

A collision between porous aggregates can have a number of outcomes, ranging from perfect sticking to catastrophic fragmentation. For silicates, Blum & Wurm (2008) and Güttler et al. (2010) offer reviews of the various outcomes as observed in laboratory experiments. For porous ices, experimental investigations are scarce, and we have to turn to numerical simulations when predicting the outcome (e.g., Dominik & Tielens 1997; Wada et al. 2007; Suyama et al. 2008; Wada et al. 2009).

In general, a collision can result in sticking, erosion, or fragmentation, depending on the relative velocity and the mass ratio $R^{(m)} \equiv m_i/m_j \leq 1$ of the colliding bodies. Collisions between particles with comparable masses result in catastrophic fragmentation if they collide above the fragmentation velocity (Sect. 4.2.3). When colliding bodies have a mass ratio $R^{(m)} \ll 1$, catastrophic fragmentation of the larger body is difficult, but the collision can result in erosion if the velocity is high enough. The transition from erosion to the fragmentation regime occurs at a mass ratio $R^{(m)}_{\rm crit}$, specified in Sect. 4.2.3. In an erosive event, the larger body will lose mass. From Figure 4.2 it is clear that the highest velocities are reached between particles with very different masses, and thus erosion might very well be a common collisional outcome. We discuss erosion in more detail in Sect. 4.2.3. We should note at this point that we do not consider bouncing collisions. For relatively compact silicate particles, bouncing is frequently observed in the laboratory (e.g., Güttler et al. 2010), and indeed can halt growth in protoplanetary disks (Zsom et al. 2010). However, in porous aggregates, the average coordination number (the number of contacts per monomer) is much lower than in compact ones. As a result, collision energy is more easily dissipated, and it is safe to neglect bouncing (Wada et al. 2011; Seizinger & Kley 2013).

mass-to-area ratio of a porous aggregate (Okuzumi et al. 2011). The size of this standard deviation, normalized by the mean mass-to-area ratio, is parametrized as ε, which we take to equal 0.1, following Okuzumi et al. (2011).

Catastrophic fragmentation

For collisions between roughly equal icy aggregates (mass ratio $R^{(m)} \geq 1/64$), Wada et al. (2013) find a critical fragmentation velocity of

$$v_{\rm frag} \simeq 20 \left(\frac{E_{\rm break}}{m_0} \right)^{1/2} \simeq 80 \left(\frac{a_0}{0.1\,\mu{\rm m}} \right)^{-5/6} \ {\rm m\ s^{-1}}. \tag{4.12}$$

The quantity $E_{\rm break}$ represents the energy needed to break a single mononer-monomer contact (Dominik & Tielens 1997). Collisions below this critical velocity result in sticking, while collisions at or above $v_{\rm frag}$ result in fragmentation of the collision partners.

The case for erosion

The relative velocity between similar-sized aggregates will generally not reach the fragmentation velocity (Eq. 4.12) behind the snow line in a protoplanetary disk, especially not if the turbulence is weak. However, relative velocities between particles with very different masses can be much larger than velocities between similar particles, especially when radial and azimuthal drift are important (Figure 4.2). In this paper, we study the effects of an erosive regime, where collisions at low mass ratios will produce erosive fragments at velocities below a critical erosion threshold velocity $v_{\rm eros} \lesssim v_{\rm frag}$. Here, we briefly revisit numerical and experimental studies of erosion, before outlining the erosion model used in this work. The process of erosion can be described by two main quantities: the erosion threshold velocity, $v_{\rm eros}$, above which erosion takes place, and the (normalized) erosion efficiency, $\epsilon_{\rm eros}$, that indicates how much mass is eroded in units of projectile mass.

For silicate particles, Güttler et al. (2010) summarize a number of experimental investigations and describe a threshold velocity of a few m s^{-1}, and an erosion efficiency that increases roughly linearly with collision velocity. Similar trends were observed by Schräpler & Blum (2011), who found an erosion threshold velocity of a few m s^{-1} using micron-size silicate projectiles. We note that the threshold velocity is comparable to the monomer sticking velocity of micron-size silicate particles (Poppe et al. 2000). In the experiments of Schräpler & Blum (2011), the erosion efficiency also increased with impact velocity, reaching $\sim$10 for the highest velocity of 60 m s^{-1} (their Figure 5). Seizinger et al. (2013) used molecular dynamics simulations, based on a new viscoelastic model (Krijt et al. 2013), to reproduce the experimental results. In addition, Seizinger et al. (2013) studied the variation on the threshold velocity and erosion efficiency with projectile mass, showing a trend of decreasing erosion threshold with decreasing mass ratio (e.g., their Figure 11). For monomer projectiles, the threshold velocity equals the monomer-monomer sticking velocity $v_s \simeq \sqrt{E_{\rm break}/m_0}$, after which it increased linearly with velocity to eventually flatten off around 10 m s^{-1}. This flattening off indicates the onset of catastrophic fragmentation, and occurs at a mass ratio of $\sim 10^{-2}$.

For ice particles, Gundlach & Blum (2015) present recent experimental results on the sticking and erosion threshold of (sub)micron-size particles. For a projectile distribution between $0.2 - 6\ \mu$m (with a mean value of 1.5 μm) impinging an icy target with a filling factor $\phi \simeq 0.5$, an erosion threshold of 15.3 m s^{-1} was found. These results confirm the

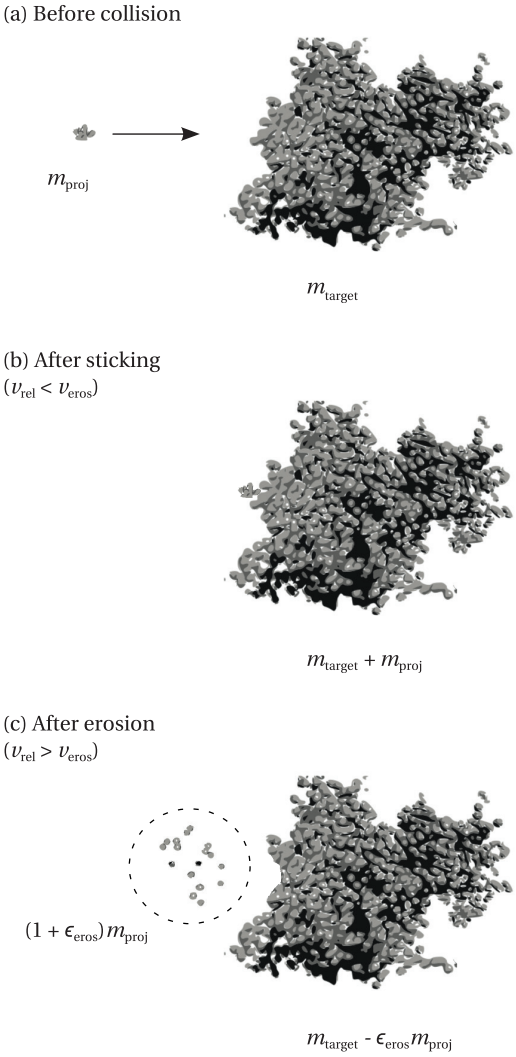

Figure 4.3: (a) Schematic of a collision between unequal particles with a mass ratio $R^{(m)} = (m_{\text{proj}}/m_{\text{target}}) \ll 1$. (b) Sticking occurs when $v_{\text{rel}} < v_{\text{eros}}$. The mass of the projectile is added to the target. (c) Collisions above the erosion threshold velocity lead to erosion. The mass loss of the target is given by the erosion efficiency ϵ_{eros} and the mass of the projectile.

increased stickiness of ice compared to silicate particles, and indicate v_{eros} could indeed be very high for (monodisperse) 0.1-μm monomers, possibly even >60 m s^{-1}. However, the aggregates acting as targets in the simulations presented here have a much higher porosity ($\phi \sim 10^{-3}$), and the lower coordination number is expected to reduce the erosion threshold (Dominik & Tielens 1997). Lastly, while Gundlach & Blum (2015) used a distribution

of grain sizes, numerical investigations (e.g., Seizinger et al. 2013; Wada et al. 2013), for computational reasons, often employ a monodisperse monomer distribution, making a direct comparison difficult. For a single grain size, the size significantly influences the strength of the aggregates, with larger monomers leading to weaker aggregates (Eq. 4.12). Little is known about the expected grain sizes in the icy regions of protoplanetary disks, let alone their size distribution, or about the effect a monomer size distribution has on the strength and collisional behavior of porous aggregates.

For these reasons, we believe that the existence of an erosive regime for icy aggregates is plausible. However, at present the data are unfortunately ambiguous with other simulations indicating the opposite trend: that the mass-loss in low mass ratio collisions is relatively small. Using molecular dynamics N-body simulations Wada et al. (2013) find that the threshold velocity (where fragmentary collisions become more numerous than sticky collisions) increases for smaller mass ratios, suggesting that only similar-size particles colliding at $v_{\rm frag}$ fragment efficiently. This trend of an increased erosion threshold for smaller size ratios is corroborated by recent simulations by Tanaka et al. (in prep). This would imply that for monodisperse submicron grains, both threshold velocities might not be reached (cf. Eq. 4.12 and Figure 4.2). In this paper, we bury the uncertainty of the erosion threshold velocity in the parameter $v_{\rm eros}$, which we vary to investigate the implications of effective versus ineffective erosion.

Erosion model

Erosive collisions only occur below a mass ratio $R^{(m)}_{\rm crit}$, and their outcome is parametrized in terms of a (velocity-dependent) erosion efficiency. In accordance with Güttler et al. (2010) and Seizinger et al. (2013) we will use $R^{(m)}_{\rm crit} = 10^{-2}$. For smaller mass ratios, we will assume a constant value for $v_{\rm eros}$, that does not depend on mass ratio or projectile/target porosity. We vary $v_{\rm eros}$ between 20 and 60 m s^{-1}, corresponding to $(1/4)v_{\rm frag}$ and $(3/4)v_{\rm frag}$ for 0.1 μm monomers (Eq. 4.12). In the erosive regime, the normalized erosion efficiency can be written as

$$\epsilon_{\rm eros} = c_1 \left(\frac{v_{\rm rel}}{v_{\rm eros}} \right)^{\gamma}, \tag{4.13}$$

with $c_1 \sim 1$ (Güttler et al. 2010; Seizinger et al. 2013). While in supersonic cratering collisions $\gamma = 16/9$ (Tielens et al. 1994), the velocities encountered in this work are not that high and at most comparable to the sound speed in porous aggregates (Paszun & Dominik 2008). Hence, we will use $\gamma = 1$, in agreement with both numerical and experimental work in the appropriate velocity range (Güttler et al. 2010; Schräpler & Blum 2011; Seizinger et al. 2013).

Lastly, we need a prescription for the filling factors after an erosive collision. We assume that *i*) the filling factor of the target remains unchanged, and *ii*) the filling factor of the fragments is found by assuming they have the same fractal dimension as the target, where the target's fractal dimension D_f is estimated as

$$D_f \simeq 3 \left[1 - \frac{\log(\phi)}{\log(m/m_0)} \right]^{-1}. \tag{4.14}$$

The assumptions of the erosion model employed in this work are discussed further in Sect. 4.6.

4.2.4 Aggregate compaction

An aggregate's porosity can be altered through collisions, or through non-collisional mechanisms. In this section, we first describe how porosity can increase and decrease as the result of sticking collisions. Then, we discuss gas- and self-gravity compaction.

Collisional compaction

When two particles i and j collide at a relative velocity $v_{\rm rel}$ that is below the thresholds for fragmentation or erosion, the particles stick, and form a new aggregate with mass $m_i + m_j$. The internal density of the new particle depends on how the impact energy compares to the energy needed for restructuring. When the impact energy is not enough to cause significant restructuring, particles grow by hit-and-stick collisions, and very fractal aggregates can be formed (Kempf et al. 1999). When the impact energy is much larger, significant restructuring can take place, reducing the internal density of the dust aggregates. In this work, we will make use of the model presented in Suyama et al. (2012) and Okuzumi et al. (2012). Specifically, we use Eq. 15 of Okuzumi et al. (2012) to calculate the volume of the a newly-formed aggregate, as a function of the masses and volumes of particles i and j, the impact velocity, and the rolling energy $E_{\rm roll}$; the energy needed to roll two monomers over an angle of 90° (Dominik & Tielens 1997).

Gundlach et al. (2011) measured the rolling force between ice particles with radii of $\sim$1.5 μm to be 1.8×10^{-3} dyn, implying a rolling energy of 1.8×10^{-7} erg. Assuming the rolling force is size-independent (Dominik & Tielens 1995), the rolling energy is then often extrapolated using $E_{\rm roll} \propto a_0$. Recently however, Krijt et al. (2014) showed that the rolling force scales with the size of the area of the monomers that is in direct contact, resulting in $F_{\rm roll} \propto a_0^{2/3}$, and $E_{\rm roll} \propto a_0^{5/3}$, leading to significantly smaller rolling energies when extrapolating down to monomer radii well below a micrometer. In this work, we use the scaling law of Krijt et al., resulting in a rolling energy of 4×10^{-9} erg for 0.1-μm radius ice particles. Physically, a lower rolling energy means less energy is needed to start restructuring of an aggregate. As a result, a lower rolling energy will lead to compacter aggregates.

Gas and self-gravity compaction

Aggregates can also be compressed by the ram pressure of the gas, or their own gravity, if they become very porous or massive. For low internal densities, Kataoka et al. (2013b) found that the external pressure a dust aggregate can just withstand equals

$$P_c = \frac{E_{\rm roll}}{a_0^3}\phi^3. \tag{4.15}$$

This pressure can then be compared to the pressure arising form the surrounding gas and from self-gravity

$$P_{\rm gas} = \frac{v_{\rm dg} m}{\pi a^2 t_s}, \qquad P_{\rm grav} = \frac{G m^2}{\pi a^4}, \tag{4.16}$$

with G the gravitational constant, in order to see whether an aggregate will be compacted as a result of these non-collisional processes (Kataoka et al. 2013a). In this work, we will take these effects into account in a self-consistent way, while calculating the collisional evolution of the dust distribution.

4.3 Monte Carlo approach

Numerical techniques for studying coagulation can be divided in two categories[2]: integro-differential methods (e.g., Weidenschilling 1980; Dullemond & Dominik 2005; Birnstiel et al. 2010), and Monte Carlo (MC) methods (Gillespie 1975; Ormel et al. 2007; Zsom & Dullemond 2008). Tracing particle porosity as well as mass becomes computationally expensive in the integro-differential approach. A solution to this issue was presented by Okuzumi et al. (2012), who assumed the porosity distribution for a given mass bin was narrow, but could vary in time. Since we are interested in including erosive processes, this assumption is not expected to hold, and for this reason we opt for the Monte Carlo method.

The approach to calculate the collisional evolution is based on the distribution method as described in Ormel & Spaans (2008). In this section, we briefly revisit the method, focussing on what is new in this work.

We let $f(\vec{x})$ be the (time-dependent) particle distribution function, with $\vec{x_i}$ the unique parameters describing dust particle i, in our case mass and filling factor[3]. For every pair of particles i and j, one can determine the collision rate as

$$C_{ij} = K_{ij}/\mathcal{S}, \tag{4.17}$$

with $\mathcal{S}$ the surface area of the column[4], and K_{ij} the collision kernel, which in this case equals

$$K_{ij} = \frac{\sigma_{ij}}{2\pi h_{d,i} h_{d,j}} \int_{-\infty}^{\infty} v_{\rm rel}(z) \exp\left(\frac{-z^2}{2h_{d,ij}^2}\right) {\rm d}z, \tag{4.18}$$

where $h_{d,i}$ is given by Eq. 4.6, and $h_{d,ij} = (h_{d,i}^{-2} + h_{d,j}^{-2})^{-1/2}$ and $\sigma_{ij} = \pi(a_i + a_j)^2$ equals the collisional cross section (Okuzumi et al. 2012). This rate equation takes into account that particles with different properties inhabit different vertical scale heights, and is correct as long as the coagulation timescale is longer than the vertical settling/diffusion timescale. In this work, we approximate the integral over z by assuming the mid plane relative velocity

[2] See Drążkowska et al. (2014) for a comparison between the two methods in the breakthrough growth case.

[3] All other quantities (e.g., stopping time, volume, size) can be calculated from these two numbers.

[4] The size of the column is set by the total mass in the simulation and the dust surface density at the column's location.

is a good indication for $v_{\rm rel}$ throughout the column. This allows us to solve the integral analytically and write

$$K_{ij} \simeq \frac{\sigma_{ij} h_{d,ij}}{\sqrt{2\pi} h_i h_j} v_{\rm rel}(z=0). \tag{4.19}$$

For the purpose of this paper, this approximation is sufficiently accurate, since most of the growth is expected to take place near the mid plane.

Then, we can define the total collision rate for particle $C_i = \sum_{j>i} C_{ij}$, and the total collision rate $C_{\rm tot} = \sum_i C_i$. With all these rates known, 3 random numbers are used to identify which particles collide, and the time Δt after which this collision occurs. The colliding particles are then removed from f, and the collision product is added. As a result, all collision rates C_i have to be adjusted, since the particle distribution f has changed. This cycle is then repeated.

The simple method has two main drawbacks. First, the time needed for updating the rates in between collisions scales with N^2, where N is the total number of particles. Second, this method describes 1 collision per cycle, which can become a problem whenever the mass distribution is broad.

4.3.1 Grouping method

Rather than following every particle individually, identical particles can be grouped together. In our approach, the dust distribution is described by N_f particle families. Within a single family, all particles have identical properties, in our case mass and internal density. In every family i, there are w_i particle groups, each containing 2^{z_i} individual particles, where we call z_i the zoom factor. The total number of particles in a single family therefor equals $g_i = w_i 2^{z_i}$, and the total number of particles is $N = \sum_i g_i$. Instead of 2 particles colliding per cycle, collisions now happen between *groups* of particles (see Ormel & Spaans 2008, for details about this method). Letting i refer to the group with the lower zoom factor, we obtain for the group collision rates

$$\lambda_{ij} = \begin{cases} w_i w_j 2^{z_i} C_{ij} & \text{for } i \neq j, \\ w_i (w_i 2^{z_i} - 1) C_{ii} & \text{for } i = j, \end{cases} \tag{4.20}$$

where the $i = j$ case in Eq. 4.20 describe so-called *in-group* collisions. Like before, we can define the total collision rate per family $\lambda_i = \sum_{j \geq i} \lambda_{ij}$, and the total collision rate $\lambda_{\rm tot} = \sum_i \lambda_i$, which can be used to determine which groups collide and when. This grouped approach has tremendous advantages, but there are also pitfalls, which we discuss in the following section.

4.3.2 Sequential collisions

Imagine the collision between a group of large bodies i with a group of much smaller bodies j, such that $m_i \gg m_j$. Thus, a total of 2^{z_i} i-particles will collide with 2^{z_j} j-particles. Assuming $z_j \gg z_i$, every i-particle in the group will collide with $2^{z_j - z_i}$ j-particles in a

single sequence before the collision rates are updated and the next groups to collide are chosen. We are assuming that the collision rates and the relative velocity between i and j particles are constant during this sequence, but this is only true if the properties of particle i do not change significantly. For this reason we include the group splitting factor N_ε, that limits the number of collisions to $2^{z_j - z_i - N_\varepsilon}$.

We let δm_i be the change in the mass of the larger particle i, after a single collision with a j-particle. Assuming the changes are small, we can then extrapolate to find the total change after the full sequence of collisions

$$\frac{\Delta m_i}{m_i} = \frac{2^{z_j - z_i - N_\varepsilon} \delta m_i}{m_i}. \tag{4.21}$$

Now, by imposing that $(\Delta m_i / m_i) \leq f_m$, we obtain

$$N_\varepsilon^{(m)} = \left[-\log_2 \left(\frac{f_m m_i 2^{z_i}}{\delta m_i 2^{z_j}} \right) \right], \tag{4.22}$$

where the square brackets indicate that $N_\varepsilon^{(m)}$ is truncated to integers ≥ 0, which has the effect of particles with mass ratios $\geq f_m$ always colliding 1-on-1. In the case of perfect sticking, obviously $\delta m_i = m_j$, and Eq. 4.22 reduces to Eq. 12 of Ormel & Spaans (2008). We write an equivalent expression for the filling factor of the bigger grain

$$N_\varepsilon^{(\phi)} = \left[-\log_2 \left(\frac{f_\phi \phi_i 2^{z_i}}{\delta \phi_i 2^{z_j}} \right) \right], \tag{4.23}$$

where $\delta \phi_i$ denotes the change in ϕ after a single collision. The two limits are combined by writing

$$N_\varepsilon = \max \left(N_\varepsilon^{(m)}, N_\varepsilon^{(\phi)} \right), \tag{4.24}$$

and ensure that neither the filling factor, nor the mass of the larger particle change by too much during a single Monte Carlo cycle. We note that N_ε is not only a function of the masses and densities of both particles, but also of the relative velocity, since this influences $\delta \phi_i$ (and δm_i, when erosion is present). In this work, we will typically use $f_m = f_\phi = 0.1$.

Imposing this limit has two consequences. First, since the group of i-particles can now only collide with *part of* the group of j-particles, this needs to be taken into account when the group collision rates are calculated, changing Eq. 4.20 into

$$\lambda_{ij} = \begin{cases} w_i w_j 2^{z_i + N_\varepsilon} C_{ij} & \text{for } i \neq j, \\ w_i (w_i 2^{z_i} - 1) C_{ii} & \text{for } i = j. \end{cases} \tag{4.25}$$

Second, since it can occur that only part of a group collides, group numbers w_i can now become fractional. This is fine as long as $w_i \geq 1$, ensuring that at least one full group collision can occur in the future (Ormel & Spaans 2008).

4.3.3 The distribution method

For a given number of family members g_i, we have some freedom in choosing z_i; either creating many groups with a few members (low z_i) or a few groups with many members (high z_i). This choice for the zoom factors is crucial because it determines how many groups of a certain mass exist, which is related to the numerical resolution in that part of the mass range. Two approaches for determining the zoom factors have been proposed by Ormel & Spaans (2008).

One approach is the so-called *equal mass method*, in which one strives to have groups of equal total mass. This method is essentially identical to the method of Zsom & Dullemond (2008). With this approach, the peak of the mass distribution is very well traced, but parts of the particle distribution that carry little mass are described by a few groups, resulting in larger uncertainties. The second option is the *distribution method*, where one strives to have an equal number of groups per mass decade, independent of the total mass present in that interval. The difference between the two methods is nicely illustrated in Figure 4 of Ormel & Spaans (2008). Since we are interested in erosion, it is crucial to resolve the particle distribution over the entire mass range. It is for that reason that we adopt the distribution method.

In practice, this means that at certain times during the simulation, we calculate the total number of particles N_{10} in every mass decade. The optimal zoom number for families in that mass range then equals

$$z^* = \left\lfloor \log_2 \left(\frac{N_{10}}{w^*} \right) \right\rfloor, \tag{4.26}$$

where w^* is the desired number of groups per mass decade. In this way, we construct a function $z^*(m)$, which gives the desired zoom number for a family with particle mass m. We then check every existing family: if a certain zoom number is too big, we magnify the group ($z_i \to z_i - 1$, $w_i \to 2w_i$) until $z_i = z^*(m_i)$. Similarly, if the zoom number is too small, we demagnify ($z_i \to z_i + 1$, $w_i \to w_i/2$). The (de)magnification process conserves particle number, but does force one to update the various collision rates. A more detailed description of (de)magnification is given by Ormel & Spaans (2008). In the rest of this work, we calculate and update the zoom factors after every 10^2 collision cycles, whenever the peak or average mass has changed by >5%, or when the maximum mass has changed by >50%, which we found to ensure a smooth evolution of the zoom factors. We will use $w^* = 60$ for the perfect sticking calculations, and $w^* = 40$ for the ones including erosion.

4.3.4 Merging

Lastly, we have to address the merging of families. It can occur that demagnification results in a group number $w_i < 1$, which is not allowed. When this occurs, the family does not contain enough individual particles to adopt $z_i = z^*(m_i)$. At this point, the family is insignificant. As we are simulating a fixed volume and the total mass needs to be conserved, we merge the family with another, healthy (meaning $w_i > 1$) one. First, we find the family j that resembles family i the most. In order to do so, we find the family that

gives the largest product $(R^{(m)})(R^{(\phi)})^3$, where $R^{(\phi)} \leq 1$ is the ratio of the filling factors[5]. Then, we merge the families into a new family k with properties

$$g_k = g_i + g_j, \quad m_k = \frac{m_i g_i + m_j g_j}{g_i + g_j}, \quad \phi_k = \frac{\phi_i g_i + \phi_j g_j}{g_i + g_j}. \tag{4.27}$$

The new zoom- and group numbers are chosen such that $z_k = z^*(m_k)$. Merging is necessary to suppress the total number of groups.

4.3.5 Non-collisional compaction

Non-collisional compaction is implemented as follows: whenever a new aggregate is created in a collision, we calculate its compressive strength using Eq. 4.15, and compare this to the external pressures from gas ram pressure and self-gravity, calculated with Eq. 4.16 (Kataoka et al. 2013a). If either one of the external pressures exceeds P_c, we compactify the dust grain (i.e., increase ϕ) until the aggregate can withstand the external pressures.

4.3.6 Erosion

For every collision, we check if the conditions for erosion are met (i.e., $v_{\rm rel} > v_{\rm eros}$ and $R^{(m)} < R^{(m)}_{\rm crit}$), and if so, we determine the erosion efficiency using Eq. 4.13. After a single erosive event, the mass that does *not* end up in the target body equals $(1 + \epsilon_{\rm eros})m_{\rm proj}$, see Figure 4.3. To limit the number of new families, we redistribute this mass over fragments with a mass of $m_{\rm frag} = m_{\rm proj}/10$.

4.4 Results

In this section we show the results of our simulations for different erosion recipes, compaction mechanisms, turbulence strengths, and disk locations. When discussing the particle distribution at a given time, we shall use a number of quantities. These are the *average* mass and porosity

$$m_a = \langle m_i \rangle, \quad \phi_a = \langle \phi_i \rangle, \tag{4.28}$$

which trace the properties of the average particle, and the *peak* mass and filling factor

$$m_p = \frac{\langle m_i^2 \rangle}{\langle m_i \rangle}, \quad \phi_p = \frac{\langle m_i \phi_i \rangle}{\langle m_i \rangle}, \tag{4.29}$$

which trace the properties of the mass-dominating particle. We will also use the maximum mass $m_{\rm max}$, which is simply the mass of most massive particle.

[5]This combination of $R^{(m)}$ and $R^{(\phi)}$ is used because the spread in masses is typically larger than the one in porosities, and we want to avoid merging particles with very different porosities if possible.

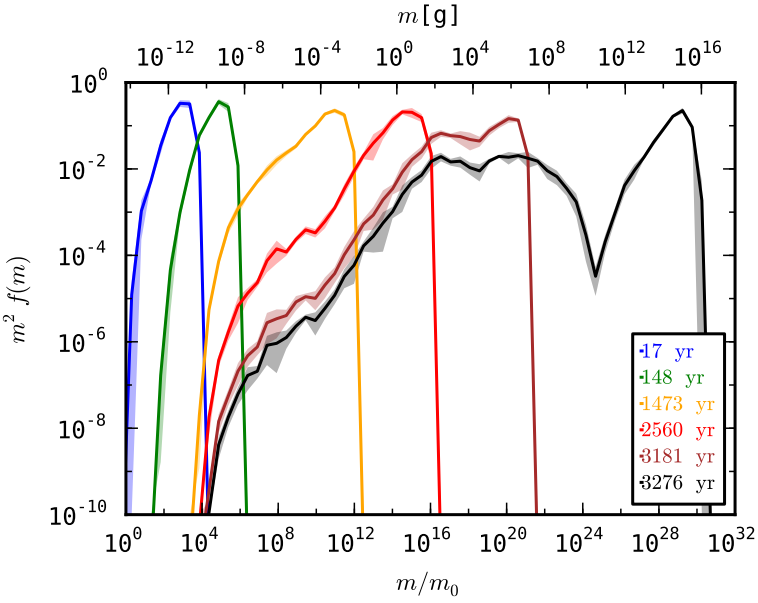

Figure 4.4: Evolution of the normalized particle mass distribution at 5 AU with $\alpha = 10^{-3}$, assuming perfect sticking and without compaction through gas and self-gravity. Only Epstein are Stokes drag are considered. Solid lines indicate averages over 4 Monte Carlo runs with identical starting conditions, and the shaded areas represent a spread of 1σ.

4.4.1 Perfect sticking

Collisional-compaction-only scenario

As a test for the Monte Carlo approach, we attempt first to match the trends observed in Okuzumi et al. (2012), who assumed perfect sticking between the dust grains. We adopt a turbulence strength parameter of $\alpha = 10^{-3}$, and focus on a vertical column at 5 AU in a typical MMSN disk. At this point, we only include collisional compaction and omit erosion. To allow a direct comparison to the work of Okuzumi et al., we do not include the effects of Newton drag for particles with large Reynolds numbers in this simulation. In the rest of this work, Newton drag is always included self-consistently.

Figure 4.4 shows the evolution of the normalized mass distribution $m^2 f(m)$ as a function of time. Solid lines mark the average over 4 Monte Carlo runs. Thanks to the distribution method described in Sect. 4.3.3, the sampling of the mass distribution is very good over the entire mass range: even at later times, when most of the mass is located in particles with masses of $\sim 10^{15}$ g, the distribution of particles all the way down to 10^{-9} g is resolved remarkably well, despite these particles only making up a very small fraction of the total mass.

When we compare Figure 4.4 to Figure 7 of Okuzumi et al. (2012), it is clear that our local MC method yields very similar results. We recognize the familiar narrow mass peak

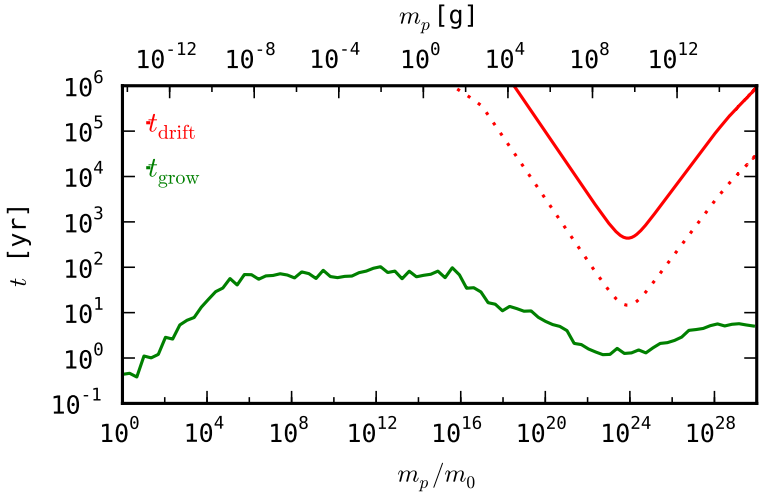

Figure 4.5: Evolution of the growth- and radial drift timescale of the peak mass for the perfect sticking model at 5 AU with $\alpha = 10^{-3}$. The dotted line indicates ($t_{\rm drift}/30$). Only collisional compaction has been taken into account.

when growth is governed by Brownian motion, followed by a broader distribution once turbulence kicks in. Once particles reach $\Omega t_s \sim 1$ ($m_j \simeq 10^{10}$ g in this case), systematic drift greatly increases their collision rate, and very rapid growth ensues. The slight difference in timescales is attributed to *i*) the slightly different value for the rolling energy, *ii*) our approximation of Eq. 4.18, and *iii*) our use Eq. 4.8 to calculate the stopping times, while Okuzumi et al. used $t_s = t_s^{(\rm Ep)} + t_s^{(\rm St)}$ to ensure a smooth transition between Epstein and Stokes drag (S. Okuzumi, private communication).

While we take into account drift-induced relative velocities, the dust particles are bound to our simulated column and cannot move radially through the disk. To test the validity of this assumption, we compare the growth timescale of the peak mass, defined as

$$t_{\rm grow} \equiv \frac{m_p}{({\rm d}m_p/{\rm d}t)}, \tag{4.30}$$

to the radial drift timescale at that mass

$$t_{\rm drift} \equiv \frac{R}{v_{\rm drift}(m_p)}. \tag{4.31}$$

The radial drift velocity is given by (Weidenschilling 1977a)

$$v_{\rm drift} = -\frac{2\Omega t_s}{1 + (\Omega t_s)^2}\eta v_K, \tag{4.32}$$

where $v_K = R\Omega$ is the Keplerian orbital velocity, and η can be written as (Nakagawa et al.

1986)

$$\eta \equiv -\frac{1}{2}\left(\frac{c_s}{v_K}\right)^2 \frac{\partial \ln(\rho_g c_s^2)}{\partial \ln R} = 4 \times 10^{-3} \left(\frac{R}{5\ \mathrm{AU}}\right)^{1/2} . \tag{4.33}$$

Figure 4.5 shows both the growth and radial drift timescales during the complete evolution of the peak mass. Initially, relative velocities are dominated by Brownian motion. Since this velocity drops with increasing particle mass, the growth timescale increases. Around a mass of 10^{-9} g, turbulent velocities start to dominate the relative velocity, and the growth timescale stays approximately constant. Particles larger than 10^3 g enter the second turbulent regime as $t_s(m_p) > t_\eta$. In this regime, velocities between similar particles are increased (see Eq. 4.11), which leads to a decrease in the growth timescale. Since the growth timescale is always much smaller than the drift timescale, the aggregates in this simulation do indeed out-grow the radial drift barrier.

Including gas and self-gravity compaction

The next step is to include compaction by gas pressure and self-gravity, as described in Sect. 4.2.4. In addition, we now take into account Newton drag for particles with large Reynolds numbers. Figure 4.6 shows the results for the same disk parameters as before. The general shape of the evolution looks similar to Figure 4.4 initially, but from the corresponding times it is clear that the growth is slower for the largest aggregates. The main reason for this is that the largest dust grains are compacted by the gas and self-gravity, resulting in a smaller collisional cross section. In addition, the aerodynamic properties are different, which affects the relative velocities.

The growth- and drift timescales are plotted in Figure 4.7. When we compare Figures 4.5 and 4.7, we confirm that the growth close to the drift barrier is slower when using the full compaction recipe. For the largest particles, the growth timescale is increased by more than 2 orders of magnitude. In addition, including Newton drag has broadened the drift barrier somewhat. Nonetheless, the growth is still fast enough to prevent particles from drifting significant distances.

Evolution of internal densities

It is interesting to compare the evolution of the internal densities of the particles for the models with and without non-collisional compaction. In Figure 4.8, the peak filling factor is plotted versus the peak mass for the simulations described so far. The symbols correspond to important points in the evolution of the aggregates: open circles are related to the stopping time of the aggregates, and closed symbols indicate the onset of various compaction mechanisms[6].

Initially, aggregates grow through hit-and-stick collisions, and evolve along a line of constant fractal dimension close to 2. In the collisional-compaction-only scenario, particles reach a filling factor of $\sim 10^{-5}$ during hit and stick growth, before collisional com-

[6]The particle actually undergoing this compaction can have a mass and porosity that differ slightly from m_p and ϕ_p.

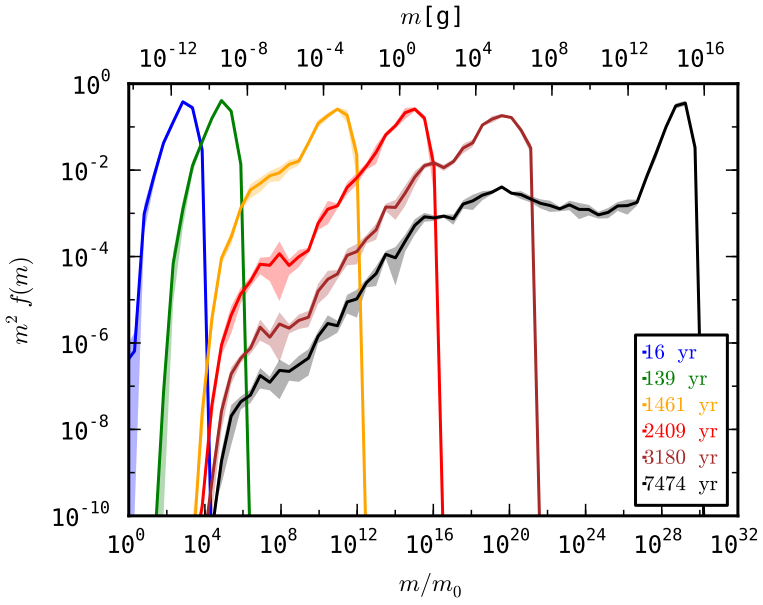

Figure 4.6: Like Figure 4.4, but with compaction through gas and self-gravity and Newton drag for particles with $\mathrm{Re_p} > 1$.

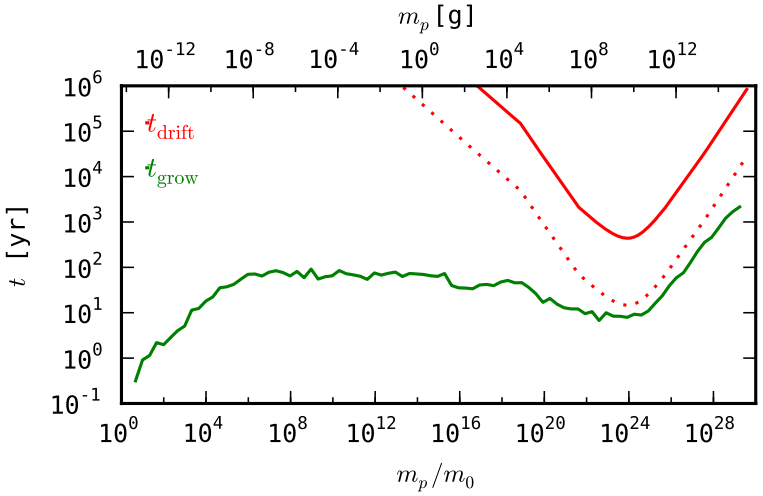

Figure 4.7: Evolution of the growth- and radial drift timescale of the peak mass for the perfect sticking model at 5 AU with $\alpha = 10^{-3}$. The dotted line indicates $(t_{\mathrm{drift}}/30)$. Compaction from gas and self-gravity, and Newton drag have been taken into account.

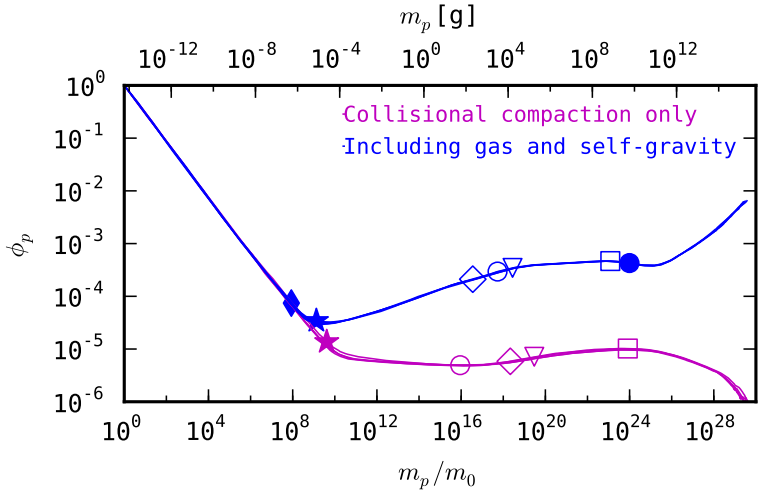

Figure 4.8: Evolution of the internal structure of the mass-dominating particles, for the perfect sticking models at 5 AU, for the models with and without non-collisional compaction mechanisms. Aggregates start out as monomers in the top left corner, and grow towards larger sizes and porosities. Lines show individual simulations. Open symbols correspond to points where the mass dominating particles reach $a = \lambda_{\rm mfp}$ (○); $t_s = t_\eta$ (◇); $\Omega t_s = \alpha$ (▽); and $\Omega t_s = 1$ (□). Filled symbols show peak mass and filling factor at the times of first: collisional compaction (★); gas-pressure compaction (⧫); and self-gravity compaction (●).

paction kicks in, after which ϕ stays almost constant. When $\Omega t_s(m_p) > 1$, the internal density drops even further. The general picture, as well as the location of the various turnover points, is consistent with the top panel of Figure 10 of Okuzumi et al. (2012). When non-collisional compaction is included, the filling factor, in general, is much higher at later times, and follows the boundaries that have been described by Kataoka et al. (2013a) (e.g., their Figure 3). For this particular combination of turbulence, rolling energy, and monomer size, compacting by gas ram pressure actually occurs *before* the first collisional compaction event takes place[7]. Significant settling occurs when $\Omega t_s > \alpha$, which corresponds to $m \sim 10^{-3}$ g for compact particles (see Figure 4.1). From Figure 4.8 however, we see that porous particles only begin to settle when their masses reach $\sim 10^4 - 10^5$ g. Lastly, aggregates with masses above $\sim 10^{10}$ g are compacted by self-gravity, causing the filling factor for the largest bodies to be several orders of magnitude higher. In the remainder of this work, we include both collisional and non-collisional compaction mechanisms, and Epstein, Stokes, and Newton drag self-consistently.

[7] In fact, the gas compaction starts when the aggregates are still in the Epstein drag regime. Eq. 4.15 is determined by *static* compression of porous aggregates, and Eq. 4.16 assumes the external pressure can be treated as continuous. However, if the collision frequency of gas molecules with individual monomers of the aggregate is low compared to the frequency at which monomer-monomer contacts oscillate and dissipate energy, this approach might not be accurate. Future work is encouraged to investigate the effect of collisions between the aggregate and gas molecules in this regime.

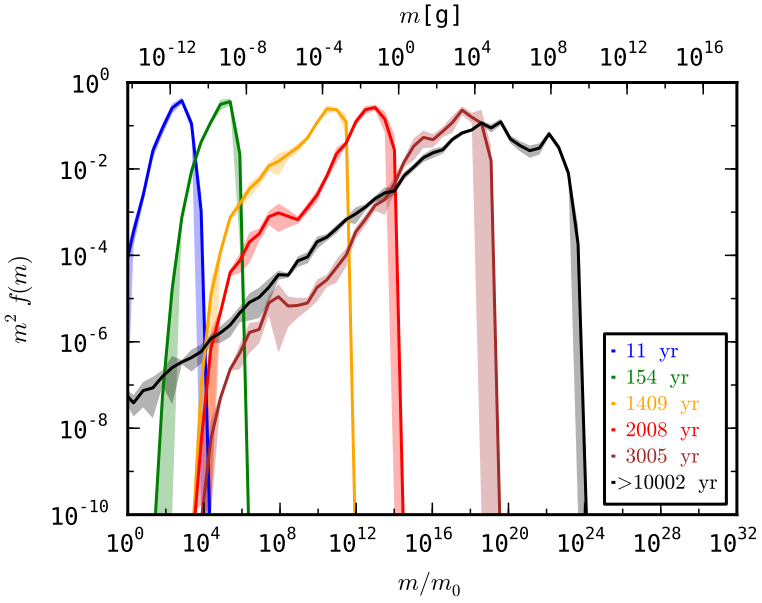

Figure 4.9: Evolution of the normalized particle mass distribution at 5 AU with $\alpha = 10^{-3}$, assuming $v_{\mathrm{eros}} = 20$ m s^{-1}. The full compaction model is used.

4.4.2 Erosion

With this framework in place, the final step is to include the erosion model of Sect. 4.2.3 in the simulations, and calculate the evolution of the particle distribution self-consistently. Figure 4.9 shows the mass distribution at various times for $v_{\mathrm{eros}} = 20$ m s^{-1}. Initially, the evolution proceeds just like in 4.6, but as the largest aggregates approach $\Omega t_s = 1$, their velocity relative to smaller particles is high enough for erosion, and their growth stalls. As a direct consequence of the erosion, the amount of small particles increases, and after ~4000 yr a steady-state is reached, with a significant amount of mass residing in particles smaller than a few grams.

To investigate how erosion halts the growth of the largest bodies, it is instructive to plot so-called projectile mass distributions (Okuzumi et al. 2009). For a certain particle mass m_t, these distributions show the contribution to the growth of that particle as a function of projectile mass $m \leq m_t$. An example of such a plot is shown in Figure 9 of Okuzumi et al. (2012), where the distribution function is plotted at various times for $m_t = m_p$. For our distribution plots, we make two important changes: First, since we are interested in the growth of the largest bodies, we plot projectile distributions for $m_t = m_{\mathrm{max}}$, with m_{max} the *largest* mass in the simulation at a given time. Second, to illustrate the effect of erosive collisions, we calculate the mass loss for every erosive collision, taking into account the correct erosion efficiency[8]. As a result, the sign of the distribution function can be both

[8] A sticking collision, where the mass of the projectile is added to the target, is described by $\epsilon_{\mathrm{eros}} = -1$.

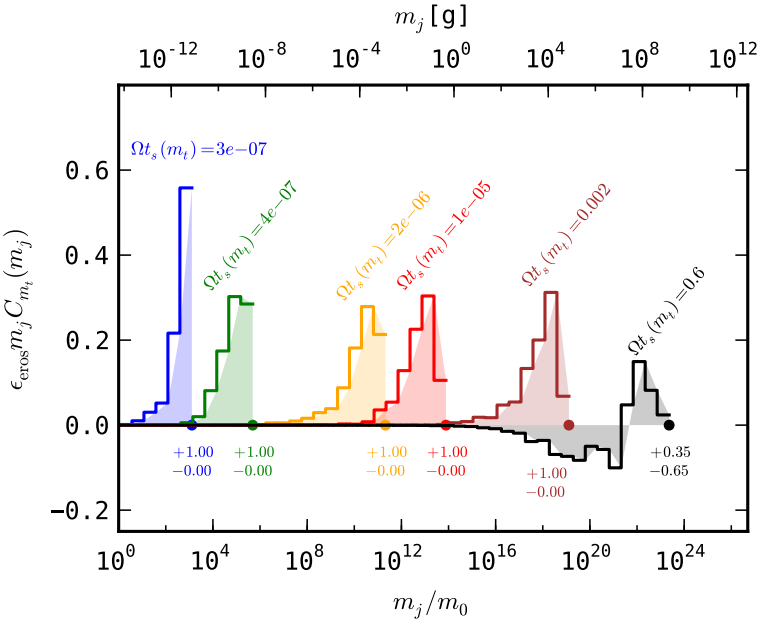

Figure 4.10: Projectile distribution mass functions for simulation E1, constructed for the *maximum* masses (m_t = •) at various times. Colors and times correspond to Figure 4.9. For each distribution, the stopping time of the m_t-particle is given, and the weights of the total positive and negative area are plotted. The distributions have been normalized in such a way, that the absolute sum of the contributions equals 1.

positive and negative. Figure 4.10 shows the distribution for one of the simulations of Figure 4.9 (colors correspond to the same times). When we examine the right-most projectile mass distribution, corresponding to a time $t = 10^4$ yr, it is immediately clear how erosion affects the evolution of particles with $\Omega t_s \sim 1$. While these aggregates grow by collisions with similar-sized bodies, they lose mass by colliding with particles that have a mass below $10^{-2} m_t$. This could have been predicted by looking at Figure 4.2, from which it is clear that the highest velocities are attained between particles with mass ratios well below unity. The importance of this erosion however, depends on the current mass distribution, and can only be tested through dedicated simulations like the ones presented here. Since the area under the negative part of the projectile distribution outweighs the positive part, the erosion is so effective that it stops the growth of the largest bodies, resulting in the behavior seen in Figure 4.9.

We define a parameter ζ using the positive and negative areas under the projectile mass distributions

$$\zeta = \frac{\sum C_+ - \sum C_-}{\sum C_+ + \sum C_-}, \tag{4.34}$$

with $\sum C_+$ and $\sum C_-$ the sums of the positive and negative part of the projectile mass

distribution respectively. The parameter ζ ranges from 1 (no erosion) to -1 (only erosion), and equals 0 when there is a balance between growth and erosion.

The top panel of Figure 4.11 shows the evolution of ζ for the most massive particle during one of the simulations of Figure 4.9, plotted as a function of Ωt_s of the maximum mass. Early on, there is no erosion present and $\zeta = 1$, but as the largest bodies grow towards $\Omega t_s = 1$, erosion increases and ζ drops. When $0 < \zeta < 1$, the massive particles still grow faster then they are eroded, but the erosion can be significant in that it results in the creation of more small particles, thus increasing its destructive effect. When $\zeta < 0$, erosion dominates over growth and the most massive particles are loosing considerable mass. This causes the curve in Figure 4.11 to turn around. As bodies shrink, there is less erosion and ζ increases again. A quasi steady-state is reached with ζ just below unity and $\Omega t_s(m_{\rm max}) \sim 0.6$. The reason $\zeta \neq 0$ during the steady state, is that it is not the same particle that is the most massive at all times. Instead, particles take turn at being the most massive body. Since the largest particles are stuck at a mass and size for which drift is fastest, they will move radially towards the central star. For this combination of parameters, we conclude that growth beyond the drift barrier is impeded by erosion.

The other panels of Figure 4.11 show similar plots but for different erosion threshold velocities. For $v_{\rm eros} = 40$ m s^{-1} (middle panel), erosion is less efficient and the largest bodies grow to $\Omega t_s \simeq 10$ before they start to lose mass rapidly. The reason particles can grow larger is twofold. First, the threshold velocity itself is somewhat higher, causing erosion to start for higher masses. Second, since the erosion efficiency is proportional to $(v_{\rm rel}/v_{\rm eros})$, the high-velocity projectile are less efficient in excavating mass from the targets. Both effects together cause the largest mass in the steady state to be about a factor of 10 larger than in the top panel of Figure 4.11. Finally, the bottom panel shows the results for $v_{\rm eros} = 60$ m s^{-1}. This is a special case, since now the erosion threshold velocity can only be reached around $\Omega t_s = 1$, with radial drift, azimuthal drift, and turbulence contributing (see Figure 4.2). Indeed, erosion is strongest around $\Omega t_s = 1$, but it is inefficient and ζ never drops below 0. When $\Omega t_s > 20$, erosion reappears, as a result of smaller particles drifting into the larger bodies, but since $\zeta \sim 1$, bodies can continue to grow relatively unaffected.

Variation in porosity

One of the biggest advantages of the Monte Carlo method is that aggregate mass and porosity are treated truly independently. In other words, aggregates of identical mass can have a very different porosity. However, the collision model used in this work immediately implies that the spread in porosities (for a given particle mass) will be narrow, when sticking collisions dominate the evolution. For example, the collision model, at the moment, does not include an impact-parameter dependence in collisions, or a random component in the relative velocity. As a result, collisions between particles with certain properties always occur at the same relative velocity, and always result in the same collision product(s). Moreover, when gas compaction (or self-gravity compaction) limits the porosity of an aggregate, bodies will evolve along $P_c = P_{\rm gas}$ (or $P_c = P_{\rm grav}$), according to Equations 4.15 and 4.16. As a result, mass-porosity relations as shown in Figure 4.8

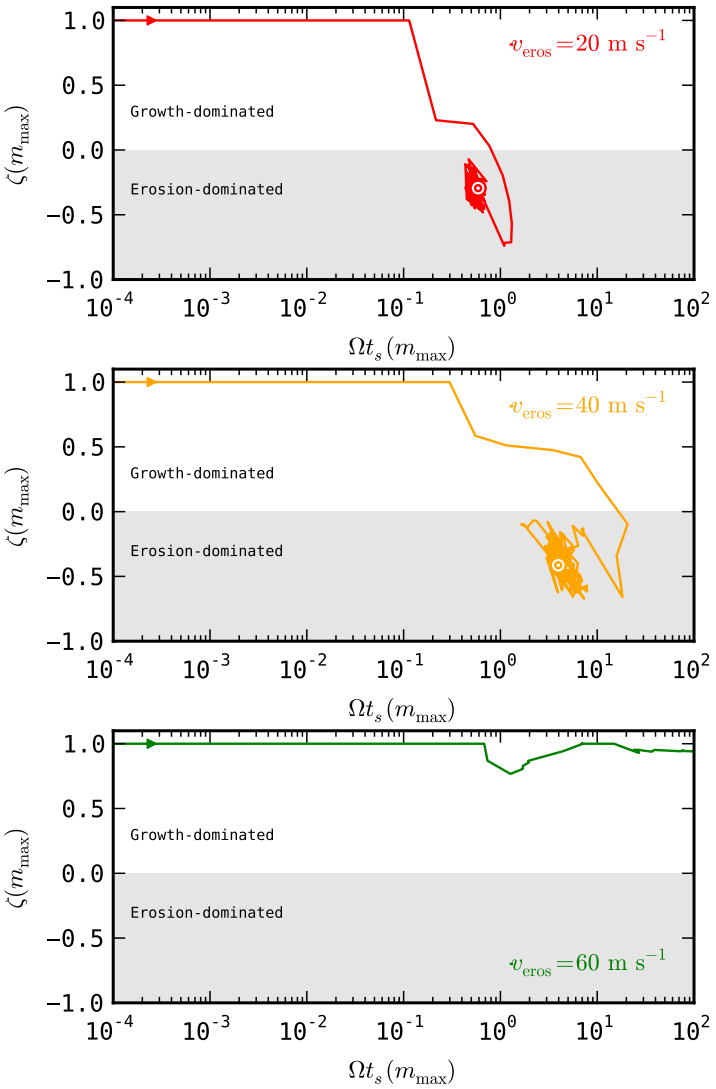

Figure 4.11: Evolution of $\zeta(m_{\rm max})$ for erosive simulations with $v_{\rm eros} = 20, 40, 60$ m s^{-1} as a function of $\Omega t_s(m_{\rm max})$, showing the impact of erosion on the ability of the largest bodies to grow. In the upper two panels, the steady-state is indicated by the ◎-symbol.

accurately represent the internal structure of the majority of aggregates.

This picture changes when erosion starts to play a role. Figure 4.12 shows the evolution of the properties of each family in one of the E1 simulations. We note that each dot corresponds to a single family, and that the total masses and number of family members

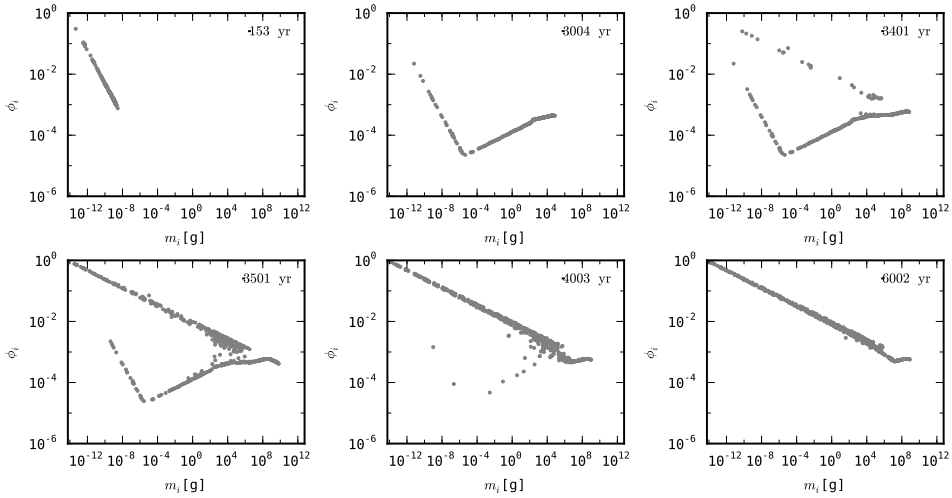

Figure 4.12: Masses and filling factors of all unique families at different times, for simulation E1. One dot corresponds to one family, and does not provide information about the total mass or number of members in that family.

can vary significantly between families. Nonetheless, Figure 4.12 gives a good indication of the spread in porosity. For the reasons described above, the spread in porosity is very small during the first 3000 years of the evolution. After 3400 years, the first erosive collisions have occurred, and created a population of fragments with a fractal dimension set by the parent body. At this point, the porosity distribution becomes bimodal, and the assumption of a single porosity parameter - which only depends on aggregate mass - is untenable. Later, after ∼6000 years, the original population of aggregates, whose porosity was set by their growth history, has disappeared. A steady-state is reached in which the internal structure of the fragments is dominated by the porosity of the particles that act as targets for erosion, i.e., the large bodies with $\Omega t_s \sim 1$.

4.5 Semi-analytical model

The evolution of the mass-dominating particles can be captured in a simple semi-analytical model. Assuming the entire dust mass is located in particles of identical mass m_p, the growth rate can be written as (Okuzumi et al. 2012)

$$\frac{\mathrm{d}m_p}{\mathrm{d}t} = \frac{\Sigma_d}{\sqrt{2\pi}h_d}\sigma_{\mathrm{col}}v_{\mathrm{rel}}. \tag{4.35}$$

The collisional cross section depends directly on the particle porosity, and the relative velocity and dust scale height depend on ϕ through the particle stopping time. As a simple model for the aggregate's internal structure, we assume the aggregates initially grow with

a constant fractal dimension of ∼2, until the kinetic energy in same-sized collisions exceeds $E_{\rm roll}$. After that, the internal structure can be calculated through Eq. 31 of Okuzumi et al. (2012), but in practice is always dominated by the gas/self-gravity compression of Kataoka et al. (2013a), see Sect. 4.2.4.

This approach, similar to Kataoka et al. (2014, Sect. 5.3), is valid when particles grow primarily through collisions with similar-sized particles. This is valid in most regimes, but not true in the first turbulence regime. Here, relative velocities between identical particles are suppressed, and aggregates grow by collecting smaller particles. However, it can be shown that in this regime the growth timescale is approximately constant (Okuzumi et al. 2009). Hence, we will assume that $t_{\rm grow}$ is constant in the regime where turbulence dominates $v_{\rm rel}$, and $t_s < t_\eta$.

At the same time, the radial drift of the particles is governed by

$$\frac{{\rm d}R}{{\rm d}t} = -v_{\rm drift}, \tag{4.36}$$

with the drift velocity a function of Ωt_s. Assuming a fixed dust to gas ratio of 10^{-2} throughout the disk, we can solve Equations 4.35 and 4.36 to obtain the evolution of the vertically integrated peak mass. Catastrophic fragmentation is taken into account by setting $({\rm d}m_p/{\rm d}t) = 0$ when $v_{\rm turb} > v_{\rm frag}$ for two particles of mass m_p. Figure 4.13 shows lines along which the dust evolves, starting from $m = m_0$ at various locations in the disk. The left plot shows the results for compact growth (i.e., $\phi = 1$ at all times), after 10^6 yr. (For the compact case, we have temporarily set $v_{\rm frag} = 10$ m s^{-1}.) Initially, growing aggregates are not moving radially, resulting in vertical lines in Figure 4.13. As the particles' Stokes numbers increase, collision velocities and drift speeds increase. In the inner regions of the disk, the maximum size is limited by fragmentation through same-sized collisions. Particles cannot grow larger than ∼cm, and will inevitably drift inwards. In the intermediate region, from 20 − 100 AU, the fragmentation velocity is not reached. Here, the maximum size is set by radial drift. In the outermost disk (beyond 10^2 AU), growth is very slow because of the low dust densities, and 10^6 yr is not enough to reach the size necessary to start drifting. The general behavior is identical to what is observed in full compact coagulation models (see Figure 3 in Testi et al. 2014).

The gray lines in the right-hand panel of Figure 4.13 show the results of the semi-analytical model for porous growth, where ϕ is set by collisional, gas pressure, and self-gravity compaction, assuming perfect sticking. Since we are assuming the m_p particles carry the total dust mass, we do not have any information about the mass-distribution of smaller particles. Nonetheless, we can mimic the effect of effective erosion, by setting $({\rm d}m_p/{\rm d}t) = 0$ when the relative velocity between the mass dominating particle and small projectiles (taken to be monomers) exceeds $v_{\rm eros}$. The black solid lines in the right panel of Figure 4.13 show the results for $v_{\rm eros} = 40$ m s^{-1}, while the red lines indicate results for the peak mass of the full Monte Carlo models for the same erosion threshold velocity (although that the maximum mass reached in these models can be a factor of ∼10 larger). We have also included a full model run at 200 AU, which we evolved for 10^6 yrs. The results of the semi-analytical model agree with the simulations of the previous section remarkably well.

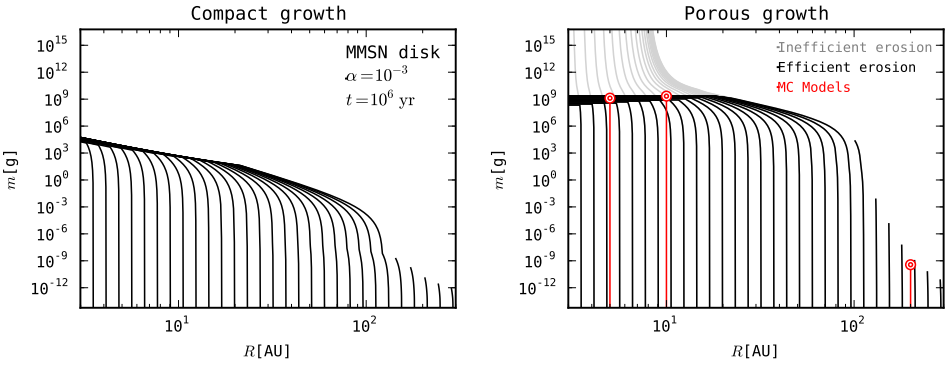

Figure 4.13: Evolution of $m_p(t)$ and $R(t)$ for dust coagulation as obtained from the semi-analytical model (Equations 4.35 and 4.36), for an MMSN disk and $\alpha = 10^{-3}$. Lines indicate different starting conditions $R(t = 0)$, and are evolved for 10^6 yrs. *Left:* Compact growth: $\phi = 1$ at all times, and $v_{\rm frag} = 10$ m s^{-1}. *Right:* Porous growth: the internal structure of the aggregates is set by hit and stick growth, followed by collisional compaction or gas and self-gravity compaction. Grey lines have no erosion, while black lines show the results for $v_{\rm eros} = 40$ m s^{-1}. Colored lines and ◎-symbols indicate the evolution and steady state peak mass obtained through local Monte Carlo simulations (Sect. 4.4.2).

4.6 Discussion

From the maximum sizes fluffy aggregates can reach at a given location, we identify three zones in the protoplanetary disk:

- **3 – 10 AU**: Assuming perfect sticking, the combination of Stokes drag and enhanced collisional cross sections allows the porous aggregates in the inner disk to out-grow the radial drift barrier, and reach planetesimal sizes without experiencing significant drift. However, when erosion is efficient, mass loss in erosive collisions stalls the growth around $\Omega t_s \sim 1$, preventing the porous aggregates from crossing the radial drift barrier (Figure 4.11).

- **10 – 100 AU**: At intermediate radii growth timescales increase and radial drift takes over, even before aggregates reach sizes and stopping times that allow erosive collisions to take place.

- **>100 AU**: In the outer disk, the disk lifetime is not long enough for particles to grow to sizes where significant drift occurs. In the porous growth scenario, aggregates this far out are in the hit-and-stick regime, and their surface-to-mass ratio does not change when they gain mass. As a result, hardly any drift is visible. In the compact case, an increase in mass automatically results in a decrease in the surface-to-mass ratio, and the onset of radial drift is already visible for very low particle masses.

For erosion to start, the collision velocity between target and projectile needs to exceed $v_{\rm eros}$. In the limit where the projectiles are monomers that couple to the gas extremely well, this collision velocity equals the relative velocity of the large bodies with respect to the gas. When the largest particle has $\Omega t_s \gg 1$, it moves on a Keplerian orbit, and $v_{\rm dg} \simeq \eta v_K$, while bodies with $\Omega t_s = 1$ have a slightly larger velocity with respect to the gas (Weidenschilling 1977a). For the disk model employed in this work (Sect. 4.2.1), the quantity ηv_K does not depend on R, and thus the maximum drift speed is constant though out the disk. It is clear then from Eq. 4.33 that growing aggregates in colder disks (lower c_s), or disks with a (locally) shallower gas density profile might suffer less from erosion.

It is clear from Figure 4.11 that the size of $v_{\rm eros}$ is an essential parameter: its value, together with ηv_K, determines whether growth beyond $\Omega t_s = 1$ is possible or not. Unfortunately, the value of $v_{\rm eros}$, or even its relation to $v_{\rm frag}$, is not accurately known for the large and highly-porous icy bodies in question (Sect. 4.2.3). Numerical investigations, showing conflicting trends for erosion efficiency with mass ratio, often employ monodisperse grain sizes (e.g., Seizinger et al. 2013; Wada et al. 2013), and the threshold velocities depend almost linearly on the grain radius (Eq. 4.12), a parameter which itself is not well constrained. At the same time, the only available experimental work on erosion for ices used a distribution of grain sizes (Gundlach & Blum 2015). In addition, both numerical and experimental studies are restricted to sizes $\lesssim$mm and porosities $\gtrsim 10^{-1}$, and cover a soberingly small portion of the parameter space encountered in this work (e.g., Figure 4.8). Future studies, numerical as well as experimental, are encouraged to elucidate these matters, and constrain the threshold for erosion and its dependence on target/projectile sizes and porosity. Finally, we assume that material that is eroded locally is removed from the target. In reality, the fate of the fragments will be determined by the local gas flow and the velocity with which they are ejected. For very porous targets, the gas flow through and around the surface of the target might result in these fragments being re-accreted (Wurm et al. 2004). If efficient, this re-accretion might be a way to alleviate the destructive influence of erosive collisions. On the other hand, the flow through a body is likely to be insignificant, unless it is extremely porous (Sekiya & Takeda 2005).

So far we have assumed that while erosion can play an important role, catastrophic fragmentation does not occur. The maximum velocity between same-sized bodies is reached for $\Omega t_s = 1$, and equals $\sim(3/2)\alpha^{1/2} c_s$ (Eq. 4.11). Since the sound speed diminishes for increasing radii, this velocity is highest in the inner disk. For typical turbulence strengths ($\alpha \lesssim 10^{-3}$) and small icy monomers, this velocity will not exceed the fragmentation threshold velocity (Eq. 4.12), and, especially in the outer disk, fragmentation of icy bodies through catastrophic fragmentation is very unlikely. However, if *all* collisions result in sticking, small particles ($\lesssim 100\,\mu$m) are removed from the protoplanetary nebula very rapidly, contradicting observational constraints (Dullemond & Dominik 2005; Dominik & Dullemond 2008). Drift-induced erosion can alleviate these issues, since the maximum drift velocity is high throughout the entire disk.

In this work, we have assumed collisions below the fragmentation threshold to result in perfect sticking, i.e., the mass of the resulting aggregate equals the sum of both colliding masses. However, even for collisions below the fragmentation threshold velocity, a significant amount of mass may be ejected during a collision, especially if the colli-

sion occurs at a large impact parameter (Paszun & Dominik 2009; Wada et al. 2013). An advantage of a Monte Carlo model approach like the one presented here, is that it is relatively straightforward to include an additional random number to determine, for example, the impact parameter. The difficulty lies in obtaining a collision model that describes the collisional outcome as a function of this parameter. A good start would be the work of Wada et al. (2013), who show the growth efficiency as a function of impact parameter (Figure 4). Basically, head-on collisions promote growth, while collisions with a large impact parameter result in little mass gain. Unfortunately, much less is known about the porosities of the resulting aggregates.

At the heart of the model of Sect. 4.3 lies the assumption that an aggregate is adequately described by two quantities: its mass and (average) porosity. While this represents a considerable improvement on the compact coagulation assumption, a single average porosity does not allow a complex internal structure of the aggregates. For small grains, the accuracy of this assumption will depend on their collisional history. For example, one can imagine a porous aggregate with a denser outer shell being formed if the aggregate is compacted through many collisions with small mass ratios (Meisner et al. 2012). Such a compact rim will hardly alter the aggregate's average porosity, but can influence its sticking and erosion behavior (Schräpler & Blum 2011). Likewise, gas- and self-gravity compaction need not result in a homogenous internal structure. With instruments such as CONCERT on board ESA's Rosetta and Philae capable of probing the internal structure of large Solar System objects, studies focussing on the internal structure of the larger bodies, as determined by its growth and compaction history would be very interesting. The Monte Carlo method developed in this paper would be suitable for such studies, since adding parameters describing the aggregates is relatively straightforward.

4.6.1 Future work and implications

Pebble accretion

A novel idea in the field of planet formation is the process of pebble accretion, where protoplanets grow very efficiently by accreting small pebbles (Ormel & Klahr 2010; Lambrechts & Johansen 2012, 2014; Kretke & Levison 2014). These models rely on the radial influx of particles drifting in from the outer disk. As in the compact case, porous growth leads to the creation of rapidly drifting bodies in the region between 10 and 10^2 AU (Figure 4.13). While the Stokes numbers of these particles are similar to the drifting pebbles in the compact case, their masses, sizes, and porosities can differ by many orders of magnitude (see also Figure 4.14). In addition, the drag regime that the drifting bodies experience differs from the compact case (Figure 4.1). Future studies are needed to address the effect of these factors on the efficiency of pebble accretion.

Streaming instability

While – depending on the critical erosion velocity – rapid coagulation into masses as large as planetesimals might be prevented by erosive collisions, the conditions created

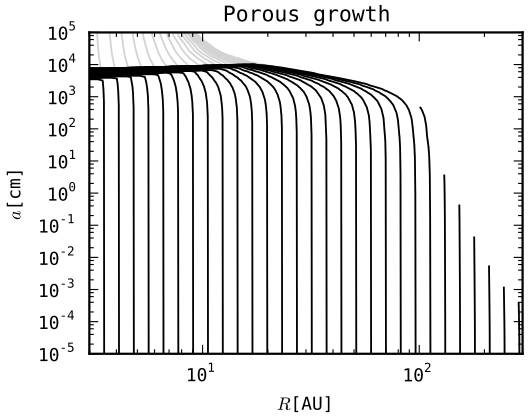

Figure 4.14: Same as the right-hand plot of Figure 4.13, but with aggregate size on the vertical axis.

by this process might be favorable for triggering planetesimal formation by streaming instability (Youdin & Goodman 2005; Johansen et al. 2007; Bai & Stone 2010a,b). To trigger streaming instability, the majority of mass needs to reside in particles with high Stokes numbers; the mid plane dust to gas ratio has to be close to unity; and the local vertically integrated dust-to-gas ratio needs to exceed ∼0.03 (Drążkowska & Dullemond 2014). The first two conditions can be studied with simulations like the ones presented in this work. For example, for the steady-state distribution reached for $v_{\rm eros} = 40$ m s^{-1} at 5 AU for $\alpha = 10^{-3}$, approximately 50% of the dust mass resides in particles with $\Omega t_s > 10^{-2}$, and the mid plane dust-to-gas ratio is $\sim 10^{-1}$. For weaker turbulence, the mid plane dust-to-gas ratio will be increased further, since $h_d \sim \alpha^{1/2}$ (Eq. 4.6). Because our simulations are local, the vertically integrated dust-to-gas ratio stays constant at 10^{-2}. To fulfill the third condition, the dust-to-gas ratio either has to be larger from the beginning, or must increase by material drifting in from the outer disk. To study this, a global model is required, that calculates the evolution of the dust surface density in the presence of radial drift and erosion. In conclusion, drift-induced erosion appears to be a robust way of concentrating mass around $\Omega t_s \sim 1$, and is expected to create conditions favorable for streaming instability.

The breakthrough case

For compact silicate bodies in the inner disk, bouncing and fragmentation are very effective in stopping growth at mm-cm sizes. The breakthrough scenario, in which a small number of lucky particles still manages to gain mass, might render further growth possible (Windmark et al. 2012b; Garaud et al. 2013). The total mass fraction of these lucky particles can be extremely small, making this a challenging process to model for both differential and Monte Carlo methods (Drążkowska et al. 2014). The distribution method used in this work, as outlined in Sect. 4.3.3, is capable of resolving the entire mass distri-

bution, including parts that contribute very little to the total dust mass, and appears to be suitable for studying the breakthrough case.

Opacities of porous grains

The optical properties of dust distributions resulting from porous growth are very different from populations containing exclusively solid particles. Not only are the mass distributions themselves different (e.g., Figure 4.13), but also the scattering and absorption opacities of the individual grains are affected significantly by porosity (Kataoka et al. 2014; Cuzzi et al. 2014). For simple dust mass distributions, the effect of grain porosity on the appearance of protoplanetary disks has been investigated by Kirchschlager & Wolf (2014). Combining self-consistent coagulation models - including erosion and fragmentation - with porosity-dependent dust opacities will reveal the full impact porous growth has on the appearance of protoplanetary disks.

4.7 Conclusions

Porous growth is very different from compact growth (Figure 4.13). For example, porous particles have larger collisional cross sections than compact particles of the same mass. More importantly, the aerodynamical properties of porous aggregates can differ greatly from those of compact particles (Figure 4.1), causing differences in relative velocities (Figure 4.2), vertical settling, and radial drift.

We have modeled the coagulation of porous icy particles in the outer parts of protoplanetary disks, tracing the evolution of the mass and filling factor of the individual aggregates in time. We consider compaction through collisions, gas pressure, and self-gravity (Figure 4.8), and include a physical model for erosive collisions (Sects. 4.2.3 and 4.2.3). The main findings of this work are:

1. Porous icy aggregates can outgrow the radial drift barrier in the inner ∼10 AU, despite increased growth timescales resulting from gas- and self-gravity compaction, if the perfect sticking assumption holds (Figures 4.7 and 4.13). This is in agreement with Okuzumi et al. (2012) and Kataoka et al. (2013b).

2. While the maximum collision velocity between similar particles ($\sim\alpha^{1/2}c_s$) typically does not exceed the critical fragmentation threshold velocity for icy bodies, the velocity between drifting aggregates (with $\Omega t_s \geq 1$) and smaller bodies is much larger ($\sim\eta v_\mathrm{K}$), and can exceed the critical threshold velocity for erosion (Figure 4.2).

3. In these cases, we find that the mass loss through erosive collisions can balance the growth through same-size collisions, halting the growth of the largest bodies (Figures 4.10 and 4.11). In our local simulations, this results in a steady-state where the largest bodies have $\Omega t_s \sim 1$, and the porosity of the small fragment distribution is dominated by the fact that all fragments have at some point been part of these

large eroded particles (Figures 4.9 and 4.12). Only for the highest erosion threshold velocity we considered ($v_{\rm eros} = 60$ m s^{-1}) do the aggregates with $\Omega t_s \sim 1$ manage to gain mass and grow through the drift barrier.

4. A simple semi-analytical model (Sect. 4.5) accurately describes the growth and drift behavior of the mass-dominating bodies. While no information is obtained about the dust mass distribution, such an approach is very useful for investigating how the size of the largest bodies depends on disk parameters such as the total disk mass, turbulence strength, or dust-to-gas ratio; and aggregate properties such as monomer size and erosion/fragmentation threshold velocities.

Acknowledgements

Dust studies at Leiden Observatory are supported through the Spinoza Premie of the Dutch science agency, NWO. S.K. would like to thank C.P. Dullemond, J. Drążkowska and T. Birnstiel for useful discussions, and B. Okuzumi for comments and helping with the comparison to his work. The authors thank B. Gundlach and J. Blum for sharing a version of their manuscript. C.W.O. acknowledges support for this work by NASA through Hubble Fellowship grant No. HST-HF-51294.01-A awarded by the Space Telescope Science Institute, which is operated by the Association of Universities for Research in Astronomy, Inc., for NASA, under contract NAS 5-26555.

5

A panoptic model for planetesimal formation

S. Krijt, C. W. Ormel, C. Dominik, and A. G. G. M. Tielens
Astronomy & Astrophysics, to be submitted

Abstract

The journey from dust particle to planetesimal is a complex one, involving processes acting on very small scales (the physics governing the sticking and restructuring of porous aggregates) to the largest scales (the global structure of the turbulent protoplanetary nebula). Considering these processes simultaneously is essential when studying planetesimal formation. The goal of this work is to quantify where and when planetesimal formation can occur as the result of porous coagulation of realistic icy grains, and to understand how the process is influenced by the properties of the protoplanetary disk. We develop a novel, global, semi-analytical model for the evolution of the mass-dominating dust particles in a turbulent protoplanetary disk, that takes into account the evolution of the dust surface density, while preserving the essential characteristics of the porous coagulation process. The method is used to study the conversion of initially microscopic dust into planetesimals in disks around Sun-like stars. Disk parameters such as mass, size, metallicity, and temperature are varied to constrain regions where planetesimals can form, either through coagulation, or through inducing streaming instability (SI). For highly-porous ices, unaffected by collisional fragmentation and erosion, rapid growth to planetesimal sizes is possible in a zone stretching out to 20 AU for massive and dust rich disks. When porous coagulation is limited by erosive collisions, the formation of planetesimals through direct coagulation is not possible, but the creation of a large population of aggregates with Stokes numbers close to unity might trigger SI. We find that reaching conditions necessary for SI is possible in the inner regions of cold disks, or disks with a super-Solar

metallicity, but only if the turbulence is sufficiently weak. For perfectly sticking ices, planetesimal formation is a very efficient progress, and, depending on the turbulence strength, a significant fraction of the available dust mass is converted into planetesimals within 10^6 yrs. If growth is frustrated by erosive collisions, conditions suitable for SI could be reached for weakly turbulent disks, but the absence of dust pile-ups in the case of particles coagulating in a smooth nebula limits this possibility to either dust-rich or very cold disks.

5.1 Introduction

Protoplanetary disks are believed to be the sites of planet formation. In these disks, the coagulation of microscopic dust particles, already present in the interstellar medium, into kilometer-size planetesimals constitutes the first - and arguably least understood - step in the assembly of fully-grown planets (e.g., Testi et al. 2014; Johansen et al. 2014). Initially, the dust aggregates, held together by surface forces, grow by sticking to each other in gentle, low-velocity collisions (e.g., Kempf et al. 1999). As a result, aggregates form very open, porous structures. As the aggregates gain mass and their relative velocities increase, collisions become more energetic, leading to compaction and ultimately catastrophic fragmentation (Dominik & Tielens 1997; Blum & Wurm 2000). A second hurdle is presented in the form of the radial drift barrier: particles with certain aerodynamic properties decouple from the gas, and drift radially on short timescales (Whipple 1972; Weidenschilling 1977a; Brauer et al. 2008b).

In the inner few AU of the protoplanetary disk, dust grains consist mainly of silicates, and these aggregates bounce of each other in collisions, or even disrupt completely upon impact, at collision velocities above several m s^{-1} (Blum & Wurm 2008; Güttler et al. 2010). These collisional processes limit the growth beyond a centimeter or so in the inner disk (Brauer et al. 2008b; Zsom et al. 2010; Windmark et al. 2012a).

Outside the snow line, located typically at ~3 AU (Min et al. 2011), water ice becomes an important constituent of the dust grains. This is beneficial for growth, because aggregates composed of (mostly) ice are capable of sticking at tens of m s^{-1} (Wada et al. 2009, 2013; Gundlach & Blum 2015). In addition, these icy particles maintain highly-porous structures (Suyama et al. 2008, 2012), making them less likely to bounce in collisions (Wada et al. 2011; Seizinger & Kley 2013), and allowing them to out-grow the radial drift barrier in the inner ~10 AU of the protoplanetary nebula (Okuzumi et al. 2012; Kataoka et al. 2013a). However, the growth of these porous aggregates might be frustrated by high-velocity erosive collisions (Krijt et al. 2015).

Instead of coagulating directly, planetesimals can also be formed through particle concentration mechanisms (Johansen et al. 2014, and references thererin). One promising mechanism is the streaming instability (SI) (Youdin & Goodman 2005; Johansen et al. 2007; Bai & Stone 2010a,b), which can be triggered by creating a dense midplane layer of (partially) decoupled dust particles. Recently, Drążkowska & Dullemond (2014) have defined a set of conditions for SI, and compared them to dedicated models of compact coagulation. They found that in the inner disk, where the growth of silicates is limited by bouncing/fragmentation, particles can not grow to Stokes number large enough for trig-

gering SI. Outside the snow-line however, rapidly-growing highly-porous ice aggregates can grow to large Stokes numbers (Okuzumi et al. 2012), at which point their growth is possibly limited by erosive collisions (Krijt et al. 2015). The possibility of triggering SI through rapid porous coagulation has not yet been investigated, but the mass distributions obtained from erosion-limited porous growth appear very promising (Krijt et al. 2015).

We set out to study the formation of the first generation of planetesimals. Giant planets have not yet formed, hence the protoplanetary disk is smooth. We neglect possible presence of pressure bumps, dead zones, etc., and concentrate on the outer regions where ice dominates the sticking properties. The focus is to understand the evolution of the mass-dominating particles in disks around Sun-like stars, and understand how their evolution influences the dust surface density. Ultimately, the goal is to identify regions in both space and time where the first planetesimals can form, either through direct (porous) coagulation (e.g., Okuzumi et al. 2012) or through coagulation triggering SI (Drążkowska & Dullemond 2014). In order to answer these questions, we develop a global, semi-analytical, panoptic model that captures the evolution of the mass-dominating particles as they grow and drift radially in the protoplanetary disk.

The semi-analytical model is developed in Sect. 5.2. The method allows us to calculate the evolution of global dust surface density together with the masses and porosities of the growing dust particles, capturing processes such as porous growth, radial drift, bouncing/fragmentation and erosion in a way that is accurate as well as easy to follow. In Sect. 5.3 we use this model to study formation of planetesimals through direct coagulation, looking at both compact and porous growth. Then, in Sect. 5.4 we study under which conditions compact and porous growth can lead to conditions suitable for triggering SI. The results are discussed in Sect. 5.5 and the conclusions are summarized in Sect. 5.6.

5.2 Method

We consider a turbulent disk of gas around a $1M_\odot$ star, and focus on the region behind the snow line, where ices are an important part of the solid mass reservoir. The gas disk model (Sect. 5.2.1) assumes a smooth and static disk, with a mass that we will vary between $10^{-3} - 0.2M_\odot$. The method we will use for calculating the dust evolution is based on the semi-analytical model for porous growth of Krijt et al. (2015), which is combined with a new 'dust batch approach' that allows us to probe the evolution of the mass-dominating particles on a global scale, while preserving the essential characteristic of all porous growth process.

5.2.1 Nebula model

Following Lynden-Bell & Pringle (1974); Hartmann et al. (1998b), we adopt a truncated powerlaw for the surface density distribution

$$\Sigma_g = \Sigma_0 \left(\frac{R}{R_c}\right)^{-\gamma} \exp\left[-\left(\frac{R}{R_c}\right)^{2-\gamma}\right]. \tag{5.1}$$

We will vary the power law exponent between $\gamma = 3/2$, appropriate for the Minimum Mass Solar Nebula (MMSN) (Hayashi 1981); and $\gamma = 1$, consistent with observations (Andrews et al. 2009) and accretion disk theory (e.g. Armitage 2010). Disk masses and radii will be varied between $M_D = 10^{-3} M_\odot$ and $0.2 M_\odot$ and $R_c = 30 - 100$ AU, consistent with observational constraints for disks in the Taurus star forming region (Andrews & Williams 2005; Andrews et al. 2013). We adopt temperature structure appropriate for an optically thin disk around a solar type star

$$T = 125 \left(\frac{R}{5 \text{ AU}} \right)^{-1/2} \text{ K}, \tag{5.2}$$

appropriate for an optically thin disk, and in agreement with observational constraints (Andrews & Williams 2005). However, to probe the effect of the disk temperature, we will also consider colder disk models, in which the temperature is reduced by 50% with respect to Eq. 5.2.

Most other quantities are derived, together with assumptions about the turbulence and vertical structure, from Eqs. 5.1 and 5.2. The gas sound speed is given by

$$c_s = \sqrt{k_\text{B} T / m_g}, \tag{5.3}$$

with k_B the Boltzmann constant and $m_g = 3.9 \times 10^{-24}$ g for a mean molecular weight of 2.34. The Kepler frequency equals

$$\Omega = \sqrt{G M_\odot / R^3} = 1.8 \times 10^{-8} \left(\frac{R}{5 \text{ AU}} \right)^{-3/2} \text{ s}^{-1}. \tag{5.4}$$

Assuming an isothermal column, the gas density drops with increasing distance from the midplane z according to

$$\rho_g = \frac{\Sigma_g}{\sqrt{2\pi} h_g} \exp\left(\frac{-z^2}{2 h_g^2} \right), \tag{5.5}$$

with the vertical scale height of the gas $h_g = c_s / \Omega$. The turbulent viscosity is parametrized as $\nu_\text{turb} = \alpha c_s^2 / \Omega$ following Shakura & Sunyaev (1973).

5.2.2 Dust batch approach

At $t = 0$, we distribute a number of 'batches' of dust at different radii r_i in the protoplanetary disk. Each batch represents a swarm of dust particles with identical properties and growth histories. Typically, we will space the batches between 3 and 200 AU. Depending on the spacing of the batches, and the assumed dust density of the protoplanetary disk, a batch holds/represents a total dust mass M_i. The individual dust particles represented by a batch at any given time are assumed to be mono-disperse, and can be described by a particle mass m_i and a particle porosity ϕ_i. These four numbers (the total batch mass, batch location, and dust particle mass and porosity) fully describe the batch at time t. While M_i is constant in time, the other three properties vary in time. The location of the batch is

altered by radial drift, while the properties of the dust (so m_i and ϕ_i) evolve as the result of coagulation.

Using the locations and total masses of the batches, we define the cumulative dust mass

$$M_C(R) = \sum_{i,r_i<R} M_i, \tag{5.6}$$

which gives the total dust mass within a radius R. Using the cumulative mass, we can then obtain the dust surface density as

$$\Sigma_d(R) = \frac{1}{2\pi R} \frac{\mathrm{d}M_C(R)}{\mathrm{d}R}. \tag{5.7}$$

At $t = 0$, the r_i can be chosen arbitrarily (we will distribute them logarithmically), but their masses M_i are then fixed through Eqs. 5.6 and 5.7 and the assumed initial dust distribution. Initially, the dust density is set by the gas density, and $\Sigma_d/\Sigma_g = Z_0$, with $Z_0 \sim 10^{-2}$ the (vertically integrated) 'metallicity'. The dust is assumed to be in compact spherical monomers with radii a_0 and masses $m = m_0 = (4/3)\pi\rho_0 a_0^3$. Being compact spheres, monomers have $\phi = 1$. We use $\rho_0 = 1.4$ g cm^{-3} for icy particles and $\rho_0 = 2.6$ g cm^{-3} for silicate ones. As the batches evolve in time, dust masses and porosities change. In the rest of this section, we explain how we obtain $\dot{m}_i$, $\dot{r}_i$ and the evolution of ϕ_i.

5.2.3 Radial drift

As batches drift in, the radial density distribution batches changes, triggering a modification of the surface density. The radial drift velocity is given by (Weidenschilling 1977a)

$$\dot{r}_i = v_{\mathrm{drift}} = -\frac{2\Omega t_s}{1 + (\Omega t_s)^2} \eta v_{\mathrm{K}}, \tag{5.8}$$

where $v_{\mathrm{K}} = R\Omega$ is the Keplerian orbital velocity, and η can be written as (Nakagawa et al. 1986)

$$\eta \equiv -\frac{1}{2}\left(\frac{c_s}{v_{\mathrm{K}}}\right)^2 \frac{\partial \ln(\rho_g c_s^2)}{\partial \ln R}. \tag{5.9}$$

The drift timescale is defined as $t_{\mathrm{drift}} \equiv (r_i/\dot{r}_i)$ and depends on the masses and porosities of the dust particles through their dimensionless stopping time Ωt_s (see Appendix 5.A).

To test the treatment of radial drift, we run a model without coagulation. Dust particles are assumed to be compact micrometer icy spheres, in a disk with $\alpha = 10^{-3}$. Without coagulation, $\dot{m}_i = 0$ for all batches, and radial drift alone is responsible for changing the dust surface density. The results are shown in Fig. 5.1. Since, for a single grain size, Stokes numbers are largest in the outer part of the disk, particles further out will drift faster. As a result, the outer disk is slowly depleted of dust and pile-ups are created closer in. This picture is consistent with Youdin & Chiang (2004) and Birnstiel & Andrews (2014). The pile-ups are caused by the slowing down of particles as they drift into the more dense inner disk, and are the result of the assumption of a fixed (maximum) size

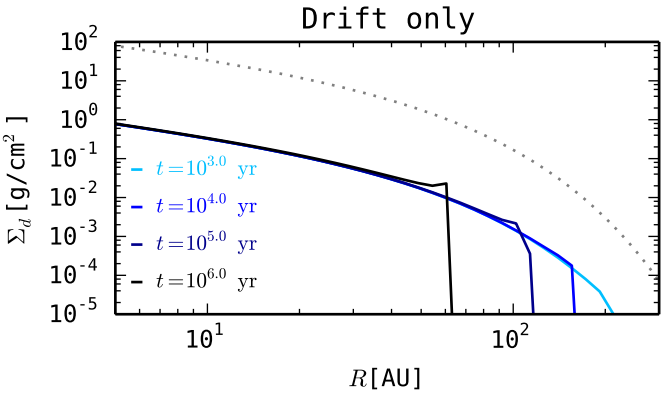

Figure 5.1: Evolution of the dust surface density for the case without coagulation: All dust particles are assumed to be compact micrometer-size silicate particles at all times. The initial metallicity equals $Z_0 = 0.01$ throughout the entire disk, and the dotted line shows the surface density of the gas corresponding to $M_D = 10^{-2} M_\odot$, $\gamma = 1$, and $R_c = 30$ AU.

of the particles. Below we will see that when grain sizes are limited by aerodynamical properties, no such pile-ups are created.

5.2.4 Porous coagulation

The model for porous coagulation is based on the semi-analytical model of Krijt et al. (2015, Sect. 5). Here, we briefly revisited the model, and describe how we take into account bouncing, fragmentation, and erosive collisions.

Growth timescales and porosity

For a mono-disperse dust population, the growth rate is given by

$$\dot{m}_i = \frac{\Sigma_d}{\sqrt{2\pi} h_d} \sigma_{\rm col} v_{\rm rel}, \tag{5.10}$$

with h_d the dust scale height, $\sigma_{\rm col}$ the collisional cross section, and $v_{\rm rel}$ the relative velocity between same-size dust particles. Appendix 5.B describes how the relative velocity is calculated. The growth timescale is then defined as

$$t_{\rm grow} \equiv \frac{m}{\dot{m}}. \tag{5.11}$$

The (relative) dust scale height is given by (Youdin & Lithwick 2007)

$$\frac{h_d}{h_g} = \left(1 + \frac{\Omega t_s}{\alpha} \frac{1 + 2\Omega t_s}{1 + \Omega t_s}\right)^{-1/2}. \tag{5.12}$$

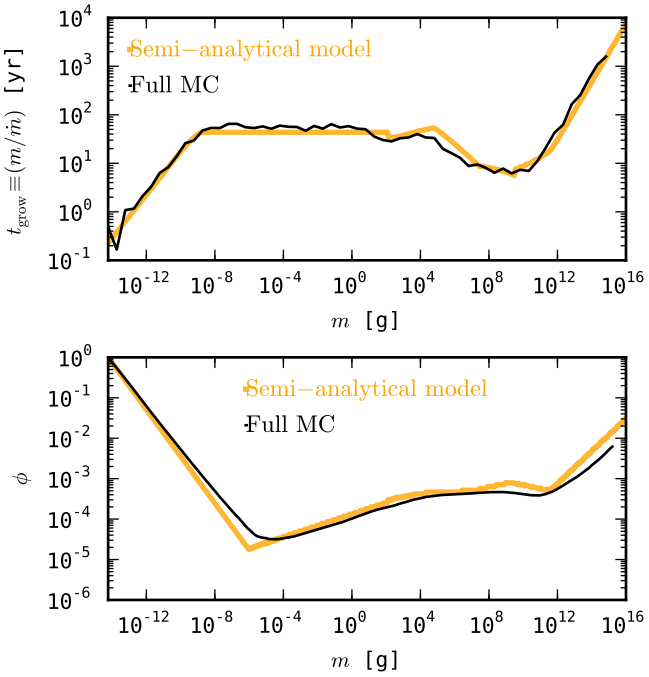

Figure 5.2: Comparison between semi-analytical model of Sect. 5.2.4 and full Monte Carlo (MC) model of Krijt et al. (2015) for icy aggregates coagulating locally at 5 AU in an MMSN disk with $\alpha = 10^{-3}$. Aggregates start as 0.1-μm monomers, and perfect sticking is assumed. *Top:* Growth timescale as a function of particle mass. *Bottom:* Volumetric filling factor as a function of mass.

The dust scale height depends on the particle Stokes number Ωt_s, with the stopping time t_s a function of the particle mass and porosity, and the local gas properties. The evolution of the particle porosity ϕ_i is not obtained with a time derivative. Instead, one can think of the porosity being set by the particle mass: $\phi_i = \phi(m_i)$. This is particularly true when the porosity is limited by gas compaction or self-gravity. Earlier in the evolution, the porosity is influenced predominantly by a dust particle's collisional history. Appendix 5.C describes the determination of $\phi(m_i)$ in more detail.

At the heart of the semi-analytical lies the assumption that the local dust population can be approximated by a mono-disperse grain population, with a single porosity. This assumption is valid when *i)* the full mass distribution has a clearly defined peak mass and porosity; and *ii)* the growth (and porosity-evolution, if dominated by collisions) of the peak-mass grains is mainly due to collisions with similar-size particles. These assumptions generally hold for populations resulting from porous coagulation (e.g., Ormel et al. 2007; Okuzumi et al. 2012; Krijt et al. 2015). To test assumption *ii)*, we compare the semi-analytical model the full Monte Carlo model of Krijt et al. (2015). For this comparison, drift is switched off ($\dot{r} = 0$), and perfect sticking is assumed. The results are shown

in Fig. 5.2. The trends in growth rates and internal density evolution obtained in from the full models are reproduced remarkably well by the semi-analytical model.

Bouncing, fragmentation, and erosion

Bouncing and fragmentation are modeled in the same way: by setting $\dot{m}_i = 0$ whenever the relative velocity between same-size particles exceeds the fragmentation or bouncing threshold velocity. Efficient erosion on the other hand, is taken into account by setting $\dot{m}_i = 0$ when the relative velocity between *dissimilar* particles exceeds the erosion threshold velocity. Specifically, we calculate the relative velocity between batch particles and single monomers, and compare that to the erosion threshold velocity.

When further growth is impeded by bouncing, fragmentation, or erosion, we will assume the dust particle porosity is constant in time as well. In the bouncing case in particular, this assumption might not be accurate because significant compaction through bouncing collisions is expected (Güttler et al. 2010; Zsom et al. 2010).

5.2.5 Combining drift and coagulation

Having tested drift and coagulation separately, we can now combine the two. To calculate drift and coagulation self-consistently, one needs to solve Eqs. 5.7, 5.8, and 5.10 simultaneously, while keeping track of the particle porosity in every batch. We do this by using a global time step Δt that is determined by the shortest drift- or growth-timescale present. We make sure $\Delta t \leq \min(0.5t_{\rm grow}, 0.05t_{\rm drift})$. In practice, this means one is limited by the (relatively short) growth timescales in the inner disk, until the dust there has drifted inside the snow line, cannot coagulate further because of destructive processes (bouncing/fragmentation or erosion), or has been converted into planetesimals.

Should the particle mass reach $m_i \geq m_p$, we call the particles planetesimals. At this point, we no longer calculate the evolution of these bodies, but rather treat the planetesimal formation process as finished. In this work, we will use $m_p = 10^{16}$ g, corresponding to a compact object of $\sim$ km in size. Once particles become planetesimals, we consider planetesimal formation to have been successful and set $\dot{m}_i = \dot{r}_i = 0$ for that batch. Also, their masses no longer contribute to Σ_d, but a separate planetesimal-surface-density Σ_p is calculated (a similar way as Σ_d in Eq. 5.7). Similarly, when a batch drifts inside of $R = R_{\rm min}$, we stop following it, since we are interested mainly in the region outside of the snow line. Conservatively, we place $R_{\rm min} = 1$ AU. We use between 10^2 and 10^3 batches per simulation. Using a larger number of batches did not result in significant changes of the resulting planetesimal populations.

5.3 Planetesimal formation through coagulation

For this section, we focus on the coagulation process and do not take into account effects of SI. To illustrate the difference between compact and porous growth, we first study the

coagulation of compact silicates (Sect. 5.3.1), and then discuss porous coagulation of ices in Sect. 5.3.2.

5.3.1 Compact growth

For compact growth, we start with submicron silicate particles and assume the porosity of the aggregates is always $\phi = 1$. In addition, we impose a fragmentation threshold velocity $v_{\rm frag} = 5$ m s^{-1} (Güttler et al. 2010; Wada et al. 2013). We assume a total disk mass of $M_D/M_\odot = 10^{-2}$, and (initial) metallicity of $Z_0 = 0.01$ throughout the disk[1]. The turbulence is constant throughout the disk and parameterized by $\alpha = 10^{-3}$.

The resulting surface density evolution is shown in the top panel of Fig. 5.3. At $t = 0$, the metallicity $Z_0 = 0.01$ throughout the disk, and the dust density follows the gas surface density (dotted line). After 10^3 yr not much has changed, as particles have not had enough time to grow large. After 10^4 and 10^5 yr, respectively, dust in the inner ∼10 and ∼30 AU has grown large enough to drift efficiently, and the inner regions become depleted in dust. Finally, after 10^6 yr the entire dust disk is depleted. Since the disk is smooth and cleared from the 'inside-out', no pile-ups are created, contrasting the fixed-size case of Fig. 5.1.

The bottom two panels of 5.3 show the 'lifelines' of a selection of dust batches for the same simulation. Dust particles start as monomers are 0.1 μm, and are evolved for 10^6 yr, close to the typical lifetime of a protoplanetary disk (Haisch et al. 2001). In Fig. 5.3, batches move *up* as their constituent grains gain mass, and to the *left* as they drift inward. The background colors show the history of porosities (middle panel) and Stokes number Ωt_s (bottom panel). Initially, particles couple well to the gas ($\Omega t_s \ll 10^{-3}$) and grow on relatively short timescales. Growth is faster in the inner disk, because both relative velocities and dust spatial densities are largest here. In the compact case however, an increase in particle mass inevitably results in a decrease of the surface-to-mass ratio, and the Stokes numbers increases. Aggregates with a mass of a few grams have $\Omega t_s \sim 1$, and drift inward rapidly. In addition, the largest particles in the inner ∼20 AU suffer from fragmentation, which limits their growth. This picture is as expected for compact growth, and the general trends are in good agreement with full models of compact coagulation (e.g., Okuzumi et al. 2012; Testi et al. 2014).

An alternative way of looking at the evolution of the dust is presented in Fig. 5.4. Here, the lifelines of the dust batches are plotted in terms of space and time. Green shaded regions indicate where $10^{-3} \leq \Omega t_s \leq 1$, and the letters denote current locations of Jupiter, Saturn, Uranus, and Neptune. While the individual lines do not give information about the masses and porosities of the dust particles making up the batch, it is clear growth is fastest in the inner disk, since the particles reach $\Omega t_s = 10^{-3}$ already after 10^3 yr. In the outer disk, around 100 AU, growth towards similar Stokes numbers takes almost 10^6 yr.

5.3.2 Porous growth

Here, we add the porosity evolution as described in Appendix 5.C. Because icy aggregates have high fragmentation threshold velocities (Dominik & Tielens 1997; Wada et al. 2013),

[1] A metallicity of $Z = 0.01$ is referred to as 'Solar'.

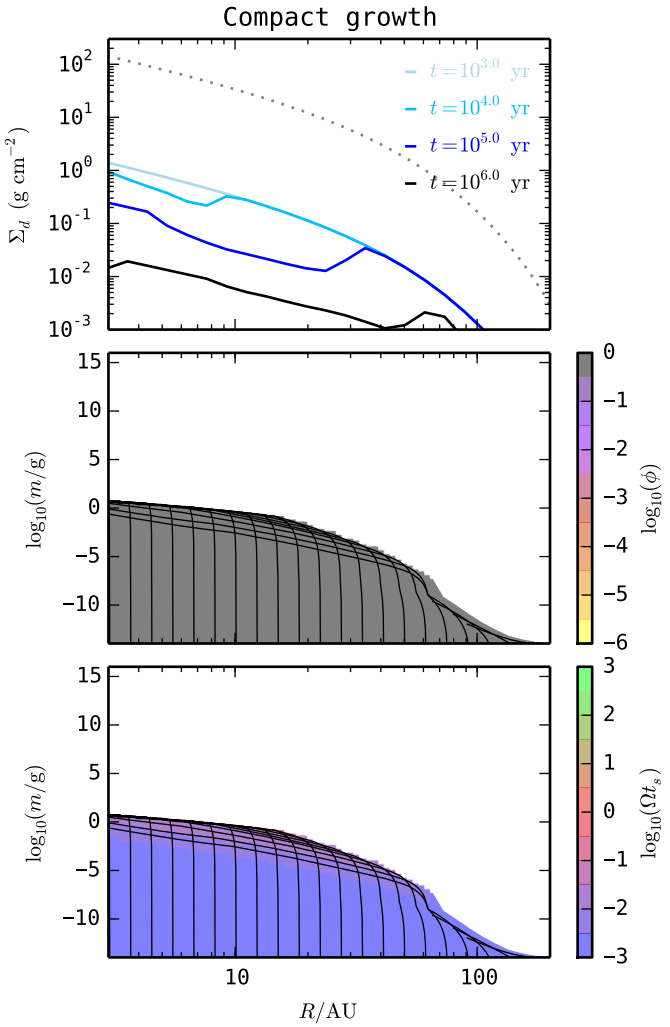

Figure 5.3: Coagulation of compact silicate particles with a fragmentation velocity of 5 m s^{-1}. The disk parameters were $M_D = 10^{-2} M_\odot$, $\gamma = 1$, and $R_c = 30$ AU. *Top:* Surface density evolution in time. The dotted line shows the gas surface density (Eq. 5.1), which is assumed to be static in time. *Middle:* Evolutionary histories of a selection of dust batches. Particles start out in the bottom of the plot as submicron-size monomers ($m \sim 10^{-14}$ g), and move up as they gain mass, and to the left as they drift inward. The background color indicates the porosity history of the grains. For compact coagulation, $\phi = 1$ at all times. *Bottom:* Similar to the middle panel, but now the colors indicate particle Stokes number. Bodies with $\Omega t_s \sim 1$ drift inward the fastest.

we do not include fragmentation. Recently however, Krijt et al. (2015) argued that erosion by small particles can be an effective way of halting growth when drift starts to play a

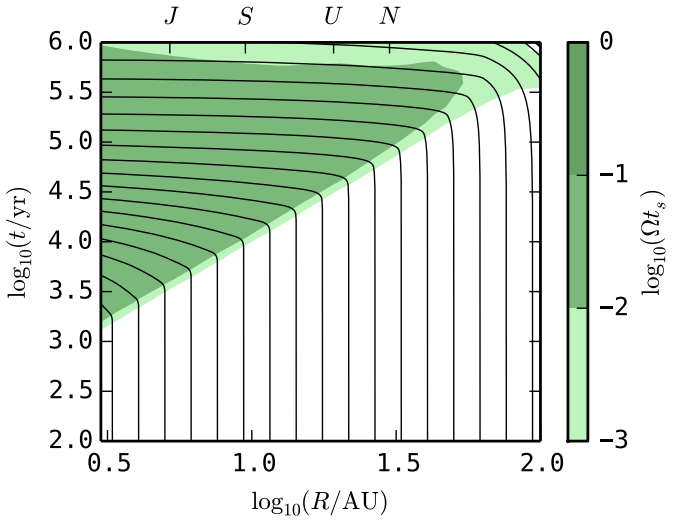

Figure 5.4: Evolution of dust batches in space and time for the model of Fig. 5.3 (compact growth with fragmentation at 5 m s^{-1}). Background colors show regions where particle Stokes numbers $10^{-3} \leq \Omega t_s \leq 1$.

role. Unfortunately, the threshold velocity above which erosion becomes significant is not accurately known for the highly-porous ice aggregates in question (see Krijt et al. 2015, Sect. 2.3.2.). Therefore, we will consider both cases: perfect sticking (Sect. 5.3.2), and effective erosion (Sect. 5.3.2).

Perfect sticking

Initially, we employ the same disk model as in the previous section, but because ice is added to the available solids, we start from $Z_0 = 0.02$. In Sects. 5.3.2 and 5.3.2, the effects of various disk parameters (e.g., total mass, size, and temperature) will be studied as well.

Fig. 5.5 shows the results for porous growth with perfect sticking. The top panel shows the surface density evolution in the case of porous growth. The solid lines correspond to Σ_d, and the dashed lines show Σ_p, the planetesimals. Aggregates in the inner disk (just outside the snow-line) can grow through the drift barrier, as found by Okuzumi et al. (2012); Kataoka et al. (2013a); Krijt et al. (2015), causing a pile up of solids around 5 AU, and a depletion of dust in the region further out. Although Okuzumi et al. (2012) used a different disk model and did not include gas- and self-gravity-compaction, this general picture is also obtained in their full global model (Okuzumi et al. 2012, Fig. 6). After 10^6 years, the entire disk is depleted in dust, and planetesimals have formed in the region just behind the snow line.

Focussing on the porosity (middle panel), we find that the porosities first decrease quickly as the result of hit-and-stick growth, and are then roughly constant due to collisional-

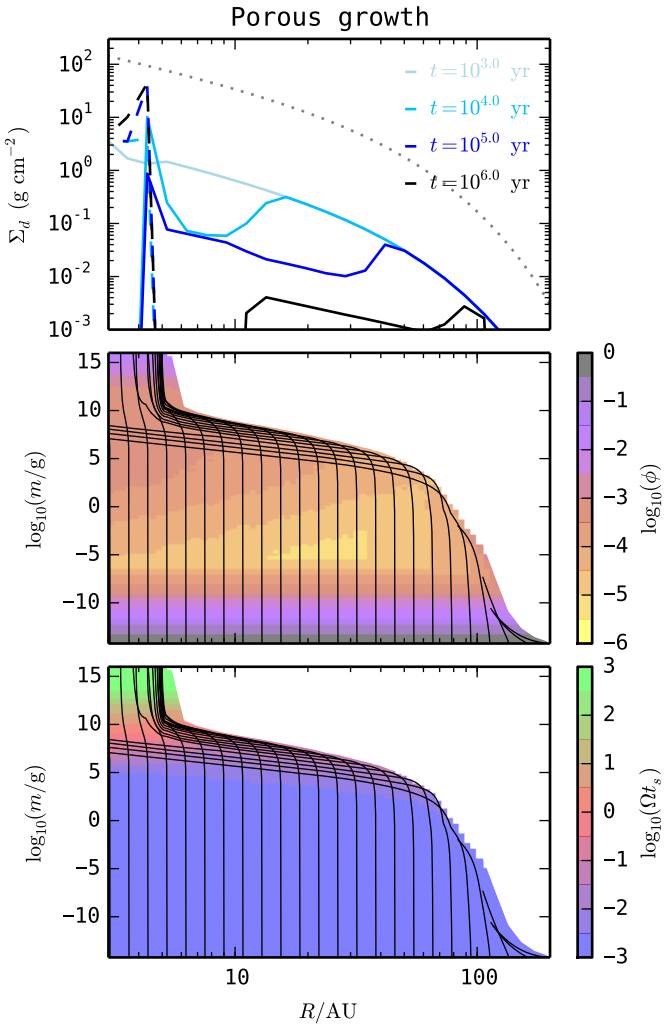

Figure 5.5: Porous growth with perfect sticking, for a disk with $M_D/M_\odot = 0.01$, $Z_0 = 0.02$, $R_c = 30$ AU, and $\gamma = 1$. *Top:* the surface densities of the gas (dotted), dust (solid), and planetesimals (dashed) are shown. *Middle:* Aggregates reach filling factors as low as 10^{-5}, before being compacted by gas ram pressure and collisions. *Bottom:* In the inner disk, aggregates can out-grow the radial drift barrier, and form massive, relatively compact, planetesimals with $\Omega t_s > 10^3$.

and (mostly) gas-compaction. For bodies with $m > 10^{12}$ g, self-gravity dominates the porosity and the filling factor increases to $\sim 10^{-1}$, consistent with Fig. 5.2, Kataoka et al. (2013a) and Krijt et al. (2015).

The bottom panel of Fig. 5.5 illustrates how aggregates grow through the radial drift

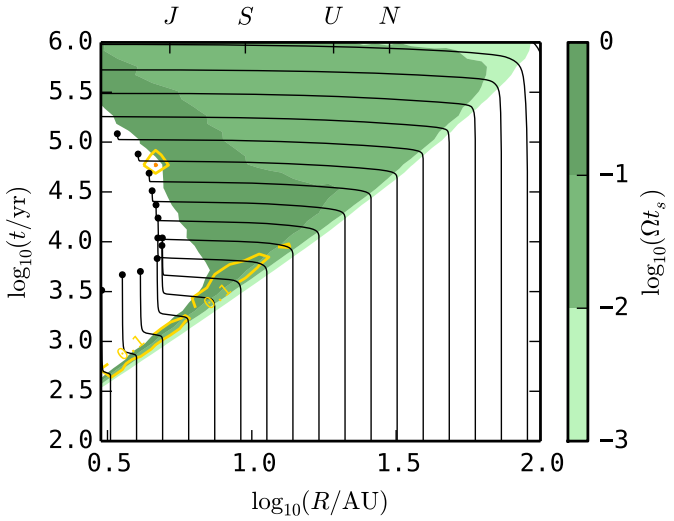

Figure 5.6: Evolution of dust batches in time for the simulation of Fig. 5.5 (porous growth with perfect sticking). The •-symbols indicate planetesimal formation through coagulation, and contours depict the midplane dust-to-gas ratio of particles with high Stokes numbers (see Sect. 5.4). For this particular disk model, planetesimal can form out to ∼5 AU.

barrier. Initially, aggregates grow through hit-and-stick collisions and their surface-to-mass ratio hardly changes (cf. Fig. 5.2). As a result, the aggregates' Stokes number stays $\ll 1$ while the mass increases over many orders of magnitude. Only when masses $>10^5$ g do particles start to experience substantial drift. In the inner disk, $\Omega t_s = 1$ corresponds to $m \sim 10^9$g (Krijt et al. 2015, Fig. 8). However, we also see particles with masses $10^7 - 10^8$ drifting to radii <3 AU. These tracks belong to particles that started out in the outer disk, and spent a lot of time in the early growth phase. By the time they started to drift and reached the inner disk, the dust surface density was already significantly decreased, making it difficult for the newly-arrived aggregates to grow since $\dot{m} \propto \Sigma_d$ (Eq. 5.10). Since planetesimals do not contribute to Σ_d, they do not influence the evolution of the drifting dust particles. This assumption is discussed further in Sect. 5.5.

In Fig. 5.6, the results of the porous coagulation model are plotted in a similar way as Fig. 5.4. The black solid spheres correspond to successful planetesimal formation through coagulation (i.e., $m_i \geq 10^{16}$ g). For this particular gas disk model, planetesimals can be seen to form out to ∼5 AU (cf. Fig. 5.5). In the inner disk, where the aggregates out-grow the radial drift barrier, the aggregates spend very little time having $10^{-3} \leq \Omega t_s \leq 1$. Again, we see that particles that start out in the outer disk take much longer to start drifting, and eventually drift through the planetesimal populations after $\sim 10^5$ yr.

Total planetesimal mass

By keeping track of the total mass of batches that have been converted into planetesimals, we obtain the total planetesimal mass as a function of time. Fig. 5.7 plots this mass $\Sigma m_{\rm pl}$ as a function of time for a grid of models with different disk masses and initial metallicities. All disks shared $\alpha = 10^{-3}$ and $R_c = 30$ AU. Most planetesimals form in the first 10^5 yrs, and it is clear that both a higher disk mass, and a higher initial metallicity lead to a larger total mass of planetesimals. For disk masses between 0.01 and 0.2 $M_\odot$, and metallicities between $Z_0 = 0.01 - 0.05$, between 10 and $\sim 10^3 M_\oplus$ of planetesimals can form through porous coagulation. These masses represent a considerable fraction of the total dust mass that is present in the disk.

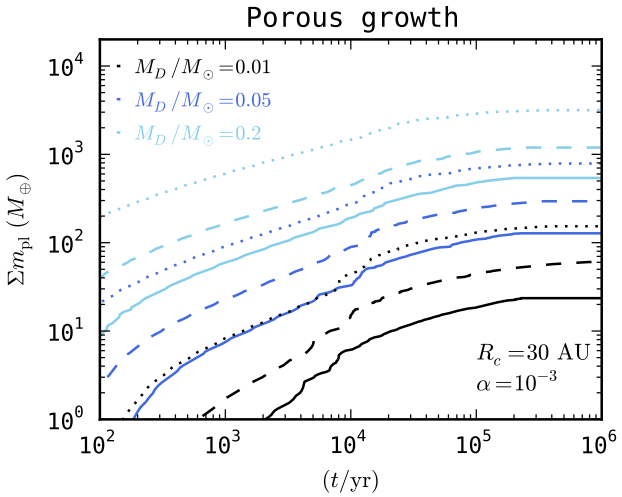

Figure 5.7: Total mass of planetesimals as a function of time for porous growth without erosion. Different linestyles indicate $Z_0 = 0.01$ (solid); $Z_0 = 0.02$ (dashed); and $Z_0 = 0.05$ (dotted). The total planetesimal mass increases significantly with disk mass and disk metallicity.

The top panel of Fig. 5.8 shows the same results but normalized to the total available dust mass $Z_0 M_D$. All disks considered here convert over 70% of their dust to planetesimals within a million years. Dust-rich, massive disks are most efficient, with an efficiency of ~90% after 10^6 yrs. The middle and bottom panel of Figure 5.8 show similar plots for more extended protoplanetary disks ($R_c = 100$ AU), with $\alpha = 10^{-3}$ and 10^{-5}, respectively. An increased physical size of the protoplanetary disk causes a decrease in the planetesimal-formation efficiency. In addition, a lower turbulence strength leads to slower growth, and $\Sigma m_{\rm pl}/(Z_0 M_D)$ reaches only 0.2-0.5 within 10^6 yr, depending on the disk parameters.

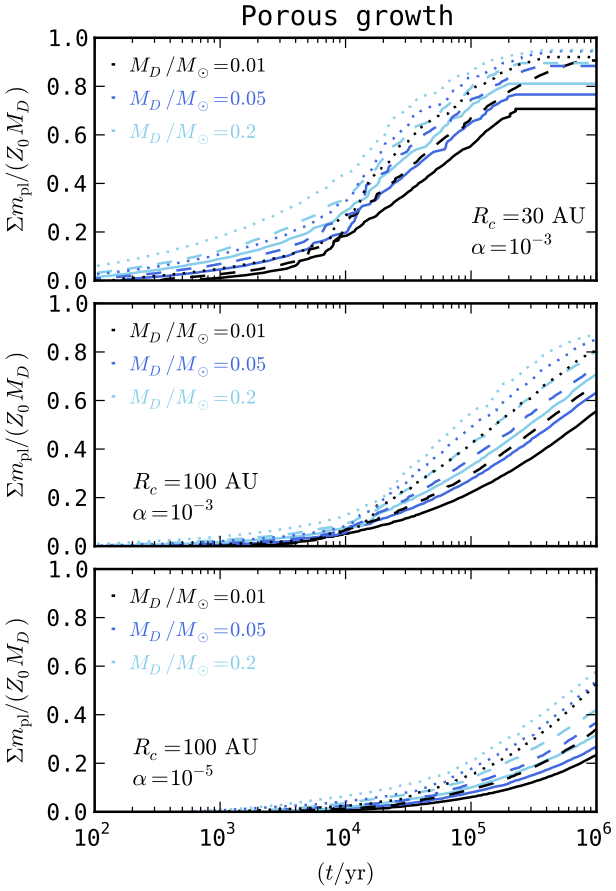

Figure 5.8: Fraction of total dust mass $Z_0 M_D$ that has been converted into planetesimals as a function of time, for different disk models. *Top:* MMSN-like disk with $\alpha = 10^{-3}$. *Middle:* More extended and shallower disk, also with $\alpha = 10^{-3}$. *Bottom:* The same extended disk, but with a weaker turbulence ($\alpha = 10^{-5}$). In general, porous growth in combination with perfect sticking is a very efficient way of turning dust into planetesimals; the efficiency being highest for disks with a high initial dust content. Weaker turbulence results in slower growth.

Planetesimal formation region

The size of the zone where aggregates can out-grow the radial drift barrier depends on disk parameters as well. Fig. 5.9 shows how the outer edge of this 'planetesimal formation zone' varies with total disk mass and metallicity for a compact disk (R_c = 30 AU, dotted), and a more extended disk (R_c = 100 AU, solid).

This dependency on disk mass was also noted by Okuzumi et al. (2012), and results from both a high dust density, and a lower gas molecule mean free path $\lambda_{\rm mfp}$; the length of

the mean free path (together with the aggregate's size) determines in which drag regime the aggregates are situated, and has a large impact on the growth timescale (see Sect. 5.A and Okuzumi et al. 2012). An increased metallicity directly results in a larger local dust density, making it easier for dust particles to outgrow radial drift, also increasing the size of the planetesimal formation zone. The planetesimal belt is somewhat larger for compact disks than for extended ones with identical total mass. The reason is that, for a given total disk mass, a smaller R_c leads to a higher dust surface density at radii $R < R_c$, and the higher the local dust surface density, the easier it becomes to outgrow radial drift. Comparing the distances to the current locations of the planets in our Solar System, we find that massive disks ($M_D/M_\odot = 0.2$) with a high dust content ($Z_0 = 0.05$) can form planetesimals as far out as ∼20 AU, or the current location of Uranus. Figure 5.10 shows the impact of varying the slope of the surface density power law γ, and the disk temperature. An increase in γ has a similar effect as a decrease in R_c: mass becomes more concentrated in the inner disk, resulting in a smaller planetesimal formation zone. Cold disks are flatter (smaller h_g), and have a lower maximum drift velocity ηv_K. The combined effects of lowering the temperature by a factor 2 with respect to Eq. 5.2 has a tremendous impact, increasing the outer edge of the planetesimal belt by almost a factor of 2.

At small radii, the icy particles needed for porous and perfect-sticking growth might not be present. The snow line, inside of which temperatures are too high to allow for water ice to be present, typically lies at ∼3 AU, but varies with turbulence strength and accretion rate (Min et al. 2011). The gray shaded area in Figs. 5.9 and 5.10 indicate the region within 3 AU. The assumption that dust particles are not destroyed in collisions is expected to break down in this region. Thus, low-mass disks ($M_D \sim 10^{-3} M_\odot$) might bot be able to form planetesimals through direct coagulation. Finally, while we only consider grain growth by coagulation, growth by water vapor condensation can be an efficient way of gaining mass close to the snow line (Cuzzi & Zahnle 2004; Ros & Johansen 2013), locally enhancing the growth rates.

Erosion-limited growth

In the previous section we have assumed perfect sticking for the highly-porous icy aggregates. Now, to mimic the effect of efficient erosion, we set $\dot{m}_i = 0$ whenever the relative velocity between the dust particles in the batch and monomers exceeds some erosion threshold velocity. The best data on erosion of icy particles comes from Gundlach & Blum (2015), who measured an erosion threshold velocity of ∼15 m s^{-1} for aggregates composed of (sub)micron-size monomers.

Fig. 5.11 shows the results for the same model as Fig. 5.5, but now including an erosion threshold velocity of 20 m s^{-1}. For low Stokes numbers, collision velocities are too low to cause erosion, and growth proceeds similarly to Fig. 5.5. Then, as aggregates grow towards $\Omega t_s \sim 1$, the collision velocity with small, well-coupled monomers approaches the maximum drift velocity of $\sim \eta v_K$, which is well above 20 m s^{-1} for this particular disk model. Erosion, assumed to be efficient, then acts to halt further growth, and prevents formation of planetesimals through direct coagulation. Since coagulation is fastest in the

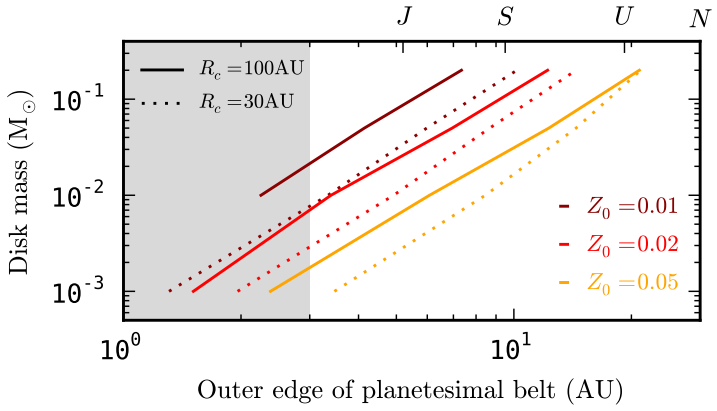

Figure 5.9: Outer edge of planetesimal formation zone as a function of disk mass M_D and initial metallicity Z_0, assuming R_c = 100 AU (solid); and R_c = 30 AU (dotted). Letters refer to the (current) locations of Jupiter, Saturn, Uranus and Neptune. For more massive, and more dust-rich disks, the planetesimal formation zone extends further out.

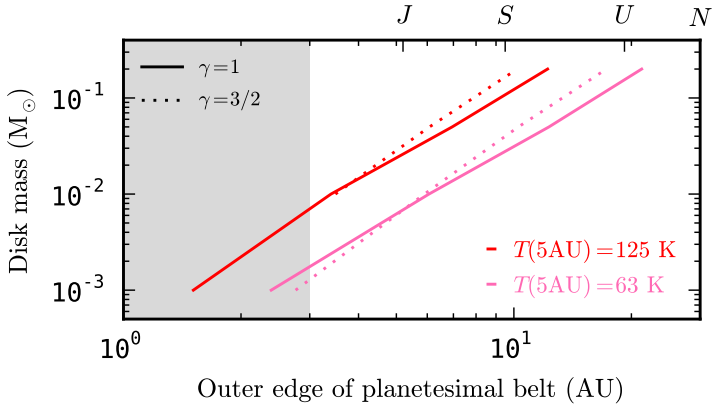

Figure 5.10: The effect of disk temperature and surface density exponent on the size of the planetesimal formation zone, for a fixed metallicity Z_0 = 0.02 and R_c = 100 AU. The effect of varying γ is small compared to the effect of reducing the temperature by 50%.

inner regions of the disk, erosion-limited growth results in an inside-out removal of the dust (similar to what was found for fragmentation-limited compact growth of Fig. 5.3). At later times, a sharp drop in Σ_d can be observed in Fig. 5.11 around $R \sim 5$ AU. This sudden drop in dust surface density is an artifact of the dust batch approach and can occur when, as a result of drift, the dust population in the dust-depleted region is represented by a small number of batches (see Sect. 5.5.1).

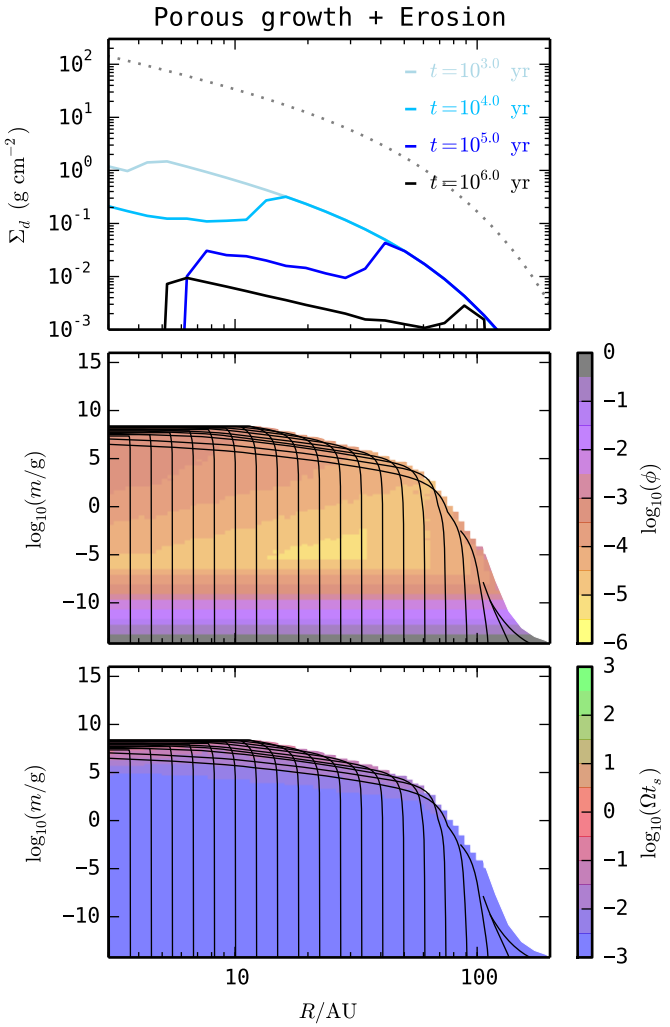

Figure 5.11: Porous growth followed by erosion. Dust and disk models are the same as in Fig. 5.5, but with efficient erosion above drift velocities of 20 m s^{-1}.

5.4 Planetesimal formation through SI

In addition to coagulating directly, planetesimals can also form through streaming instability (SI) (e.g., Youdin & Goodman 2005; Johansen et al. 2007; Bai & Stone 2010a,b). In this section, we investigate how coagulation (both compact and porous) can lead to conditions suitable for triggering SI.

5.4.1 Conditions for SI

We make use of the work of Drążkowska & Dullemond (2014), who, based on the work of Johansen et al. (2007, 2009); Bai & Stone (2010a,b) defined three conditions for triggering SI. For a mono-disperse particle distribution, these conditions are equivalent to:

i) The Stokes number of the mass dominating particles needs to be close to unity; specifically, $10^{-2} \leq \Omega t_s \leq 1$;

ii) The midplane dust-to-gas ratio of these particles needs to exceed, or be close to, unity;

iii) The vertically integrated metallicity should be a few times Solar;

Lastly, SI needs time to develop and will not be triggered if the growth timescales of the particles are too short. Thus, we add a final condition:

iv) The growth timescale needs to be longer than the timescale for SI instability to develop: $t_{\rm grow} > \Omega^{-1}$.

The first two conditions are related to efficient momentum transfer between dust particles and the gas. Particles with much higher Stokes numbers do not effectively interact with the gas, while particles with with much smaller stopping times do not result in strong clumping. Conditions *iii)* is related to supressing midplane turbulence. For high metallicities, the strength of this turbulence drops sharply (Bai & Stone 2010a).

We focus on conditions *i)*, *ii)*, and *iv)*, and address *iii)* in Sect. 5.4.4. Armed with the semi-analytical model of Sect. 5.2, we can now identify regions in space and time where these conditions are met. We will look at compact coagulation first, and then turn to porous coagulation. We define the midplane dust-to-gas ratio of decoupled particles as $(\rho_d^*/\rho_g)_{z=0}$, where the asterisk indicates that only particles with $10^{-2} \leq \Omega t_s \leq 1$ contribute to the dust density. For a mono-disperse particle distribution

$$(\rho_d^*/\rho_g)_{z=0} = \frac{(\Sigma_d/h_d)^*}{\Sigma_g/h_g} = Z^* \frac{h_g}{h_d}, \tag{5.13}$$

where the dust scale height depends on the particle Stokes number through Eq. 5.12.

5.4.2 Compact coagulation

For compact particles, Drążkowska & Dullemond (2014) find that bouncing and fragmentation prevent particles from growing to $\Omega t_s > 10^{-2}$, making the condition *i)* of Sect. 5.4.1 hard to fulfill. In our compact model, shown in Fig. 5.4, particles did reach high enough Stokes numbers; the reason is that we used a (rather optimistic) bouncing/fragmentation threshold of 5 m s^{-1}, while Drążkowska & Dullemond (2014) used 0.1 m s^{-1}. To test the influence of the threshold velocity, we ran a model identical to the earlier compact coagulation one, but now assuming a growth barrier for velocities above 1 m s^{-1}; the results are shown in Fig. 5.12. While there is a large region in the disk where the mass-dominating

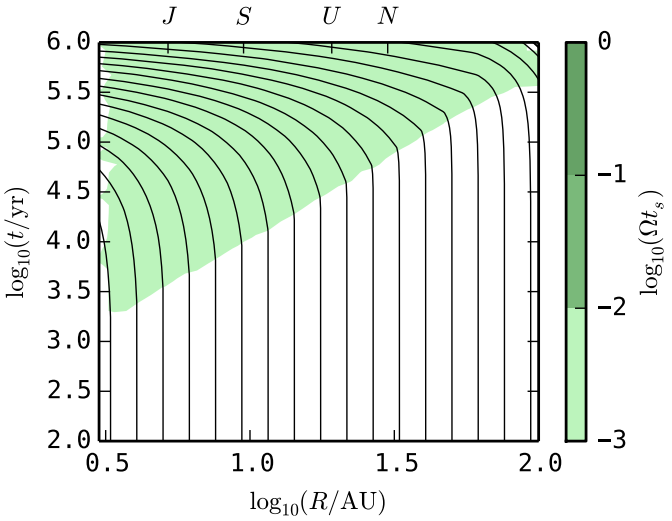

Figure 5.12: Evolution of dust batches assuming compact coagulation with a fragmentation/bouncing threshold velocity of 1 m s^{-1}. A compact $10^{-2} M_\odot$ disk was assumed, with initial metallicity $Z_0 = 0.01$ and $\alpha = 10^{-3}$. Compact particles do not reach $\Omega t_s > 10^{-2}$, and the dust-to-gas ratio in the midplane never exceeds 10^{-1}.

particles have $\Omega t_s > 10^{-3}$, the combination of drift and bouncing/fragmentation prevents particles from growing to Stokes numbers sufficient for SI.

The Stokes number at which particles fragment as a result of turbulence equals (e.g., Birnstiel et al. 2009)

$$(\Omega t_s)_{\max} \simeq \alpha^{-1} \left(\frac{v_{\rm frag}}{c_s} \right)^2, \tag{5.14}$$

with $v_{\rm frag}$ the fragmentation velocity. At 5 AU, assuming the temperature structure of Eq. 5.2, this leads to $(\Omega t_s)_{\max} \sim 10^{-3}$ for $v_{\rm frag} = 1$ m s^{-1} and $\alpha = 10^{-3}$. For low turbulence strengths, the relative velocities come from differential drift, resulting in (e.g., Birnstiel et al. 2012)

$$(\Omega t_s)_{\max} \simeq \frac{v_{\rm frag}}{\eta v_{\rm K}}, \tag{5.15}$$

with $\eta v_{\rm K} \simeq 50$ m s^{-1} in an MMSN-disk.

5.4.3 Porous coagulation

For ices, $v_{\rm frag}$ is much larger, several tens of m s^{-1} (Dominik & Tielens 1997; Wada et al. 2013), and growth to larger Stokes numbers is possible. Focussing on the perfect sticking case first, Fig. 5.6 shows that condition *i)* is fulfilled in a large part of the protoplanetary disk. In the inner disk however, growth *through* the drift barrier is so rapid, that aggregates

spend very little time having Stokes numbers that are suited for triggering SI (Okuzumi et al. 2012, Sect. 5.2.2.). As a result, condition *iv)* is not met in the inner disk.

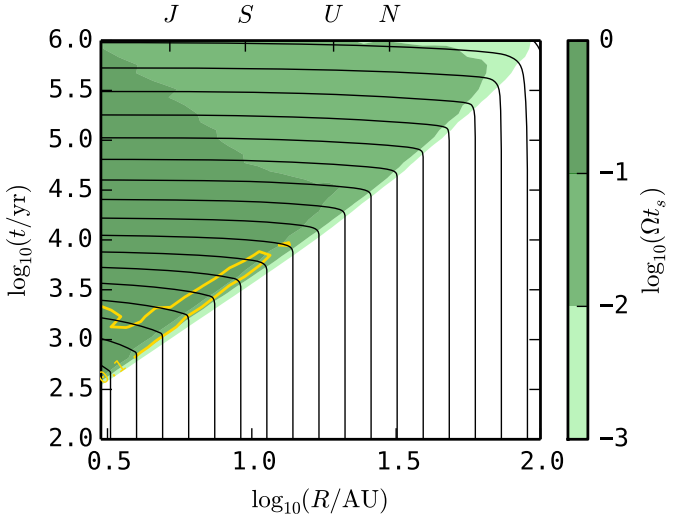

Figure 5.13: Dust evolution for porous growth followed by erosion, in a compact $0.01 M_\odot$ disk with $\alpha = 10^{-3}$ and $Z_0 = 0.02$ (same model as Fig. 5.11). Times/locations where the mass-dominating particles have $10^{-3} \leq \Omega t_s \leq 1$ have been colored green, and the contours depict $(\rho_d^*/\rho_g)_{z=0} = \{0.1;0.5;1\}$.

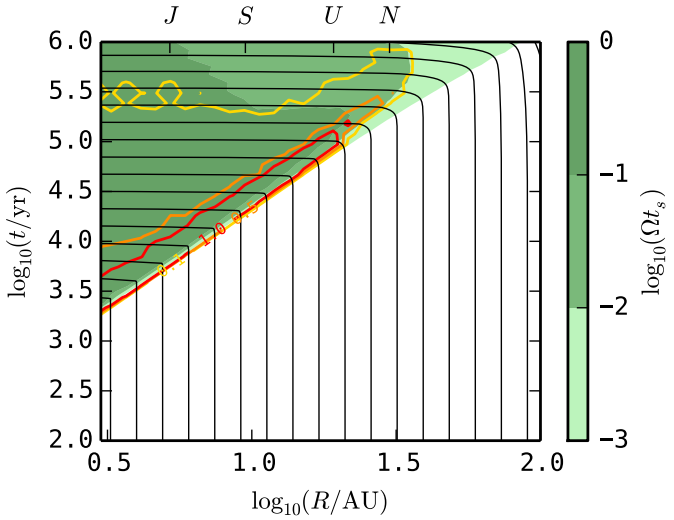

Figure 5.14: Same as Fig. 5.13, but using $\alpha = 10^{-5}$ and $Z_0 = 0.05$. The lower turbulence strength results in slower growth, but allows a higher mass loading in the midplane. Contours depict $(\rho_d^*/\rho_g)_{z=0} = \{0.1;0.5;1\}$.

Porous coagulation followed by drift-induced erosion however, is a robust way of creating *and keeping* a large amount of mass in aggregates with Stokes numbers around unity. This is illustrated in Fig. 5.13. The limiting criterion now becomes condition *ii)*: a dense midplane layer of solids. From Fig. 5.13 we learn that a turbulence strength of $\alpha = 10^{-3}$ at most results in a midplane dust-to-gas ratio of ∼0.1, about a factor of 10 too low. In Fig. 5.14, we have lowered the strength of the turbulence to $\alpha = 10^{-5}$, and increased the initial metallicity to $Z_0 = 0.05$. For this extreme case, we see that a region exists where conditions *i)*, *ii)*, and *iv)* are all met. The conditions are first met in a region in the inner disk after a few 10^3 yr, after which this region moves outward, reaching the current location of Uranus after 10^5 yr. In this 'front', marked by the red contour, we would expect SI to occur, and planetesimals to be formed locally.

5.4.4 Midplane turbulence

However, we cannot choose arbitrarily small values for α: the presence of decoupled particles can lead to Kelvin-Helmholtz instability (KH) and SI, and will give rise to a turbulence with strength (Takeuchi et al. 2012)

$$\alpha_{\rm mp} = \left[(C_1 C_{\rm eff}\eta Z)^{-2/3} + (C_2 C_{\rm eff}\eta/Z)^{-2}\right]^{-1} \Omega t_s, \tag{5.16}$$

where $C_1 = 1$, $C_2 = 1.6$, $C_{\rm eff} = 0.19$, η is given by Eq. 5.9, and $\Omega t_s < 1$ is the Stokes number of the mass-dominating particles responsible for the instability. For the disk models used in this work, $\alpha_{\rm KH} \simeq 10^{-6}$ and 10^{-4} in the inner disk for $\Omega t_s = 10^{-2}$ and 1 respectively (depending slightly on the metallicity Z), and increases by about a factor of 10 towards the outer disk. The turbulence strength obtained in Eq. 5.16 can be used as a minimum value for the turbulence, i.e., $\alpha \geq \alpha_{\rm mp}$. Making use of Eq. 5.13, we can then constrain the maximum midplane dust-to-gas ratio as

$$Z^*(h_g/h_d) \sim Z^*(\Omega t_s/\alpha)^{1/2} \leq Z^*(\Omega t_s/\alpha_{\rm mp})^{1/2}, \tag{5.17}$$

where we have used that $h_d/h_g \sim (\alpha/\Omega t_s)^{1/2}$ for high Stokes numbers (see Eq. 5.12). From Eq. 5.16 we find $\alpha_{\rm mp} \propto \Omega t_s$, so the dependence on particle Stokes number drops out of the expression for the maximum midplane mass loading, which is now a function only of the pressure profile η and metallicity Z^*.

Fig. 5.15 shows the midplane dust-to-gas ratio for different metallicities and disk models, assuming that the turbulence strength is given by Eq. 5.16 and the mass-dominating particles have been able to reach $10^{-2} \leq \Omega t_s \leq 1$. The figure shows that in order to reach the required dust-to-gas ratio in the midplane of an MMSN disk (upper panel), despite the turbulence triggered in the midplane, one needs a local metallicity (of high Stokes-number particles) of $Z^* = 0.03$ in the inner ∼10 AU, and $Z^* = 0.05$ in the region out to 80 AU. This indicates that, for a given metallicity, SI is easier to trigger at *smaller* radii. The reason can be understood as follows; if $\alpha_{\rm mp}$ is the main source of turbulence, the height of the dust layer is approximately $h_g/h_d \sim \eta v_{\rm K}/c_s \sim c_s/v_{\rm K} \sim h_g/R$. In other words, the relative height of the dust layer scales with the opening angle of the disk. In the MMSN

disk model, $h_g/R \propto R^{1/4}$, and disks with $\gamma = 1$ are flaring as well. As a result, creating a dense midplane layer of solids appears easier in the inner disk.

For a more extended disk with a shallower surface density profile (middle panel), the results are similar, and $Z^* = 0.03$ and $Z^* = 0.05$ result in $(\rho_d^*/\rho_g)_{z=0} \leq 1$ in the inner ~20 and 90 AU respectively. Since rapid porous growth followed by erosion results in an inside-out clearing of the dust in the disk (Fig. 5.11), pile-ups will not occur in the smooth disks considered in this work, and the only way to reach such high local metallicities is to start out with a super-Solar Z_0. A possible solution might be to lower the disk's temperature. The temperature structure used so far (Eq. 5.2) is based on an optically thin disk. However, (midplane) temperatures in disks might be significantly lower, especially if the disk is optically thick (e.g., Andrews et al. 2009). In a colder disk η will be smaller, reducing the strength of the midplane instability, and making it easier to form a dense midplane layer. The bottom panel of Fig. 5.15 uses $R_c = 100$ AU, and disk temperature that is reduced by 50% with respect to Eq. 5.2. In this relatively cold disk, $Z^* = 0.02$ could be enough to trigger SI in the inner 10 AU, and $Z^* = 0.03$ suffices out to 50 AU (provided there is no stronger source of turbulence present). However, in colder disks the maximum drift velocity is lower as well, possibly reducing the efficiency of erosion.

5.5 Discussion

5.5.1 Dust batch approach

The numerical method used in this work (Sect. 5.2.2), in which batches of dust are followed as they grow and drift in the protoplanetary nebula, provides an intuitive and flexible way to calculate (local) porous coagulation and the evolution of the global surface density simultaneously. Growth-limiting collisional processes such as bouncing, erosion and fragmentation can be incorporated in an straightforward manner. The flexibility and speed of this approach allow us to calculate a large number of models, and to study the impact of variations in parameters quickly by exploring a large parameter space while preserving the essential characteristics of the growth process. The method can readily be extended to more complicated gas disks. For example, rather than using a static and smooth $\Sigma_g(R)$, the method could be extended to deal with more complex $\Sigma_g(R, t)$, based on simulations of MRI turbulence, zonal flows, and embedded planets (e.g., Raettig et al. 2013; Uribe et al. 2013; Dittrich et al. 2013; Flock et al. 2015).

The method has two main drawbacks. First, it traces only the mass-dominating particles, and does not provide information about the number distribution for smaller masses. If the distribution can be assumed to be in growth/fragmentation equilibrium, the complete mass distribution may be reconstructed (e.g., Birnstiel et al. 2011), though this has not yet been attempted for porous growth, or for a steady state between growth and erosion. Second, in cases where drift is rapid (i.e., high $\dot{r}$), the radial distances between successive batches are increased. Because we use the radial distribution of the batches to obtain the dust surface density, the determination of $\Sigma_d(R)$ becomes less accurate in regions where few batches are present. A solution could be to simply increase the number

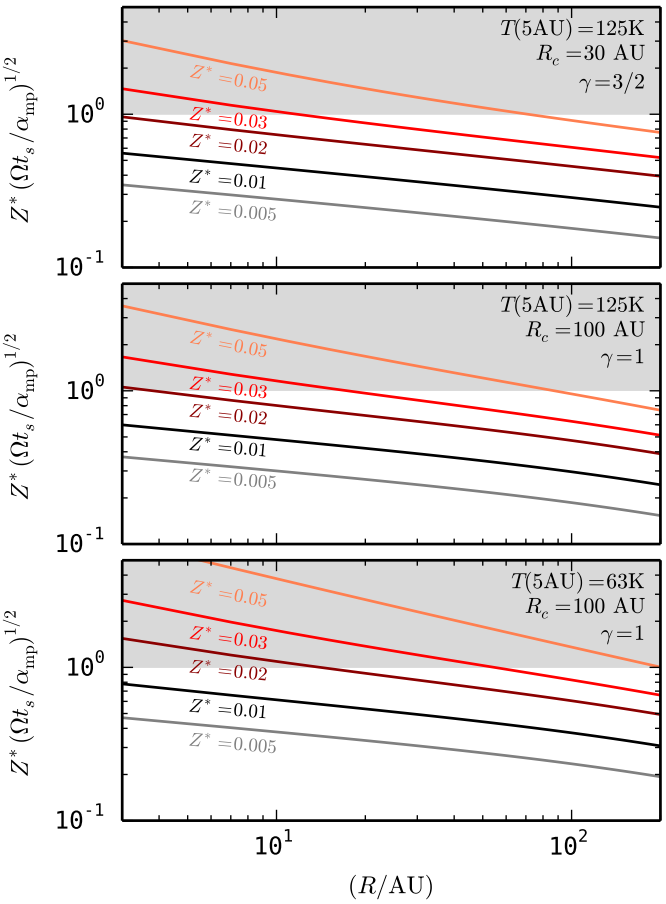

Figure 5.15: Midplane dust-to-gas ratio assuming the turbulence strength is given by Eq. 5.16, and the mass-dominating particles have $10^{-2} \leq \Omega t_s \leq 1$, for an MMSN-like disk (upper panel), a larger and shallower disk (middle panel), and a colder disk (bottom panel). Colors correspond to different metallicities, ranging from $0.5-5\times$ Solar. The grey shaded area indicates conditions necessary for planetesimal formation through SI.

of batches. Alternatively, if one is interested in a particular disk region or epoch, the initial radial distribution r_i could be chosen such to achieve highest numerical resolution in that region. Because we are mainly interested in the sites where planetesimals can form, i.e., places where Σ_d is high, our results are not affected by these issues.

5.5.2 Direct coagulation

In Sect. 5.3, we applied the method to study compact and porous coagulation behind the snow line. For compact particles, we considered a fragmentation threshold velocity of

several m s^{-1}, and found that growth beyond a cm in size is always impeded by fragmentation or radial drift (Fig. 5.3). However, there are still possibilities for compact grains to grow larger. If particles are sufficiently 'lucky', and participate only in relatively low-velocity collisions, they could potentially grow by effectively sweeping up small particles (Windmark et al. 2012a,b; Garaud et al. 2013; Drążkowska et al. 2014).

For porous icy aggregates however, fragmentation occurs only at very high velocities (Wada et al. 2013), and these fluffy aggregates can grow through the radial drift barrier. Rapid growth is harder to achieve in the outer disk, since timescales are longer and dust and gas spatial densities are lower. As a result, planetesimals form in a zone confined to the inner ~10 AU. Figs. 5.9 and 5.10 show how the size of this region depends on disk mass, temperature, and initial metallicity. Comparing the planetesimal formation zone to the current locations of the Solar System planets, we find that it is hard to form planetesimals out to the current location of Neptune. In the *Nice* model however, the giant planets of the Solar System were originally located much closer in, roughly between 5 and 17 AU, migrating out at later times (Tsiganis et al. 2005; Morbidelli et al. 2005; Gomes et al. 2005). At these locations[2], direct planetesimal formation through porous growth can be achieved, albeit only for relatively massive or cold disks. The calculations in Sect. 5.3 indicate the planetesimal surface density is highest near the outer boundary of the planetesimal zone. One could envision a scenario where enough material accumulates to trigger the formation of Jupiter early on. At that point, the assumptions in our model break down and the presence of Jupiter will steer the evolution of the disk and planet formation therein (e.g., Pollack et al. 1996; Pinilla et al. 2012a; Kobayashi et al. 2012).

The efficiency with which dust is converted into planetesimals can be very high, reaching up to 90% within 10^6 yr for relatively compact and dust-rich disks (Fig. 5.8). When the full mass distribution is taken into account, this efficiency will be lowered slightly, depending on how much mass is present in the low-mass end of the distribution. This picture of efficient dust-to-planetesimal conversion on a Myr timescale is consistent with the findings of Najita & Kenyon (2014), who, by comparing masses and locations of detected exoplanets to measured reservoirs of solids in T Tauri disks, concluded that a large fraction of the available solids has to be either hidden in the inner parts of the protoplanetary disk, and/or efficiently converted into large objects, avoiding detection.

Lastly, in the semi-analytical model of Sect. 5.2, planetesimals and dust do not interact with each other: the planetesimals do not contribute to the surface density of Eq. 5.10, and they do not sweep up drifting dust particles. As a result, aggregates that drift in at later times can drift *through* the planetesimal zone unaffected, as observed in Figs. 5.5 and 5.6. These conditions, a belt of planetesimals in the inner disk, and a reservoir of dust drifting in from the outer disk, are the starting conditions for pebble accretion[3] (Ormel & Klahr 2010; Lambrechts & Johansen 2012, 2014; Kretke & Levison 2014). If efficient, pebble accretion would result in an even higher planetesimal formation efficiency, since the mass present in the outer disk (which is substantial for large R_c) will be added to the

[2]The cores of the terrestrial planets require a different formation mechanism, as their close distances to the Sun do not allow the presence of sticky ices in their formation zone.

[3]Although the drifting particles in Fig. 5.6 are much larger and much more porous than the word 'pebble' would suggest.

planetesimals. However, the filtering of dust by planetesimals is not necessary efficient, depending on the turbulence strength and planetesimal characteristics (Guillot et al. 2014).

5.5.3 Streaming Instability

In Sect. 5.4, we investigated for which disk parameters compact and porous growth might lead to conditions favorable for triggering SI (Sect. 5.4.1), as defined by Drążkowska & Dullemond (2014). We found that porous growth followed by erosion (unlike compact growth followed by bouncing or fragmentation) naturally leads to a population of aggregates with Stokes numbers $10^{-2} \leq \Omega t_s \leq 1$ in a large portion of the protoplanetary disk. The most difficult condition to fulfill is then the creation of a dense midplane layer of solids. While this is possible for disks with a high metallicity and relatively weak turbulence (Fig. 5.14), the presence of the decoupled dust aggregates will lead to a turbulence that can be parametrized by Eq. 5.16 (Takeuchi et al. 2012), placing a lower limit on the local metallicity needed to achieve a dust-to-gas ratio of unity in the midplane. In that sense, condition *iii)* of Sect. 5.4.1 is not so much a separate criterion, but can be thought of as a prerequisite for criterion *ii)* in the presence of strong midplane turbulence.

For MMSN-like disks, and disks with a shallower profile (Upper and middle panel of Fig. 5.15), this lower limit is $Z^* \sim 0.03$ in the inner ~10 AU, and even higher in the outer disk. Since we only consider smooth disks, and porous growth leads to an inside-out clearing of the dust, pile-ups (as seen in Fig. 5.1) are not created and the only way to achieve these desired metallicities is to start from a high initial metallicity Z_0. For colder disks, a metallicity of $Z^* = 0.02$ might suffice to create a dense midplane layer inside of 10 AU. However, in colder disks the maximum drift velocity ηv_K is reduced as well, making the process of erosion less efficient. Without strong erosion, particles readily grow to larger Stokes numbers in the inner disk, not fulfilling condition *iv)* of Sect. 5.4.1.

We have employed a vertically isothermal disk, described by a simple temperature power-law. In reality, the midplane will be colder than the disk upper layers, and its temperature sensitive to the dust opacities (e.g., Min et al. 2011). To fully appreciate the interplay between porous growth, erosion, and SI, future models will have to self-consistently model the full particle mass- and porosity-distribution as it evolves through coagulation and erosion, while taking into account the feedback of the particles onto the gas. For example, small grains will influence the local temperature, and the massive, marginally decoupled grains can trigger Kelvin-Helmholtz instability or SI. In addition, when clumping through SI occurs, the collision velocities inside the clumps can be lowered (e.g., Bai & Stone 2010a), possibly altering the dominant collisional outcomes.

Observations show clear evidence for small dust grains in relatively old disks (e.g., Birnstiel et al. 2009). Thus, any mechanism that is capable of efficiently converting dust in to planetesimals (be it rapid porous growth, or SI) must not be too efficient, i.e., a population of small grains has to has to be sustained for over $\sim 10^6$ yr. In the outer parts of weakly turbulent disks, fragmenting collisions between similar-size aggregates are not expected to occur, though some mass loss may occur even in 'sticking' collisions (Wada et al. 2013, Sect. 4.3). In these regions, erosive collisions (i.e., high-speed collisions between aggregates with a high mass ratio) might be a way to keep a population of small

grains around; a population that is removed quickly when *all* collisions result in perfect sticking (Dullemond & Dominik 2005). To study these issues, models that resolve the full mass distribution are necessary.

5.5.4 Planetesimal characteristics and further evolution

Focussing on the growth towards planetesimals, we stopped following the planetesimals when they reached masses of $m \geq 10^{16}$ g, and described the planetesimal populations only in terms of their total mass, without specifying the properties of the individual planetesimals. An interesting question is how the considered formation mechanisms (direct coagulation and SI) affect the internal structure and composition of the formed planetesimals.

Focussing on the mechanical properties first, we see from Fig. 5.5 that the coagulated planetesimals are fairly compact, $\phi \sim 10^{-1}$, despite their highly porous history. This relatively high internal density is the result of self-gravity compaction, not of collisional compaction (Kataoka et al. 2013b; Krijt et al. 2015). Skorov & Blum (2012) and Blum et al. (2014) argue that the tensile strengths of planetesimals formed out of direct coagulation of (sub)micron-size icy monomers are too large to explain the activity of comets at relatively large separations from the Sun, and conclude that a gravitational collapse of larger, mm-sized particles is more in line with the observed cometary activity. However, the porous aggregates capable of triggering SI in Sect. 5.4 are much larger and more porous than mm-sized pebbles, and it is not clear what the mechanical properties would be of a planetesimal formed out of their collapse. Nonetheless, studying the internal mechanical structure of large bodies will certainly lead to a better understanding of their formation history.

Second, the composition of the planetesimals might well be different for both formation mechanisms. Fig. 5.6 shows that the planetesimals, even though they form exclusively inside of 5 AU, contain material that was originally located between $\sim 3 - 60$ AU. As the disk's temperature and chemical structure shows significant variations at these (length-)scales, we can expect information about these variations to be locked up in the planetesimals. The formation of planetesimals through SI should lead to 'local' planetesimals; while the zone where SI-conditions are reached in Fig. 5.14 moves outward in time, it preferentially contains dust batches that originate from very close by.

5.6 Conclusions

We have developed a novel approach for calculating the evolution of the mass-dominating dust aggregates as they grow and drift in a protoplanetary disk. The dust population is described by a collection of dust batches, each one containing a mono-disperse dust population, which can move through the disk as a result of radial drift. The method allows the calculation of the global evolution of the dust surface density on Myr timescales, while preserving the essential characteristic of the porous growth process. The method is fast

and flexible, and can be readily extended to include more complex or time-dependent gas disk models.

We have used the method the study the formation of the first generation of planetesimals - the one that is capable of forming out of a smooth gaseous nebula - in disks around Sun-like stars. When fragmentation and erosion are inefficient, planetesimals can form through porous coagulation in the inner ∼10 AU (Okuzumi et al. 2012). In these cases:

1. Planetesimals form between $\sim 10^3$ and 10^5 yr for $\alpha = 10^{-3}$, and can include material that originates from very far out in the disk (Fig. 5.6). In more extended disks ($R_c = 100$) and disks with a weaker turbulence, the timescales for planetesimal formation are increased.

2. Planetesimal formation is very efficient, with a large fraction of the initial dust content of the disk ending up in planetesimals (Figs. 5.7 and 5.8). Relatively compact and dust-rich disks have the highest planetesimal formation efficiency, converting up to 90% of their dust into planetesimals within a million years.

3. The extent of the planetesimal formation zone depends on the total disk mass and metallicity (Fig. 5.9) and the disk temperature structure (Fig. 5.10). Massive disks ($0.2 M_\odot$) that are dust-rich ($Z_0 = 0.05$) or relatively cold, can form planetesimals out to 20 AU.

Alternatively, when erosion balances growth around $\Omega t_s \sim 1$ (Krijt et al. 2015), further coagulation is not possible, but conditions necessary for streaming instability (SI) might be reached. While for compact growth, terminated by bouncing/fragmentation at a collision velocity of ∼m s^{-1}, maximum Stokes numbers lie below $\Omega t_s \sim 10^{-2}$ (Fig. 5.12 and Drążkowska & Dullemond 2014), we find that:

4. Porous growth limited by drift-induced erosion is an effective way of creating aggregates with $10^{-2} \leq \Omega t_s \leq 1$ in a large region of the disk (Figs. 5.13, 5.14 and Krijt et al. 2015).

5. In a smooth gas disk, the most stringent condition for triggering SI is creating and maintaining a dense midplane layer of solids. We find both a high initial metallicity ($Z_0 = 0.05$) and low turbulence strength ($\alpha = 10^{-5}$) are needed to create such a layer. In such cases, a dense midplane layer (with a dust-to-gas ratio ≥1) will first form in the inner disk after several kyr, and then move out in time (Fig. 5.14).

6. When KH and SI give rise to a midplane turbulence given by Eq. 5.16, we can calculate the local metallicity that is needed to reach a mass loading of unity in the midplane (Fig. 5.15). We find that for typical disks, a super-Solar metallicity is needed ($Z^* \geq 0.03$), with the highest midplane density being reached at small radii. For example, for $Z^* = 0.03$, the region where $(\rho_d^*/\rho_g)_{z=0} \geq 1$ extends out to 10 AU. For colder disks, $Z^* = 0.02$ suffices in the inner 10 AU.

7. For a smooth disk profile, rapid porous growth followed by erosion leads to an inside-out clearing of the dust disk (Fig. 5.11). In such a scenario, no pile-ups are created, and the only way to reach high metallicities is to start out with them.

Acknowledgements

Dust studies at Leiden Observatory are supported through the Spinoza Premie of the Dutch science agency, NWO. S.K. would like to thank C.P. Dullemond, J. Drążkowska, and T. Birnstiel for encouraging discussions.

5.A Particle stopping time

The particle stopping time is a function of an aggregate's mass m and size a, and the properties of the local gas. Depending on the aggregate size in relation to a gas molecule mean free path $\lambda_{\rm map}$, the stopping time is given by the Epstein or Stokes drag regime through

$$t_s = \begin{cases} t_s^{(\rm Ep)} = \dfrac{3m}{4\rho_g v_{\rm th} A} & \text{for } a < \dfrac{9}{4}\lambda_{\rm mfp}, \\ t_s^{(\rm St)} = \dfrac{4a}{9\lambda_{\rm mfp}} t_s^{(\rm Ep)} & \text{for } a > \dfrac{9}{4}\lambda_{\rm mfp}, \end{cases} \tag{5.18}$$

with $v_{\rm th} = \sqrt{8/\pi} c_s$ the mean thermal velocity of the gas molecules. The mean free path depends on the gas density and is given by $\lambda_{\rm mfp} = m_g/(\sigma_{\rm mol}\rho_g)$, with $\sigma_{\rm mol} = 2 \times 10^{-15}$ cm^2 the molecular cross section. For porous aggregates, the cross section A equals the orientation-averaged projected cross-section Okuzumi et al. (2009).

Eq. 5.18 is valid when the particle Reynolds number $\mathrm{Re_p} = 4a v_{\rm dg}/(v_{\rm th}\lambda_{\rm mfp}) < 1$, with $v_{\rm dg}$ the relative velocity between the gas and the dust particle. For the largest bodies however, this condition is often not met. In these cases, it is useful to write the stopping time as

$$t_s = \frac{2m}{C_D \rho_g v_{\rm dg} A}, \tag{5.19}$$

with C_D the drag coefficient. Following Weidenschilling (1977a), we use

$$C_D = \begin{cases} 24(\mathrm{Re_p})^{-1} & \text{for } \mathrm{Re_p} < 1, \\ 24(\mathrm{Re_p})^{-3/5} & \text{for } 1 < \mathrm{Re_p} < 800, \\ 0.44 & \text{for } 800 < \mathrm{Re_p}. \end{cases} \tag{5.20}$$

For large Reynolds numbers, the stopping time depends the velocity relative to the gas, and one has to iterate to obtain t_s.

5.B Particle relative velocity

The relative velocity between particle 1 and particle 2 is obtained by adding various velocity sources quadratically. We take into account relative velocities arising from Brownian

motion, turbulence, radial drift, and azimuthal drift. The Brownian motion relative velocity is given by

$$\Delta v_{\rm BM} = \sqrt{\frac{8 k_{\rm B} T (m_1 + m_2)}{\pi m_1 m_2}}, \tag{5.21}$$

and depends only on the particle masses.

The turbulence-induced relative velocity between two particles with stopping times $t_{s,1}$ and $t_{s,2} \leq t_{s,1}$ has three regimes (Ormel & Cuzzi 2007)

$$\Delta v_{\rm turb} \simeq \delta v_g \times \begin{cases} {\rm Re_t}^{1/4}\, \Omega (t_{s,1} - t_{s,2}) & \text{for } t_{s,1} \ll t_\eta, \\ 1.4 \ldots 1.7 \left(\Omega t_{s,1}\right)^{1/2} & \text{for } t_\eta \ll t_{s,1} \ll \Omega^{-1}, \\ \left(\dfrac{1}{1+\Omega t_{s,1}} + \dfrac{1}{1+\Omega t_{s,2}} \right)^{1/2} & \text{for } t_{s,1} \gg \Omega^{-1}, \end{cases} \tag{5.22}$$

where $\delta v_g = \alpha^{1/2} c_s$ is the mean random velocity of the largest turbulent eddies, and $t_\eta = {\rm Re_t}^{1/2} t_L$ is the turn-over time of the smallest eddies. The turbulence Reynolds number ${\rm Re_t} = \alpha c_s^2 / (\Omega \nu_{\rm mol})$, with the molecular viscosity $\nu_{\rm mol} = v_{\rm th} \lambda_{\rm mfp}/2$.

The relative velocity from radial drift just equals $\Delta v_r = |v_{\rm drift}(\Omega t_{s,1}) - v_{\rm drift}(\Omega t_{s,2})|$, with the drift velocity given by Eq. 5.8. The azimuthal relative velocity is obtained in a similar way, as $\Delta v_\phi = |v_\phi(\Omega t_{s,1}) - v_\phi(\Omega t_{s,2})|$ with

$$v_\phi = -\frac{\eta v_{\rm K}}{1 + (\Omega t_s)^2}. \tag{5.23}$$

Finally, the total relative velocity is given by

$$v_{\rm rel} = \sqrt{(\Delta v_{\rm BM})^2 + (\Delta v_{\rm turb})^2 + (\Delta v_r)^2 + (\Delta v_\phi)^2}. \tag{5.24}$$

The particle stopping times and relative velocities are calculated in the midplane of the gas disk, as this is where most of the coagulation occurs.

5.C Particle porosity evolution

Initially, particles grow through low-energy hit-and-stick collisions. During this growth phase, the fractal dimension $D_f \simeq 2$, and the porosity is given by

$$\phi \simeq (m/m_0)^{1/2}. \tag{5.25}$$

The fractal growth regime ends when collisions become energetic enough for compaction, or when gas ram pressure compaction becomes effective. Collisional compaction occurs when the kinetic energy in a (same-size) collision exceeds the critical rolling energy $E_{\rm roll}$ (Dominik & Tielens 1997). Based on experimental investigations (Heim et al. 1999; Gundlach et al. 2011) and theoretical work (Krijt et al. 2014) we use

$$E_{\rm roll} = \left(\frac{a_0}{1\ \mu{\rm m}} \right)^{5/3} \times \begin{cases} 1.8 \times 10^{-7}\ {\rm erg} & \text{for ice particles,} \\ 8.5 \times 10^{-9}\ {\rm erg} & \text{for silicate particles.} \end{cases} \tag{5.26}$$

If the collisional energy E_K exceeds the critical energy for rolling, we make use of Eq. 31 of Okuzumi et al. (2012), which, depending on the turbulent velocity regime, predicts how the internal density (which is proportional to ϕ) scales with increasing particle mass. In practice, collisional compaction results in the porosity staying roughly constant in the regime where $E_K > E_{roll}$ (Okuzumi et al. 2012).

For low internal densities, Kataoka et al. (2013b) found that the external pressure a dust aggregate can just withstand equals

$$P_c = \frac{E_{roll}}{a_0^3}\phi^3. \tag{5.27}$$

This pressure can then be compared to the pressure arising form the surrounding gas and from self-gravity (Kataoka et al. 2013a)

$$P_{gas} = \frac{v_{dg}m}{\pi a^2 t_s}, \qquad P_{grav} = \frac{Gm^2}{\pi a^4}, \tag{5.28}$$

with G the gravitational constant.

In our semi-analytical model, we start by assuming fractal growth according to Eq. 5.25. At every increase in mass, we check *i)* if the energy in same-size collisions exceeds the critical energy for rolling, and *ii)* whether gas- or self-gravity compaction are expected. This involves calculating the stopping time, and relative collision velocity as a function of the current location in the gas disk. If collisional compaction is expected we make use of Eq. 31 of Okuzumi et al. (2012), and calculate the new porosity from the previous one. If gas- or self-gravity compaction are important we calculate $\phi(m)$ by setting Eq. 5.27 equal to Eq. 5.28.

6

A dearth of small particles in debris disks: An energy-constrained smallest fragment size

S. Krijt & M. Kama
Astronomy and Astrophysics, Volume 566, L2 (2014)

Abstract

A prescription for the fragment size distribution resulting from dust grain collisions is essential when modelling a range of astrophysical systems, such as debris disks and planetary rings. While the slope of the fragment size distribution and the size of the largest fragment are well known, the behaviour of the distribution at the small size end is theoretically and experimentally poorly understood. This leads debris disk codes to generally assume a limit equal to, or below, the radiation blow-out size. We use energy conservation to analytically derive a lower boundary of the fragment size distribution for a range of collider mass ratios. Focussing on collisions between equal-sized bodies, we apply the method to debris disks. For a given collider mass, the size of the smallest fragments is found to depend on collision velocity, material parameters, and the size of the largest fragment. We provide a physically motivated recipe for the calculation of the smallest fragment, which can be easily implemented in codes for modelling collisional systems. For plausible parameters, our results are consistent with the observed predominance of grains much larger than the blow-out size in Fomalhaut's main belt and in the *Herschel* cold debris disks.

6.1 Introduction

Fragmenting collisions are important in a range of astrophysical systems. While the slope of the fragment size distribution and the size of the largest fragment are well characterized and can be used confidently in models, the smallest fragment size is less well understood and is usually assumed to be constant for all collisions. We provide a framework for self-consistently calculating the smallest fragment size as a function of material and collision parameters (Sect. 6.2), and discuss its implications for modelling debris disks (Sect. 6.3).

Numerous experimental studies have looked at the fragment size distribution of destructive collisions, focussing on the slope of the power law(s), and on the size of the largest fragment (Davis & Ryan 1990; Ryan et al. 1991; Nakamura & Fujiwara 1991; Ryan 2000). The smaller end of the size distribution has received considerably less attention; the smallest fragments are hard to count experimentally, and require a very high resolution to be captured in numerical simulations. Fragment distributions are therefore incomplete below sizes of 100 μm, or masses below 10^{-3} g (Fujiwara et al. 1977; Takagi et al. 1984). Molecular dynamics (e.g., Dominik & Tielens 1997) or smooth particle hydrodynamics (Geretshauser et al. 2010) simulations have limited resolution and tend to focus on the fragmentation threshold velocity rather than the smallest fragments.

6.2 Minimum fragment size in a single collision

We consider collisions below the hypervelocity regime, i.e., the relative velocity of the colliders is much smaller than their internal sound speed, generally implying $v_{\rm rel} \lesssim 1$ km/s. Based on experiments, we adopt the standard fragment size distribution

$$n(s) = C \cdot s^{-\alpha}, \tag{6.1}$$

with $3 < \alpha < 4$, and C a coefficient we express below. While the mass is dominated by the largest particles, the surface area and thus the surface energy is dominated by the smallest fragments. As the creation of infinitely small fragments would require an infinite amount of energy, while the amount of kinetic energy available in a collision is finite, the power law must stop or flatten at some small fragment size. To the best of our knowledge, however, the regime of fragment sizes relevant for the analysis below has not yet been probed by available experimental data nor described theoretically in an astrophysical context.

Assuming spherical fragments with sizes between $s_{\rm min}$ and $s_{\rm max} (\gg s_{\rm min})$, the total fragment mass and surface area are

$$M_{\rm frag} = \frac{4\pi\rho C}{3(4-\alpha)} s_{\rm max}^{4-\alpha}, \qquad A_{\rm frag} = \frac{4\pi C}{\alpha - 3} s_{\rm min}^{3-\alpha}. \tag{6.2}$$

For a collision between two bodies of size s_0 and mass $M_0 = (4\pi/3)\rho s_0^3$, mass conservation implies $M_{\rm frag} = 2M_0$, and thus

$$C = 2(4-\alpha)s_0^3 s_{\max}^{\alpha-4}. \tag{6.3}$$

The pre-collision kinetic energy is simply $U_{\rm K} = (1/2)\mu v_{\rm rel}^2$, where $\mu = M_0/2$ denotes the reduced mass. The difference in surface energy before and after the collision equals $\Delta U_{\rm S} = \gamma(A_{\rm frag} - 8\pi s_0^2)$, where γ equals the surface energy per unit surface of the material. Assuming that only a fraction η of the kinetic energy is used for creating new surface, we can combine Eqs. 6.2 and 6.3 to obtain a lower limit for the smallest fragment size. For the specific case of $\alpha = 3.5$, this reduces to

$$s_{\min} = \left(\frac{24\gamma s_0}{\eta\rho s_0 v_{\rm rel}^2 + 24\gamma} \right)^2 s_{\max}^{-1}, \tag{6.4}$$

and gives the size of the smallest fragments created in a collision at $v_{\rm rel}$, assuming $\alpha = 3.5$ and $s_{\max} \gg s_{\min}$.

Instead of forming a fragment distribution, we imagine the limiting case in which the kinetic energy just suffices to split both colliders in half[1], i.e., $\eta U_{\rm K} = 2\pi s_0^2 \gamma$. Solving for s_0, we obtain

$$s_0^{\rm split} = \frac{3\gamma}{\eta\rho v_{\rm rel}^2}, \tag{6.5}$$

which is the smallest particle that can be split in half. The smallest fragment is slightly smaller, but does not have a rigorously defined radius because we assume spherical particles. Equation 6.5 is similar to the result of Biermann & Harwit (1980) if $\eta = 1$.

The same limit can be explored using Eq. 6.4, by forcing $s_{\min} \sim s_{\max} \sim 2^{-1/3} s_0$. This results in

$$s_{\min} \simeq \frac{5\gamma}{\eta\rho v_{\rm rel}^2}, \tag{6.6}$$

which is very similar to Eq. 6.5. To summarise, in an energetic collision in which many fragments are created, the size of the smallest fragment is given by Eq. 6.4. When the relative velocity is decreased, the fragment distribution becomes more and more discrete, until we reach the limit described by Eq. 6.6, in which particles can only just be split into two.

Figure 6.1 shows the minimum size from Eq. 6.4 as a function of collider size, assuming $v_{\rm rel} = 20$ m/s, $\eta = 10^{-2}$, and a maximum fragment that carries half of the initial collider mass. Gravity is important for bodies larger than 100 m (see below). Smaller bodies are weaker, and can produce fragments down to the $s_{\min}$ indicated by the solid curve. For example, SiO_2 fragments smaller than a micron can, at this velocity, *only* be formed by collisions of bodies larger than a few centimeters. The shaded region, top left, is forbidden, as there $M_{\rm frag} > 2M_0$ and mass is not conserved. Close to $s_{\min} \sim s_0$, the solid curves are non-linear as the pre- and post-collision surface areas become comparable.

[1]One could imagine splitting only one of the colliders, or indeed chipping off only small parts of one of the collider bodies. Since less surface area is created, this would still be allowed at very low velocities. However, in that case the largest fragment is of the same size as s_0. We refrain from identifying this as fragmentation, and use the size derived in Eq. 6.5 as the size below which fragmentation becomes inefficient.

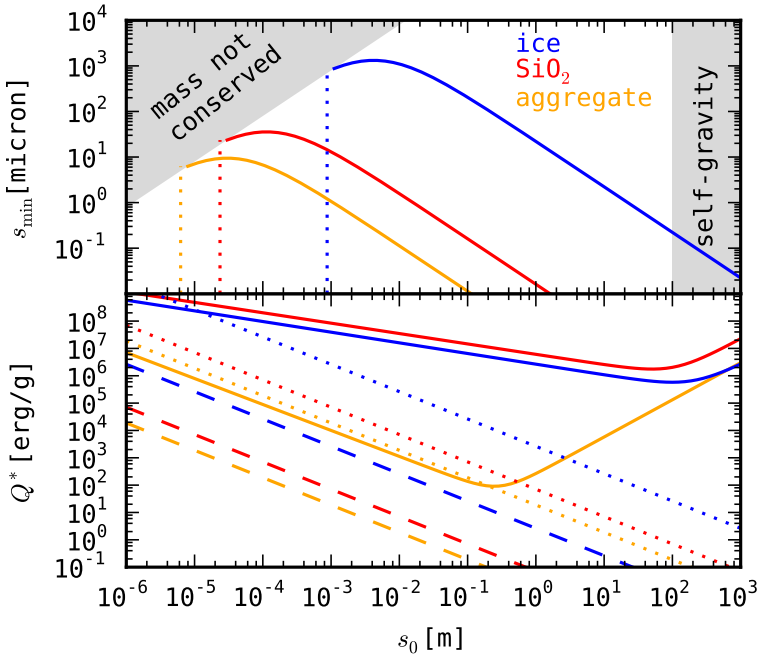

Figure 6.1: *Top:* Minimum fragment size $s_{\rm min}$ in a 20 m/s collision (Eq. 6.4) for three materials, as a function of collider size s_0. We have assumed $\eta = 10^{-2}$ and $s_{\rm max} = 2^{-1/3} s_0$. The grey shaded areas are excluded because of mass conservation (left), and self-gravity (right). The dotted lines indicate the limit of Eq. 6.6. *Bottom:* Critical energies versus size for equal-sized collisions. The energy needed to split a particle (e.g., Eq. 6.6) is shown for $\eta = 10^{-3}$ (dotted) and $\eta = 1$ (dashed). The solid curves correspond to catastrophic fragmentation of aggregates (Beitz et al. 2011), and ice and basalt (Benz & Asphaug 1999), showing both the strength-dominated (small sizes) and self-gravity dominated regimes (large sizes).

It is interesting to compare Eq. 6.6 with the traditional form of the catastrophic fragmentation threshold velocity in equal-sized collisions: $v_f^2 = 8Q^*$. The critical energy, Q^*, has units of erg/g, and varies with particle mass. For small bodies, the strength is dominated by cohesion, and for large ones by gravity (Benz & Asphaug 1999). For solid bodies, this transition occurs around 100 meters in size. Values of $Q^* \sim 10^7$ erg/g are often taken as typical for asteroids, and experimentally obtained values for small grains (mm to cm sizes) can be several orders of magnitude smaller (Blum & Münch 1993; Beitz et al. 2011). Figure 6.1 shows the critical energy for splitting predicted by Eq. 6.6 as a function of size for the materials in Table 6.1 assuming $\eta = 10^{-3}$ and $\eta = 1$. The solid lines indicate critical fragmentation energies for basalt and ice (Benz & Asphaug 1999) and silicate aggregates (Beitz et al. 2011). The critical fragmentation energies exceed the splitting energy, indicating that substantially more energy is required to destroy – rather than split – colliders. The values plotted for ice and basalt were obtained at collision

Material	ρ (g cm^{-3})	γ (J m^{-2})
Silicate	2.6	0.05
Ice	1.0	0.74
Aggregate	$\sim 10^{-1}$	$\sim 10^{-4} - 10^{-3}$

Table 6.1: Material properties for silicate and ice used in this work. The values for the typical aggregate are explained in Appendix 6.A.

velocities of 3 km/s, substantially higher than the velocities considered here, and Q^* is known to depend on velocity (Leinhardt & Stewart 2012). While such a velocity dependence appears absent in the splitting energy, it might be implicitly included in η. In fact, η is expected to vary with material and impact energy. We adopt a constant value of $\eta = 10^{-2}$.

Appendix 6.B investigates similar limits for colliders with different mass ratios, and shows that collisions with a mass ratio close to unity are the most effective at creating small fragments.

6.3 Application to debris disks

Debris disks are leftovers of planet formation, and are usually described by a birth-ring of km-sized asteroid-like particles orbiting their parent star, together with a population of smaller bodies formed in a collisional cascade (for a recent review, see Matthews et al. 2014). A steady-state and scale-independent population of bodies will follow a size distribution given by a power law with $\alpha = 3.5$ (Dohnanyi 1969). Some variation in α has been found in different simulations. Pan & Schlichting (2012) find up to $\alpha = 4$ for cohesion-dominated collisional particles, and up to $\alpha = 3.26$ for gravity-dominated ones.

Models of debris disks most often assume a smallest fragment size equal to the blow-out size, $s_{\rm blow}$ (Wyatt & Dent 2002; Wyatt et al. 2010), or some constant, but arbitrary, $s_{\rm min} < s_{\rm blow}$ for all collisions (Thébault et al. 2003; Krivov et al. 2008). The blow-out size corresponds to particles with $\beta = 1/2$, where

$$\beta = 1.15 Q_{\rm pr} \left(\frac{L_\star}{L_\odot}\right) \left(\frac{M_\star}{M_\odot}\right)^{-1} \left(\frac{\rho}{\rm g\ cm^{-3}}\right)^{-1} \left(\frac{s}{\mu\rm m}\right)^{-1}, \tag{6.7}$$

is the ratio of the radiation and gravitational force. Particles with $\beta > 1/2$ are removed from the system by radiation pressure. Alternatively, Gáspár et al. (2012) calculate a collision-dependent $s_{\rm min}$ from mass conservation, but do not study the surface energy.

If, however, for any relevant collision Eq. 6.4 predicts $s_{\rm min} > s_{\rm blow}$, extrapolating the fragment size distribution down to these sizes is not justified. For example, starting from Eq. 2 of Krivov et al. (2008), cm-sized bodies have $Q^* \simeq 5 \times 10^6$ erg/g. In the Krivov et al. framework, a collision between two such bodies at 70 m/s will then result in fragmentation, as the kinetic energy ($\simeq$12 J, assuming $\rho = 2.35$ g/cm^3) slightly exceeds the critical energy ($= 2mQ^* \simeq 10$ J), and fragments will be created from a size comparable

to the impactor (Eq. 21 of Krivov et al. 2006) down to the blow-out size. For this particular collision, Eq. 6.4 yields $s_{\rm min} \ll s_{\rm blow}$ for $\eta = 0.1$ and $\gamma = 0.1$ J/m^2, but $s_{\rm min} \simeq 6\,\mu$m for $\eta = 10^{-3}$. Thus, the difference between our results and the fragment sizes of Krivov et al. may be substantial, depending on the true value of η. We stress that our theory is valid for $3 > \alpha > 4$, and does not apply to models that use shallower power laws, for example Sect. 4.2 of Krivov et al. (2013).

The importance of the limit given by Eq. 6.4 depends on the parameters, and can vary per individual collision, depending on the collision velocity and choice for $s_{\rm max}$. In the rest of this section, we explore in which cases this limit is most relevant.

In a debris disk, a particle of size s_0 is most likely formed in a collision between only slightly larger particles. In addition, we focus on collisions between equal-sized particles, as these are most efficient at forming small fragments (Appendix 6.B). Therefore, we use Eq. 6.6 as an indication for the lower limit of the particle size distribution. Quantitative comparisons require relative collision velocities, which for the largest bodies are often written in terms of the Keplerian orbital velocity at the corresponding distance from the central object. For bodies on orbits with identical semi-major axes, the relative velocity can then be written in terms of orbital eccentricity and inclination as $f \equiv v_{\rm rel}/v_{\rm K} = (1.25e^2 + i^2)^{1/2}$, with $v_{\rm K} = (GM_\star/a)^{1/2}$ the Keplerian orbital velocity (Wyatt & Dent 2002). In a debris disk, a range of eccentricities and inclinations will be present. For a rough comparison, we use average quantities $\langle e \rangle$ and $\langle i \rangle$ to obtain typical collision velocities. In reality, $\langle e \rangle$ and $\langle i \rangle$ are poorly constrained. Estimates range from $\langle e \rangle \sim \langle i \rangle \sim 10^{-3} - 10^{-1}$, depending on the level of stirring (Matthews et al. 2014).

The ratio between the smallest grain size from Eq. 6.6 and the blow-out size then becomes

$$\frac{s_{\rm min}}{s_{\rm blow}} = 2.4 \left(\frac{a}{5{\rm AU}}\right) \left(\frac{L_\star}{L_\odot}\right)^{-1} \left(\frac{f}{10^{-2}}\right)^{-2} \left(\frac{\eta}{10^{-2}}\right)^{-1} \left(\frac{\gamma}{0.1\ {\rm J\ m^{-2}}}\right), \tag{6.8}$$

where both the stellar mass and the material density drop out, and we assumed $Q_{\rm pr} = 1$. Figure 6.2 compares this ratio with observations of debris disks at large radii, where we predict the most pronounced effect. We have used a fixed $\gamma = 0.1$ J m^{-2}, $f = 10^{-2}$, and $\eta = 10^{-2}$, and the arrows indicate the dependence of $s_{\rm min}/s_{\rm blow}$ on various parameters. For the main dust belt around Fomalhaut, Min et al. (2010) found the scattering properties to be consistent with predominantly $\sim$100 μm silicate grains ($s_{\rm blow} = 13\,\mu$m Acke et al. 2012). The relative velocities in Fomalhaut are typically taken a factor of 10 higher (Wyatt & Dent 2002). For HD105, Donaldson et al. (2012) derived $s_{\rm min} = 8.9\,\mu$m ($s_{\rm blow} = 0.5\,\mu$m) at orbital distances above $\sim$50 AU. Notably, very large grain sizes of $\sim$100 μm ($s_{\rm blow} \lesssim 1\,\mu$m) are inferred for the recently discovered "*Herschel* cold debris disks" (Krivov et al. 2013), which are seen around F, G, and K type stars. Krivov et al. were not able to model these systems with a collisional cascade reaching down to $s_{\rm min} = 3\,\mu$m, and proposed that the large grains in these systems are primordial, unstirred material. Our calculations suggest that they can also be explained as the outcome of a collisional cascade. However, the model is highly degenerate, as material properties (η and γ) and belt properties (f) are usually poorly known, and all have a large impact on $s_{\rm min}$.

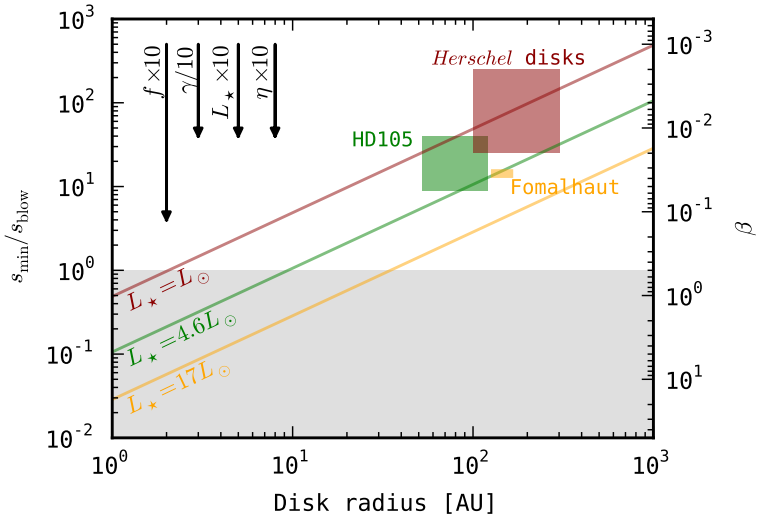

Figure 6.2: Predicted $s_{\rm min}/s_{\rm blow}$ in debris disks, as a function of disk radius. Arrows indicate how the ratio changes with stellar luminosity, surface energy, f, and η. Coloured regions indicate observational constraints on $s_{\rm min}/s_{\rm blow}$ for various systems (see text), and the diagonal solid lines give our calculations for each system. We fix $\gamma = 0.1\,{\rm J\,m^{-2}}$, $f = 10^{-2}$, and $\eta = 10^{-2}$ for this comparison.

In Figure 6.2, we assume constant and equal relative velocities for all particles. In reality, radiation pressure will also increase the eccentricities of small particles with $\beta \lesssim 0.5$. The enhanced eccentricity can be written as $e_\beta = \beta/(1-\beta)$. The relative velocity of such a radiation-influenced particle scales with its size as $v_{\rm rel} \propto \beta \propto s^{-1}$, while Eq. 6.6 predicts the fragmentation velocity scales as $v_{\rm rel} \propto s_0^{-1/2}$. Hence, the relative velocity between the smallest particles increases *faster* than the velocity needed for fragmentation. As a result, particles can reach arbitrarily small sizes in this regime. Particles smaller than $s_{\rm blow}$ are then removed on a short timescale. For a more detailed estimation, β should be evaluated for each particular case, considering the optical properties of the material and the shape of the stellar spectrum.

A dearth of small grains in weakly stirred disks is also predicted by Thébault & Wu (2008), but the cause is not a limit on $s_{\rm min}$. In their scenario, $s_{\rm min}$ is fixed and the production rate of the smallest grains decreases with weaker stirring, while the destruction rate is determined by radiation forces and is unaffected by stirring. While the smallest grains present are always of blow-out size, their abundance is set by the balance between their creation and destruction (their Figure 7).

While the theory developed in this work predicts that the smallest particles that can fragment further can be quite large and sizes just below this will be depleted, some smaller particles will still be created as a result of erosive collisions, collisions between larger bodies, and collisions that occur above the average collision velocity. Detailed debris disk

models implementing the surface energy constraint are needed to determine the resulting size distribution.

6.4 Discussion

Of the fundamental parameters in our model, the largest uncertainty affects η, the fraction of kinetic energy used for the creation of new surface. While information may be available about the kinetic and surface energy of the largest fragments, it is hard to quantify whether the remainder of the available energy went into surface creation, heat generation, or kinetic energy of the smallest fragments. Experimentally, studying η is challenging, since it requires sensitive and complete measurements down to very small sizes. Once the functional form of η is quantified by laboratory and numerical experiments, observations of $s_{\min}$ in a system of interest may constrain f and thus the local relative velocities.

During the preparation of this manuscript, we discovered that a similarly defined $s_{\min}$ to the one we present has been explored in a more abstract framework, and without elaborating on applications, by Bashkirov & Vityazev (1996). We note that the lack of data on the size distribution of small collision fragments, as well as the fraction of kinetic and internal energy in the fragments already noted by Bashkirov & Vityazev, still prevails and we encourage further experiments to quantify these important parameters.

Thus far, we have focussed on equal-sized collisions. While collisions with a larger mass ratio might not lead to catastrophic fragmentation, cratering and erosion may still be important, and might be able to form small particles (Appendix 6.B). Assuming a fixed relative velocity, we focus on a particle of size s_1. We define a mass loss rate $\dot{m}(s)$ for the larger particle, dependent on collider size s. Assuming a collision with a particle of size $s < s_1$ erodes a mass $\propto s^3$, and noting the collision timescale is proportional to the particle density and collision cross-section, we obtain for the *total* mass loss rate $\dot{M} = \dot{m}(s)\,\mathrm{d}s \propto s^{-3.5} s^3 (s + s_1)^2\,\mathrm{d}s$. If the collisional cross-section is dominated by s_1, we find $\dot{M} \propto s_1^2 s^{1/2}$, and thus the mass loss is dominated by the *larger* bodies. When $s \sim s_1$, we obtain $\dot{M} \propto s^{5/2}$.

We have adopted a constant value of 50% of the collider mass for the largest fragment. However, experiments show $s_{\max}$ can be substantially smaller as a function of material and impact velocity (e.g., Davis & Ryan 1990; Ryan et al. 1991). Such results can easily be implemented in Eq. 6.4 (and Eqs. 6.10 and 6.11) as necessary. Since $s_{\min} \propto s_{\max}^{-1}$, smaller sizes for the largest remnant will make the production of small particles even more difficult.

Other collisional systems where the proposed fragment size limit operates include planetary rings. Our calculations are consistent with the observed dominant grain sizes in the rings of Saturn, Jupiter, and Uranus. Because of additional relevant physics, such as tidal and electromagnetic effects, consistency does not directly imply the dominant grain size in all these rings is fragmentation-dominated.

The full implications of an energy-limited $s_{\min}$ on systems such as debris disks and planetary rings can only be assessed with models tracking the full particle population with all relevant processes included. For example, if small particles cannot be destroyed

in collisions, Poynting-Robertson (PR) drag will influence their orbits, and cause particles to drift towards the star on timescales of Gyrs in the outer parts of disks (Wyatt 2005; van Lieshout et al. 2014). Such modelling is outside the scope of the present paper.

6.5 Conclusions

We investigated the energetic constraints on the lower size limit in a distribution of collision fragments. A quantification of the lower limit of such size distributions is relevant for the modelling of debris disks and other astrophysical systems where collisional fragmentation is important.

1. Based on surface energy constraints, we derive a parameterised recipe for the smallest fragment size in individual grain-grain collisions.
2. The smallest size in a distribution of fragments from a two-particle collision, constrained by the collision energy, is given by Eq. 6.4, and illustrated in Figure 6.1. For example, at 20 m/s, submicron silicate particles can only be effectively produced by centimeter-sized colliders.
3. In the limit where the colliding bodies are split in half, the fragmentation threshold velocity is given by Eq. 6.6.
4. While dedicated models are needed to reveal the full implications of the fragment size limit, Figure 6.2 offers an indication of where the size distribution is expected to be influenced.
5. In systems where the collision velocities are low, our theory may offer a natural explanation for a paucity of small grains in debris at large orbital distances, such as observed in Fomalhaut and the *Herschel* cold debris disks (Figure 6.2).

Acknowledgements

The authors wish to thank Carsten Dominik and Xander Tielens for comments and discussions. Dust studies at Leiden Observatory are supported through the Spinoza Premie of the Dutch science agency, NWO. Astrochemistry in Leiden is supported by NOVA, KNAW and EU A-ERC grant 291141 CHEMPLAN.

6.A Applicability to aggregates

For porous aggregates, the basic principles explored here are expected to hold, but some material properties have to be altered. First, aggregates have an internal filling factor $\phi = \rho_{\rm agg}/\rho$ that is < 1, and might be as low as 10^{-4} in some extreme cases (Okuzumi et al. 2012; Kataoka et al. 2013a). Second, the 'effective' surface energy $\gamma_{\rm agg}$ will be smaller, since there is only limited contact between the aggregate's constituents to begin with. Assuming the parent bodies are built up of spherical monomers, the effective surface energy

can be estimated as $\gamma_{\rm agg} \sim (a/R)^2\phi^{2/3}\gamma$, where a and R denote the radius of the contact area shared by monomers, and the radius of the monomers themselves. The fraction (a/R) depends on the size of the monomers and the material properties, but for 0.1-micron-sized monomers, $(a/R) \sim 0.1$ is reasonable.

For aggregates, N-body simulations have been performed with particles containing up to 10^6 monomers, and values of η range from close to unity (Dominik & Tielens 1997; Wada et al. 2009), to several orders of magnitude less (Ringl et al. 2012), and depend on the employed contact model (Seizinger et al. 2013).

6.B Collisions with different mass ratios

Here we extend the theory to collisions between 'targets' and 'projectiles' of arbitrary sizes $s_{\rm t} > s_{\rm p}$. Assuming the fragment distribution can be described as before, we can still use Eq. 6.2, while the pre-collision kinetic energy now equals

$$U_{\rm K} = \frac{1}{2}\mu v_{\rm rel}^2 = \frac{1}{2}\frac{m_{\rm p}m_{\rm t}}{m_{\rm p}+m_{\rm t}}v_{\rm rel}^2. \tag{6.9}$$

For a given collision velocity, we might then think of two cases, complete fragmentation when $s_{\rm p} \sim s_{\rm t}$, and erosion/cratering when $s_{\rm t} \gg s_{\rm p}$.

6.B.1 Catastrophic fragmentation

Since both particles are destroyed completely we may set $M_{\rm frag} = m_{\rm p} + m_{\rm t}$. For simplicity we will assume in this section that the change in surface energy is dominated by the fragments $\Delta U_{\rm S} = \gamma A_{\rm frag}$. Using the same definition for η as before and focussing on the $\alpha = 3.5$ case, we obtain

$$s_{\rm min} = \left[\frac{6\gamma(s_{\rm p}^3 + s_{\rm t}^3)^2}{\eta\rho v_{\rm rel}^2 (s_{\rm p}s_{\rm t})^3}\right]^2 s_{\rm max}^{-1}. \tag{6.10}$$

6.B.2 Erosion

When the mass ratio becomes very large, it is no longer realistic to assume the target is completely disrupted. Rather, such collisions result in erosion, and the eroded mass is typically of the order of the mass of the projectile (Schräpler & Blum 2011). Thus, we write $M_{\rm frag} = \kappa m_{\rm p}$, with κ of the order of unity. For large mass ratios $\mu \to m_{\rm p}$. Furthermore, assuming that the change in surface energy is dominated by the new fragments, $\Delta U_S = \gamma A_{\rm frag}$, we obtain

$$s_{\rm min} = \left(\frac{6\gamma\kappa}{\eta\rho v_{\rm rel}^2}\right)^2 s_{\rm max}^{-1}. \tag{6.11}$$

Consider now a particle with a size s_0 close to the smaller end of the size distribution, colliding with particle of sizes s_x, ranging from slightly smaller to much larger than s_0. Figure 6.3 shows the minimum size of the fragments produced as a function of collider

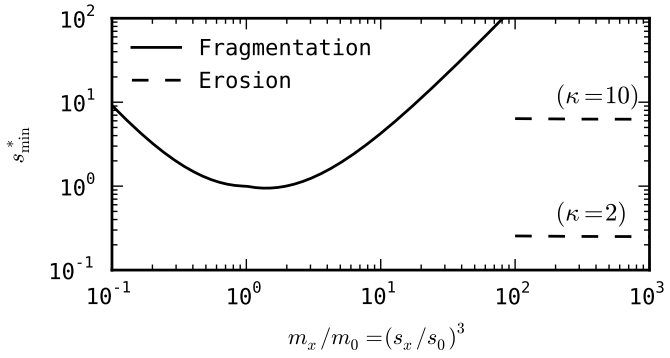

Figure 6.3: Minimum fragment size resulting from destructive unequal collisions, assuming $s_{\rm min} \ll s_{\rm max}$, and relating the largest fragment size to the heavier collider. The y-axis has been normalized with the value for $s_{\rm min}$ in equal-mass collisions.

size s_x. The y-axis is normalized to the value obtained in equal-sized collisions (i.e., between two s_0 particles). For mass ratios below unity, s_0 acts as the target, and the mass of the largest fragment is assumed to equal $m_0/2$. For large mass ratios, s_0 acts as a projectile instead, and the largest fragment mass is set to $m_x/2$. Collisions at mass ratios above 10^2 are assumed to be erosive (Seizinger et al. 2013), with the largest fragment equalling $m_0/2$. Since both the excavated mass, and the largest fragment mass, depend on the projectile, the curves in the erosive regime do not depend on the mass ratio directly. However, the size of the target does set an upper limit on κ.

7

Summary and outlook

The first step in the planet-formation process is the growth, through collision after collision, of microscopic dust grains into kilometer-size planetesimals. The goal of this thesis has been to achieve a better understanding of the microphysics that govern the collisional evolution of dust aggregates, and to understand not only how the physical structure of the growing aggregate is determined by its collisional history, but also how it influences the particle's future within the protoplanetary disk, and its chances of eventually growing into a planetesimal.

Here, I reiterate the main results of this thesis, and describe promising avenues for future research.

7.1 Collisions

Collisions are an important theme throughout this thesis: they help us understand the adhesive contact (Chapter 2); are the main drivers of dust evolution in protoplanetary disks (Chapters 4 and 5); and they are responsible for the production of small grains in debris disks (Chapter 6).

To understand and predict the behavior of aggregates in collisions, an intimate knowledge of the physical interaction between their microscopic constituents is required (see Sect. 1.3). By adding viscoelasticity and plastic deformation to the description of the adhesive contact, and comparing the theory to a collection of available experiments in the physics and astronomy literature, we have improved our knowledge of the forces governing head-on collisions (Chapter 2) and rolling motion (Chapter 3) of microscopic grains. These new force laws can readily be included in molecular dynamics simulations of macroscopic dust aggregates, themselves composed of large numbers of microspheres, to improve the collision model for aggregates.

Apart from silicates, experiments involving astronomically relevant materials (e.g., ices, organics, or mixtures of these materials) are scarce, and cover only a small part of the parameter space (grain size, aggregate porosity, etc.). Future experiments are necessary, not only to constrain the underlying physical model of Chapters 2 and 3, but also as a test for the molecular dynamics simulations of macroscopic aggregates.

7.2 Modeling coagulation

Simulating coagulation in protoplanetary disks is a challenging task, mainly because of the tremendous variety in particle sizes, collision velocities, and timescales that are involved. In this thesis, two very different numerical methods have been used to model the dust coagulation, each with their own advantages and disadvantages.

In Chapter 4, we employed a Monte Carlo (MC) technique to study coagulation locally, in a single vertical column of the protoplanetary disk. The MC method that was used is based on the distribution method of Ormel & Spaans (2008). The power of this approach is immediately clear from figures like Fig. 4.4: the method captures the complete mass distribution, even though at later times the smaller grains carry an insignificant amount of mass. This ability to resolve the full mass range is unique amongst Monte Carlo methods, and offers many possibilities for future research (see Sect. 4.6). The main disadvantages are that the model is local (though it treats the vertical direction in an integrated way), and that the simulations can slow down significantly when a steady-state is reached.

In Chapter 5, the semi-analytical model introduced in Sect. 4.5 is developed further to include the dust surface density evolution on a global scale. While this approach traces only the mass-dominating particles, it has the advantage of being very fast and flexible, while still capturing the essential features of the porous growth and radial drift processes. In principle, the method developed in Chapter 5 can readily be combined with more complex, time-dependent gas disk models, especially when the feedback of the dust onto the gas is small or dominated by the mass-dominating particles.

Understanding the aerodynamical properties of particles is very important when modeling their evolution. The coupling with the gas determines the collision velocity, but also the settling and radial drift behavior of the aggregate. In addition, compaction as a result of gas ram pressure can be an important mechanism to lower aggregate porosity. At the moment, the gas drag laws in the Epstein and Stokes regime are based on the assumption that the particles are compact and spherical (Whipple 1972). Future work is needed to test how accurate these drag laws are for highly-porous and irregular aggregates.

7.3 Growth barriers and planetesimal formation

The goal of this thesis has been to study how the microphysics influence the growth from grains to planetesimals, focussing in particular on their impact on several growth barriers (Sect. 1.2.3). It is clear that the microphysics are extremely important. For example, the

bouncing barrier disappears when aggregates can grow highly porously (Wada et al. 2011; Seizinger & Kley 2013). At the same time, the difference in adhesive/elastic properties of ice versus silicate grains results in a factor of ∼10 increase in the fragmentation threshold velocity (Dominik & Tielens 1997; Wada et al. 2013). With bouncing and catastrophic fragmentation less relevant for porous ice aggregates, the major hurdle for growth is then rapid radial drift.

One possibility to circumvent the drift barrier is to grow very rapidly when Stokes numbers are around unity (Okuzumi et al. 2012). Such rapid growth is possible in a region behind the snow line (aggregates must be icy to avoid fragmentation) that can extend out to 20 AU for the most massive and dust-rich disks (Chapter 5). This planetesimal formation mechanism is an efficient process, and converts a large fraction of the available solid mass into planetesimals.

However, an important result of this thesis is that growth through the drift barrier can be frustrated by erosion: mass-loss as the result of high-velocity impacts with small projectiles (Chapter 4). When this occurs, conditions suitable for triggering streaming instability might be reached in weakly-turbulent and cold disks. The model of Chapter 5 can be used to pinpoint points in time and space where conditions for SI can be reached. The next step here would be to model the coagulation inside the formed clumps, while taking into account the feedback of the dust on the gas motions. Such models are needed to determine the efficiency of planetesimal formation through SI, and the properties (i.e., sizes, masses) of the formed bodies.

Chapter 5 shows two clear pathways to planetesimal formation in the region of the disk where ices are present: rapid growth through direct coagulation, and formation through streaming instability (SI). The next step would be to model the further evolution of the planetesimals formed through direct growth or SI, and compare the characteristics of the planets that form to the observed exoplanet population. To take this step, effects such as gravitational focussing, stirring by gas density fluctuations and pebble accretion have to be included (Johansen et al. 2014). The method developed in Chapter 5 can act as a starting point for such models, as it gives the locations and total mass of the formed planetesimals, as well as the radial flux and characteristics of material drifting in as a function of time.

7.4 Realistic disks and opacities of porous grains

The disk models employed throughout this thesis have been fairly simple, with the gas and temperature structure being described by power laws and the turbulence parametrized by a single and constant α. Moreover, the properties of the gas disk were assumed to be static in time, and were not influenced by the dust population. In reality, disks are more complex environments, and the properties of the turbulence will vary with location, depending on the mechanism that is driving it (e.g., Turner et al. 2014). Moreover, the strength of the turbulence can be influenced by the dust particle properties. For example, the abundance of small grains influences the ionization degree, important for MRI turbulence, while the presence of a dense midplane layer of decoupled dust particles can trigger Kelvin-

Helmholtz or streaming instability. The next generation of models will have to combine these effects in a self-consistent way.

Lastly, in this thesis we have focussed on the mechanical properties of porous grains and their ability to grow larger, but perhaps equally important is connecting coagulation models to observations of protoplanetary disks. The majority of current models for millimeter emission from protoplanetary disks assume compact dust particles, and directly relate the spectral index at these wavelengths to a dominating dust particle size (e.g., Testi et al. 2014). However, from the simulations in Chapters 4 and 5 it is evident that aggregates do not resemble compact grains anywhere in the disk. Moreover, studies focussing on optical properties of porous grains (e.g., Cuzzi et al. 2014; Kataoka et al. 2014), find that absorption and scattering properties at micrometer-millimeter wavelengths are profoundly affected by particle porosity. To fully appreciate the impact grain porosity has on the appearance of the dust population in protoplanetary disks, self-consistent porous coagulation models will have to be combined with porosity-dependent dust opacities. The models developed in this thesis are an important step in that direction.

Bibliography

Acke, B., Min, M., Dominik, C., et al. 2012, Astronomy and Astrophysics, 540, A125

Alexander, R., Pascucci, I., Andrews, S., Armitage, P., & Cieza, L. 2014, Protostars and Planets VI, 475

Andrews, S. M., Rosenfeld, K. A., Kraus, A. L., & Wilner, D. J. 2013, The Astrophysical Journal, 771, 129

Andrews, S. M. & Williams, J. P. 2005, The Astrophysical Journal, 631, 1134

Andrews, S. M., Wilner, D. J., Hughes, A. M., Qi, C., & Dullemond, C. P. 2009, The Astrophysical Journal, 700, 1502

Armitage, P. J. 2010, Astrophysics of Planet Formation, ed. Armitage, P. J. (Cambridge University Press)

Aumatell, G. & Wurm, G. 2014, The Monthly Notices of the Royal Astronomical Society, 437, 690

Bai, X.-N. & Stone, J. M. 2010a, The Astrophysical Journal, 722, 1437

Bai, X.-N. & Stone, J. M. 2010b, The Astrophysical Journal, Letters to the Editor, 722, L220

Balbus, S. A. & Hawley, J. F. 1991, The Astrophysical Journal, 376, 214

Baney, J. M. & Hui, C.-Y. 1999, Journal of Applied Physics, 86, 4232

Barenblatt, G. 1962, in Advances in Applied Mechanics, Vol. 7, (Elsevier), 55 – 129

Barthel, E. & Frétigny, C. 2009, Journal of Physics D: Applied Physics, 42, 195302

Baruteau, C., Crida, A., Paardekooper, S.-J., et al. 2014, Protostars and Planets VI, 667

Bashkirov, A. G. & Vityazev, A. V. 1996, Planetary and Space Science, 44, 909

Beckwith, S. V. W., Sargent, A. I., Chini, R. S., & Guesten, R. 1990, The Astronomical Journal, 99, 924

Beitz, E., Güttler, C., Blum, J., et al. 2011, The Astrophysical Journal, 736, 34

Benz, W. & Asphaug, E. 1999, Icarus, 142, 5

Biermann, P. & Harwit, M. 1980, The Astrophysical Journal, Letters to the Editor, 241, L105

Birnstiel, T. & Andrews, S. M. 2014, The Astrophysical Journal, 780, 153

Birnstiel, T., Dullemond, C. P., & Brauer, F. 2009, Astronomy and Astrophysics, 503, L5

Birnstiel, T., Dullemond, C. P., & Brauer, F. 2010, Astronomy and Astrophysics, 513, A79
Birnstiel, T., Klahr, H., & Ercolano, B. 2012, Astronomy and Astrophysics, 539, A148
Birnstiel, T., Ormel, C. W., & Dullemond, C. P. 2011, Astronomy and Astrophysics, 525, A11
Blum, J., Gundlach, B., Mühle, S., & Trigo-Rodriguez, J. M. 2014, Icarus, 235, 156
Blum, J. & Münch, M. 1993, Icarus, 106, 151
Blum, J. & Wurm, G. 2000, Icarus, 143, 138
Blum, J. & Wurm, G. 2008, Annual Review of Astronomy and Astrophysics, 46, 21
Blum, J., Wurm, G., Kempf, S., et al. 2000, Physical Review Letters, 85, 2426
Brauer, F., Dullemond, C. P., & Henning, T. 2008a, Astronomy and Astrophysics, 480, 859
Brauer, F., Dullemond, C. P., & Henning, T. 2008b, Astronomy and Astrophysics, 480, 859
Brenner, S. S. 1956, Journal of Applied Physics, 27, 1484
Brenner, S. S. 1957, Journal of Applied Physics, 28, 1023
Brilliantov, N. V., Albers, N., Spahn, F., & Pöschel, T. 2007, Physical Review E, 76, 051302
Brilliantov, N. V. & Pöschel, T. 1998, EPL (Europhysics Letters), 42, 511
Brilliantov, N. V. & Pöschel, T. 1999, European Physical Journal B, 12, 299
Brilliantov, N. V., Spahn, F., Hertzsch, J.-M., & Pöschel, T. 1996, Physical Review E, 53, 5382
Brown, N. 1971, Materials Science and Engineering, 8, 69
Casassus, S., van der Plas, G., M, S. P., et al. 2013, Nature, 493, 191
Chaudhury, M. K. & Owen, M. J. 1993, The Journal of Physical Chemistry, 97, 5722
Chaudhury, M. K. & Whitesides, G. M. 1991, Langmuir, 7, 1013
Chen, Y. L., Helm, C. A., & Israelachvili, J. N. 1991, The Journal of Physical Chemistry, 95, 10736
Chokshi, A., Tielens, A. G. G. M., & Hollenbach, D. 1993, The Astrophysical Journal, 407, 806
Connelly, J. N., Bizzarro, M., Krot, A. N., et al. 2012, Science, 338, 651
Cuzzi, J. N., Estrada, P. R., & Davis, S. S. 2014, The Astrophysical Journal, Supplement Series, 210, 21
Cuzzi, J. N., Hogan, R. C., Paque, J. M., & Dobrovolskis, A. R. 2001, The Astrophysical Journal, 546, 496
Cuzzi, J. N., Hogan, R. C., & Shariff, K. 2008, The Astrophysical Journal, 687, 1432
Cuzzi, J. N. & Zahnle, K. J. 2004, The Astrophysical Journal, 614, 490
Dahneke, B. 1975, Journal of Colloid and Interface Science, 51, 58
Davies, M. B., Adams, F. C., Armitage, P., et al. 2014, Protostars and Planets VI, 787
Davis, D. R. & Ryan, E. V. 1990, Icarus, 83, 156
Demyk, K., Meny, C., Coupeaud, A., et al. 2012, in EAS Publications Series, Vol. 58, EAS Publications Series, ed. C. Stehlé, C. Joblin, & L. d'Hendecourt, 405–408

Derjaguin, B., Muller, V., & Toporov, Y. 1975, Journal of Colloid and Interface Science, 53, 314
Ding, W., Howard, A. J., Peri, M. D. M., & Cetinkaya, C. 2007, Philosophical Magazine, 87, 5685
Dittrich, K., Klahr, H., & Johansen, A. 2013, The Astrophysical Journal, 763, 117
Dohnanyi, J. S. 1969, Journal of Geophysical Research, 74, 2531
Dominik, C. & Dullemond, C. P. 2008, Astronomy and Astrophysics, 491, 663
Dominik, C. & Tielens, A. G. G. M. 1995, Philosophical Magazine, Part A, 72, 783
Dominik, C. & Tielens, A. G. G. M. 1996, Philosophical Magazine, Part A, 73, 1279
Dominik, C. & Tielens, A. G. G. M. 1997, The Astrophysical Journal, 480, 647
Donaldson, J. K., Roberge, A., Chen, C. H., et al. 2012, The Astrophysical Journal, 753, 147
Drążkowska, J. & Dullemond, C. P. 2014, Astronomy and Astrophysics, 572, A78
Drążkowska, J., Windmark, F., & Dullemond, C. P. 2014, Astronomy and Astrophysics, 567, A38
Dugdale, D. 1960, Journal of Mechanics Physics of Solids, 8, 100
Dullemond, C. P. & Dominik, C. 2005, Astronomy and Astrophysics, 434, 971
Dullemond, C. P., Hollenbach, D., Kamp, I., & D'Alessio, P. 2007, Protostars and Planets V, 555
Dunn, P. F., Brach, R. M., & Caylor, M. J. 1995, Aerosol Science and Technology, 23, 80
Dutrey, A., Semenov, D., Chapillon, E., et al. 2014, Protostars and Planets VI, 317
Flock, M., Ruge, J. P., Dzyurkevich, N., et al. 2015, Astronomy and Astrophysics, 574, A68
Frenkel, J. 1926, Zeitschrift für Physik A Hadrons and Nuclei, 37, 572
Fujiwara, A., Kamimoto, G., & Tsukamoto, A. 1977, Icarus, 31, 277
Gail, H.-P., Trieloff, M., Breuer, D., & Spohn, T. 2014, Protostars and Planets VI, 571
Gammie, C. F. 2001, The Astrophysical Journal, 553, 174
Garaud, P., Meru, F., Galvagni, M., & Olczak, C. 2013, The Astrophysical Journal, 764, 146
Gáspár, A., Psaltis, D., Özel, F., Rieke, G. H., & Cooney, A. 2012, The Astrophysical Journal, 749, 14
Geretshauser, R. J., Speith, R., Güttler, C., Krause, M., & Blum, J. 2010, Astronomy and Astrophysics, 513, A58
Gillespie, D. T. 1975, Journal of Atmospheric Sciences, 32, 1977
Gilman, J. J. 1960, Journal of Applied Physics, 31, 2208
Goldreich, P. & Ward, W. R. 1973, The Astrophysical Journal, 183, 1051
Gomes, R., Levison, H. F., Tsiganis, K., & Morbidelli, A. 2005, Nature, 435, 466
Greenwood, J. & Johnson, K. 2006, Journal of Colloid and Interface Science, 296, 284
Greenwood, J. A. 2004, Journal of Physics D: Applied Physics, 37, 2557
Greenwood, J. A. & Johnson, K. L. 1981, Philosophical Magazine A, 43, 697
Greenwood, J. A., Johnson, K. L., Choi, S.-H., & Chaudhury, M. K. 2009, Journal of Physics D: Applied Physics, 42, 035301

Griffith, A. A. 1921, Philosophical Transactions of the Royal Society of London. Series A, Containing Papers of a Mathematical or Physical Character, 221, 163
Guillot, T., Ida, S., & Ormel, C. W. 2014, Astronomy and Astrophysics, 572, A72
Gundlach, B. & Blum, J. 2015, The Astrophysical Journal, 798, 34
Gundlach, B., Kilias, S., Beitz, E., & Blum, J. 2011, Icarus, 214, 717
Güttler, C., Blum, J., Zsom, A., Ormel, C. W., & Dullemond, C. P. 2010, Astronomy and Astrophysics, 513, A56
Güttler, C., Heißelmann, D., Blum, J., & Krijt, S. 2012, ArXiv e-prints 1204.0001
Haisch, Jr., K. E., Lada, E. A., & Lada, C. J. 2001, The Astrophysical Journal, Letters to the Editor, 553, L153
Hardy, C., Baronet, C. N., & Tordion, G. V. 1971, International Journal for Numerical Methods in Engineering, 3, 451
Hartmann, L., Calvet, N., Gullbring, E., & D'Alessio, P. 1998a, The Astrophysical Journal, 495, 385
Hartmann, L., Calvet, N., Gullbring, E., & D'Alessio, P. 1998b, The Astrophysical Journal, 495, 385
Hayashi, C. 1981, Progress of Theoretical Physics Supplement, 70, 35
Heim, L.-O., Blum, J., Preuss, M., & Butt, H.-J. 1999, Phys. Rev. Lett., 83, 3328
Hertz, H. 1882, Journal für die reine und angewandte Mathematik, 92, 156
Hogerheijde, M. 1998, PhD thesis, The molecular environment of low-mass protostars
Hui, C.-Y., Baney, J. M., & Kramer, E. J. 1998, Langmuir, 14, 6570
Johansen, A., Blum, J., Tanaka, H., et al. 2014, Protostars and Planets VI, 547
Johansen, A., Oishi, J. S., Mac Low, M.-M., et al. 2007, Nature, 448, 1022
Johansen, A., Youdin, A., & Mac Low, M.-M. 2009, The Astrophysical Journal, Letters to the Editor, 704, L75
Johnson, K. L. 1987, Contact Mechanics, ed. Johnson, K. L. (Cambridge University Press)
Johnson, K. L. & Greenwood, J. A. 1997, Journal of Colloid and Interface Science, 192, 326
Johnson, K. L., Kendall, K., & Roberts, A. D. 1971, Royal Society of London Proceedings Series A, 324, 301
Johnson, W. L. & Samwer, K. 2005, Phys. Rev. Lett., 95, 195501
Kalas, P., Graham, J. R., Chiang, E., et al. 2008, Science, 322, 1345
Kalas, P., Graham, J. R., & Clampin, M. 2005, Nature, 435, 1067
Kataoka, A., Okuzumi, S., Tanaka, H., & Nomura, H. 2014, Astronomy and Astrophysics, 568, A42
Kataoka, A., Tanaka, H., Okuzumi, S., & Wada, K. 2013a, Astronomy and Astrophysics, 557, L4
Kataoka, A., Tanaka, H., Okuzumi, S., & Wada, K. 2013b, Astronomy and Astrophysics, 554, A4
Kempf, S., Pfalzner, S., & Henning, T. K. 1999, Icarus, 141, 388
Kim, O. & Dunn, P. 2007a, Journal of Aerosol Science, 39, 373
Kim, O. & Dunn, P. 2007b, Journal of Aerosol Science, 38, 532

Kirchschlager, F. & Wolf, S. 2014, Astronomy and Astrophysics, 568, A103
Klahr, H. 2004, The Astrophysical Journal, 606, 1070
Klahr, H. H. & Bodenheimer, P. 2003, The Astrophysical Journal, 582, 869
Kobayashi, H., Ormel, C. W., & Ida, S. 2012, The Astrophysical Journal, 756, 70
Kothe, S., Güttler, C., & Blum, J. 2010, The Astrophysical Journal, 725, 1242
Kozey, V. V. & Kumar, S. 1994, Journal of Materials Research, 9, 2717
Kraft, O., Gruber, P. A., Mönig, R., & Weygand, D. 2010, Annual Review of Materials Research, 40, 293
Kraus, A. L. & Ireland, M. J. 2012, The Astrophysical Journal, 745, 5
Krause, M. & Blum, J. 2004, Physical Review Letters, 93, 021103
Kretke, K. A. & Levison, H. F. 2014, The Astronomical Journal, 148, 109
Kretke, K. A. & Lin, D. N. C. 2007, The Astrophysical Journal, Letters to the Editor, 664, L55
Krijt, S. & Dominik, C. 2011, Astronomy and Astrophysics, 531, A80
Krijt, S., Dominik, C., & Tielens, A. G. G. M. 2014, Journal of Physics D Applied Physics, 47, 175302
Krijt, S., Güttler, C., Heißelmann, D., Dominik, C., & Tielens, A. G. G. M. 2013, Journal of Physics D Applied Physics, 46, 5303
Krijt, S., Ormel, C. W., Dominik, C., & Tielens, A. G. G. M. 2015, Astronomy and Astrophysics, 574, A83
Krivov, A. V., Eiroa, C., Löhne, T., et al. 2013, The Astrophysical Journal, 772, 32
Krivov, A. V., Löhne, T., & Sremčević, M. 2006, Astronomy and Astrophysics, 455, 509
Krivov, A. V., Müller, S., Löhne, T., & Mutschke, H. 2008, The Astrophysical Journal, 687, 608
Król, P. & Król, B. 2006, Journal of the European Ceramic Society, 26, 2241
Kuwabara, G. & Kono, K. 1987, Japanese Journal of Applied Physics, 26, 1230
Lagrange, A.-M., Bonnefoy, M., Chauvin, G., et al. 2010, Science, 329, 57
Lakes, R. 2009, Viscoelastic Materials (Cambridge University Press)
Lambrechts, M. & Johansen, A. 2012, Astronomy and Astrophysics, 544, A32
Lambrechts, M. & Johansen, A. 2014, Astronomy and Astrophysics, 572, A107
Landau, L. D. & Lifshitz, E. M. 1965, Elastizitaetstheorie, ed. Landau, L. D. & Lifshitz, E. M.
Leinhardt, Z. M. & Stewart, S. T. 2012, The Astrophysical Journal, 745, 79
Li, X., Dunn, P., & Brach, R. 1999, Journal of Aerosol Science, 30, 439
Lifshitz, J. & Kolsky, H. 1964, Journal of the Mechanics and Physics of Solids, 12, 35
Lissauer, J. J., Ragozzine, D., Fabrycky, D. C., et al. 2011, The Astrophysical Journal, Supplement Series, 197, 8
Lorenz, B., Krick, B. A., Mulakaluri, N., et al. 2013, Journal of Physics Condensed Matter, 25, 225004
Lynden-Bell, D. & Pringle, J. E. 1974, The Monthly Notices of the Royal Astronomical Society, 168, 603
Mark, J. E. 1999, Polymer Data Handbook, ed. J. E. Mark (Oxford University Press)
Marois, C., Macintosh, B., Barman, T., et al. 2008, Science, 322, 1348

Mathis, J. S., Rumpl, W., & Nordsieck, K. H. 1977, The Astrophysical Journal, 217, 425
Matthews, B. C., Krivov, A. V., Wyatt, M. C., Bryden, G., & Eiroa, C. 2014, Protostars and Planets VI, 521
Maugis, D. 1985, Journal of Materials Science, 20, 3041
Maugis, D. 1992, Journal of Colloid and Interface Science, 150, 243
Maugis, D. & Barquins, M. 1978, Journal of Physics D: Applied Physics, 11, 1989
Mayor, M. & Queloz, D. 1995, Nature, 378, 355
Meisner, T., Wurm, G., & Teiser, J. 2012, Astronomy and Astrophysics, 544, A138
Mesarovic, S. D. & Fleck, N. A. 2000, International Journal of Solids and Structures, 37, 7071
Min, M., Dullemond, C. P., Kama, M., & Dominik, C. 2011, Icarus, 212, 416
Min, M., Kama, M., Dominik, C., & Waters, L. B. F. M. 2010, Astronomy and Astrophysics, 509, L6
Morbidelli, A., Levison, H. F., Tsiganis, K., & Gomes, R. 2005, Nature, 435, 462
Mukai, T., Ishimoto, H., Kozasa, T., Blum, J., & Greenberg, J. M. 1992, Astronomy and Astrophysics, 262, 315
Muller, V., Yushchenko, V., & Derjaguin, B. 1980, Journal of Colloid and Interface Science, 77, 91
Murillo, N. M., Lai, S.-P., Bruderer, S., Harsono, D., & van Dishoeck, E. F. 2013, Astronomy and Astrophysics, 560, A103
Muzerolle, J., Calvet, N., Briceño, C., Hartmann, L., & Hillenbrand, L. 2000, The Astrophysical Journal, Letters to the Editor, 535, L47
Najita, J. R. & Kenyon, S. J. 2014, The Monthly Notices of the Royal Astronomical Society, 445, 3315
Nakagawa, Y., Sekiya, M., & Hayashi, C. 1986, Icarus, 67, 375
Nakamura, A. & Fujiwara, A. 1991, Icarus, 92, 132
Natta, A. & Testi, L. 2004, in Astronomical Society of the Pacific Conference Series, Vol. 323, Star Formation in the Interstellar Medium: In Honor of David Hollenbach, ed. D. Johnstone, F. C. Adams, D. N. C. Lin, D. A. Neufeeld, & E. C. Ostriker, 279
Natta, A., Testi, L., Calvet, N., et al. 2007, Protostars and Planets V, 767
Okuzumi, S., Tanaka, H., Kobayashi, H., & Wada, K. 2012, The Astrophysical Journal, 752, 106
Okuzumi, S., Tanaka, H., & Sakagami, M.-a. 2009, The Astrophysical Journal, 707, 1247
Okuzumi, S., Tanaka, H., Takeuchi, T., & Sakagami, M.-a. 2011, The Astrophysical Journal, 731, 95
Ormel, C. W. & Cuzzi, J. N. 2007, Astronomy and Astrophysics, 466, 413
Ormel, C. W. & Klahr, H. H. 2010, Astronomy and Astrophysics, 520, A43
Ormel, C. W. & Spaans, M. 2008, The Astrophysical Journal, 684, 1291
Ormel, C. W., Spaans, M., & Tielens, A. G. G. M. 2007, Astronomy and Astrophysics, 461, 215
Ossenkopf, V. 1993, Astronomy and Astrophysics, 280, 617
Pan, L., Padoan, P., Scalo, J., Kritsuk, A. G., & Norman, M. L. 2011, The Astrophysical Journal, 740, 6

Pan, M. & Schlichting, H. E. 2012, The Astrophysical Journal, 747, 113
Paszun, D. & Dominik, C. 2006, Icarus, 182, 274
Paszun, D. & Dominik, C. 2008, Astronomy and Astrophysics, 484, 859
Paszun, D. & Dominik, C. 2009, Astronomy and Astrophysics, 507, 1023
Pérez, L. M., Carpenter, J. M., Chandler, C. J., et al. 2012, The Astrophysical Journal, Letters to the Editor, 760, L17
Pérez, L. M., Isella, A., Carpenter, J. M., & Chandler, C. J. 2014, The Astrophysical Journal, Letters to the Editor, 783, L13
Peri, M. D. M. & Cetinkaya, C. 2005, Journal of Colloid and Interface Science, 288, 432
Peri, M. D. M. & Cetinkaya, C. 2005a, Philosophical Magazine, 85, 1347
Peri, M. D. M. & Cetinkaya, C. 2005b, Applied Physics Letters, 86, 194103
Petch, N. J. 1953, J. Iron Steel Inst., 174, 25
Petch, N. J. 1968, Fracture, ed. H. Liebowitz, Vol. 1 (Academic, New York), 351
Petigura, E. A., Howard, A. W., & Marcy, G. W. 2013, Proceedings of the National Academy of Science, 110, 19273
Pfalzner, S., Steinhausen, M., & Menten, K. 2014, The Astrophysical Journal, Letters to the Editor, 793, L34
Pinilla, P., Benisty, M., & Birnstiel, T. 2012a, Astronomy and Astrophysics, 545, A81
Pinilla, P., Birnstiel, T., Ricci, L., et al. 2012b, Astronomy and Astrophysics, 538, A114
Pollack, J. B., Hubickyj, O., Bodenheimer, P., et al. 1996, Icarus, 124, 62
Pontoppidan, K. M., Salyk, C., Bergin, E. A., et al. 2014, Protostars and Planets VI, 363
Poppe, T., Blum, J., & Henning, T. 2000, The Astrophysical Journal, 533, 454
Pöschel, T., Brilliantov, N. V., & Schwager, T. 2003, Physica A: Statistical Mechanics and its Applications, 325, 274
Quanz, S. P., Amara, A., Meyer, M. R., et al. 2013, The Astrophysical Journal, Letters to the Editor, 766, L1
Raettig, N., Lyra, W., & Klahr, H. 2013, The Astrophysical Journal, 765, 115
Rayleigh, L. 1906, Philosophical Magazine Series 6, 11, 283
Raymond, S. N., Kokubo, E., Morbidelli, A., Morishima, R., & Walsh, K. J. 2014, Protostars and Planets VI, 595
Reed, J. 1985, Journal of Physics D: Applied Physics, 18, 2329
Ricci, L., Testi, L., Natta, A., & Brooks, K. J. 2010, Astronomy and Astrophysics, 521, A66
Ringl, C., Bringa, E. M., Bertoldi, D. S., & Urbassek, H. M. 2012, The Astrophysical Journal, 752, 151
Ros, K. & Johansen, A. 2013, Astronomy and Astrophysics, 552, A137
Russell, S. S., Hartmann, L., Cuzzi, J., et al. 2006, Timescales of the Solar Protoplanetary Disk, ed. D. S. Lauretta & H. Y. McSween, 233–251
Ryan, E. V. 2000, Annual Review of Earth and Planetary Sciences, 28, 367
Ryan, E. V., Hartmann, W. K., & Davis, D. R. 1991, Icarus, 94, 283
Safronov, V. S. 1972, Evolution of the protoplanetary cloud and formation of the earth and planets.
Salo, H. 1995, Icarus, 117, 287

Salo, H., Schmidt, J., & Spahn, F. 2001, Icarus, 153, 295
Schapery, R. 1975a, International Journal of Fracture, 11, 141
Schapery, R. 1975b, International Journal of Fracture, 11, 369
Schapery, R. 1989, in Structural Integrity, ed. E. Folias (Springer Netherlands), 163–189
Schräpler, R. & Blum, J. 2011, The Astrophysical Journal, 734, 108
Schwager, T. & Pöschel, T. 1998, Physical Review E, 57, 650
Seizinger, A. & Kley, W. 2013, Astronomy and Astrophysics, 551, A65
Seizinger, A., Krijt, S., & Kley, W. 2013, Astronomy and Astrophysics, 560, A45
Seizinger, A., Speith, R., & Kley, W. 2012, Astronomy and Astrophysics, 541, A59
Sekiya, M. & Takeda, H. 2005, Icarus, 176, 220
Shakura, N. I. & Sunyaev, R. A. 1973, Astronomy and Astrophysics, 24, 337
She, H., Malotky, D., & Chaudhury, M. K. 1998, Langmuir, 14, 3090
Shu, F. H., Adams, F. C., & Lizano, S. 1987, Annual Review of Astronomy and Astrophysics, 25, 23
Siegel, D. J., Hector, L. G., & Adams, J. B. 2003, Phys. Rev. B, 67, 092105
Skorov, Y. & Blum, J. 2012, Icarus, 221, 1
Sorace, C., Louge, M., Crozier, M., & Law, V. 2009, Mechanics Research Communications, 36, 364
Sperling, L. H. 2007, Introduction to physical polymer science, 4th Edition (John Wiley & Sons)
Stronge, W. J. 1990, Proceedings of the Royal Society of London. Series A: Mathematical and Physical Sciences, 431, 169
Sümer, B. & Sitti, M. 2008, Journal of Adhesion Science and Technology, 22, 481
Suyama, T., Wada, K., & Tanaka, H. 2008, The Astrophysical Journal, 684, 1310
Suyama, T., Wada, K., Tanaka, H., & Okuzumi, S. 2012, The Astrophysical Journal, 753, 115
Tabor, D. 1955, Royal Society of London Proceedings Series A, 229, 198
Tabor, D. 1977, Journal of Colloid and Interface Science, 58, 2
Takagi, Y., Mizutani, H., & Kawakami, S.-I. 1984, Icarus, 59, 462
Takeuchi, T., Muto, T., Okuzumi, S., Ishitsu, N., & Ida, S. 2012, The Astrophysical Journal, 744, 101
Tanaka, H., Wada, K., Suyama, T., & Okuzumi, S. 2012, Progress of Theoretical Physics Supplement, 195, 101
Testi, L., Birnstiel, T., Ricci, L., et al. 2014, Protostars and Planets VI, 339
Thébault, P., Augereau, J. C., & Beust, H. 2003, Astronomy and Astrophysics, 408, 775
Thébault, P. & Wu, Y. 2008, Astronomy and Astrophysics, 481, 713
Thornton, C. & Ning, Z. 1998, Powder Technology, 99, 154
Tielens, A. G. G. M., McKee, C. F., Seab, C. G., & Hollenbach, D. J. 1994, The Astrophysical Journal, 431, 321
Tobin, J. J., Hartmann, L., Chiang, H.-F., et al. 2012, Nature, 492, 83
Tsai, Pui, & Liu. 1990, Aerosol Science and Technology, 12, 497
Tsiganis, K., Gomes, R., Morbidelli, A., & Levison, H. F. 2005, Nature, 435, 459
Turner, N. J., Fromang, S., Gammie, C., et al. 2014, Protostars and Planets VI, 411

Uribe, A. L., Klahr, H., & Henning, T. 2013, The Astrophysical Journal, 769, 97
van der Marel, N., van Dishoeck, E. F., Bruderer, S., et al. 2013, Science, 340, 1199
van Lieshout, R., Dominik, C., Kama, M., & Min, M. 2014, Astronomy and Astrophysics, 571, A51
Vigil, G., Xu, Z., Steinberg, S., & Israelachvili, J. 1994, Journal of Colloid and Interface Science, 165, 367
Voelk, H. J., Jones, F. C., Morfill, G. E., & Roeser, S. 1980, Astronomy and Astrophysics, 85, 316
Volkert, C. A. & Lilleodden, E. T. 2006, Philosophical Magazine, 86, 5567
Wada, K., Tanaka, H., Okuzumi, S., et al. 2013, Astronomy and Astrophysics, 559, A62
Wada, K., Tanaka, H., Suyama, T., Kimura, H., & Yamamoto, T. 2007, The Astrophysical Journal, 661, 320
Wada, K., Tanaka, H., Suyama, T., Kimura, H., & Yamamoto, T. 2009, The Astrophysical Journal, 702, 1490
Wada, K., Tanaka, H., Suyama, T., Kimura, H., & Yamamoto, T. 2011, The Astrophysical Journal, 737, 36
Wahl, K., Asif, S., Greenwood, J., & Johnson, K. 2006, Journal of Colloid and Interface Science, 296, 178
Wall, S., John, W., Wang, H.-C., & Goren, S. L. 1990, Aerosol Science and Technology, 12, 926
Weidenschilling, S. J. 1977a, The Monthly Notices of the Royal Astronomical Society, 180, 57
Weidenschilling, S. J. 1977b, Astrophysics and Space Science, 51, 153
Weidenschilling, S. J. 1980, Icarus, 44, 172
Whipple, F. L. 1972, in From Plasma to Planet, ed. A. Elvius, 211
Williams, J. P. & Cieza, L. A. 2011, Annual Review of Astronomy and Astrophysics, 49, 67
Wilner, D. J., D'Alessio, P., Calvet, N., Claussen, M. J., & Hartmann, L. 2005, The Astrophysical Journal, Letters to the Editor, 626, L109
Windmark, F., Birnstiel, T., Güttler, C., et al. 2012a, Astronomy and Astrophysics, 540, A73
Windmark, F., Birnstiel, T., Ormel, C. W., & Dullemond, C. P. 2012b, Astronomy and Astrophysics, 544, L16
Wu, C.-y., Li, L.-y., & Thornton, C. 2003, International Journal of Impact Engineering, 28, 929
Wu, C.-Y., Li, L.-Y., & Thornton, C. 2005, International Journal of Impact Engineering, 32, 593
Wurm, G., Paraskov, G., & Krauss, O. 2004, The Astrophysical Journal, 606, 983
Wurm, G., Paraskov, G., & Krauss, O. 2005, Icarus, 178, 253
Wyatt, M. C. 2005, Astronomy and Astrophysics, 433, 1007
Wyatt, M. C., Booth, M., Payne, M. J., & Churcher, L. J. 2010, The Monthly Notices of the Royal Astronomical Society, 402, 657

Wyatt, M. C. & Dent, W. R. F. 2002, The Monthly Notices of the Royal Astronomical Society, 334, 589
Yano, O. & Wada, Y. 1971, Journal of Polymer Science B Polymer Physics, 9, 669
Yoshizawa, H., Chen, Y. L., & Israelachvili, J. 1993, The Journal of Physical Chemistry, 97, 4128
Youdin, A. N. & Chiang, E. I. 2004, The Astrophysical Journal, 601, 1109
Youdin, A. N. & Goodman, J. 2005, The Astrophysical Journal, 620, 459
Youdin, A. N. & Lithwick, Y. 2007, Icarus, 192, 588
Zhu, Y., Qin, Q., Xu, F., et al. 2012, Phys. Rev. B, 85, 045443
Zsom, A. & Dullemond, C. P. 2008, Astronomy and Astrophysics, 489, 931
Zsom, A., Ormel, C. W., Dullemond, C. P., & Henning, T. 2011, Astronomy and Astrophysics, 534, A73
Zsom, A., Ormel, C. W., Güttler, C., Blum, J., & Dullemond, C. P. 2010, Astronomy and Astrophysics, 513, A57

Curriculum vitae

I was born on January 13, 1987 in Leidschendam, in the province of Zuid-Holland, and grew up in Voorburg, a town famous for its Roman roots and for 'Hofwijck', the country house of the Huygens family. I attended Basisschool de Lusthof together with my brother and sister, and started my high school education at the nearby Huygenslyceum in 1998.

After graduating high school in 2005, I decided to move to the Dutch capital and start the Bachelor of Physics at the University of Amsterdam, from which I graduated with honors early 2009. Enjoying life in Amsterdam, I subsequently started the Master of Astronomy and Astrophysics at the UvA. During these years, I was drawn towards the 'low-energy' part of the curriculum, and particularly enjoyed the courses on the solar system, planet formation, and the interstellar medium. In the second year of the Master, I started a research project with Prof. dr. Carsten Dominik studying the effect of migrating planets of populations of asteroids. During this project, which resulted in my first scientific publication (Krijt & Dominik 2011), I realized how much I liked doing research, and I was delighted when I got the opportunity to start a PhD at Leiden Observatory under the supervision of Prof. dr. Xander Tielens and Prof. dr. Carsten Dominik in January 2011.

I spent the first half of my PhD examining the adhesive contact between microscopic grains, after which I applied this knowledge to study dust coagulation in planet-forming regions. In addition, I was a teaching assistant for 'Praktische Sterrenkunde' and 'Sterrenkunde Practicum 2' by Prof. dr. Snellen and Dr. Hoekstra. During my PhD, I presented the results of this thesis at international conferences in the Netherlands, Sweden, and Germany, and during visits to several universities in the United States.

List of publications

First-author articles

1. **S. Krijt**, C. W. Ormel, C. Dominik, and A. G. G. M. Tielens
   A panoptic model for planetesimal formation
   Astronomy & Astrophysics, to be submitted

2. **S. Krijt**, C. W. Ormel, C. Dominik, and A. G. G. M. Tielens
   Erosion and the limits to planetesimal growth
   Astronomy & Astrophysics, Volume 574, A83 (2015)

3. **S. Krijt** and M. Kama
   A dearth of small particles in debris disks:
   An energy-constrained smallest fragment size
   Astronomy & Astrophysics, Volume 566, L2 (2014)

4. **S. Krijt**, C. Dominik, and A. G. G. M. Tielens
   Rolling friction of adhesive microspheres
   Journal of Physics D: Applied Physics, Volume 47, Issue 17 (2014)

5. **S. Krijt**, C. Güttler, D. Heißelmann, C. Dominik, and A. G. G. M. Tielens
   Energy dissipation in head-on collisions of spheres
   Journal of Physics D: Applied Physics, Volume 46, Issue 43 (2013)

6. **S. Krijt** and C. Dominik
   Stirring up the dust: A dynamical model for halo-like dust clouds in transitional disks
   Astronomy & Astrophysics, Volume 531, A80 (2011)

Co-authored articles

7. B. B. Ochsendorf, N. J. L. Cox, **S. Krijt**, F. Salgado, O. Berné, J. P. Bernard, L. Kaper, and A. G. G. M. Tielens
Blowing in the wind: The dust wave around σ Ori AB
Astronomy & Astrophysics, Volume 563, A65 (2014)

8. A. Seizinger, **S. Krijt**, and W. Kley
Erosion of dust aggregates
Astronomy & Astrophysics, Volume 560, A45 (2013)

9. C. Güttler, D. Heißelmann, J. Blum, and **S. Krijt**
Normal Collisions of Spheres: A Literature Survey on Available Experiments
arXiv:1204.0001 (2012)

Nederlandse samenvatting

Overal Aardklooten

Aan het einde van de 17e eeuw schreef Christiaan Huygens in zijn *Cosmotheoros*, zich richtend tot zijn broer Constantijn:

> "Welk een wonderbaarlijke, welk een verbazende grootte en heerlijkheid van de Wereld moet men dan met het verstand bezeffen! Zoo vele Zonnen, zoo vele Aardklooten, en een yder van haar met zoo vele Kruiden, Boomen, Dieren, met zoo vele Zeen en Bergen vercierd! Een verwondering, die nog zal vergroot worden, indien iemand in overweging neemt het gene wy van den afstand en de menigte der Vaste Starren gezegt hebben."

Meer dan 300 jaar later blijkt de visie van Christiaan Huygens bijzonder accuraat. Missies naar planeten en manen in ons eigen zonnestelsel resulteren in spectaculaire beelden van Zeen (niet van water, maar toch) en Bergen, sommige vele malen hoger dan de hoogste bergen op Aarde. Planeten buiten ons zonnestelsel (exoplaneten) zijn vanwege hun afstand moeilijker te zien en te bestuderen, maar door slim gebruik te maken van geavanceerde telescopen zowel op Aarde als in de ruimte kunnen sterrenkundigen ze toch ontdekken. Bovendien kunnen we steeds meer zeggen over de eigenschappen van deze werelden. Sinds de ontdekking van de eerste exoplaneet door Mayor & Queloz in 1995, zijn er nu 1876 exoplaneten bekend en het aantal groeit vrijwel iedere dag[1]. Planetenstelsels blijken de regel, niet de uitzondering: kies een willekeurige ster aan de (nachtelijke) hemel en je kunt ervan uitgaan dat er meerdere planeten omheen draaien. Bovendien denken we nu dat om één op de vijf zon-achtige sterren een aard-achtige planeet draait; een planeet die ongeveer even groot is als de Aarde, op een dusdanige afstand van zijn ster dat de temperatuur er de aanwezigheid van vloeibaar water toestaat. Als leven elders lijkt op het leven op Aarde, zijn deze planeten goede plaatsen om te zoeken naar Huygens' Kruiden, Boomen en Dieren.

[1] De tussenstand wordt bijgehouden op `http://exoplanet.eu`.

De ontdekking dat het in de kosmos wemelt van de planeten brengt een aantal prangende vragen met zich mee: Hoe zijn al deze planeten gevormd en welke processen spelen een rol bij hun geboorte? Wat bepaalt de grootte van de planeet, zijn dichtheid, en de samenstelling van zijn atmosfeer? Vandaag de dag hebben astronomen een globaal beeld van ster- en planeetvorming. Dit beeld is opgebouwd uit kennis van ons eigen zonnestelsel en waarnemingen van sterren en planeten ver daarbuiten, aangevuld met experimenteel en theoretisch onderzoek.

Ster- en planeetvorming

De ruimte tussen sterren is gevuld met een dun moleculair gas. Op de meeste plekken in de kosmos is dit gas extreem ijl, met doorgaans maar een paar atomen per kubieke centimeter. Op sommige plaatsen, in zogeheten moleculaire wolken, zijn de dichtheden echter hoger, met soms wel een miljoen atomen per kubieke centimeter. Sommige moleculaire wolken worden zo zwaar dat ze ineen storten onder hun eigen zwaartekracht. Wanneer dit gebeurt, vormt zich een nieuwe (proto)ster, met daaromheen een protoplanetaire schijf. Deze schijf is een noodzakelijk bijproduct van het stervormingsproces en is typisch zo'n 100 AU groot[2]. De massa van de schijf is ongeveer 100 maal kleiner dan die van de jonge ster zelf. Figuur 7.1 laat een opname van de Orionnevel zien, met daarin een aantal pasgeboren sterren omringd door gas en stof. Uit het gas en stof in deze protoplanetaire schijven ontstaan planeten. In ons eigen zonnestelsel, nu ongeveer 4.567 miljard jaar oud, is de protoplanetaire gasschijf allang vervlogen, maar we zien er wel tekenen van terug. Zo liggen de banen van alle planeten nagenoeg in hetzelfde vlak en draaien de planeten in dezelfde richting rond de zon.

Protoplanetaire schijven bestaan voor 99% uit gas, voornamelijk waterstof, en voor 1% uit stof: kleine microscopische deeltjes van silicaten, koolstof, ijs, en een aantal andere elementen. Uit dit stof worden de kernen van planeten gevormd. De stofkorrels, aanvankelijk niet groter dan een micrometer, botsen en plakken aan elkaar, en vormen zo steeds grotere deeltjes. Pas als de deeltjes een aantal kilometer groot zijn begint hun zwaartekracht een rol te spelen en wordt hun groei versneld. Deze grote deeltjes noemen we *planetesimalen*, de bouwstenen van planeten. De planetesimalen botsen en groeien verder, totdat er planeetkernen zijn gevormd. Deze kernen hebben een sterke zwaartekracht en zijn hierdoor in staat gas uit de protoplanetaire schijf aan zich te binden; ze vormen een primitieve atmosfeer. Verreweg de meeste gasschijven worden waargenomen rond zeer jonge, pasgeboren sterren, niet ouder dan een paar miljoen jaar. De kernen van gasreuzen zoals Jupiter en Saturnus moeten gevormd zijn toen de schijf rijk aan gas was, wat ons vertelt dat het proces van planeetvorming hooguit een paar miljoen jaar kan duren. Figuur 7.2 laat zien hoe planeetvorming er uit zou kunnen zien in een protoplanetaire schijf.

Het bestuderen van de groei van een stofkorrel tot planeet is een uitdagende onderneming, bemoeilijkt door het feit dat we het proces niet direct kunnen waarnemen. Daar

[2]Een AU = 149597871 km is ongeveer de afstand tussen de Aarde en de Zon.

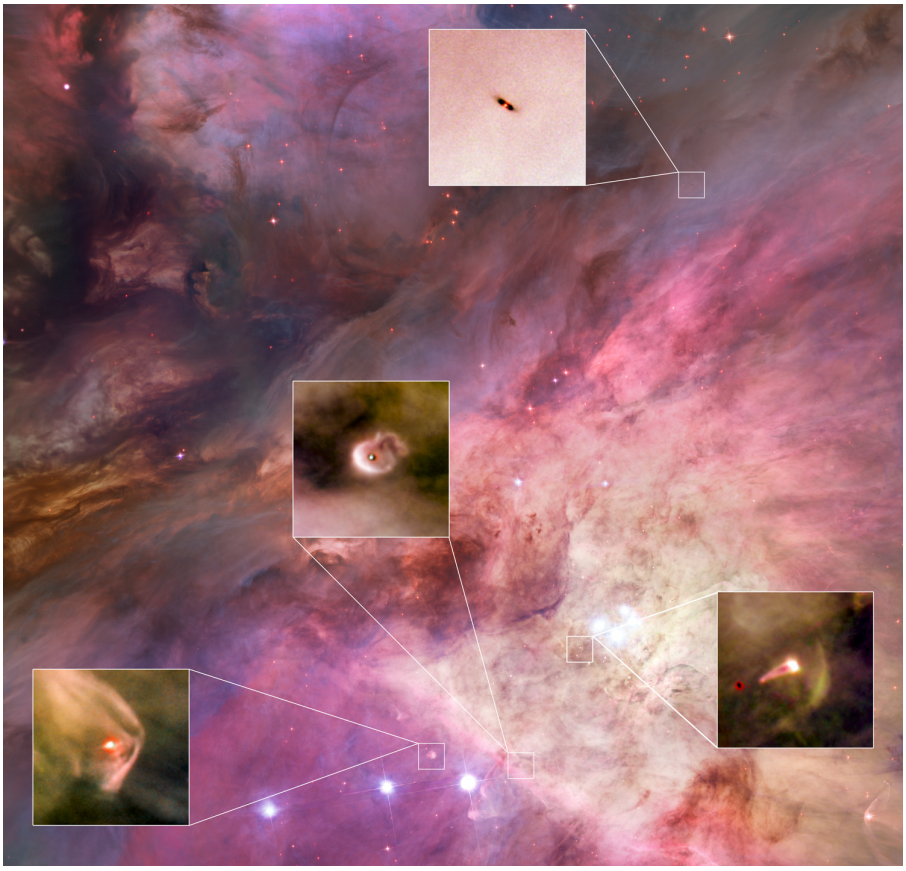

Figuur 7.1: Jonge sterren met protoplanetaire schijven in de Orionnevel. Zulke opnamen vormen een direct bewijs voor het bestaan van protoplanetaire schijven. Foto: NASA, ESA, M. Robberto (Space Telescope Science Institute/ESA), the Hubble Space Telescope Orion Treasury Project Team and L. Ricci (ESO).

waar we rond jonge sterren wel de kleinste stofkorrels kunnen zien (omdat ze het sterlicht op een efficiënte manier beïnvloeden) en de grootste planeten kunnen waarnemen (bijvoorbeeld omdat ze voor hun ster langs schuiven), zijn de tussenproducten vrijwel onzichtbaar. Onderzoek naar deze tussenliggende stappen gebeurt daarom vaak met theoretische modellen en computersimulaties.

Van stofkorrel tot planetesimaal

De eerste stap in het bouwen van planeten, die van stofkorrel tot planetesimaal, is misschien wel de minst begrepen stap. Computersimulaties en experimenten in laboratoria

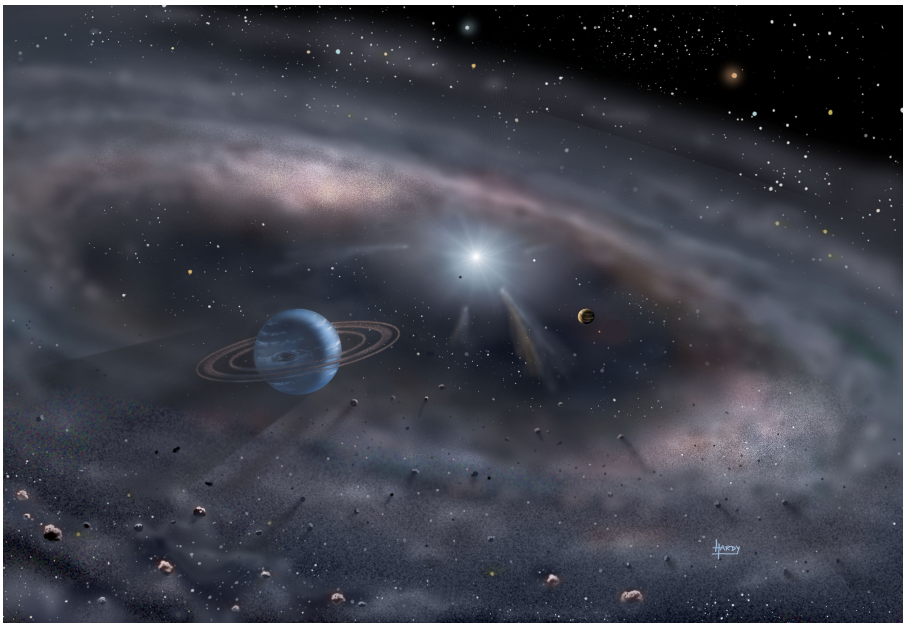

Figuur 7.2: Artistieke weergave van een protoplanetaire schijf. Kleine stofkorrels zijn samengeklonterd tot grotere lichamen en er heeft zich een planeet met een ringsysteem gevormd. Figuur: David A. Hardy/www.astroart.org.

leren ons dat stofdeeltjes, als ze groter zijn dan ongeveer een centimeter, maar moeizaam aan elkaar blijven plakken. In de protoplanetaire schijf wordt de onderlinge botsingssnelheid tussen deze deeltjes bepaald door interactie met het gas. Deze botsingssnelheden kunnen oplopen tot enkele tientallen meters per seconde. Als deeltjes willen groeien moeten ze, zelfs met deze hoge botsingssnelheden, aan elkaar zien te plakken. Een bijkomend probleem is dat deeltjes van ongeveer een meter last hebben van 'wind tegen'. Ze vliegen rond met een snelheid die iets groter is dan die van het gas, en raken energie kwijt aan de tegenwind die ze daardoor ervaren. Als direct gevolg verliezen de deeltjes energie en vallen ze vrij snel richting de jonge ster. Hierdoor worden grote delen van de schijf schoongeveegd en stofvrij gemaakt. Geavanceerde computermodellen die de groei van grote ensembles deeltjes rond jonge sterren simuleren vinden dan ook dat, als gevolg van deze problemen, stofdeeltjes erg veel moeite hebben om groter te worden dan een centimeter of een meter.

En toch zien we overal om ons heen planeten. Kennelijk is de natuur in staat om in vrijwel elke protoplanetaire schijf, en binnen een paar miljoen jaar, meerdere planeten te vormen. Het lijkt er dus op dat er iets belangrijks ontbreekt in onze modellen.

Een relatief nieuw idee is het kijken naar de *porositeit* van groeiende stofdeeltjes. Voor het gemak werd vaak aangenomen dat stofdeeltjes compact en rond zijn, maar dit is lang niet altijd een nauwkeurige weergave van de werkelijkheid. Figuur 7.3 laat een com-

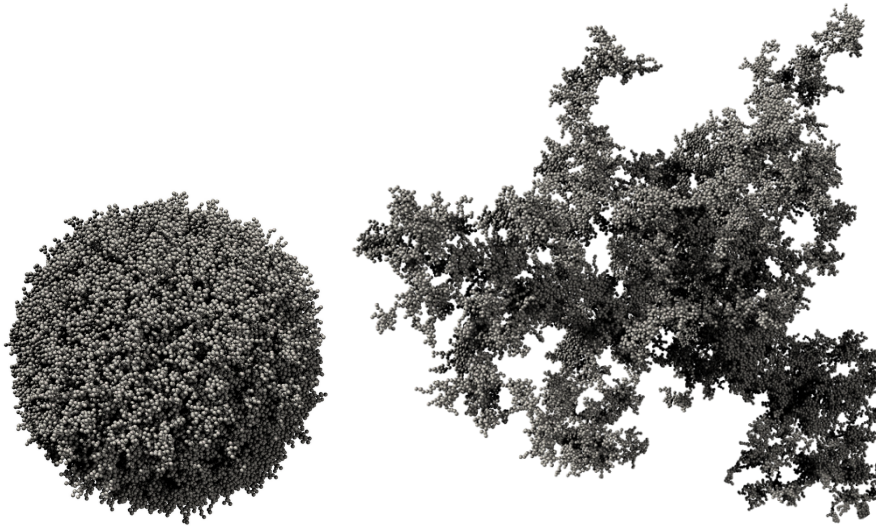

Figuur 7.3: Computermodellen van stofdeeltjes van ∼100 μm groot, opgebouwd uit ongeveer honderdduizend balletjes. Verschillen in het groeiproces kunnen leiden tot heel verschillende structuren: het linker aggregaat is compact en sferisch, het rechter is veel poreuzer en heeft een complexere structuur. Figuren uit Seizinger et al. (2013).

pact en een poreus stofdeeltje zien die zijn gemaakt in verschillende computersimulaties. Als stofdeeltjes niet compact zijn maar poreus, met een lage interne dichtheid, heeft dit serieuze gevolgen voor hun toekomst in de protoplanetaire schijf. Neem als voorbeeld hagel en sneeuw: allebei gemaakt van water en allebei te vinden in de atmosfeer van de Aarde. De poreuze structuur van sneeuw maakt dat het heel andere eigenschappen heeft dan een korrel hagel. Ten eerste is sneeuw plakkeriger (probeer maar eens een sneeuwpop te maken uit hagelstenen). Ten tweede ondervindt een poreus sneeuwdeeltje een andere wrijving van het gas om zich heen. Zo komen hagelstenen met een veel hogere snelheid uit de hemel vallen dan sneeuwvlokken. Dit heeft alles te maken met het verschil in luchtweerstand die beide deeltjes ondervinden. In een protoplanetaire schijf gebeurt iets vergelijkbaars: poreuze deeltjes koppelen beter aan het turbulente gas dan compacte deeltjes. Dit heeft grote gevolgen voor de botsingssnelheden en voor het probleem van de tegenwind. Deze effecten samen hebben tot gevolg dat stofkorrels met een hoge porositeit beter lijken te zijn in het uitgroeien tot planetesimalen.

Dit proefschrift

De porositeit van groeiende stofdeeltjes is dus belangrijk voor de eerste stappen richting de vorming van nieuwe planeten. Maar wat bepaalt hoe poreus een deeltje daadwerkelijk

is? En hoe beïnvloedt de porositeit de toekomst van het deeltje? Dat zijn de kernvragen van dit proefschrift.

Hoofdstuk 1 geeft een algemene introductie over ster- en planeetvorming. In de hoofdstukken 2 en 3 kijken we naar de krachten die een rol spelen in het contact tussen twee balletjes met een grootte van ongeveer een micrometer. Een goed begrip van deze krachten is erg belangrijk voor het bestuderen van grotere stofkorrels, die kunnen worden beschreven als verzamelingen van vele miljoenen microscopische balletjes (figuur 7.3). Door een theoretisch model te ontwikkelen en voorspellingen van dit model te vergelijken met beschikbare experimentele data over stuiterende (hoofdstuk 2) en rollende (hoofdstuk 3) balletjes hebben we een beter begrip van de onderliggende fysica verkregen. Deze modellen wordt nu gebruikt om simulaties tussen grotere stofkorrels realistischer te maken.

In de hoofdstukken 4 en 5 gebruiken we de opgedane kennis om stofgroei te simuleren in een protoplanetaire schijf. In hoofdstuk 4 richten we ons op een klein, lokaal stukje van de schijf, waarbinnen we proberen zo veel mogelijk van de aanwezige stofkorrels te volgen terwijl hun massa en porositeit evolueert door de vele botsingen. We gebruiken hiervoor een speciale methode (ontwikkeld door Ormel & Spaans 2008), die ons in staat stelt enorme aantallen deeltjes te volgen terwijl ze groeien van minder dan een micrometer tot meerdere kilometers in doorsnede, een massatoename van meer dan 30 ordes van grootte! We concluderen dat poreuze en ijzige stofdeeltjes inderdaad erg efficiënt kunnen groeien, maar dat erosie door kleinere deeltjes hierbij een probleem kan vormen. Toekomstig onderzoek, met name naar de botsingssnelheid die nodig is voor erosie, moet uitwijzen of dit proces inderdaad een onoverkomelijk obstakel vormt. In hoofdstuk 5 kijken we alleen naar de stofdeeltjes die de massa domineren, en ontwikkelen we een nieuwe methode om poreuze stofgroei te simuleren in een volledige schijf. Met het nieuwe model kunnen we laten zien in welke gebieden van de protoplanetaire schijf succesvolle vorming van planetesimalen mogelijk is. Bovendien is de methode erg flexibel, waardoor de invloed van verschillende eigenschappen van de schijf (zoals temperatuur, massa, etc.) op een snelle manier kan worden bestudeerd.

Tot slot kijken we in hoofdstuk 6 naar de deeltjesverdeling in zogeheten puinschijven. Deze schijven, vaak honderden miljoenen jaren oud, zijn de overblijfselen van protoplanetaire schijven, en hebben wel iets weg van de asteroïde-gordel in ons zonnestelsel. Het meeste gas is allang vervlogen, en de schijven bestaan voornamelijk uit oude planetesimalen die continu nieuwe kleine stofkorrels aanmaken in destructieve botsingen. Het bestuderen van deze puinschijven is interessant omdat de oude planetesimalen informatie bevatten over hun formatie.

In hoofdstuk 7 worden de belangrijkste resultaten van dit proefschrift samengevat en worden een aantal interessante mogelijkheden voor vervolgonderzoek besproken.

Acknowledgements

When I started my PhD little over four years ago, I had no idea how I was ever going to complete such a task. What I did not realize however, was how much help and support I would receive from the people around me. Not just with the scientific part, but with everything surrounding it. I cannot possibly thank everyone that contributed, but a few people should not go unmentioned.

First, I must thank Carsten and Xander for giving me this opportunity. The many discussions we had together were as much fun as they were enlightening, and without your guidance, focus, and sense of humor, the past four years would have been much less productive, and – more importantly – much less amusing.

Chris, I owe a great deal to your involvement. Your 'Ormellian' approach to scientific problems has influenced me a lot. Thank you for those long discussions in front of the blackboard, and for always making time for me when I was confused (again). Mihkel, your never-ending enthusiasm and curiosity about everything scientific have been truly inspirational. It was great fun to join forces and work together, and I hope we can keep collaborating in the future.

I also owe a lot to my collaborators and colleagues outside the Netherlands. Carsten, Daniel, and Jürgen, thank you for introducing me to the wonderful world of laboratory collision experiments, and for your hospitality during several visits to Braunschweig. Alexander, your simulations and movies are awesome, and I enjoyed working with you. Of course, some of the most memorable experiences where the conferences and work visits abroad, and I thank everyone involved for making those trips a success.

In Leiden, I was lucky to be surrounded by so many bright and open-minded people. Thank you Matteo, Mattia, Marissa, Tiffany, Paola, Xiaohu, Irene, Daniel, Monica, Marco, Gilles, Berenice, Pedro, Nicola, Steven, Jesse, Emanuele, Nienke, Willem, Alex, and all the other friends at the Sterrewacht for the countless coffee breaks, lunches, borrels, beers and parties. Thanks also to Heather, Pablo, Suklima, Francisco, Silvia, Annemieke, Lynn, Isabel, Ainil, and the other ISM-group members for the many diverse and interesting meetings, and to 'the Unbittens' for that glorious day in the summer of 2014. Bram, what can I say, it has been fantastic to meander through the Bachelor, Master, and

now PhD together. You've been a brilliant amigo, and I am thankful for the many highs and lows – actually, I can only remember highs – we shared along the way. My time at the Sterrewacht was made especially enjoyable by my fellow inhabitants of office 404. I always felt at home there, and will certainly miss the atmosphere you guys created, and the office lunches and dinners we shared. Caroline and Paula, thank you for making sure there was never a shortage of hugs and sweets. Carl, thanks for always being cheerful. Your contagious laugh and powerful forehand – especially when combined – made you a formidable opponent on the tennis court. I wish you all the very best.

I also enjoyed spending time at the Anton Pannekoek Institute in Amsterdam. Thank you APIs, for making me feel part of your institute whenever I dropped in. For someone who often skips breakfast, the weekly cookie meetings (with their mix of healthy discussions and not-so-healthy foods) were the best possible start to the day. For that, I thank Tomas, Rik, Gijs, Koen, Lucas, Michiel, Rens, Theo, Lucia, Kaustubh, and all the other cookie aficionados, past or present.

Dealing with the stresses and strains that come with finishing a dissertation was made that much easier by a special group of friends and family. Special thanks to all my buddies from the Huygenslyceum; the Physics and Astronomy program at the UvA; the members of Lokomotiv Seedorf, de Argonauten, and DVVA10; and everyone else who helped me stay relaxed and optimistic. I would like to thank my brother for helping design these pages, my sister for supporting me as my paranimf, and my entire family, včetně báby a dády a ostatních členů české větve, for their interest and encouragement. This includes of course my in-laws, your curiosity and enthusiasm were great. Finally, I want to thank my parents for their unlimited support, for raising me the way they did, and for teaching me that the most important thing in life is doing something you enjoy. In many ways, this thesis should be attributed to all of you.

Lastly, Florie, thank you for being my better half for the past five years. I cannot imagine how I would have fared without you at my side, and I look forward to our future together, wherever that may be.